

Springer Series in Geomechanics and Geoengineering

Elena Pasternak
Arcady Dyskin *Editors*

Multiscale Processes of Instability, Deformation and Fracturing in Geomaterials

Proceedings of 12th International
Workshop on Bifurcation and
Degradation in Geomechanics

 Springer

Springer Series in Geomechanics and Geoengineering

Series Editor

Wei Wu, Universität für Bodenkultur, Vienna, Austria

Geomechanics deals with the application of the principle of mechanics to geomaterials including experimental, analytical and numerical investigations into the mechanical, physical, hydraulic and thermal properties of geomaterials as multiphase media. Geoengineering covers a wide range of engineering disciplines related to geomaterials from traditional to emerging areas.

The objective of the book series is to publish monographs, handbooks, workshop proceedings and textbooks. The book series is intended to cover both the state-of-the-art and the recent developments in geomechanics and geoengineering. Besides researchers, the series provides valuable references for engineering practitioners and graduate students.

Indexed by SCOPUS, EI Compendex, INSPEC, SCImago.

Elena Pasternak · Arcady Dyskin
Editors

Multiscale Processes of Instability, Deformation and Fracturing in Geomaterials

Proceedings of 12th International Workshop
on Bifurcation and Degradation
in Geomechanics

 Springer

Editors

Elena Pasternak
Department of Mechanical Engineering
University of Western Australia
Crawley, WA, Australia

Arcady Dyskin
Department of Civil, Environmental
and Mining Engineering
University of Western Australia
Crawley, WA, Australia

ISSN 1866-8755

ISSN 1866-8763 (electronic)

Springer Series in Geomechanics and Geoengineering

ISBN 978-3-031-22212-2

ISBN 978-3-031-22213-9 (eBook)

<https://doi.org/10.1007/978-3-031-22213-9>

© The Editor(s) (if applicable) and The Author(s), under exclusive license to Springer Nature Switzerland AG 2023

This work is subject to copyright. All rights are solely and exclusively licensed by the Publisher, whether the whole or part of the material is concerned, specifically the rights of translation, reprinting, reuse of illustrations, recitation, broadcasting, reproduction on microfilms or in any other physical way, and transmission or information storage and retrieval, electronic adaptation, computer software, or by similar or dissimilar methodology now known or hereafter developed.

The use of general descriptive names, registered names, trademarks, service marks, etc. in this publication does not imply, even in the absence of a specific statement, that such names are exempt from the relevant protective laws and regulations and therefore free for general use.

The publisher, the authors, and the editors are safe to assume that the advice and information in this book are believed to be true and accurate at the date of publication. Neither the publisher nor the authors or the editors give a warranty, expressed or implied, with respect to the material contained herein or for any errors or omissions that may have been made. The publisher remains neutral with regard to jurisdictional claims in published maps and institutional affiliations.

This Springer imprint is published by the registered company Springer Nature Switzerland AG
The registered company address is: Gewerbestrasse 11, 6330 Cham, Switzerland

Committees

Organising committee

Elena Pasternak, Australia
Arcady Dyskin, Australia
Rui Xiang Wong, Australia
Maoqian Zhang, Australia

Advisory Board

R. I. Borja, USA
F. Darve, France
J. Desrues, France
H-B. Muhlhaus, Australia
F. Nicot, France
R. Wan, Canada

International Scientific Committee

M. Alsaleh, USA
A. Daouadji, France
A. V. Dyskin, Australia
D. Kolymbas, Austria
A. Murakami, Japan
E. Papamichos, Greece
E. Pasternak, Australia
A. P. S. Selvadurai, Canada

A. Tordesillas, Australia
K. T. Chau, Hong Kong
C. di Prisco, Italy
M. Guttierrez, USA
D. Muir Wood, UK
F. Oka, Japan
P. Papanastasiou, Cyprus
F. Radjai, France
J. Tejchman, Poland
T.-F. Wong, Hong Kong
W. Wu, Austria
J. D. Zhao, Hong Kong

Workshop Chairs

Elena Pasternak, University of Western Australia
Arcady V. Dyskin, University of Western Australia

Preface

The book is a collection of contributions to the 12th International Workshop on Bifurcation and Degradation in Geomechanics (IWBDG2022) held 28 November–1 December 2022 (scheduled for the year 2020 but moved to 2022 due to COVID restrictions) at the University of Western Australia, in Perth, Australia. IWBDG2022 continues the series of workshops started in Karlsruhe, Germany, in February 1988. Since then, the workshops were held in Gdansk, Poland, September 1989; Aussois, France, September 1993; Gifu, Japan, September 1997; Perth, Australia, November 1999; Minneapolis, USA, June 2002; Crete, Greece, June 2005; Lake Louise, Canada, May 2008; Porquerolles Island, France, May 2011; Hong Kong, China, May 2014; and Limassol, Cyprus, May 2017. The proceedings are published in Springer Series in Geomechanics and Geoengineering. The papers report new achievements in the theoretical and experimental investigation of instability, bifurcation, localisation and fracturing in geomaterials and the accompanying seismicity with applications to the analysis and monitoring of dangerous deformations and failures in geomaterials and engineering structures. The papers present recent advances in theoretical and experimental methods. Each paper is peer-reviewed by two experts in the field. The book is intended for academics, engineers and research students, working in the fields of geomechanics, rock mechanics and geotechnical engineering.

We thank all authors for their timely submission and participation in IWBDG2022, the reviewers of the papers and members of Scientific and Organising Committees for their support.

Crawley, WA, Australia

Elena Pasternak
Arcady Dyskin

Contents

Localisation and Instability in Geomaterials

Mechanical Stability Analysis of Engineering Structures with Use of the Bifurcation Domain Concept	3
Antoine Wautier, Anthony Mouyeaux, François Nicot, Richard Wan, and Félix Darve	
Predicting Bifurcation Using Implicit Integration of Constitutive Relations	13
Marte Gutierrez and Randall Hickman	
Finite Element Continuation Analysis for Cnoidal Waves in Solids	24
Thomas Poulet, Roberto J. Cier, Sergio Rojas, Manolis Veveakis, and Victor M. Calo	
Spatiotemporal Evolution of Strain and Compaction Localization in Leitha Limestone: Synchrotron Tomographic Imaging and Digital Volume Correlation	31
Fanbao Meng, Lingcao Huang, Patrick Baud, and Teng-fong Wong	
Prediction of the Onset and Orientation of Shear Bands in Partially Saturated Soils Using a Coupled Hydro-Mechanical Model	41
Dat G. Phan, Giang D. Nguyen, Ha H. Bui, and Terry Bennett	
Identification of Creep-Quake Cycles in Calcareous Sands	51
Leonardo Crespo-Parraga, François Guillard, and Itai Einav	
Liesegang Patterns Interpreted as a Chemo-Hydromechanical Instability	59
Chong Liu, Manman Hu, and Klaus Regenauer-Lieb	
Cross-Scale Dynamic Interactions in Compacting Porous Geomaterials as a Trigger to Instabilities	67
Qingpei Sun, Manman Hu, and Klaus Regenauer-Lieb	

Instability of Granular Soil Under Conventional Triaxial and Constant Stress Paths	74
N. Benahmed, J. Zuo, and A. Wautier	
Fracturing, Failure and Seismicity	
Influence of Crystalline Structure on Strength Anisotropy of Silica Sand	87
Wadi H. Imseeh, Khalid A. Alshibli, Peter Kenesei, and Hemant Sharma	
The Role of Seismic Slip Velocity in the Evolution of Shear Band Thickness	99
Alexandros Stathas and Ioannis Stefanou	
Modelling of Hydraulic Fracturing in Rocks in Non-isothermal Conditions Using Coupled DEM/CFD Approach with Two-Phase Fluid Flow Model	114
M. Krzaczek, M. Nitka, and J. Tejchman	
A Mechanism of Unstable Growth of Hydraulic Fractures in Laboratory Experiments	127
Arcady V. Dyskin, Elena Pasternak, and Junxian He	
Asymptotic Modelling of Fractures with Constricted Opening	136
Elena Pasternak and Arcady V. Dyskin	
An Experimental Study on Silt Desiccation Cracking with Different Basal Constraints and Various Humidity	144
Ruoyu Chen, Winston Lindqwister, Tomasz Hueckel, and Manolis Veveakis	
Modeling Fault Rupture Through Layered Geomaterials with SPH	155
Enrique M. del Castillo, Alomir H. Fávero Neto, and Ronaldo I. Borja	
Progressive Failure in Viscoplastic Materials: The Case of Creeping Landslides	162
Luca Flessati and Claudio di Prisco	
Implication of Different Types of Post-peak Behaviour in Lateral Direction on Failure of Class II Rocks in Uniaxial Compression	173
H. Wang, B. Jeffcoat-Sacco, P. Dight, A. V. Dyskin, and E. Pasternak	
Anomalous Fall-Off in Velocity Power Spectra Caused by Sliding with Asymmetric Friction	182
Rui X. Wong, Elena Pasternak, and Arcady V. Dyskin	

Deformation Processes

Validity and Stability of Alternative Effective Stress—Specific Volume Relationship for Sands 193
 Tomislav Ivšić and Dunja Perić

Predicting the Yield Stress of Geomaterials from Their Microstructure 205
 Martin Lesueur, Xinrui Zhang, Thomas Poulet, and Manolis Veveakis

Perturbations in Granular Materials: Subtleties in DEM Modeling 212
 Mojtaba Farahnak, Richard Wan, Mehdi Pouragha, and François Nicot

Modelling of Capillary Pressure-driven Water Flow in Unsaturated Concrete Using Coupled DEM/CFD Approach 220
 Marek Krzaczek, Michał Nitka, and Jacek Tejchman

DEM Analyses of Interface Behaviour Between Cohesionless Sand and Rigid Wall of Different Roughness 230
 Aleksander Grabowski, Michał Nitka, and Jacek Tejchman

Modelling Recurrent Stress Drops in Porous Media 240
 David Riley, Itai Einav, and François Guillard

Multiscale Modeling of Elasto-Plasticity in Heterogeneous Geomaterials Based on Continuum Micromechanics 251
 Mahdad Eghbalian, Mehdi Pouragha, and Richard Wan

Author Index 259

Localisation and Instability in Geomaterials



Mechanical Stability Analysis of Engineering Structures with Use of the Bifurcation Domain Concept

Antoine Wautier¹✉, Anthony Mouyeaux¹, François Nicot^{2,3}, Richard Wan⁴,
and Félix Darve⁵

¹ INRAE, Aix Marseille University, UMR RECOVER, Aix-en-Provence, Marseille, France
antoine.wautier@inrae.fr

² Université Grenoble Alpes, INRAE, UR ETNA, St-Martin-d'Hères, France

³ Laboratoire EDYTEM - USMB/CNRS, UMR 5204, Université Savoie Mont Blanc, Le
Bourget-du-Lac, France

⁴ Civil Engineering Department, University of Calgary, Calgary, AB, Canada

⁵ Laboratoire 3SR UMR5521, Université Grenoble Alpes, CNRS, G-INP, Grenoble, France

Abstract. Because of their non-associated plastic behavior, the failure modes of geomaterials are much more diverse than those of materials following associated plasticity. For instance, it is well established that failure can occur before reaching the plastic limit surface and before the vanishing of the determinant of the acoustic tensor. This is well illustrated by the static liquefaction of loose sand subjected to undrained triaxial tests in the lab or by the recent failure of Brumadinho dam in 2019. In the wake of the pioneering work of Hill [4], the second-order work criterion, as proposed by Nicot et al. [11], Wan et al. [18], has been shown to be the most general criterion to anticipate failure for non-associated materials. This criterion defines a bifurcation domain corresponding to a set of states for which there exists a potential for failure if (i) the material is subjected to an incremental load leading to the vanishing of the second-order work, (ii) the mode of control allows for an inertial transition through a sudden burst of kinetic energy. In this work, it is proposed to extend the concept of bifurcation domain from the material point scale to the engineering structure scale. In this respect, an earth dam is modeled using the finite element software Cast3M [3]. By virtue of directional analyses carried out both numerically and analytically at different location points in the dam body, the set of material points that belongs to the bifurcation domain is identified. This enables us to map the spatial domain of the dam where conditional failure may occur. This map can be used to anticipate unsafe changes in loading conditions on the dam boundaries. Such a contribution proposes a modern and innovative view of failure in geomaterials at the engineering scale, in particular with respect to the risk of liquefaction.

Keywords: Mechanical stability · Second-order work criterion · Engineering scale · Liquefaction

1 Introduction

A correct design of engineering structures relies on an accurate prediction of failure modes. Historically, the mechanical stability analysis of earth dikes or dams has been assessed thanks to Limit Equilibrium Methods (LEM) [2, 15, 16]. Such methods postulate the existence of a failure surface with a given geometry (usually circular) and the equilibrium of the expected sliding mass is solved by dividing it into slices in contact. Repeating the procedure for several failure surfaces enables us to assess the stability of the structure. In this approach, the failure mechanism is postulated a priori, which leads to the definition of an upper bound for mechanical stability. Since there could exist other failure mechanisms not accounted for, safety margins are considered with the use of a large safety factor (the ratio between resistive forces over the maximal resistive forces allowed by the sliding criterion). LEM methods are still frequently used in engineering approaches, because of their simplicity and even if they generally lead to overdesign.

With the increase in computer power, more refined methods were proposed based on the use of Finite Element Modeling (FEM). Based on the knowledge of the material constitutive behaviors and the designed geometry, stress and strain fields can be computed. Zones in which the mechanical state is close to the failure limit are then identified, as well as potential failure surfaces. As long as the numerical computation converge, the static equilibrium of the structure is obtained. In this sense, FEM provides a lower bound for mechanical stability. However, to account for uncertainties in determining material properties, a safety factor is also used. In FEM framework, it can be defined with the use of the shear strength reduction technique [21]. This technique consists in decreasing the shear resistance of the soil until failure occurs, which is often detected in practice from a lack in numerical convergence.

In both cases, the standard engineering methods used to assess the mechanical stability of earth dikes or dams relate the current stress state to the plastic ultimate state that the soil can bear without considering any perturbation. However, geomaterials are known to exhibit a non-associated plastic behavior. As a result, their failure modes are much more diverse than those of materials following associated plasticity. They can fail before reaching the plastic limit surface through the formation of shear bands for instance, or through static liquefaction. The formation of shear bands is well detected by the vanishing of the determinant of the acoustic tensor [8, 14] but not the static liquefaction (frequently observed for loose sand subjected to undrained triaxial tests) which requires the use of the second-order work criterion [4, 11, 18, 19]. The second-order work criterion corresponds to the loss of positive definitiveness of the elasto-plastic matrix, i.e. when the determinant of the symmetric part of this matrix is negative. For associated plasticity, the elasto-plastic matrix is symmetric and material bifurcations appear therefore on the plastic limit surface. But for non-associated plasticity, the vanishing of the second-order work occurs strictly before the plastic limit conditions is fulfilled and before the vanishing of the acoustic tensor [1, 18]. Under the assumptions of small strains and negligible geometrical effects, the second-order work criterion reads:

$$\exists(d\boldsymbol{\sigma}, d\boldsymbol{\varepsilon}) \text{ linked by the constitutive behavior such that } W_2 = d\boldsymbol{\sigma} : d\boldsymbol{\varepsilon} < 0 \quad (1)$$

The second-order work criterion defines the concept of bifurcation domain at the material point scale which corresponds to the set of states (defined by states variables) for which

conditional failure is expected [17, 18]. For such states, a proper loading direction and a proper mode of control will trigger material failure in the form of an inertial transition from a quasi-static to a dynamic regime [19]. Such potential for failure is assessed at the material point scale thanks to the use of directional analyses [19], which consists in applying any possible stress or strain perturbation from a reference state, recording the material response and evaluating the sign of the corresponding second order work.

At the engineering structure scale, the vanishing of the second-order work was used so far only along a given loading path in order to anticipate the failure of the structure [5, 7, 10, 13, 20]. Such approaches have proved to be relevant to detecting the onset of instabilities when the engineering structure is subjected to a monotonic change of its boundary conditions, but such approaches fails to predict whether there exists any critical incremental perturbations detrimental to safety for a structure at equilibrium initially. To the best of our knowledge, only the work of Prunier, Laouafa et al. [6, 12] provided some clues to answer this question at the scale of an engineering structure, by observing the vanishing of the determinant of the global stiffness matrix that relates to unknown degrees of freedom of a FEM problem. Such an approach is however computationally demanding because the size of the matrix is huge.

The present work intends to apply the concept of bifurcation domain at the engineering structure scale. FEM simulations are conducted for a dam made of a non-associated Drucker-Prager elasto-plastic material. For each point of the dam, strain control directional analyses are conducted from an analytical point of view to detect which points of the dam are in the bifurcation domain from a material scale viewpoint. By analyzing the directions of the instability cone thus detected, the existence of potential internal failure surfaces are estimated. The present study intends to generalize the use of second-order work at the scale of an engineering structure, and the notion of conditional stability in mechanical stability analyses. In the context of dam safety, we hope that our methodology may be used to better anticipate failure through static liquefaction as illustrated by the Brumadinho dam failure in 2019 in Brazil.

2 Dam Modeling with FEM

In this study, a simple trapezoidal dam is modeled in plane strain conditions with the finite element software Cast3M [3]. The dam body and the foundation are both assumed to behave as a standard non-associated elasto-plastic material following Drucker-Prager criterion. The constitutive behavior is summarized as

$$\left\{ \begin{array}{ll} \text{Elasticity (Hooke law)} : & \boldsymbol{\sigma} = \lambda \text{Tr}(\boldsymbol{\epsilon}^e) \mathbf{1} + 2\mu \boldsymbol{\epsilon}^e \\ \text{Strain decomposition:} & \boldsymbol{\epsilon} = \boldsymbol{\epsilon}^e + \boldsymbol{\epsilon}^p \\ \text{Drucker-Prager yield surface:} & f(\boldsymbol{\sigma}) = \alpha \text{Tr}(\boldsymbol{\sigma}) + \sigma_{eq} < K \\ \text{Drucker-Prager plastic potential:} & g(\boldsymbol{\sigma}) = \beta \text{Tr}(\boldsymbol{\sigma}) + \sigma_{eq} \\ \text{Non-associated flow rule:} & \dot{\boldsymbol{\epsilon}}^p = \dot{\eta} \frac{\partial g}{\partial \boldsymbol{\sigma}} = \dot{\eta} \left(\beta \mathbf{1} + \frac{3}{2} \frac{\boldsymbol{\sigma}}{\sigma_{eq}} \right), \quad \dot{\eta} \geq 0 \\ \text{Hardening (not activated)} : & \dot{K} = H \dot{\epsilon}_{eq}^p, \quad K \in [K_0, K_{max}] \end{array} \right. \quad (2)$$

In the above equations, the invariants σ_{eq} and ϵ_{eq}^p are expressed as $\sigma_{eq} = \sqrt{\frac{3}{2} \boldsymbol{s} : \boldsymbol{s}}$ with $\boldsymbol{s} = \boldsymbol{\sigma} - \frac{1}{3} \text{Tr}(\boldsymbol{\sigma}) \mathbf{1}$ the deviatoric stress tensor, and $\epsilon_{eq}^p = \sqrt{\frac{2}{3} \boldsymbol{\epsilon}_{dev}^p : \boldsymbol{\epsilon}_{dev}^p}$ with $\boldsymbol{\epsilon}_{dev}^p = \boldsymbol{\epsilon}^p -$

$\frac{1}{3}\text{Tr}(\mathbf{e}^p)\mathbf{1}$ the deviatoric part of the plastic strain. In all this study, continuum mechanics sign convention is used with positive traction and extension. Note that hardening can be accounted for if $H > 0$.

In plane strain conditions, the plastic coefficients α , β and K can be expressed in terms of friction angle φ , cohesion c' and dilatancy angle ψ (see for instance [9]), while the elastic Lamé coefficients relates to Young's modulus E and Poisson's ratio ν as:

$$\left\{ \begin{array}{l} \lambda = \frac{Ev}{(1+\nu)(1-2\nu)} \\ \mu = \frac{E}{2(1+\nu)} \end{array} \right., \quad \left\{ \begin{array}{l} \alpha = \frac{\sqrt{3} \tan \varphi}{\sqrt{9+12 \tan^2 \varphi}} \\ \beta = \frac{\sqrt{3} \tan \psi}{\sqrt{9+12 \tan^2 \psi}} \\ K_0 = \frac{3\sqrt{3}c'}{\sqrt{9+12 \tan^2 \varphi}} \end{array} \right. . \quad (3)$$

The material parameters and the geometrical characteristics of the dam are summarized in Table 1. The dam has a drainage system located on the interface with the foundation and starting 10 m downstream from the middle of the crest.

The static equilibrium of the dam is computed with a simplified two steps procedure:

1. In the first step, gravity is progressively increased while the water reservoir remains empty. The dam geometry is set once for all and the construction of a real dam in lifts is not accounted for. Thus, this step corresponds to an approximate modeling of the dam construction.
2. Then, a pore water pressure field is applied by gradually increasing the pore water pressure from zero to the values corresponding to a column of 7 m in the dam reservoir. This step corresponds roughly to the filling of the dam reservoir. The water pressure field is obtained from a separate hydraulic simulation performed in Cast3M with an horizontal hydraulic permeability of 10^{-6} m/s in the dam body and in the foundation and of 10^{-3} m/s in the drainage system. In both cases, anisotropic permeability is considered with the vertical permeability being ten times larger. The pore water pressure field is applied in the form of external forces on the mesh elements according to local pressure gradients.

Once the mechanical equilibrium is achieved, the stress and strain fields are extracted to be analyzed from a material point scale with respect to the concept of bifurcation domain.

3 Material Scale Stability Analysis

If we limit our analyses to divergence instabilities, it is well established that the most general criterion to study these bifurcations is the so-called *second-order work criterion* (1) as introduced by Hill [4] and reviewed extensively in [18]. Based on this definition, the mechanical stability of a material is assessed thanks to directional analyses. For instance, this can be performed in the strain space, by imposing $d\boldsymbol{\varepsilon}$ and recording $d\boldsymbol{\sigma}$ according to the constitutive behavior. In the most general case, $d\boldsymbol{\varepsilon}$ resides in a space of six dimensions. However, by considering the principal strain directions, the directional

Table 1. Material parameters and the geometrical characteristics of the dam.

	E (MPa)	ν	φ ($^{\circ}$)	ψ ($^{\circ}$)	c' (kPa)	H (kPa)	ρ (kg m^{-3})	Height (m)	Crest width (m)	Slopes
Dam	45	0.35	25	12	5	0	2150	10	6	1.25 H/1 V
Foundation	50	0.35	25	12	5	0	2150	–	–	–

analysis can be restricted to the diagonal $d\boldsymbol{\varepsilon}$ with only three independent components. By use of the spherical coordinates, $d\boldsymbol{\varepsilon}$ is imposed as:

$$\begin{cases} d\varepsilon_I = d\varepsilon \cos \phi \sin \theta \\ d\varepsilon_{II} = d\varepsilon \sin \phi \sin \theta \\ d\varepsilon_{III} = d\varepsilon \cos \theta \end{cases} \quad (4)$$

with $\theta \in [0, \pi]$ and $\phi \in [0, 2\pi]$. θ and ϕ correspond to the *direction* of the incremental strain perturbation in the principal strain space.

For the constitutive behavior summarized in Eq. (2), an analytical expression can be derived for W_2 . The expression depends on whether plasticity is activated, the plasticity activation condition being $f(\boldsymbol{\sigma} + d\boldsymbol{\sigma}^e) > K$ where $d\boldsymbol{\sigma}^e = \lambda \text{Tr}(d\boldsymbol{\varepsilon})\mathbf{1} + 2\mu d\boldsymbol{\varepsilon}$.

– In the elastic case, $f(\boldsymbol{\sigma} + d\boldsymbol{\sigma}^e) < K$, and the second-order work reads:

$$W_2^e = K_{comp} \text{Tr}^2(d\boldsymbol{\varepsilon}) + 2\mu \|d\boldsymbol{\varepsilon}_{dev}\|^2 \quad (5)$$

– In the plastic case, $f(\boldsymbol{\sigma} + d\boldsymbol{\sigma}^e) > K$, and the second-order work reads:

$$W_2^p = W_2^e - \frac{\left[\frac{f(\boldsymbol{\sigma}) - K}{3} + \alpha K_{comp} \text{Tr}(d\boldsymbol{\varepsilon}) + \mu \frac{s : d\boldsymbol{\varepsilon}_{dev}}{\sigma_{eq}} \right] \left[\beta K_{comp} \text{Tr}(d\boldsymbol{\varepsilon}) + \mu \frac{s : d\boldsymbol{\varepsilon}_{dev}}{\sigma_{eq}} \right]}{\alpha \beta K_{comp} + \frac{\mu}{3} + \frac{H}{9} \frac{s : d\boldsymbol{\varepsilon}_{dev}^p}{\sigma_{eq} \varepsilon_{eq}^p}} \quad (6)$$

In the above equations, $K_{comp} = \lambda + 2\mu/3$ is the compressibility modulus, $d\boldsymbol{\varepsilon}_{dev}$ and s the deviatoric parts of the incremental strain and the stress tensors respectively.

Note that, plasticity needs to be activated in order to observe the vanishing of the second-order work in (6) as $W_2^e \geq 0$. In that case, it is interesting to underline that hardening ($H > 0$) will limit the possibility to observe the vanishing of the second-order work in (6). If the initial state is on the plastic yield surface ($f(\boldsymbol{\sigma}) = K$), Eq. (6) simplifies a little. And for the case of associated plasticity ($\alpha = \beta$) with no hardening ($H = 0$), the use of Cauchy-Schwarz inequality shows that W_2 is always greater or equal to zero¹.

Based on the analytical expression given in Eqs. (5) and (6), the normalized second-order work $W_2^{norm} = \frac{W_2}{\|d\boldsymbol{\sigma}\| \|d\boldsymbol{\varepsilon}\|}$ can be plotted with a spherical representation for all the points of the dam body as illustrated in Fig. 1.

In Fig. 1, an elliptical cone of instability is observed in the principal strain space for some points of the dam for incremental loading directions corresponding generally to $d\varepsilon_I > 0$ (extension), $d\varepsilon_{II} < 0$ (compression) and $d\varepsilon_{III} > 0$ (extension). Such results are consistent with the usual instability cone directions observed in the literature [13, 19]. In the case where $d\varepsilon_I + d\varepsilon_{II} = 0$ (close to the situation observed in Fig. 1, the cone direction corresponds to pure shear in the plane (e_I, e_{II}) with an extension in the out of plane direction. The elliptical shape of the instability cone has been previously reported in [13] for different constitutive relations.

¹ Vanishing requires $d\boldsymbol{\varepsilon}_{dev}^p$ to be positively co-linear to s and $\text{Tr}(d\boldsymbol{\varepsilon}) = \alpha \sqrt{6} \|d\boldsymbol{\varepsilon}_{dev}^p\| > 0$ (increase in volume).

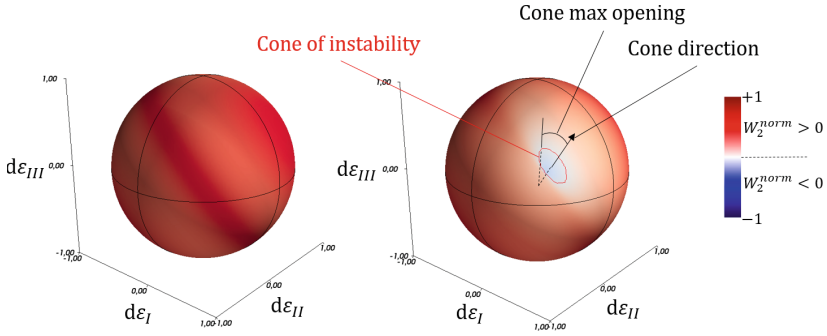


Fig. 1. Spherical representation in the principal strain space of the normalized second-order work for two points of the dam body: out of (left) and in (right) the bifurcation domain. The set of loading directions with $W_2 < 0$ forms an elliptic cone of instability characterized by a mean direction and a maximal opening angle.

4 Bifurcation Domain Definition and Instability Cone Directions

In the previous section, the mechanical stability was assessed from a material scale viewpoint. In order to assess the mechanical stability of an engineering structure according to Eq. (1), there is a need to define the bifurcation domain Ω_{bif} of an engineering structure

$$\begin{aligned} \mathbf{x} \in \Omega_{bif} \text{ if and only if } \exists (\mathbf{d}\boldsymbol{\sigma}, \mathbf{d}\boldsymbol{\varepsilon}), \text{ such that} \\ \mathbf{d}\boldsymbol{\sigma} = \mathbf{C}(\boldsymbol{\sigma}(\mathbf{x})) : \mathbf{d}\boldsymbol{\varepsilon} \text{ and } W_2 = \mathbf{d}\boldsymbol{\sigma} : \mathbf{d}\boldsymbol{\varepsilon} < 0 \end{aligned} \quad (7)$$

where $\mathbf{C}(\boldsymbol{\sigma}(\mathbf{x}))$ is the tangent constitutive tensor of the material located at point \mathbf{x} .

For the points located in the bifurcation domain, there exists a set of incremental directions that will lead to material failure (provided that the imposed perturbation on the dam boundaries allows for an increase in kinetic energy). The cone direction (θ_c, ϕ_c) (illustrated in Fig. 1) corresponds to an incremental strain tensor $\mathbf{d}\boldsymbol{\varepsilon}_{cone}$ with principal strain values $(d\varepsilon_I, d\varepsilon_{II}, d\varepsilon_{III})$ expressed according to (4) and principal directions coinciding with the principal strain directions (by definition of the set of incremental strain considered in the directional analysis). Because of the plane strain condition, one principal strain direction is the out of plane direction z . The two other directions lie in the (x, y) plane and depends on the strain field.

A representation of the dam bifurcation domain together with the corresponding strain perturbation leading to the vanishing of the second order work (i.e. the cone directions) is given in Fig. 2.

For the dam considered, the bifurcation domain is quite extensive and looks consistent with the shapes of failure observed in situ. However, one can notice that most of the cone directions have a non negligible off plane component, making them not compatible with plane strain mechanisms. If we restrict the admissible failure mechanisms to plane strain conditions (this correspond to the equatorial plane in Fig. 1), the bifurcation domain is largely reduced as illustrated in Fig. 3. It no longer spans across the dam body.

As a result, we can conclude from these graphs that there exists some plausible mechanisms that can lead to the failure of the dam considered; provided that the plane

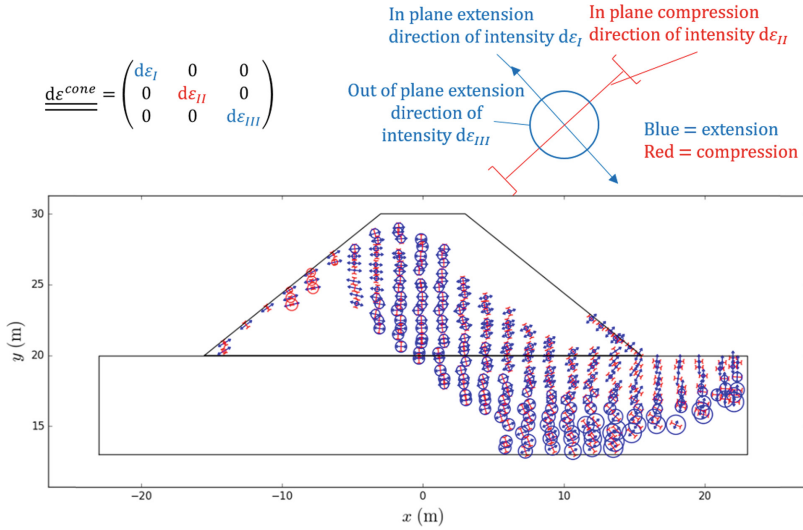


Fig. 2. Bifurcation domain of a dam. For each material point in the bifurcation domain, the cone direction is represented. Such representation corresponds to local deformation mechanisms likely to trigger underlying material instability.

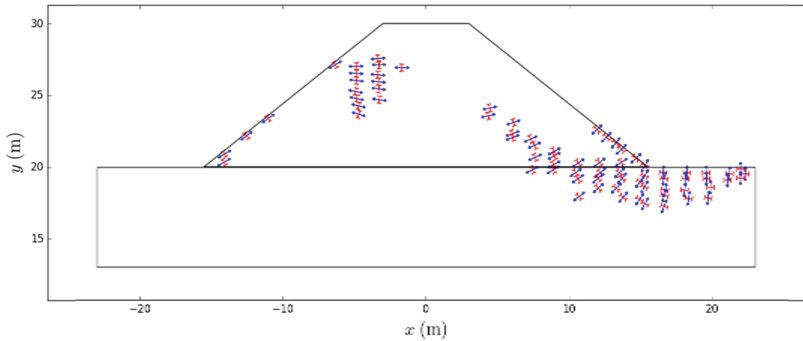


Fig. 3. Bifurcation domain of a dam restricted to plane strain perturbations. For each material point in the bifurcation domain, the plane strain cone direction is represented as in Fig. 2.

strain assumption is lifted. These mechanisms cannot develop fully without allowing an extension of the dam in the out-of-plane direction.

5 Conclusion

In this paper, we have proposed a method to extend the concept of bifurcation domain from the material scale viewpoint to the scale of engineering structures in the form of bifurcation maps. The use of this advanced criterion enables us to think outside the box to detect potential failure modes that are not accounted for in more standard approaches and with more restrictive instability criteria. In the present example, perturbations with an

out of plane extension of the dam are probably able to activate a significant proportion of the bifurcation domain. Such perturbations are likely to exist in practice since the plane strain condition is strictly valid only for a dam of infinite out of plane length. Out-of-plane extension might come for instance from displacements of the lateral supporting points or from the digging of a transverse trench in maintenance work or after overtopping erosion. A 3D FEM modeling of the dam should be considered to simulate such perturbations.

In the present study, an analytical expression of the second-order work criterion has been derived for the specific constitutive behavior of Eq. (2). However, it should be underlined that directional analyses can be performed numerically at the material point scale with any kind of rate-independent constitutive behavior. Among others, this include the use of micromechanical models [17] or even discrete element modeling (DEM) [19] in case FEMxDEM approaches are considered. A proof of feasibility has been performed in the present study (not shown here) and the analytical results of Eqs. (5) and (6) have been recovered with auxiliary FEM computations on a unit volume of material. Before conducting the directional analysis, this unit volume was pre-loaded according to the stress states encountered in the dam body.

Even if the present study highlights the potential use of the bifurcation domain concept at the scale of an engineering structure, there is now an inverse problem to solve to identify the adverse changes in the boundary conditions that will effectively trigger the underlying material instabilities. Eventually, we will need to assess whether the mode of control may allow the inertial transition to take place leading to the dam liquefaction. The answers to these questions are the last missing links to making an efficient use of the second-order work criterion in practical design of engineering structures.

References

1. Bigoni, D., Hueckel, T.: Uniqueness and localization—I. Associative and non-associative elastoplasticity. *Int. J. Solids struct.* 28(2):197–213 (1991)
2. Bishop, A.W.: The use of the slip circle in the stability analysis of slopes. *Geotechnique* 5(1), 7–17 (1955)
3. Commissariat à l’Energie Atomique (CEA) - DEN/DM2S/SEMT. Cast3M finite element code. <http://www-cast3m.cea.fr/> (2017)
4. Hill, R.: A general theory of uniqueness and stability in elastic-plastic solids. *J. Mech. Phys. Solids* 6(3), 236–249 (1958)
5. Hu, J., Li, Z., Darve, F., Feng, J.: Advantages of second-order work as a rational safety factor and stability analysis of a reinforced rock slope. *Can. Geotech. J.* 57(5), 661–672 (2020)
6. Laouafa, F., Prunier, F., Daouadji, A., Gali, H.A., Darve, F.: Stability in geomechanics, experimental and numerical analyses. *Int. J. Numer. Anal. Methods Geomech.* 35(2), 112–139 (2011)
7. Lignon, S., Laouafa, F., Prunier, F., Khoa, H., Darve, F.: Hydro-mechanical modelling of landslides with a material instability criterion. *Geotechnique* 59(6), 513–524 (2009)
8. Mandel, J.: Conditions de stabilité et postulat de drucker. In: *Rheology and soil mechanics/Rhéologie et mécanique des sols*, pp. 58–68. Springer (1966)
9. Mestat, P.: Lois de comportement des géomatériaux et modélisation par la méthode des éléments finis. *Etudes et recherches des laboratoires des ponts et chaussées-série géotechnique (GT 52)* (1993)

10. Nicot, F., Lerbet, J., Darve, F.: Second-order work criterion: from material point to boundary value problems. *Acta Mechanica* **228**(7), 2483–2498 (2017). <https://doi.org/10.1007/s00707-017-1844-1>
11. Nicot, F., Sibille, L., Darve, F.: Bifurcation in granular materials: an attempt for a unified framework. *Int. J. Solids Struct.* **46**(22–23), 3938–3947 (2009)
12. Prunier, F., Laouafa, F., Lignon, S., Darve, F.: Bifurcation modeling in geomaterials: from the second-order work criterion to spectral analyses. *Int. J. Numer. Anal. Methods Geomech.* **33**(9), 1169–1202 (2009)
13. Prunier, F., Nicot, F., Darve, F., Laouafa, F., Lignon, S.: Three-dimensional multiscale bifurcation analysis of granular media. *J. Eng. Mech.* **135**(6), 493–509 (2009)
14. Rudnicki, J.W., Rice, J.: Conditions for the localization of deformation in pressure-sensitive dilatant materials. *J. Mech. Phys. Solids* **23**(6), 371–394 (1975)
15. Sarma, S.: Seismic stability of earth dams and embankments. *Geotechnique* **25**(4), 743–761 (1975)
16. Spencer, E.: A method of analysis of the stability of embankments assuming parallel inter-slice forces. *Geotechnique* **17**(1), 11–26 (1967)
17. Veylon, G., Nicot, F., Zhu, H., Darve, F.: Microstructure incidence on the bifurcation domain topology in granular materials. *J. Eng. Mech.* **144**(6), 04018031 (2018)
18. Wan, R., Nicot, F., Darve, F.: *Failure in geomaterials: a contemporary treatise*. Elsevier (2017)
19. Wautier, A., Bonelli, S., Nicot, F.: Micro-inertia origin of instabilities in granular materials. *Int. J. Numer. Anal. Methods Geomech.* **42**(9), 1037–1056 (2018)
20. Xiong, H., Yin, Z.-Y., Nicot, F.: A multiscale work-analysis approach for geotechnical structures. *Int. J. Numer. Anal. Methods Geomech.* **43**(6), 1230–1250 (2019)
21. Zienkiewicz, O.C., Humpheson, C., Lewis, R.: Associated and non-associated visco-plasticity and plasticity in soil mechanics. *Geotechnique* **25**(4), 671–689 (1975)



Predicting Bifurcation Using Implicit Integration of Constitutive Relations

Marte Gutierrez¹ (✉) and Randall Hickman²

¹ Colorado School of Mines, Golden, CO 80401, USA
mgutierr@mines.edu

² Ikon Science, Houston, TX 77079, USA

Abstract. Implicit integration schemes for elastoplastic constitutive equations have been developed in recent years as an alternative to explicit schemes. The consistent tangent constitutive matrix \mathbf{D}^{con} that results from implicit schemes makes the global stiffness matrix consistent with the implicit integration procedure and differs from the traditional continuum tangent constitutive matrix \mathbf{D}^{ep} that results from explicit schemes. Onset of strain localization and shear banding has been traditionally predicted using the continuum tangent constitutive matrix. It is shown that different criteria for onset of shear-band formation are obtained depending on whether \mathbf{D}^{con} or \mathbf{D}^{ep} is used. It is shown that shear band prediction using \mathbf{D}^{con} is step-size dependent, and that the use of \mathbf{D}^{con} influences the predicted onset of strain localization in frictional materials. An analytical equation for prediction of the onset of shear-band formation using \mathbf{D}^{con} for the Mohr-Coulomb model is developed, and a numerical example is presented.

Keywords: Bifurcation · Constitutive relations · Strain localization

1 Introduction

The use of implicit integration schemes of elastoplastic response of geomaterials has increased in use in recent years (e.g., Runesson 1987; Jeremic and Sture 1997). The main feature of implicit algorithms is the use of the final stress point in the constitutive response in calculating all the relevant derivatives and internal variables required in the constitutive relations (Simo and Taylor 1985; Jeremic and Sture 1997). Since this point is not known in advance, a set of Newton iterations is used to advance the solution toward the final point for each load increment. In comparison, explicit integration schemes use the initial stress point to determine the derivatives and internal variables required to form the constitutive relations. Since a solution is assumed to exist, implicit methods generally guarantee that a converged solution will be obtained on the constitutive level, even for highly nonlinear models (Ortiz and Popov 1985).

The resulting discretized constitutive relation obtained using implicit schemes is called the consistent tangent operator or the consistent tangent constitutive matrix \mathbf{D}^{con} and differs considerably from the continuum tangent constitutive matrix \mathbf{D}^{ep} obtained using explicit schemes.

The use of \mathbf{D}^{con} to form the global stiffness matrix for a finite element assemblage preserves the quadratic convergence of the iterative global convergence method, and thus achieves faster convergence in finite element calculations than the use of \mathbf{D}^{ep} (Simo and Taylor 1985). \mathbf{D}^{ep} evaluates the gradients to the yield surface and to the plastic potential surface at the same stress point, namely the initial stress point. In comparison, \mathbf{D}^{con} is formulated to be consistent with the integration method, and so evaluates the gradients to the yield surface and to the plastic potential surface at different stress points. Therefore, \mathbf{D}^{con} is generally non-symmetric even when applied to models with associated flow rules. In contrast, \mathbf{D}^{ep} is only non-symmetric for non-associated flow.

Bifurcation in the stress-strain relation occurs when the acoustic tensor \mathbf{B} (defined below) becomes non-positive definite and produces negative eigenvalues for certain wave propagation directions. In bifurcation theory, such negative eigenvalues imply strain localization and instability, following Mandel's (1964) stability criterion. Rudnicki and Rice (1975) showed that non-symmetry of \mathbf{D} causes \mathbf{B} to become non-positive definite under hardening conditions, in which peak strength has not yet been mobilized.

A review of the different studies that have been performed so far reveals that, so far, implicit integration schemes and their effects on prediction of shear band formation have not been investigated. This is even though implicit schemes have gained wide acceptance and use finite element modeling. Three properties of \mathbf{D}^{con} may affect the prediction of shear band formation. These properties include: (1) non-symmetry even for associated flow, (2) reduced stiffness, and (3) step-size dependence. The effects of using \mathbf{D}^{con} instead of \mathbf{D}^{ep} to predict the onset of strain localization are investigated in this paper. The objective of this paper is to show the effects of using implicit integration in predicting the onset of strain localization in frictional-cohesive geomaterials.

2 Constitutive Equations

Constitutive relations for elastoplastic models are given by the following set of equations:

$$d\varepsilon_{ij} = d\varepsilon_{ij}^e + d\varepsilon_{ij}^p \quad (1)$$

$$d\sigma_{ij} = D_{ijkl}^e d\varepsilon_{kl}^e \quad (2)$$

$$d\varepsilon_{ij}^p = \lambda \frac{\partial g}{\partial \sigma_{ij}} \quad (3)$$

$$dq_\alpha = \lambda h_\alpha \quad (4)$$

where $d\varepsilon_{ij}$, $d\varepsilon_{ij}^e$, and $d\varepsilon_{ij}^p$ are the increments of the total, elastic, and plastic strain tensors; $d\sigma_{ij}$ is the increment of the Cauchy stress tensor; D_{ijkl}^e is the elastic constitutive tensor; λ is the plastic multiplier; $\partial g / \partial \sigma_{ij}$ is the gradient to the plastic potential surface; q_α is the set of plastic hardening variables; and h_α is the plastic hardening rule. Equations (1)–(4) represent the properties of strain additivity, incremental elasticity, plastic flow rule, and plastic hardening rule, respectively.

Equations (1)–(3) may be combined into a single equation to solve for the stress increment $d\sigma_{ij}$ for a given strain increment $d\varepsilon_{ij}$:

$$d\sigma_{ij} = D_{ijkl}^e \left(d\varepsilon_{kl} - \lambda \frac{\partial g}{\partial \sigma_{ij}} \right) \quad (5)$$

Implementation of the constitutive model requires the numerical integration of Eqs. (1)–(4). For rate-independent elastoplasticity, the values of f and λ are restricted by the Kuhn-Tucker loading-unloading criterion:

$$f(\sigma_{ij}, q_\alpha) \leq 0; \lambda \geq 0 \text{ and } f\lambda = 0 \quad (6)$$

Equations (6) must be satisfied simultaneously for all loading conditions. Equation (6) specifies that the yield function must be non-positive for any set of stresses and hardening variables. For elastoplastic loading, the stress point must lie on the yield surface at all stages of loading, which generally requires that plastic strain occurs and $\lambda > 0$. The goal of a numerical calculation for an elastoplastic loading step is to find the correct value of λ such that the final stress point is consistent with the final yield surface ($f = 0$). Using Eqs. (4) and (5) to satisfy the first equation of Eq. (6) yields:

$$\begin{aligned} f(\sigma_{ij,f}, q_{\alpha,f}) &= f(\sigma_{ij,0} + d\sigma_{ij}, q_{\alpha,0} + dq_\alpha) \\ &= f\left(\sigma_{ij,0} + D_{ijkl}^e \left(d\varepsilon_{kl} - \lambda \frac{\partial g}{\partial \sigma_{kl}} \right), q_{\alpha,0} + \lambda h_\alpha\right) = 0 \end{aligned} \quad (7)$$

For linear elastic models, the plastic flow direction is the only quantity in Eq. (7) that depends on the loading increment and continuously evolves during loading. Implicit numerical integration schemes for elastoplasticity satisfy Eq. (7) by using the plastic flow direction at the final stress point $\sigma_{ij,f}$

$$\frac{\partial g}{\partial \sigma_{ij,f}} = \frac{\partial g}{\partial \sigma_{ij}} \Big|_{\sigma_{ij,f}} \quad (8)$$

Implicit integration schemes continuously update the trial value of λ and the trial plastic flow direction during the iterative solution process. In Jeremic and Sture (1997), an approximate solution for the final plastic flow direction is attained readily as a function of the derivatives of the plastic flow direction by using the first two terms of the Taylor series expansion of Eq. (8), evaluated at the initial stress point $\sigma_{ij,0}$:

$$\frac{\partial g}{\partial \sigma_{ij,f}} = \frac{\partial g}{\partial \sigma_{ij}} \Big|_{\sigma_{ij,f}} \approx \frac{\partial g}{\partial \sigma_{ij}} \Big|_{\sigma_{ij,0}} + \left(\frac{\partial^2 g}{\partial \sigma_{ij} \partial \sigma_{kl}} \Big|_{\sigma_{ij,0}} \right) d\sigma_{kl} + \left(\frac{\partial^2 g}{\partial \sigma_{ij} \partial q_\alpha} \Big|_{\sigma_{ij,0}} \right) dq_\alpha \quad (9)$$

For finite element calculations, it is necessary to form a global stiffness matrix to calculate displacements for the next loading step or global iteration. The global stiffness matrix is formed using an elastoplastic constitutive matrix, which is either the continuum tangent constitutive matrix \mathbf{D}^{ep} or the consistent tangent constitutive matrix \mathbf{D}^{con} . \mathbf{D}^{con} has been shown to promote faster global convergence, as discussed earlier. These two constitutive matrices and their differences in final form are discussed below.

Both \mathbf{D}^{ep} and \mathbf{D}^{con} are formed by combining Eq. (5) and Prager's consistency condition:

$$df = \frac{\partial f}{\partial \sigma_{ij}} d\sigma_{ij} + \frac{\partial f}{\partial q_\alpha} dq_\alpha \quad (10)$$

Ultimately, both \mathbf{D}^{ep} and \mathbf{D}^{con} are formed using the difference between the elastic and plastic tangent matrices:

$$D_{ijkl}^{ep} = D_{ijkl}^e - D_{ijkl}^p = D_{ijkl}^e - \frac{D_{ijmn}^e \frac{\partial g}{\partial \sigma_{mn,0}} \frac{\partial f}{\partial \sigma_{pq}} D_{pqkl}^e}{H_p + H} \quad (11a)$$

$$D_{ijkl}^{con} = R_{ijkl}^e - R_{ijkl}^p = R_{ijkl}^e - \frac{R_{ijmn}^e \frac{\partial m}{\partial \sigma_{mn}} \frac{\partial f}{\partial \sigma_{pq}} R_{pqkl}^e}{H_p + H} \quad (11b)$$

where $\partial m / \partial \sigma_{ij}$ is a modified plastic flow direction that incorporates the projected change in hardening parameter, H_p is the perfectly plastic modulus, H is the plastic hardening modulus, and R_{ijkl}^e is a modified stiffness tensor that Jeremic and Sture (1997) call the "reduced stiffness tensor". The following expressions for H_p are obtained for \mathbf{D}^{ep} and \mathbf{D}^{con} :

$$H_p = \frac{\partial f}{\partial \sigma_{rs}} D_{rstu}^e \frac{\partial g}{\partial \sigma_{tu,0}} \quad \text{for } \mathbf{D}^{ep} \quad \text{and} \quad H_p = \frac{\partial f}{\partial \sigma_{rs}} R_{rstu}^e \frac{\partial m}{\partial \sigma_{tu}} \quad \text{for } \mathbf{D}^{con} \quad (12)$$

Both \mathbf{D}^{ep} and \mathbf{D}^{con} can be expressed in a single general form:

$$\left\{ D_{ijkl}^{ep}, D_{ijkl}^{con} \right\} = E_{ijkl}^e - \frac{E_{ijmn}^e Q_{mn} \frac{\partial f}{\partial \sigma_{pq}} E_{pqkl}^e}{\frac{\partial f}{\partial \sigma_{rs}} E_{rstu}^e Q_{tu} - \frac{\partial f}{\partial q_\alpha} h_\alpha} = E_{ijkl}^e - \frac{E_{ijmn}^e Q_{mn} \frac{\partial f}{\partial \sigma_{pq}} E_{pqkl}^e}{H_p + H} \quad (13)$$

In Eq. (13), E_{ijkl}^e is a general expression for the elastic constitutive matrix and Q_{ij} is a general expression for the plastic flow direction. To form \mathbf{D}^{ep} or \mathbf{D}^{con} , the gradient to the yield function $\partial f / \partial \sigma_{ij}$ and the hardening modulus h_α are both evaluated at the initial stress point. The final forms of \mathbf{D}^{ep} and \mathbf{D}^{con} are not the same due to the differences between E_{ijkl}^e and Q_{ij} (Jeremic and Sture 1997) and as summarized in Table 1.

Table 1. Expressions for E_{ijkl}^e and Q_{ij} for \mathbf{D}^{ep} and \mathbf{D}^{con} .

	If D^{ep} is used	If D^{con} is used
E_{ijkl}^e	D_{ijkl}^e	$R_{ijkl}^e = D_{mnlk}^e \left[\delta_{mi} \delta_{nj} + \lambda D_{mnpq}^e \frac{\partial^2 g}{\partial \sigma_{pq} \partial \sigma_{ij}} \right]^{-1}$
Q_{ij}	$\frac{\partial g}{\partial \sigma_{ij,0}}$	$\frac{\partial m}{\partial \sigma_{ij}} = \frac{\partial g}{\partial \sigma_{ij,0}} + \lambda \frac{\partial^2 g}{\partial \sigma_{ij} \partial q_\alpha} h_\alpha$

Several differences between \mathbf{D}^{ep} and \mathbf{D}^{con} may be noted. First, the terms used to form \mathbf{D}^{ep} are constant at a given stress point, while the terms used to form \mathbf{D}^{con} are

functions of the magnitude of λ from the previous loading step. Since the magnitude of λ depends on the magnitude of the loading step, \mathbf{D}^{con} is step-size-dependent, while \mathbf{D}^{ep} is step-size-independent. Jeremic and Sture (1997) show that \mathbf{D}^{con} converges to \mathbf{D}^{ep} as $\lambda \rightarrow 0$, or for an infinitesimally small elastoplastic loading step. Second, the terms $Q_{mn} = \partial g / \partial \sigma_{mn}$ and $\partial f / \partial \sigma_{pq}$ in Eq. (13) are equal for associated flow, so $D_{ijkl}^{con} = D_{klij}^{con}$ and \mathbf{D}^{ep} is symmetric for associated flow. In contrast, the terms $Q_{mn} = \partial g / \partial \sigma_{mn} + \lambda h_\alpha \partial^2 g / (\partial \sigma_{mn} \partial q_\alpha)$ and $\partial f / \partial \sigma_{pq}$ in Eq. (13) are not equal for associated flow, so $D_{ijkl}^{ep} \neq D_{klij}^{ep}$ and \mathbf{D}^{con} is generally non-symmetric even for associated flow. A third difference between \mathbf{D}^{ep} and \mathbf{D}^{con} is that the material stiffness is reduced when \mathbf{D}^{con} is used, as will be demonstrated later.

Since \mathbf{D}^{con} aims to satisfy the constitutive response at the final stress point, its elements may be viewed as local secant moduli between the initial and final stress point. In contrast, \mathbf{D}^{ep} may be viewed as a tangential matrix since its components are based on the derivatives at the current stress point. This difference between \mathbf{D}^{ep} and \mathbf{D}^{con} is shown schematically in Fig. 1.

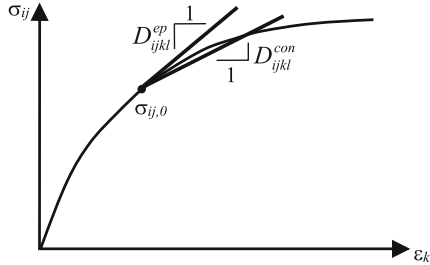


Fig. 1. Stress-strain curve illustrating the different stiffness moduli of \mathbf{D}^{ep} and \mathbf{D}^{con} .

3 Bifurcation and Shear Band Formation

Bifurcation theory is concerned with the prediction of how instability in the stress-strain response leads to localized deformations or deformation bands in elastoplastic materials. It is noted that bifurcation theory can predict not only localized deformations but also other types of instability mode that can be encountered in elastoplastic materials. As a result of strain localization instability ensues in terms of strain softening in the stress-strain relation. Strain localization manifests itself in cohesive-frictional materials as a narrow zone in which the deformation rate exceeds that in the uniformly deformed material. Since the yielding mechanism for these materials is shearing, the zone of strain localization is called a shear band although other types of deformation bands such as compression and dilation bands may occur or be predicted.

Prediction of strain localization is based on Mandel's (1964) stability criterion which states that a material is stable only when it can propagate small perturbations in the form of waves. Instability and strain localization occur when a small perturbation in the form of a wave cannot propagate across a material in the direction n_k where k is normal to

the deformation band. This condition appears when the acoustic tensor \mathbf{B} has a zero or negative determinant $|\mathbf{B}| = |B_{ik}|$, where $i = 1, 2, 3$. The acoustic tensor becomes non-positive definite, and produces negative eigenvalues. This condition may be stated as:

$$|B_{ik}| = |n_j D_{ijkl} n_l| \leq 0 \quad (14)$$

The acoustic tensor B_{ik} is a function of the constitutive matrix \mathbf{D} and of the direction of wave propagation \mathbf{n} . The shear band orientation is normal to \mathbf{n} . For the two-dimensional, plane strain condition ($i, j, k, l = 1, 2$), the unit vector \mathbf{n} may be expressed in terms of the angle θ between the shear band and the coordinate axes (i.e., between the normal to \mathbf{n} and the x -axis):

$$n_i = \begin{Bmatrix} n_1 \\ n_2 \end{Bmatrix} = \begin{Bmatrix} \sin \theta \\ \cos \theta \end{Bmatrix} \quad (15)$$

The determinant $|\mathbf{B}|$ may then be expressed in terms of D_{ijkl} and θ . If the coordinate axes are aligned with the directions of the major and minor principal stresses, the cross-terms (i.e., the terms between normal stresses and shearing strains, and between shearing stresses and normal strains) in the elastoplastic constitutive matrix disappear; that is, $D_{1112} = D_{1211} = D_{2122} = D_{2212} = 0$. This change greatly simplifies the acoustic tensor to the following (Pietruszczak and Bardet 1987):

$$\begin{aligned} |\mathbf{B}| &= (\sin^4 \theta)(D_{1111}D_{1212}) + (\cos^4 \theta)(D_{1212}D_{2222}) \\ &+ (\sin^2 \theta \cos^2 \theta)(D_{1111}D_{2222} - D_{1122}D_{2211} - D_{1122}D_{1212} - D_{1212}D_{2211}) \end{aligned} \quad (16)$$

As seen in Eqs. (10)–(13), the elastoplastic stiffness matrix is a function of H . The determinant $|\mathbf{B}|$ may become zero for certain values of H and orientations θ . The hardening modulus corresponding to $|\mathbf{B}| = 0$ is obtained by setting Eq. (16) equal to zero and solving for H (Bardet 1991). For \mathbf{D}^{ep} , H is obtained as:

$$H(\mathbf{D}^{ep}) = \frac{2G}{1-\nu} \left(\begin{array}{c} -\sin^4 \theta \left(\frac{\partial g}{\partial \sigma_{11}} - \frac{\partial g}{\partial \sigma_{22}} \right) \left(\frac{\partial f}{\partial \sigma_{11}} - \frac{\partial f}{\partial \sigma_{22}} \right) \\ + \sin^2 \theta \left(\frac{\partial g}{\partial \sigma_{11}} \left(\frac{\partial f}{\partial \sigma_{11}} - \frac{\partial f}{\partial \sigma_{22}} \right) + \frac{\partial f}{\partial \sigma_{11}} \left(\frac{\partial g}{\partial \sigma_{11}} - \frac{\partial g}{\partial \sigma_{22}} \right) \right) \\ - \frac{\partial g}{\partial \sigma_{11}} \frac{\partial f}{\partial \sigma_{11}} + \frac{(1-\nu)}{2} \frac{\partial g}{\partial \sigma_{12}} \frac{\partial f}{\partial \sigma_{12}} \end{array} \right) \quad (17)$$

where G is the shear modulus and ν is Poisson's ratio. If the coordinate axes are aligned with the major and minor principal stress directions, the major principal stress $\sigma_1 = \sigma_{11}$, the minor principal stress $\sigma_3 = \sigma_{22}$, and the shear stress $\sigma_{12} = \partial f / \partial \sigma_{12} = \partial g / \partial \sigma_{12} = 0$. The critical angle θ_c at which H is minimized may be found by differentiating Eq. (17) with respect to θ , setting the derivative equal to zero, and solving for $\theta = \theta_c$. The

resulting expression for θ_c is:

$$\theta_c(\mathbf{D}^{ep}) = \sin^{-1} \sqrt{\frac{\frac{\partial g}{\partial \sigma_1} \left(\frac{\partial f}{\partial \sigma_1} - \frac{\partial f}{\partial \sigma_3} \right) + \frac{\partial f}{\partial \sigma_1} \left(\frac{\partial g}{\partial \sigma_1} - \frac{\partial g}{\partial \sigma_3} \right)}{2 \left(\frac{\partial g}{\partial \sigma_1} - \frac{\partial g}{\partial \sigma_3} \right) \left(\frac{\partial f}{\partial \sigma_1} - \frac{\partial f}{\partial \sigma_3} \right)}} \quad (18)$$

Substituting Eq. (18) into Eq. (17) yields the expression for H_c as:

$$H_c(\mathbf{D}^{ep}) = \frac{G}{2(1-\nu)} \left[\frac{\left(\frac{\partial g}{\partial \sigma_1} \frac{\partial f}{\partial \sigma_3} - \frac{\partial f}{\partial \sigma_1} \frac{\partial g}{\partial \sigma_3} \right)^2}{\left(\frac{\partial g}{\partial \sigma_1} - \frac{\partial g}{\partial \sigma_3} \right) \left(\frac{\partial f}{\partial \sigma_1} - \frac{\partial f}{\partial \sigma_3} \right)} \right] \quad (19)$$

Equation (19) corresponds to the solution of Runesson et al. (1987), for the simplified plane strain case in which the intermediate principal stress is directed out of the plane of strain. Under these conditions, the critical hardening modulus $H_c(\mathbf{D}^{ep})$ is always non-negative and greater than 0 if $f \neq g$ in the case of non-associated flow rule.

The expression for \mathbf{D}^{con} is much more algebraically complicated than the expression for \mathbf{D}^{ep} . As such, deriving a general expression for H_c at which strain localization emerges is difficult or impossible in the general case. However, expressions for H_c may be derived for specific constitutive models. An example is shown in the following section.

4 Application to the Mohr-Coulomb Model

The effect of the form of the elastoplastic constitutive matrix on shear band formation is investigated analytically in this section using the strain hardening Mohr-Coulomb model. Shear band formation is predicted using both \mathbf{D}^{ep} and \mathbf{D}^{con} . The Mohr-Coulomb model has the following yield and plastic potential functions in p - q space:

$$f = q - p \sin \phi - c \cos \phi; \quad g = q - p \sin \psi + b \quad (20)$$

where ϕ is the friction angle, c is the cohesion, ψ is the dilatancy angle, and b is a constant which makes the plastic potential equal to zero at the point of interest. The stress invariants p and q represent the mean stress and deviatoric stress, respectively, and are defined as follows in two dimensions:

$$p = \frac{1}{2}(\sigma_1 + \sigma_3); \quad q = \frac{1}{2}(\sigma_1 - \sigma_3) \quad (21)$$

These two-dimensional invariants are analogous to the mean and deviatoric stress invariants for general three-dimensional conditions.

In terms of the invariants p and q , the critical orientation $\theta_c(\mathbf{D}_{ep})$ in Eq. (18) and the critical hardening modulus $H_c(\mathbf{D}^{ep})$ in Eq. (19) can be re-written in terms of invariants p and q as:

$$\theta_c(\mathbf{D}^{ep}) = \frac{1}{4} \left(\frac{\partial f / \partial p}{\partial f / \partial q} + \frac{\partial g / \partial p}{\partial g / \partial q} \right) \quad (22)$$

$$H_c(\mathbf{D}^{ep}) = \frac{E}{16(1-\nu^2)} \left(\frac{\partial f/\partial p}{\partial f/\partial q} - \frac{\partial g/\partial p}{\partial g/\partial q} \right)^2 = \frac{G}{8(1-\nu)} \left(\frac{\partial f/\partial p}{\partial f/\partial q} - \frac{\partial g/\partial p}{\partial g/\partial q} \right)^2 \quad (23)$$

The derivatives of f and g with respect to the invariants p and q can be obtained from Eqs. (20) as $\partial f/\partial p = -\sin \varphi$, $\partial f/\partial q = 1$, $g/\partial p = -\sin \psi$, and $\partial g/\partial q = 1$. Substituting these derivatives in Eq. (23), or using the appropriate derivatives in Eq. (19), yields an expression for H_c corresponding to \mathbf{D}^{ep} for the Mohr-Coulomb model:

$$H_c(\mathbf{D}^{ep}) = \frac{G(\sin \varphi - \sin \psi)^2}{8(1-\nu)} \quad (24)$$

Classical failure corresponds to a condition in which no further hardening is possible, and is represented by the maximum value of the hardening parameter q_α or by a zero value of H . For the case of associated flow ($\phi = \psi$), the critical hardening modulus is equal to zero; shear band formation is suppressed until classical failure occurs.

Under the plane strain conditions specified, the corresponding shear band orientation θ_c for \mathbf{D}^{ep} for the Mohr-Coulomb model becomes:

$$\theta_c(\mathbf{D}^{ep}) = \frac{1}{2} \cos^{-1} \left(\frac{\sin \varphi + \sin \psi}{2} \right) \quad (25)$$

If the difference between ϕ and ψ is small, it is possible to simplify the above to:

$$\theta_c(\mathbf{D}^{ep}) \approx 45^\circ - \frac{\varphi + \psi}{4} \quad (26)$$

Equation (26) is known as Arthur-Vardoulakis solution (Arthur et al. 1977; Vardoulakis 1980). For perfect plasticity (i.e., $H = 0$), two orientations are possible:

$$\theta_c \approx 45^\circ - \frac{\varphi}{2} \text{ or } \theta_c \approx 45^\circ - \frac{\psi}{2} \quad (27)$$

These orientations correspond, respectively, to the Mohr-Coulomb (lower bound) and Roscoe (1970) (upper bound) solutions.

A critical hardening modulus can also be derived for the Mohr-Coulomb model using \mathbf{D}^{con} . For the Mohr-Coulomb model, the dilatancy angle is constant and independent of the hardening parameters q_α . In this case, $\partial^2 g / (\partial \sigma_{ij} \partial q_\alpha) = 0$ and $\partial m / \partial \sigma_{ij} = \partial g / \partial \sigma_{ij}$. When the principal stresses are aligned with the coordinate axes, \mathbf{D}^{con} takes the following form:

$$D_{ijkl}^{con} = \begin{bmatrix} D_{1111}^{ep} & D_{1122}^{ep} & 0 \\ D_{2211}^{ep} & D_{2222}^{ep} & 0 \\ 0 & 0 & D_{1212}^{ep} \left[1 + \frac{\lambda G}{q} \right]^{-1} \end{bmatrix} = \begin{bmatrix} D_{1111}^{ep} & D_{1122}^{ep} & 0 \\ D_{2211}^{ep} & D_{2222}^{ep} & 0 \\ 0 & 0 & G \left[1 + \frac{\lambda G}{q} \right]^{-1} \end{bmatrix} \quad (28)$$

$$D_{1212}^{con} = D_{1212}^{ep} \left[1 + \frac{\lambda G}{q} \right]^{-1} = G \left[1 + \frac{\lambda G}{q} \right]^{-1} = G_{ct} \quad (29)$$

As can be seen, \mathbf{D}^{ep} and \mathbf{D}^{con} differ only in terms of D_{1212} . Since \mathbf{D}^{ep} is symmetric in the case of associated flow for any orientation of the reference axes, it can be verified that

\mathbf{D}^{con} is symmetric in the case of associated flow if the principal stresses are aligned with the reference axes. Therefore, it is not expected that use of \mathbf{D}^{con} will lead to prediction of shear band formation in the hardening regime for associated models; this behavior is like that for \mathbf{D}^{ep} .

Because the coordinate axes are aligned with the principal stress directions, the elastoplastic moduli D_{1111}^{con} , D_{1122}^{con} , D_{2211}^{con} , and D_{2222}^{con} relate principal stress increments to principal strain increments. These elastoplastic moduli, which will be called full moduli, are the same for \mathbf{D}^{con} as for \mathbf{D}^{ep} . In contrast, any applied stress increment $d\sigma_{12}$ causes principal stress rotation. The stress increment $d\sigma_{12}$ is related only to the elastoplastic modulus D_{1212}^{ep} or D_{1212}^{con} in the elastoplastic matrix. As shown in Eqs. (28) and (29), the elastoplastic modulus D_{1212}^{con} represents a reduced value from D_{1212}^{ep} . The entry D_{1212}^{con} can be thought of as a “reduced” elastoplastic modulus, respectively, in contrast to the full elastoplastic modulus D_{1212}^{ep} , and differs only due to a reduced value of the shear modulus G .

Since \mathbf{D}^{ep} represents the incremental tangent stiffness at the initial stress point and \mathbf{D}^{con} represents the incremental consistent tangent stiffness between the initial stress point and the projected final stress point, G and G_{ct} are the tangent and consistent tangent shear moduli, respectively. G_{ct} is less than G , and therefore promotes a softer response.

An expression for H_C may be derived for \mathbf{D}^{con} in the same way as was done for \mathbf{D}^{ep} . Using Eq. (26) to form \mathbf{D}^{con} , substituting the resulting expression into Eq. (16), and then solving for H yields the following expression:

$$H(\mathbf{D}^{con}) = \frac{2GG_{ct}}{G_{ct}(1-\nu) + 2(G-G_{ct})\sin^2\theta\cos^2\theta} \left(\begin{array}{l} -\sin^4\theta \left(\frac{\partial g}{\partial \sigma_{11}} - \frac{\partial g}{\partial \sigma_{22}} \right) \left(\frac{\partial f}{\partial \sigma_{11}} - \frac{\partial f}{\partial \sigma_{22}} \right) \\ + \sin^2\theta \left(\frac{\partial g}{\partial \sigma_{11}} \left(\frac{\partial f}{\partial \sigma_{11}} - \frac{\partial f}{\partial \sigma_{22}} \right) + \frac{\partial f}{\partial \sigma_{11}} \left(\frac{\partial g}{\partial \sigma_{11}} - \frac{\partial g}{\partial \sigma_{22}} \right) \right) \\ - \frac{\partial g}{\partial \sigma_{11}} \frac{\partial f}{\partial \sigma_{11}} + \frac{(1-\nu)}{2} \frac{\partial g}{\partial \sigma_{12}} \frac{\partial f}{\partial \sigma_{12}} \end{array} \right) \quad (30)$$

Comparing Eqs. (17)–(30), it may be seen that that:

$$\frac{H(\mathbf{D}^{con})}{H(\mathbf{D}^{ep})} = \frac{G_{ct}(1-\nu)}{G_{ct}(1-\nu) + (G-G_{ct})\sin^2\theta\cos^2\theta} \quad (31)$$

Equation (31) was derived using the same assumption, that the intermediate principal stress is directed out of the plane of strain, described previously. Since the relationship between G and G_{ct} is known, Eq. (31) can be simplified to:

$$\frac{H(\mathbf{D}^{con})}{H(\mathbf{D}^{ep})} = \frac{1-\nu}{1-\nu + \frac{2\lambda G}{q}\sin^2\theta\cos^2\theta} \quad (32)$$

As can be seen, the ratio between the critical hardening moduli for \mathbf{D}^{ep} and \mathbf{D}^{con} is a function of the shear band orientation θ . Although it is possible to differentiate Eq. (24)

with respect to θ to find the critical hardening modulus for \mathbf{D}^{con} , the resulting expression is very complicated and does not provide clear physical insight into the influence of \mathbf{D}^{con} on H_c and θ_c . A simpler approach is obtained if Eq. (26) is used as the expression for the critical angle θ_c for \mathbf{D}^{con} . Based on this approximation, the ratio between critical hardening moduli determined using \mathbf{D}^{con} and \mathbf{D}^{ep} is shown in the following equation:

$$\frac{H_c(\mathbf{D}^{con})}{H_c(\mathbf{D}^{ep})} = \frac{8(1 - \nu)}{8(1 - \nu) + \frac{\lambda G}{q} [4 - (\sin \varphi + \sin \psi)^2]} \quad (33)$$

The use of the shear band orientation from \mathbf{D}^{ep} given in Eq. (25) in the foregoing equation assumes that the expression for the critical angle determined by minimizing the derivative of Eq. (30) is only slightly different from Eq. (19), which was obtained by minimizing the derivative of Eq. (18). The validity of this assumption will be numerically investigated in the next section.

It is seen that the expression in Eq. (33) is always less than or equal to 1. The critical hardening modulus at which strain localization emerges is therefore reduced when \mathbf{D}^{con} is used. $H_c(\mathbf{D}^{con})$ is then:

$$H_c(\mathbf{D}^{con}) = \frac{G(\sin \varphi - \sin \psi)^2}{8(1 - \nu) + \frac{\lambda G}{q} [4 - (\sin \varphi + \sin \psi)^2]} \quad (34)$$

Since the critical hardening modulus at shear band formation using \mathbf{D}^{con} is less than the critical hardening modulus using \mathbf{D}^{ep} , the effect of implicit integration is to decrease the hardening modulus at which shear bands form. Because the hardening modulus for a shearing yield mechanism generally decreases as plastic shear deformation accumulates, the overall effect of using \mathbf{D}^{con} is to delay shear band formation until the critical hardening modulus is reduced. Note that if $\lambda = 0$, \mathbf{D}^{con} becomes equal to \mathbf{D}^{ep} , and the same critical hardening modulus is obtained using either matrix. For associated flow, the critical hardening modulus for both \mathbf{D}^{con} and \mathbf{D}^{ep} is equal to zero, and only classical failure occurs. Note that both \mathbf{D}^{con} and \mathbf{D}^{ep} are discretized incremental approximations of elastoplastic stress-strain relations.

To illustrate the differences in the predicted critical hardening moduli at bifurcation from the explicit \mathbf{D}^{con} and implicit \mathbf{D}^{ep} , Eq. (33) is plotted in Fig. 2 for values of $G = 30$ MPa, $\nu = 0.3$, $\psi = 0^\circ$, and different values of ϕ and λ . As can be seen, the ratio of the critical moduli is always less than 1.0, indicating that bifurcation is always predicted to occur earlier in the loading for the implicit integration than for explicit integration. Since the critical hardening moduli are different, the shear band orientations are also expected to differ between explicit and implicit integrations.

5 Conclusions

In general, the use of \mathbf{D}^{con} results in lower values of the critical plastic hardening modulus in comparison to the use of continuum tangent matrix \mathbf{D}^{ep} . Consequently, shear band formation occurs at a larger deformation and at higher values of mobilized friction angle for strain hardening materials. Due to the differences in critical hardening moduli, the

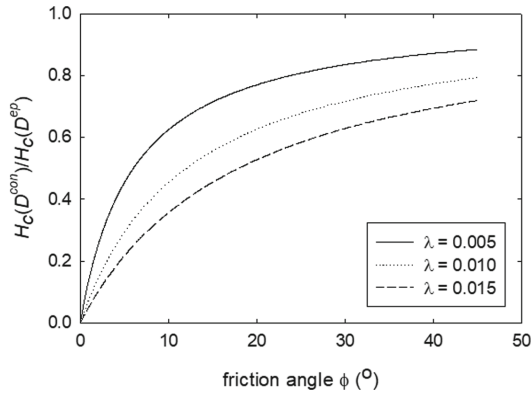


Fig. 2. Predicated ratios of the critical hardening moduli using D^{ep} and D^{con} .






shear band orientations are also expected to be different between explicit and implicit integrations. These results should be considered when using implicit integration techniques in finite element simulation of shear band formation. The actual implementation of the above analysis using the finite element method is to be discussed in another paper.

References

- Arthur, J.F.R., Dunstan, T., Assadi, Q.A.J., Assadi, A.: Plastic deformation and failure in granular material. *Géotechnique* **27**(1), 53–74 (1977)
- Bardet, J.P.: Orientation of shear bands in frictional soils. *J. Eng. Mech.* **117**, 1466–1484 (1991)
- Jeremic, B., Sture, S.: Implicit integration in elastoplastic geotechnics. *Mech. Cohesive-Frictional Mats.* **2**, 165–183 (1997)
- Mandel, J.: Conditions de stabilité et postulat de Drucker. In: *Proceedings of IUTAM Symposium on Rheology Soil Mechanics*, pp. 58–68. Grenoble, France (1964)
- Ortiz, M., Popov, E.P.: Accuracy and stability of integration algorithms for elastoplastic constitutive relations. *Intl. J. Num. Meth. Eng.* **21**, 1561–1576 (1985)
- Roscoe, K.H.: The influence of strain in soil mechanics. *Géotechnique* **20**(2), 129–170 (1970)
- Rudnicki, J.W., Rice, J.R.: Conditions for the localization of deformation in pressure-sensitive dilatant materials. *J. Mech. Phys. Solids* **23**, 371–394 (1975)
- Runesson, K.: Implicit integration of elastoplastic relations with reference to soils. *Intl. J. Num. Anal. Meth. Geomech.* **11**, 315–321 (1987)
- Simo, J.C., Taylor, R.L.: Consistent tangent operators for rate-independent plasticity. *Comp. Meth. Appl. Mech. Eng.* **48**, 101–118 (1985)
- Vardoulakis, I.: Shear band inclination and shear modulus of sand in biaxial tests. *Intl. J. Num. Anal. Meth. Geomech.* **12**, 155–168 (1980)



Finite Element Continuation Analysis for Cnoidal Waves in Solids

Thomas Poulet¹ , Roberto J. Cier² , Sergio Rojas³ , Manolis Veveakis⁴ ,
and Victor M. Calo³ 

¹ CSIRO Mineral Resources, Kensington, WA 6151, Australia
thomas.poulet@csiro.au

² School of Civil and Mechanical Engineering, Curtin University, Bentley, WA 6102, Australia

³ School of Earth and Planetary Sciences, Curtin University, Bentley, WA 6102, Australia

⁴ Civil and Environmental Engineering, Duke University, Durham, NC 27708-0287, USA

Abstract. Under compression, rate-dependent solids subject to hydro-mechanical processes have been shown to accommodate singular cnoidal wave solutions [1], as a material instability at the stationary wave limit. Given the numerical complexity to solve the corresponding equation, we use a physical regularization approach [2] to cap the infinite stress growth with chemical pressurization of the material around the singularities. In this contribution, we show the results of a stability analysis of the underlying equation using a pseudo-arclength continuation algorithm with Finite Elements [3]. This allows to identify various solutions of the system with different numbers of peaks as a function of the problem parameters. We show the influence of the main material parameter, the existence of its critical values for different types of solutions, as well the evolution of peak spacing for the different admissible solutions. Finally, we investigate which initial conditions lead to solutions with stress peaks.

Keywords: Compaction banding · Cnoidal waves · Numerical continuation

1 Cnoidal Waves in Solids

Geomaterials under compression can exhibit localisation features, known as compaction bands, that are perpendicular to the principal stress direction. These zones are characterized by pore collapse and lower porosity resulting from a stress instability and they can be explained from a purely mechanical perspective [4]. Such bands form subparallel patterns that sometimes display some regularity in their spacing [5] and some models have been derived to try and explain this pseudo-periodicity [6]. Interestingly, a radically different physical process, stemming from a hydro-mechanical instability identified as cnoidal waves in solids [1], can also lead to localisation bands under compaction with regular spacing, but with the important difference that those bands are zones of much higher permeability. This feature makes the theory particularly appealing for many applications involving fluid transport or even melt segregation [7]. Our understanding of the phenomenon, however, remains in its infancy. Only an asymptotic behavior has been

described so far, leading to a deceptively simple 1D differential equation, which proves challenging enough to solve numerically [1]. For this reason, some physical stabilization processes can be considered as well, for instance in the form of fluid-release chemical reactions, like diagenesis [2], which bound the stress while keeping the presence and location of stress peaks unchanged. We are therefore focusing our study on this stabilized version of the problem, which can be expressed in dimensionless form as the solution u of the system [2]:

$$\frac{\partial^2 u}{\partial z^2} - \lambda(1 + u)^m + \mu e^{\beta u} = 0, \quad 0 \leq z \leq 1, \quad (1)$$

$$\text{with } u(0) = u(1) = 0, \quad (2)$$

where λ , m , β and μ are material parameters and u characterizes the effective stress σ' through the relation $u = \sigma' - 1$. Stresses are taken as positive in compression. Note that the last term on the left-hand side of Eq. (1) is the stabilization term, related to diagenetic (fluid-release) reactions, introduced to keep the solution u bounded. The corresponding parameters, β (Arrhenius number for micromechanical processes) and μ (chemo-mechanical coefficient) are therefore of minor interest and taken arbitrarily in this contribution as $\beta = 10$ and $\mu = 10^{-4}$ (see [2]). Our attention lies on the influence of the other parameters, and specifically on λ , the hydro-mechanical coefficient which has the greatest flexibility to vary as it encompasses some boundary conditions of the physical problem as the ratio of mechanical generalised diffusivity over the hydraulic diffusivity [1]. This λ parameter should be strictly positive for physical reasons but could take very large values as it is proportional to the loading rate imposed on the volume considered, which is mathematically not necessarily bounded. The value of m , the power law rheology exponent, is fixed to a representative value $m = 3$. The Dirichlet boundary conditions imposed in Eq. (2) are equivalent to a fluid pressure controlled, drained experiment under constant loading rate. Here we present a stability analysis of this system with respect to λ using a numerical continuation method.

2 Pseudo-arclength Continuation

While the high non-linearity of Eq. (1) is not naturally adapted to the Finite Element Method, we note that it is nonetheless possible to solve this equation with a robust solver when starting from a sufficiently accurate initial solution. (We refer the reader to our companion study [8] for a method specifically developed to improve the resolution of this system.) We select therefore the Finite Element Redback simulator [9] and we study the sensitivity of the λ parameter with a pseudo-arclength continuation approach [10] implemented in Redback [3]. In essence, the continuation parameter (λ in this instance) is considered as a variable of the system, which is extended from Eq. (1) by imposing that the solution (u, λ) remains at an imposed distance of the previous solution during the computation of an iteration.

We initiate this iterative algorithm by solving twice Eq. (1) for close given values of $\lambda > 0$ starting from a zero initial condition $u = 0$ on $[0, 1]$. Each solution obtained for this hydro-mechanical problem is the traditional Terzaghi consolidation profile [11]

shown in Fig. 1c, stemming from pore pressure dissipation. Following the continuation algorithm for decreasing values of λ we obtain a curve shaped as a “C”, as shown in Fig. 1a. This interesting result points to the existence of an upper branch corresponding to stress profiles with a peak, as shown in Fig. 1b.

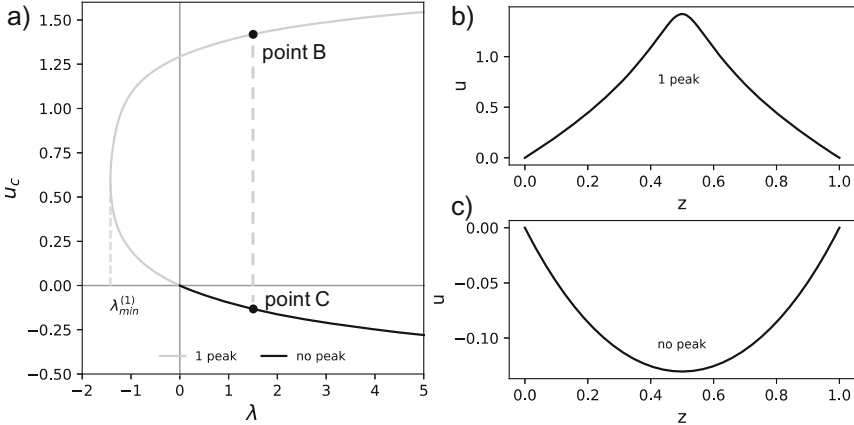


Fig. 1. (a) Stability analysis for Eq. (1) showing the central value u_c (for $z = 0.5$) of the solution profile as a function of λ , displaying a C-curve. This indicates two distinct solutions for every single value of λ . The corresponding full profiles at point B and C are shown in (b) and (c) respectively.

As previous studies [1] showed the existence of different solutions with various numbers of equidistant peaks, we now apply the same continuation method to investigate other areas of the parameter space within an arbitrary range $\lambda \leq 500$. We initiate successively the continuation algorithm from solution profiles manually identified with an imposed number p of peaks as initial condition for $\lambda = 500$ and the results are shown in Fig. 2. We observe for each p -peak profile a C-curve, with a minimum value $\lambda_{min}^{(p)}$ increasing with p .

For each of those continuation curves, we then compute the distance between the peaks as it represents the major difference between the upper and lower branches of each curve. The results are plotted in Fig. 3 and show a regular pattern. For each C-curve with p -peaks, there exists a point corresponding to a solution profile where the spacing between the peaks is exactly equal to $1/p$, noting that this point is close but not exactly at the minimum value of λ reachable. From this point, the upper branch sees the spacing increase with λ , reaching asymptotically the value $1/(p - 1)$, whereas the lower branch sees the spacing decrease with λ , reaching asymptotically the value $1/(p + 1)$.

Finally, we investigate the influence of initial conditions, with λ fixed, on the type of solution reached by the system. As a first step, we evaluate when a given initial condition profile stops converging to the Terzaghi profile of Fig. 1c when multiplied by an increasing factor. Figure 4a displays the results obtained for four different profiles, shown in Fig. 4b–e, tracking in non-solid lines the maximum value u_{max} of the initial condition profile over $[0, 1]$. These separatrices are obtained, for λ fixed, by dichotomy over the multiplying factor for a numerical precision on u_{max} of 10^{-4} . The process is

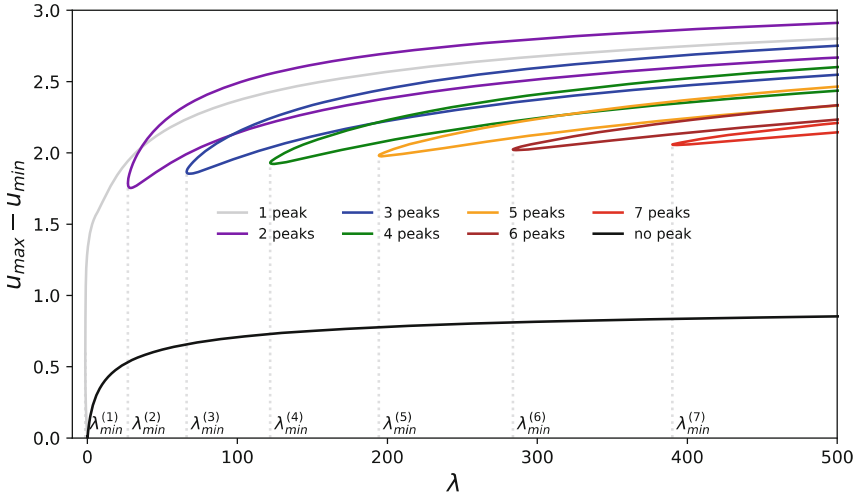


Fig. 2. Continuation results obtained for $\lambda \leq 500$, showing the ranges of values where different solutions exist, with various numbers of peaks (up to seven) and two branches each. The vertical axis represents the range of the solution profiles $\max(u) - \min(u)$ over $[0, 1]$.

repeated for each integer value of $0 \leq \lambda \leq 500$ to plot a given separatrix and we ran this process for four different profiles. Figure 4a also plots on the same graph the maximum values of the solution profiles for all the curves of Fig. 2, which superpose perfectly for all solutions with one or more peaks. These results confirm that the Terzaghi solution remains valid for any λ , but also that a high enough perturbation in effective stress can lead to a peak-profile solution. The profiles from Fig. 4b–e represent increasingly sharper peaks between the two end-members of a flat profile, Fig. 4b, and a peak over a single mesh point, Fig. 4e. Figure 4a shows that the amplitude required for the perturbation depends on the shape of the initial condition profile, and we observe naturally that the narrower the peak profile, the higher the amplitude required to escape the Terzaghi solution.

3 Conclusion

This study shows that the cnoidal waves in solids remain a complex problem that has not yet revealed all of its secrets and yet three new major conclusions can be draw. Firstly, a critical deduction is that the asymptotic description of the 1D problem, Eq. (1), can lead to solution profiles with one or more stress peaks for any value of λ , see Fig. 2, contrary to earlier suggestions regarding a threshold [1]. Secondly Fig. 4 also highlights that strong stress perturbations are needed to escape the traditional no-peak solution for that problem, with higher amplitudes required for narrower perturbations. Thirdly, the results of the continuation analysis shown in Figs. 2 and 3 indicate that various solutions can be reached for different ranges of λ , so the spacing between peaks can no longer be interpreted as a direct indicator for the value of λ . The picture painted in this study remains incomplete as the continuation methodology employed does not

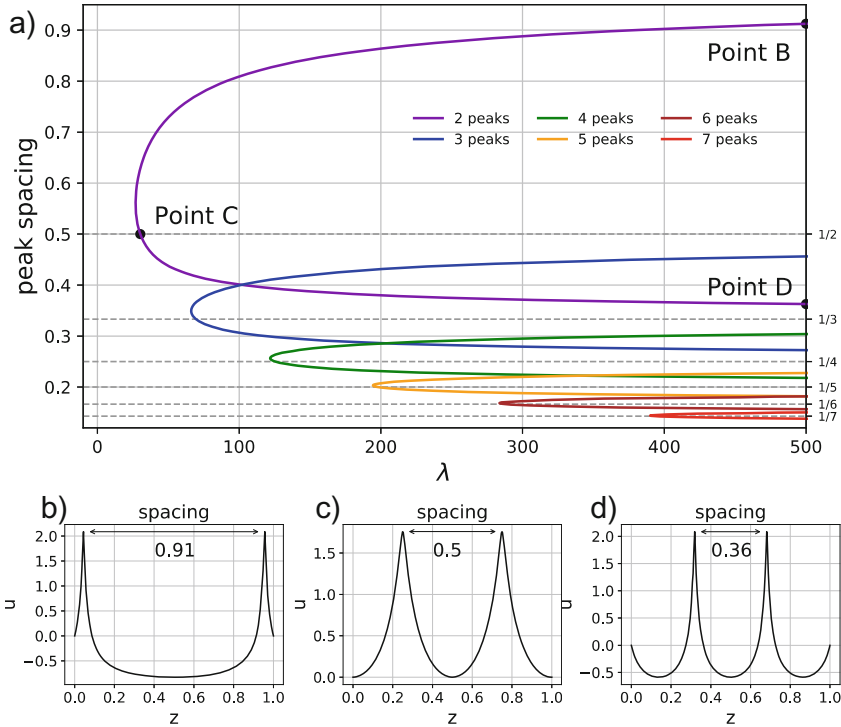


Fig. 3. (a) Spacing between the peaks for the continuation curves of Fig. 2 representing the p -peak solutions, with $1 \leq p \leq 7$. The points B, C and D illustrate, for the case $p = 2$, that each curve has a point where the spacing is exactly $1/p$, with the upper (resp. lower) branch seeing an increase (resp. decrease) of spacing. The corresponding solution profiles at those points are represented in (b), (c) and (d).

ensure the identification of all possible branches and more solutions could potentially exist. The problem appears to be much more subtle than originally anticipated and more theoretical, numerical (see [12]) and – above all – experimental work remains to be done on this topic to assess the parameters controlling the spacing between compaction features.

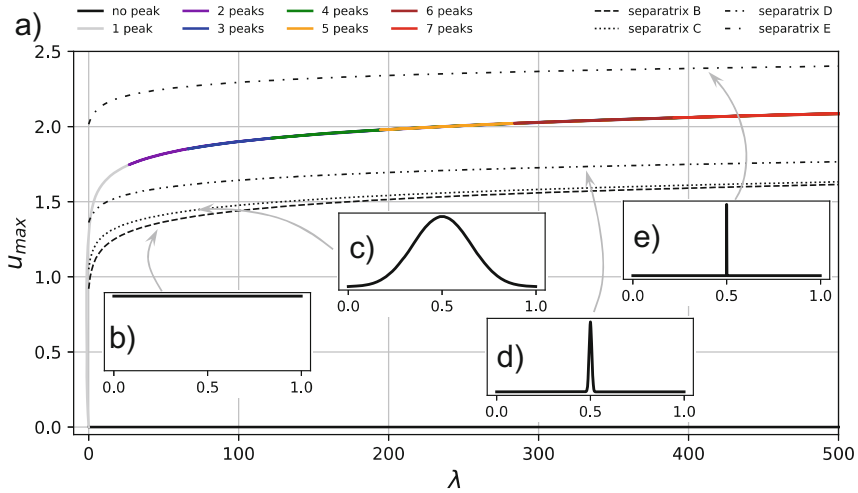


Fig. 4. (a) Separatrices for four profiles of initial conditions, shown in (b)–(e), marking the maximum value of a scaled version of the initial profile still converging to the solution profile of Fig. 1c for any given λ .

References

1. Veveakis, E., Regenauer-Lieb, K.: Cnoidal waves in solids. *J. Mech. Phys. Solids* **78**, 231–248 (2015)
2. Alevizos, S., Poulet, T., Sari, M., Lesueur, M., Regenauer-Lieb, K., Veveakis, M.: A framework for fracture network formation in overpressurised impermeable shale: deformability versus diagenesis. *Rock Mech. Rock Eng.* **50**(3), 689–703 (2017)
3. Tung, R., Poulet, T., Alevizos, S., Veveakis, E., Regenauer-Lieb, K.: Shear heating in creeping faults changes the onset of convection. *Geophys. J. Int.* **211**(1), 270–283 (2017)
4. Sulem, J.: Bifurcation theory and localization phenomena. *Eur. J. Environ. Civ. Eng.* **14**(8–9), 989–1009 (2010)
5. Sari, M., Poulet, T., Alevizos, S., Veveakis, M.: An Energy Based Constitutive Framework for Multiphysics Geomechanics, this vol., 6 p. Springer (2022)
6. Cecinato, F., Gajo, A.: Dynamical effects during compaction band formation affecting their spatial periodicity. *J. Geophys. Res.: Solid Earth* **119**(10), 7487–7502 (2014)
7. Weinberg, R., Veveakis, M., Regenauer-Lieb, K.: Compaction-driven melt segregation in migmatites. *Geology* **43**(6), 1–4 (2015)
8. Cier, R. J., Poulet, T., Rojas, S., Veveakis, M., Calo, V.M.: A Numerical Approach of the Cnoidal Wave Equation for Compaction, this vol., 6 p. Springer (2022)
9. Poulet, T., Veveakis, M.: A viscoplastic approach for pore collapse in saturated soft rocks using redback: An open-source parallel simulator for rock mechanics with dissipative feedbacks. *Comput. Geotech.* **74**, 211–221 (2016)
10. Keller, H.: Numerical solution of bifurcation and nonlinear eigenvalue problems, applications of bifurcation theory. In: *Numerical Solution of Bifurcation and Nonlinear Eigenvalue Problems*, pp. 359–384 (1977)

11. Terzaghi, K.: Theory of consolidation. In: *Theoretical Soil Mechanics*, pp. 265–296. Wiley, pp. 265–296 (1943)
12. Cier, R.J., Poulet, T., Rojas, S., Veveakis, M., Calo, V.M.: Automatically adaptive stabilized finite elements and continuation analysis for compaction banding in geomaterials. *Int. J. Numer. Methods Eng.* **122**(21), 6234–6252 (2021) (Wiley)



Spatiotemporal Evolution of Strain and Compaction Localization in Leitha Limestone: Synchrotron Tomographic Imaging and Digital Volume Correlation

Fanbao Meng^{1,2}, Lingcao Huang³, Patrick Baud⁴, and Teng-fong Wong²(✉)

¹ School of Earth Sciences and Engineering, Sun Yat-sen University, Guangzhou, China

² Earth and Environmental Sciences, The Chinese University of Hong Kong, Hong Kong, China

tfwong@cuhk.edu.hk

³ CIRES, University of Colorado Boulder, Boulder, CO, USA

⁴ Institut Terre et Environnement de Strasbourg (ITES), Strasbourg, France

Abstract. The HADES rig at the European Synchrotron Radiation Facility allows *in situ* 3D imaging of the whole rock sample as it is triaxially compressed. The μ CT data provide an integrated perspective of the spatiotemporal evolution of damage and strain localization on scales ranging from grain to continuum. An experiment was conducted on Leitha limestone at a confining pressure of 20 MPa. With increasing differential stress, the sample strain hardened in two distinct stages of yielding. The second stage was associated with development of five discrete compaction bands. The μ CT data on the voxel-scale delineate in refined details the nucleation and propagation of discrete compaction bands under quasi-static loading, as well as the micromechanical processes. To characterize quantitatively the spatiotemporal evolution of strain, we systematically applied digital volume correlation to this unique set of *in situ* synchrotron CT data. We have obtained some of the first 3D results on grain-scale heterogeneity of strain in a porous aggregate, which elucidate the mechanics of the bifurcation phenomenon, as well as the fine structures and geometric complexity of compaction bands.

Keywords: Strain localization · Compaction band · Synchrotron tomography

1 Introduction

Observations in the laboratory have shown that formation of compaction and shear bands can often be conceptualized as a bifurcation, which emerges from a pattern of deformation that is initially homogeneous or smoothly varying, culminating in the nearly simultaneous development of strain concentration at all points of the putative band (Rice 1976; Vardoulakis and Sulem 1995; Issen and Rudnicki 2000). A comprehensive understanding of the mechanics hinges on the direct observation of the spatiotemporal evolution of damage on multiple scales.

The measurement of acoustic emissions (AE) has proved to be one of the most effective techniques for such observation in a brittle rock such as granite and sandstone

(Lockner et al. 1992; Lockner 1993), the damage in which is generally accompanied by significant AE activity. Another approach that has proved to be as effective is the use of X-ray computed tomography (CT) in conjunction with digital volume correlation (DVC). In two recent studies of the brittle-ductile transition in limestones, triaxially compressed samples at different stages of deformation were retrieved from the pressure vessel and imaged *ex situ*, and DVC was used to characterize the displacement and strain fields by correlating pairs of CT images. Abdallah et al. (2021) investigated the development of compaction bands (CB) and compactive shear bands in Saint-Maximin limestone. Baud et al. (2021) characterized the strain heterogeneity and geometric complexity associated with the development of shear bands in Indiana limestone, as well as the connection with bifurcation analysis. Whereas these studies have contributed useful insights into compaction localization, they also underscore the limitations of *ex situ* imaging.

A technical advance was achieved by Renard et al. (2017), who developed a triaxial deformation apparatus at the European Synchrotron Radiation Facility (ESRF) that is transparent to the high flux of X-rays of a synchrotron. Located at Grenoble, France, the HADES rig (Renard et al. 2016) allows the *in situ* imaging of a cm-sized sample with spatial resolution of several μm , while it is stressed under elevated pressure and temperature. Huang et al. (2019) has leveraged this advance in time-lapse 3D imaging to probe the development of compaction localization in a confined sample of Leitha limestone. A total of 70 X-ray CT images were acquired at different stages of loading at stress steps of 1–2 MPa. The data have provided an integrated perspective of the quasi-static development of discrete CBs and spatiotemporal evolution of damage on scales ranging from grain to continuum. The objective of this study is to systematically apply DVC to this unique set of *in situ* synchrotron CT data, so as to characterize quantitatively the spatiotemporal evolution of strain,

2 Materials and Methods

2.1 Leitha Limestone, Triaxial Compression and in Situ X-ray CT Imaging

Quarried at Hummel St. Margarethen/ Burgenland near Vienna, Austria, the Leitha limestone is a carbonate grainstone composed of >99% calcite (Baud et al. 2017). Petrophysical properties of our limestone block were summarized by Huang et al. (2019). Average value of the porosity is 26%, which is dominated by macroporosity. A triaxial compression experiment was conducted on a nominally dry sample at room temperature in the HADES apparatus. The sample (5 mm in diameter and 10 mm in length) was jacketed with Viton, and confining medium was silicon oil. Experimental details have been presented by Huang et al. (2019).

We adopt the sign convention that a compressive stress is positive. The principal stress in the axial direction is denoted by $\sigma_1 \geq \sigma_2 = \sigma_3$, the confining pressure. The mean stress is $P = (\sigma_1 + \sigma_2 + \sigma_3)/3$, and the difference between the maximum and minimum principal stresses is the differential stress $Q = \sigma_1 - \sigma_3$. A hydrostatic stress of 20 MPa was first applied, and before the application of differential stress, the first X-ray tomography scan was acquired. While maintaining the confining pressure at 20 MPa, the axial piston was progressively advanced by increments of 1–2 MPa. After each stress increment, the differential stress was held constant as the apparatus was rotated over

180°, while 1800 X-ray radiographs were acquired with a voxel size of 6.5 μm . Each radiograph extended over $13 \times 13 \text{ mm}^2$ (2000×2000 voxels), covering full length and width of sample and parts of the pistons and confining medium. Durations of the stress step and tomography scans were 1–2 min and 3 min, respectively.

2.2 Digital Volume Correlation

For a pair of CT images acquired at two stages of deformation (1 and 2), volumetric digital image correlation is performed to maximize an appropriate coherency measure of the spatial distributions of grey level in the two images, which establishes the correspondence between the coordinates of the same material points in stages 1 and 2. Accordingly, the coordinates in stage 1 can be mapped to the corresponding coordinates in stage 2, which allows the displacement and strain fields to be evaluated. We will refer to the images in stages 1 and 2 as “reference image” and “displaced image”, respectively. We used TomoWarp2 (Tudisco et al. 2017), which has proved to be effective as a DVC tool for delineating the geometric complexity of strain localization in porous rocks (Charalampidou et al. 2011; Baud et al. 2021). Grid spacing of the DVC nodes was 5 voxels in each direction, and the correlation window was a cuboid made up of $16 \times 16 \times 16$ voxels centered on the analysis node. The code seeks the subvoxel-resolved translation, and a finite element approach is adopted to evaluate the strain tensor from the displacement field (Hall 2006).

To visualize the deformation, we will follow the code to focus on two quantities: volumetric strain $\varepsilon_v = \varepsilon_{11} + \varepsilon_{22} + \varepsilon_{33}$, and the shear strain

$$\gamma_s = \sqrt{2[(\varepsilon_{11} - \varepsilon_{22})^2 + (\varepsilon_{11} - \varepsilon_{33})^2 + (\varepsilon_{22} - \varepsilon_{33})^2] + 12\varepsilon_{12}^2 + 12\varepsilon_{23}^2 + 12\varepsilon_{13}^2}/3,$$

which correspond to the first invariant of the strain tensor and $\sqrt{2}$ times the octahedral shear strain, respectively. For the strain tensor, we adopt here the sign convention for extension to be positive, and therefore a volumetric strain $\varepsilon_v > 0$ and $\varepsilon_v < 0$ correspond to dilation and compaction, respectively.

3 Results

3.1 Two Stages of Yielding and Failure Modes

Figure 1 presents the mechanical data for the differential stress as a function of relative shortening in the axial direction, which indicate that yielding has occurred over two distinct stages. In the initial stage, onset of yielding at a differential stress of ~ 50 MPa is manifested by a deviation from linearity in the stress-strain curve. Huang et al. (2019) concluded that this initial yielding corresponds to the onset of shear-enhanced compaction, related to the collapse of isolated pores of anomalous large dimension that were located in the upper portion of the sample. After the pore space has apparently been homogenized by such pore collapse, a second stage of yielding occurred with the differential stress at a plateau of 71–74 MPa and the strain hardening rate approaching zero. Huang et al. (2019) observed that this second stage corresponds to the initiation and development of five discrete CBs.

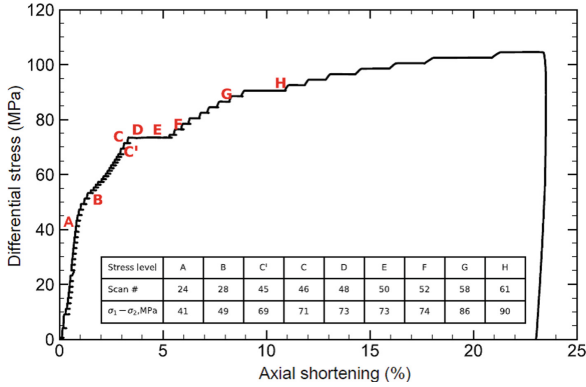


Fig. 1. Differential stress as a function of relative shortening for the Leitha limestone deformed at HADES at confining pressure of 20 MPa. The inset table lists the differential stress and scan number corresponding to the stages of deformation marked in red capital letters.

A total of nine CT images were selected for DVC analysis: the differential stresses and scan numbers are tabulated in the inset of Fig. 1. Given our focus on CB development, here we will present only the results for images C', C, D, E and F. Image C was acquired just before the hardening rate plateaued, and it will be adopted as the reference image. The displacement and strain fields derived from DVC will be denoted by two capital letters, which correspond to the displaced and reference images, respectively. For example, displacement E-C denotes the displacement vector derived by maximizing the cross-correlation of the grey-level data of the reference image C and displaced image E, and strain E-C denotes the strain tensor derived from the corresponding displacement gradients. The spatial distribution of the displacement and strain field is presented in a Cartesian coordinate system with the Z-axis aligned with the long axis of the sample and the applied stress σ_1 .

3.2 Spatiotemporal Evolution of Strain and Compaction Localization

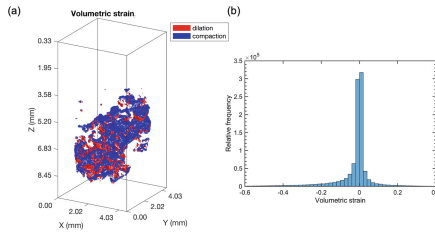


Fig. 2. Nodal volumetric strain associated with the D-C phase of deformation. (a) Spatial distribution of strain (with magnitude $\epsilon_V \leq -0.2$ for compaction or ≥ 0.2 for dilation), which concentrates in the lower half of the sample. (b) Relative frequency of the nodal volumetric strain.

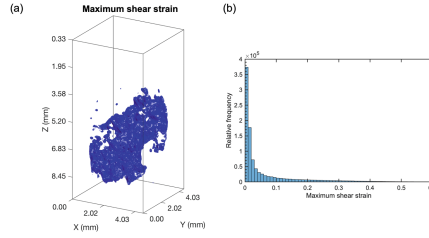


Fig. 3. Nodal shear strain associated with the D-C field. (a) Spatial distribution of shear strain concentration (with magnitude $\gamma_s \geq 0.2$). (b) Relative frequency of the nodal shear strain.

Figures 2 and 3 illustrate the spatial distribution of volumetric and shear strains at the second stage of yielding (D-C). Anomalous high strains developed predominately in the lower half of the sample. Figure 2a highlights the spatial concentration of volumetric strain (with magnitude ≤ -0.2 for compaction or ≥ 0.2 for dilation). The nodal strain ε_v ranges from compressive to extensile over a broad range of values (Fig. 2b). 3D rendition of ε_v (not presented here) indicates the clustering of compaction to be more pronounced than dilation, with the latter mostly located at the boundary of a compactive cluster. Concentration of shear strain γ_s has also developed in parallel with the compaction and dilation (Fig. 3a), with values that span over a broad range as well (Fig. 3b).

Huang et al. (2019) divided the sample into 155 layers with thickness of 10 voxels, and determined the porosities of each layer from the segmented images at each stage of deformation. The porosity profile they derived for stage C and locations of five CBs they inferred are shown in Fig. 4. For comparison, we evaluated the mesoscopic volumetric strain by averaging the nodal ε_v in each 5-voxel layer. Whereas the C'-C strains were relatively small, the mesoscopic strains associated with D-C, E-C and F-C showed five peaks with compactive strain concentration ranging up to 7%. These local maximums of compaction determined by DVC basically coincide with the CB locations inferred from the segmented images. They also correlate with local maximums in the initial porosity profile (Fig. 4). Further analysis of porosity distribution in 3D (not presented here) suggest that a large local porosity would indeed promote the initiation of compaction localization.

Integration of *in situ* μ CT imaging with DVC has revealed in fine details the spatiotemporal evolution of the strains of a CB as it initiates and propagates. Geometric complexities of the volumetric and shear strains associated with CB1 are highlighted in Fig. 5a, b, respectively, with selected serial sections on the X-Y plane for D-C, E-C and F-C. Spatial distributions of the two strain invariants are qualitatively similar, and the spatial extents of strain localization increase with increasing deformation. Analogous attributes were also observed in connection with CB2 (Fig. 6) and CB3 (Fig. 7).

To compare the spatial distribution and relative location of localized strain in the five bands, we plot in Fig. 8 the thickness-averaged volumetric strain $\bar{\varepsilon}_v(X, Y)$ of each CB associated with the deformation phase F-C field. By stage F the compaction accumulated in the five CBs covered distinct domains on the circular cross-section without significant spatial overlap. Nevertheless, if one were to project all five CBs on the same X-Y plane, they would basically cover the full circular section. We have also checked the sum of the

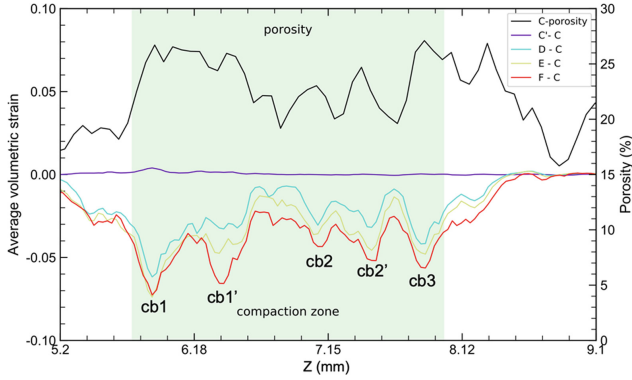


Fig. 4. Axial distribution of mesoscopic volumetric strain for C'-C, D-C, E-C and F-C. For comparison, the porosity profile for stage C and locations of five CBs inferred by Huang et al. (2019) are also shown.

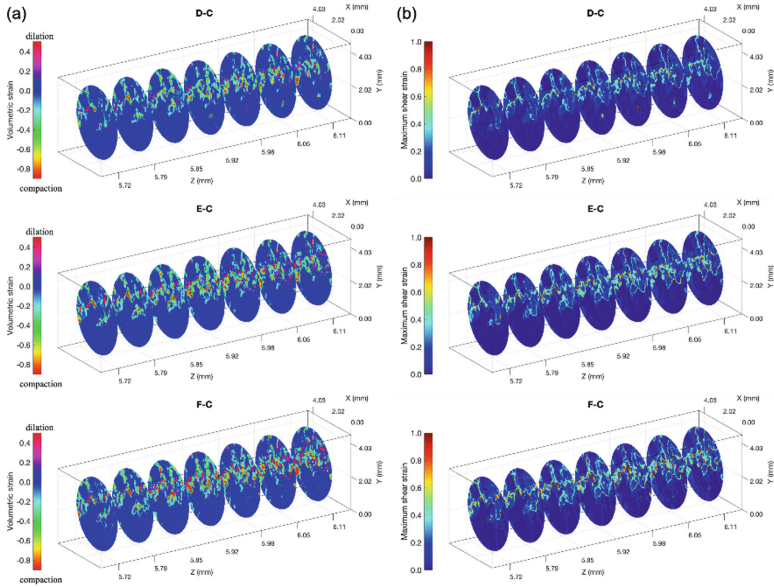


Fig. 5. Serial sections of CB1 showing the spatial distribution of nodal (a) volumetric strain ϵ_V , and (b) shear strain γ_S for three different phases of deformation: D-C, E-C and F-C.

volumetric strains distributed over all five CBs, which can indeed be approximated as a uniform compression of the sub-volume in the axial direction. The creep deformation (from C to F) led to further strain hardening, and our DVC analysis (not included here due to space limitation) has shown that enhanced compaction spread to beyond the CBs and the top layer, thus filling up the strain deficits in the gap domains.

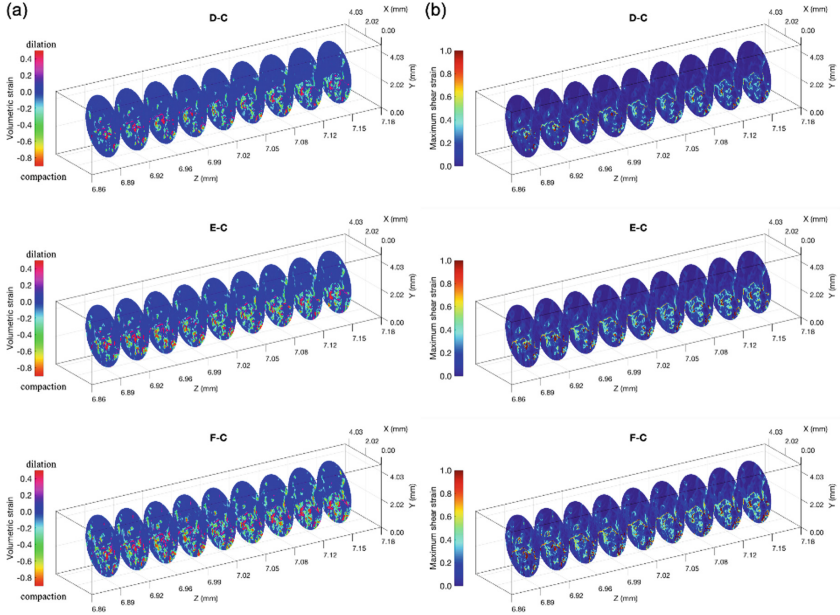


Fig. 6. Serial sections of CB2 showing the spatial distribution of nodal (a) volumetric strain ε_V , and (b) shear strain γ_s for three different phases of deformation: D-C, E-C and F-C.

4 Discussion

We have systematically applied digital volume correlation to time-lapse synchrotron μ CT data on compressive failure of a porous rock, and obtained some of the first *in situ* observations on the grain-scale heterogeneity of strain in a porous aggregate, as well as the fine structures and geometric complexity of compaction bands. The analysis has also provided useful insights into the mechanics of compressive failure at multiple scales, and important constraints on the multiscale modeling of constitutive response and failure mode.

Our DVC analysis corroborates the indirect inference of Huang et al. (2019) based on segmented CT images that five discrete CBs had developed in the synchrotron sample (Fig. 4). Most importantly, we have quantitatively delineated the spatial distributions of volumetric and shear strains, as well as the geometric attributes of the CBs (Figs. 5, 6 and 7). During the second stage of yielding, emergence of strain concentration at points of the putative compaction bands occurred almost simultaneously (Fig. 8), in basic agreement with the concept of strain localization as a bifurcation. Comparison of the CB location with the preexisting pore space indicates that a high local porosity would promote the nucleation of a CB. Abdallah et al. (2021) has recently suggested that porosity heterogeneity may play an important role in triggering compaction localization.

However, there are at least two questions that remain unresolved. First, Huang et al. (2019) pointed out that the high-frequency record of displacement for the synchrotron experiment indicates five stress drops that were separated by time steps much shorter

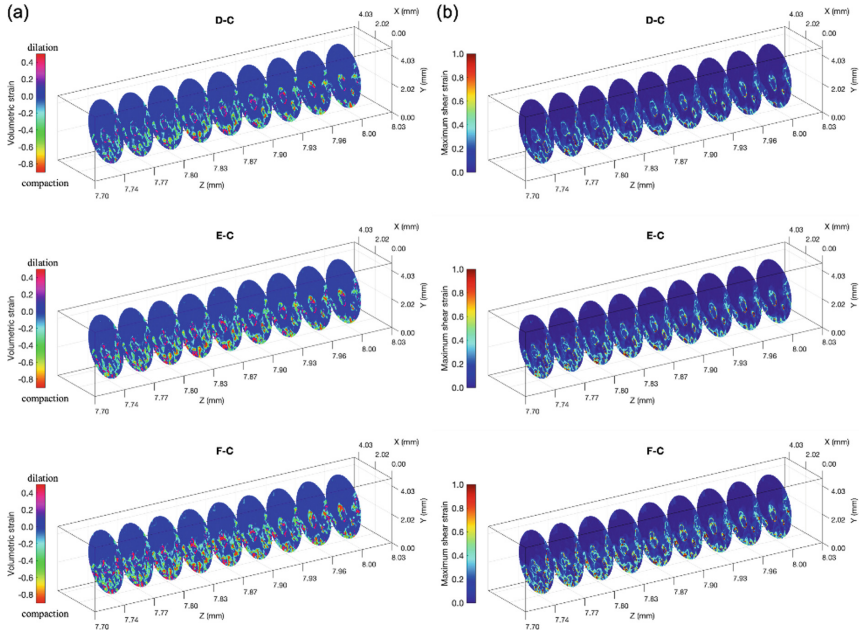


Fig. 7. Serial sections of CB3 showing the spatial distribution of nodal (a) volumetric strain ϵ_v , and (b) shear strain γ_s for three different phases of deformation: D-C, E-C and F-C.

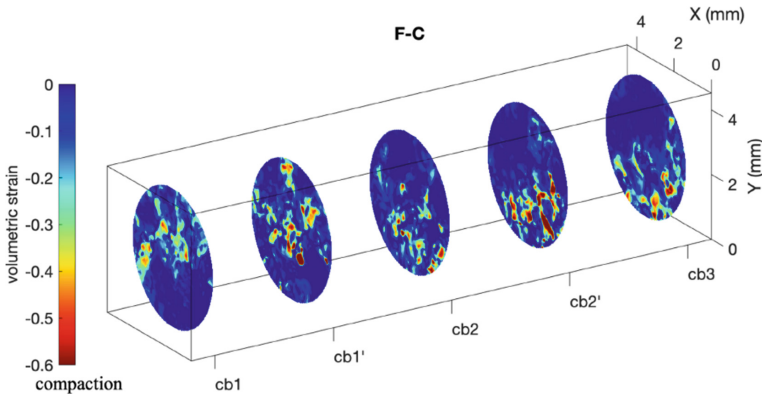


Fig. 8. Spatial distribution of the thickness-averaged volumetric strain of the five CBs that had cumulated during the F-C phase of deformation.

than the several minutes required to acquire a single set of tomographic data, which implies that sequential initiation of the five CBs was not resolved temporally by our DVC analysis of the tomographic data for the D-C phase. Second, although the orientation and alignment of strain localization suggest that the planar structures, we identified are CBs, a definitive categorization of them as CBs requires a confirmation that they are indeed

associated with normal displacement discontinuities. To tackle these two questions, one needs to probe more deeply into the spatiotemporal correlation of the strain and spatial distribution of the displacement vector and its alignment. Though beyond the scope of the present study, these are important questions which we intend to address in future research.

Acknowledgements. We have benefitted from discussion over the years with Steve Hall on digital volume correlation and the use of the code TomoWarp2. This study was partially supported by funding from the Hong Kong Research Grants Council GRF14323916, the France-Hong Kong Collaborative Program Procore 30805PM and F-CUHK405/16, CNRS (PICS 07961). Fanbao Meng was supported by the Impact Postdoctoral Fellowship Scheme of The Chinese University of Hong Kong and the Fundamental Research Funds for the Central Universities, Sun Yat-sen University-22qntd2101. The X-ray tomography data are available to the scientific community (Renard 2019).

References

- Abdallah, Y., Sulem, J., Bornert, M., Ghabezloo, S., Stefanou, I.: Compaction banding in high-porosity carbonate rocks: 1. Experimental observations. *J. Geophys. Res.: Solid Earth* **126**(1), e2020JB020538 (2021). <https://doi.org/10.1029/2020JB020538>
- Baud, P., Exner, U., Lommatsch, M., Reuschlé, T., Wong, T.-f.: Mechanical behavior, failure modes and transport properties in a porous limestone. *J. Geophys. Res.: Solid Earth* **122**(9), 7363–7387 (2017). <https://doi.org/10.1002/2017JB014060>
- Baud, P., Hall, S., Heap, M. J., Ji, Y., Wong, T.-f.: The brittle-ductile transition in porous limestone: Failure mode, constitutive modeling of inelastic deformation and strain localization. *J. Geophys. Res.: Solid Earth* **126**(5), e2020JB021602 (2021). <https://doi.org/10.1029/2020JB021602>
- Charalampidou, E.-M., Hall, S.A., Stanchits, S., Lewis, H., Viggiani, G.: Characterization of shear and compaction bands in a porous sandstone deformed under triaxial compression. *Tectonophysics* **503**, 8–17 (2011). <https://doi.org/10.1016/j.tecto.2010.09.032>
- Hall, S.A.: A methodology for 7D warping and deformation monitoring using time-lapse seismic data. *Geophysics* **71**(4), O21–O31 (2006). <https://doi.org/10.1190/1.2212227>
- Huang, L., Baud, P., Cordonnier, B., Renard, F., Liu, L., Wong, T.-f.: Synchrotron X-ray imaging in 4D: Multiscale failure and compaction localization in triaxially compressed porous limestone. *Earth Planet. Sci. Lett.* **528**, 115831 (2019). <https://doi.org/10.1016/j.epsl.2019.115831>
- Issen, K.A., Rudnicki, J.W.: Conditions for compaction bands in porous rock. *J. Geophys. Res.* **105**, 21529–21536 (2000). <https://doi.org/10.1029/2000JB900185>
- Lockner, D.: The role of acoustic emission in the study of rock fracture. *Int. J. Rock Mech. Min. Sci.* **30**, 883–900 (1993)
- Lockner, D.A., Byerlee, J.D., Kuksenko, V., Ponomarev, A., Sidorin, A.: Observations of quasi-static fault growth from acoustic emissions. In: Evans, B., Wong, T.-f. (eds.) *Fault Mechanics and Transport Properties of Rocks*, pp. 3–32. Academic Press (1992)
- Renard, F., Cordonnier, B., Kobchenko, M., Kandula, N., Weiss, J., Zhu, W.: Microscale characterization of rupture nucleation unravels precursors to faulting in rocks. *Earth Planet. Sci. Lett.* **476**, 69–78 (2017). <https://doi.org/10.1016/j.epsl.2017.08.002>
- Renard, F.: Synchrotron X-ray imaging in 4D: multiscale failure and compaction localization in triaxially compressed porous limestone. *Nor-store* (2019). <https://doi.org/10.11582/2019.00015>

- Renard, F., Cordonnier, B., Dysthe, D.K., Boller, E., Tafforeau, P., Rack, A.: A deformation rig for synchrotron microtomography studies of geomaterials under conditions down to 10 km depth in the Earth. *J. Synchrotron Radiat.* **23**(4), 1030–1034 (2016). <https://doi.org/10.1107/S1600577516008730>
- Rice, J.R.: The localization of plastic deformation. In: Koiter, W.T. (eds.) *Theoretical and Applied Mechanics*, pp. 207–220 (1976)
- Tudisco, E., Andò, E., Cailletaud, R., Hall, S.A.: TomoWarp2: a local digital volume correlation code. *SoftwareX* **6**, 267–270 (2017). <https://doi.org/10.1016/j.softx.2017.10.002>
- Vardoulakis, I.G., Sulem, J.: *Bifurcation analysis in geomechanics*, 462 pp. Blackie (1995)



Prediction of the Onset and Orientation of Shear Bands in Partially Saturated Soils Using a Coupled Hydro-Mechanical Model

Dat G. Phan¹, Giang D. Nguyen¹(✉), Ha H. Bui², and Terry Bennett¹

¹ School of Civil, Environmental and Mining Engineering, The University of Adelaide, Adelaide, SA 5005, Australia

g.nguyen@adelaide.edu.au

² Department of Civil Engineering, Monash University, Clayton, VIC 3800, Australia

Abstract. The onset and orientation of localisation bands in partially saturated soils are intrinsically dependent upon different mechanical loading and saturation conditions, besides material properties. It is analysed in this paper using a new constitutive model for partially saturated soils accounting for the strong coupling between hydraulic and mechanical responses. This strong coupling is realised in the model through a unique yield surface dependent on both stress and suction, and two evolutions rules for irrecoverable saturation and plastic strain, both of which share the same “plastic” multiplier. This automatically leads to simultaneous activation of both hydraulic and mechanical dissipative mechanisms upon yielding, and hence different hydro-mechanical responses in wetting-drying and loading-unloading paths. The tangent stiffness with cross-coupling terms always guarantees hydro-mechanical coupling upon yielding, facilitating the bifurcation analysis for the onset of localisation and corresponding orientation of shear bands under different hydro-mechanical conditions. Numerical examples based on drained and undrained triaxial tests are used to demonstrate the promising features of the new model.

Keywords: Partially saturated soils · Coupled hydro-mechanical model · Bifurcation · Shear bands

1 Introduction

The onset and orientation of localisation bands at partially saturated conditions intrinsically depend on various loading paths and saturation degrees, in addition to material properties. This is governed by the coupled hydro-mechanical inelastic responses reflected in the interactions between the grain rearrangement and liquid-bridge redistribution inside shear bands [4, 5]. The effect of mechanical and hydraulic conditions on bifurcation in partially saturated soils has been observed in several triaxial [6, 10] and biaxial [1, 3] tests where inclination angles increase with suction, and decrease with the increase of confining pressure.

The underlying features associated with suction-dependent activation and inclination of the shear band have been investigated by [13] using the classical bifurcation theory [12] without considering the effects of the Soil Water Characteristic Curve (SWCC). SWCC was taken into account in bifurcation condition in the work of [2], despite the fact that water retention behaviour is non-unique [8]. Although volume-dependent SWCC was used in [9] and [14], the effect of hydraulic irreversibility and its interaction with the mechanical behaviour described by a plasticity model on bifurcation were not fully investigated. Therefore, these existing work on bifurcation in partially saturated soils do not reflect well the coupled hydro-mechanical effects in the dependence of SWCC on mechanical behaviour and vice versa, as consequences of interactions between grain contact sliding and capillary irreversibility [4, 5].

The onset and orientation of localised failures of partially saturated soils involving the wetting-drying difference and its interdependence with the mechanical irrecoverability under various loading and saturation conditions are examined in this paper, using the bifurcation criterion based on the coupled hydro-mechanical model of [11]. This model allows the incorporation of the irreversible degree of saturation and its strong coupling with plastic strain for producing a single critical state yield function and a unique “plastic” multiplier with different evolution rules for irreversible changes of strain and saturation degree to reflect mechanisms at the grain scale for the interdependence of stress, suction, internal variables and their rates. Consequently, SWCC in this framework is path-dependent in nature, inducing different responses under hydraulic and mechanical loading conditions, while the cross-coupling terms in the tangent stiffness always guarantee hydro-mechanical coupling upon yielding to facilitate the bifurcation analysis for the onset of localisation and orientation of shear bands in various hydromechanical states. These promising features of our approach are demonstrated in several validation results and parametric studies.

2 Formulation

A summary of the basic formulations of the present approach is provided in this section by passing intermediate details on the mathematical derivations which can be found in [11].

2.1 Constitutive Model

The coupled hydro-mechanical model of [11] is employed as a basis to investigate bifurcation conditions for partially saturated soils. The following stress-strain and suction-saturation relationships are used:

$$\sigma'_{ij} = D_{ijkl}^e (\varepsilon_{ij} - \varepsilon_{ij}^p) \quad (1)$$

$$s^* = (p_u + s_0^*) \exp \left\{ \frac{S_{r0} + [(-S_r) - (-S_r^p)]}{\kappa_h} \right\} - p_u \quad (2)$$

where σ'_{ij} is the effective stress tensor; s^* is the modified suction; ε_{ij} is the total strain tensor; ε_{ij}^p is the plastic strain tensor; S_r is the total saturation degree; S_r^p is the irreversible saturation; κ_h is a parameter to control the amount of reversible energy stored in the water menisci; $p_u = 1$ kPa is to allow the consistency of unit; $D_{ijkl}^e = \frac{E}{2(1+\varrho)} \left(\frac{2\varrho}{1-2\varrho} \delta_{ij} \delta_{kl} + \delta_{ik} \delta_{jl} + \delta_{il} \delta_{jk} \right)$ is the pressure-independent elastic stiffness tensor (e.g. E denoting the Young modulus, ϱ denoting the Poisson's ratio and δ_{ij} being the Kronecker delta); s_0^* and S_{r0} denote initial values of s^* and S_r , respectively. It is noted that the minus sign of S_r and S_r^p appears in Eq. (2) since $-S_r$ and $-S_r^p$ are used as thermodynamic conjugates of modified suction (s^*) and hydraulic dissipative ($\chi_h = s^* - p_b$) stresses (see [11] for further details).

The model employs a single yield surface (y) dependent on suction and triaxial stresses (e.g. p' denoting effective mean stress, and q denoting deviator stress under geotechnical sign convention (compression positive)) as follows:

$$y = \frac{\left(p' - \frac{1}{r} p'_{c(us)}\right)^2}{\left[\left(1 - \frac{2}{r}\right)p' + \frac{1}{r} p'_{c(us)}\right]^2} + \frac{q^2}{\left[(1 - \alpha)p' + \frac{\alpha}{r} p'_{c(us)}\right]^2 M^2} - 1 \leq 0 \quad (3)$$

The coupled hydro-mechanical flow rules, based on the yield function y^* in the space of volumetric ($\chi_v = p'$), shear ($\chi_s = q$) and hydraulic ($\chi_h = s^* - p_b$) dissipative generalised stresses and a single multiplier $\dot{\lambda}_p$, are written as follows:

$$\dot{\varepsilon}_v^p = \dot{\lambda}_p \frac{\partial y^*}{\partial \chi_v} = \dot{\lambda}_p \frac{2\left(p' - \frac{1}{r} p'_{c(us)}\right)}{\left[\left(1 - \frac{2}{r}\right)p' + \frac{1}{r} p'_{c(us)}\right]^2} \exp[-\beta(1 - S_r)] \quad (4)$$

$$\dot{\varepsilon}_s^p = \dot{\lambda}_p \frac{\partial y^*}{\partial \chi_s} = \dot{\lambda}_p \frac{2q}{\left[(1 - \alpha)p' + \frac{\alpha}{r} p'_{c(us)}\right]^2 M^2} \quad (5)$$

$$-\dot{S}_r^p = \dot{\lambda}_p \frac{\partial y^*}{\partial \chi_h} = \dot{\lambda}_p \frac{2\left(p' - \frac{1}{r} p'_{c(us)}\right)^2}{(s^* - p_b) \left[\left(1 - \frac{2}{r}\right)p' + \frac{1}{r} p'_{c(us)}\right]^2} [1 - \exp[-\beta(1 - S_r)]] \quad (6)$$

It is noted that y^* plays the role of a plastic potential in classical plasticity theory, the detailed thermodynamic formulation of which can be found in [11]. In the above expressions, β ($0 < \beta \leq 1$) is used to govern the coupling between saturation and volumetric deformation upon yielding; r is a spacing ratio to control the shape of yield loci; α is a parameter governing the strength of the material and non-associativity of the flow rules; M is the slope of the critical state line in the $p' : q$ plane and p_b is a parameter controlling the stored irreversible hydraulic energy. The function $p'_{c(us)}$ is the hardening law dependent on s^* and ε_v^p :

$$p'_{c(us)} = p'_R \left[\frac{p'_{c0} \exp\left(\frac{\varepsilon_v^p}{\lambda}\right)}{p'_R} \right]^{\frac{1}{[(1-\xi)\exp(-\mu s^*) + \xi]}} \quad (7)$$

with $\bar{\lambda}$ representing the slope of the virgin compression line for saturated conditions; p'_{c0} being the initial yield pressure under isotropic compression at fully saturated conditions; p'_R denoting the stress parameter controlling the yield curve; ξ being a dimensionless parameter controlling the maximum soil stiffness, and μ being a constant related to the change of soil stiffness with modified suction.

2.2 Bifurcation Criterion

The classical discontinuous bifurcation condition [12] is used for detecting the emergence of a single tabular shear band observed in constant suction and water content tests of partially saturated soils. The discontinuous bifurcation condition based on the localisation tensor A_{ik} (or acoustic tensor) is:

$$\det(A_{ik}) = \det(D_{ijkl}n_jn_l) \leq 0 \quad (8)$$

where $n_j = \begin{bmatrix} n_a & 0 & n_r \\ 0 & n_r & n_a \end{bmatrix} = \begin{bmatrix} \cos\varphi & 0 & \sin\varphi \\ 0 & \sin\varphi & \cos\varphi \end{bmatrix}$ is the matrix form of a normal vector with the inclination of shear bands φ illustrated in Fig. 1; D_{ijkl} is the coupled hydro-mechanical tangent stiffness tensor in the constitutive relationship in terms of total stress σ_{ij} and suction s where its form for drained tests can be written as:

$$D_{ijkl} = \Lambda_{ijkl} - \frac{S_r\delta_{ij}\left[\frac{(\Omega_{kl}+s\delta_{kl})}{\phi} + s\delta_{kl}\right]}{\phi} - \left(\frac{1}{\Upsilon}\right)\left[\Pi_{ij} + \left(s - \frac{S_r\Upsilon}{\phi}\right)\delta_{ij}\right](\Omega_{kl} + s\delta_{kl}) \quad (9)$$

In the case of undrained tests, from the condition of constant gravimetric water content, D_{ijkl} can be expressed in the following form [11]:

$$D_{ijkl} = \Lambda_{ijkl} - \frac{S_r\delta_{ij}\left[\frac{(\Omega_{kl}+s\delta_{kl})}{\phi} + s\delta_{kl}\right]}{\phi} - \frac{G_s w v}{(v-1)^2}\left[\Pi_{ij} + \left(s - \frac{S_r\Upsilon}{\phi}\right)\delta_{ij}\right]\delta_{kl} \quad (10)$$

where ϕ , w , v and G_s are porosity, gravimetric water content, specific volume and bulk specific gravity, while Λ_{ijkl} , Π_{ij} , Ω_{kl} and Υ are written as follows:

$$\Lambda_{ijkl} = D_{ijkl}^e \left(1 - M_{kl} \frac{\partial y^*}{\partial \chi_{kl}}\right) \quad (11)$$

$$\Pi_{ij} = -D_{ijkl}^e H \frac{\partial y^*}{\partial \chi_{kl}} \quad (12)$$

$$\Omega_{kl} = -\frac{(s^* + p_u)}{\kappa_h} \frac{\partial y^*}{\partial \chi_h} M_{kl} \quad (13)$$

$$\Upsilon = \frac{(s^* + p_u)}{\kappa_h} \left(1 - H \frac{\partial y^*}{\partial \chi_h}\right) \quad (14)$$

In the above expressions, χ_{kl} is the dissipative generalised stress tensor with $\frac{\partial y^*}{\partial \chi_{kl}} = \frac{\partial y^*}{\partial \chi_v} \frac{\partial \chi_v}{\partial \chi_{kl}} + \frac{\partial y^*}{\partial \chi_s} \frac{\partial \chi_s}{\partial \chi_{kl}}$, while M_{kl} and H are of the following forms [11]:

$$M_{kl} = \frac{D_{ijkl}^e \frac{\partial y}{\partial \sigma'_{ij}}}{\left(\frac{\partial y}{\partial \sigma'_{ij}}\right)^T D_{ijkl}^e \frac{\partial y^*}{\partial \chi_{kl}} + \frac{\partial y}{\partial p'_{c(us)}} \frac{\partial p'_{c(us)}}{\partial s^*} \frac{(s^* + p_u)}{\kappa_h} \frac{\partial y^*}{\partial \chi_h} - \frac{\partial y}{\partial p'_{c(us)}} \frac{\partial p'_{c(us)}}{\partial p'_c} \frac{p'_c}{\lambda} \frac{\partial y^*}{\partial \chi_v}} \tag{15}$$

$$H = \frac{\frac{(s^* + p_u)}{\kappa_h} \frac{\partial y}{\partial p'_{c(us)}} \frac{\partial p'_{c(us)}}{\partial s^*}}{\left(\frac{\partial y}{\partial \sigma'_{ij}}\right)^T D_{ijkl}^e \frac{\partial y^*}{\partial \chi_{kl}} + \frac{\partial y}{\partial p'_{c(us)}} \frac{\partial p'_{c(us)}}{\partial s^*} \frac{(s^* + p_u)}{\kappa_h} \frac{\partial y^*}{\partial \chi_h} - \frac{\partial y}{\partial p'_{c(us)}} \frac{\partial p'_{c(us)}}{\partial p'_c} \frac{p'_c}{\lambda} \frac{\partial y^*}{\partial \chi_v}} \tag{16}$$

The developed bifurcation condition includes cross-coupling terms of D_{ijkl} to bring benefits in reflecting the inter-dependence between mechanical and hydraulic irreversibility. This automatically leads to the appearance of a path-dependent water retention curve, enabling our bifurcation criterion to capture the effect of the coupling between wetting-drying and unloading-loading differences on the onset and orientation of localisation bands, making the present approach distinct from existing ones [2, 9, 13, 14].

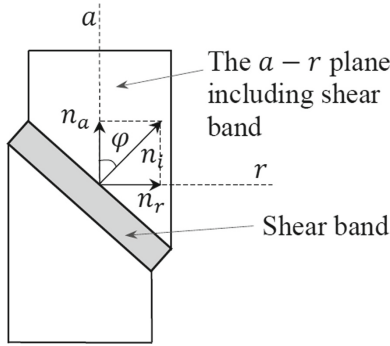


Fig. 1. Illustration of the direction vector of the localisation band in the shear tests where a represents the axial axis and r represents the radial axis

3 Results and Discussions

Both behaviour and bifurcation are considered in this study, given they are correlated and cannot be separated. Therefore, the model must be able to capture the trends of experimentally measured behaviour first, before attempts to investigate the onset and orientation of localisation band. It is noted that only the trends can be captured, as the problem becomes a boundary value problem once localisation occurs. Enhancements

to the structure of constitutive models are needed in the future to describe correctly post-localisation behaviour at the constitutive level [7]. Therefore the calibration used to determine model parameters is aimed at capturing the trends of behaviour only.

To assess the performance of our approach, we first validate the model predictions against the drained biaxial shear test on Hostun sand [1] at two levels of suction $s = 0$ kPa and 20 kPa under the confining pressure of $\bar{\sigma}_r = 50$ kPa. In this example, the stress-strain curves (e.g. $\epsilon_a : q, \epsilon_a : \epsilon_v$) at $s = 0$ kPa and $s = 20$ kPa are illustrated in Figs. 2 and 3a, respectively, while Fig. 3b shows the result on the variation of φ and $\det(A_{ij})$ at the bifurcation point for $s = 20$ kPa. The minimisation of $\det(A_{ij})$ is determined by scanning orientation φ from 0° to 90° at each step of the numerical implementation. The following model parameters: $E = 18000$ kPa; $\varrho = 0.25$; $\bar{\lambda} = 0.04$; $M = 1.035$; $p'_{c0} = 600$ kPa; $r = 1.5$; $\alpha = 0.65$ are identified using the experimental results at $s = 0$ kPa as presented in Fig. 2, while $\kappa_h = 0.9$; $p'_R = 10.41$ kPa; $\xi = 0.352$; $\mu = 0.0529$ kPa $^{-1}$; $\beta = 0.08$ and $p_b = 100$ kPa can be selected to obtain a close agreement between the computed and measured results on shear stress at $s = 20$ kPa (see Fig. 3a). Given these calibrated material constants, the measured band orientation in the case of $s = 20$ kPa is reasonably captured by the model (see Fig. 3b). Furthermore, it can be seen in Figs. 2 and 3a that the loading case of $s = 0$ kPa exhibits an earlier bifurcation mode (at $\epsilon_a = 0.0203$, $q = 250.676$ kPa) in comparison with that of $s = 20$ kPa (at $\epsilon_a = 0.0241$, $q = 307.691$ kPa), demonstrating the capacity of the proposed approach in predicting the hydraulic effects on the onset of shear bands in partially saturated soils. Nevertheless, we acknowledge a disparity between numerical and experimental data encountered in the volumetric strain at $s = 20$ kPa (see Fig. 3a) due to missing representations of the effects of orientation and thickness of the localisation band on the softening response despite their importance in the post-localisation regime.

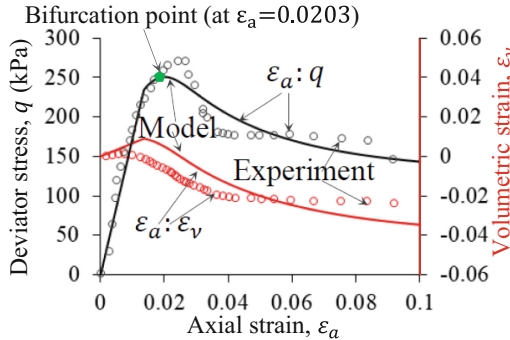


Fig. 2. Calibration of parameters $E, \varrho, \bar{\lambda}, M, p'_{c0}, r$ and α based on the drained biaxial compression test on Hostun sand at the fully saturated state ($s = 0$ kPa) with $\bar{\sigma}_r = 50$ kPa (after [1])

The model performance is further investigated using the water content-controlled triaxial shear test on compacted Kaolin soil [15] at three levels of confining pressures $\bar{\sigma}_r = 150$ kPa, 200 kPa and 300 kPa with the initial suction of $s_0 = 300$ kPa [16]. In this example, we take parameters as $E = 25000$ kPa; $\varrho = 0.25$; $\bar{\lambda} = 0.06$; $M = 1.19$; $\kappa_h = 0.16$; $p'_R = 22$ kPa; $\xi = 0.6$; $\mu = 0.0601$ kPa $^{-1}$; $p'_{c0} = 300$ kPa; $r = 1.97$;

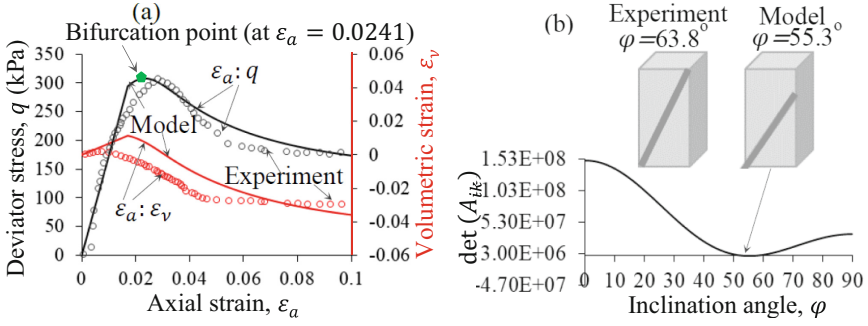


Fig. 3. Validation with the drained biaxial compression test on Hostun sand at $s = 20$ kPa with $\bar{\sigma}_r = 50$ kPa (after [1]) **a** $\epsilon_a : q$ and $\epsilon_a : \epsilon_v$ **b** $\varphi : \det(A_{ik})$ at the bifurcation point

$\alpha = 0.85$; $\beta = 0.05$; $p_b = 70$ kPa and $G_s = 2.644$ in which their calibrations are based on the best fit between the measured data and its predicted counterpart at $\bar{\sigma}_r = 200$ kPa in terms of stress-strain (see Fig. 4) and orientation of shear band (see Fig. 5). It can be seen in Fig. 4 that the current model can provide a good prediction of the experimental results on stress-strain ($\epsilon_a : \epsilon_v, \epsilon_a : q$) where the orientation of the shear band decreases (see Fig. 5) in conjunction with the less profound dilative behaviour at higher confining pressures. It is noted that the smooth transition from elastic to plastic regimes is not focused on in this study and this shortcoming will be addressed in future work. The behaviour is linear up to peak, resulting in an abrupt change in the slope of the stress-strain curve. This change of slope is however less profound for the loading path in drained biaxial compression test as illustrated in Figs. 2 and 3, thanks to the confinement in the out of plane direction (plane strain condition).

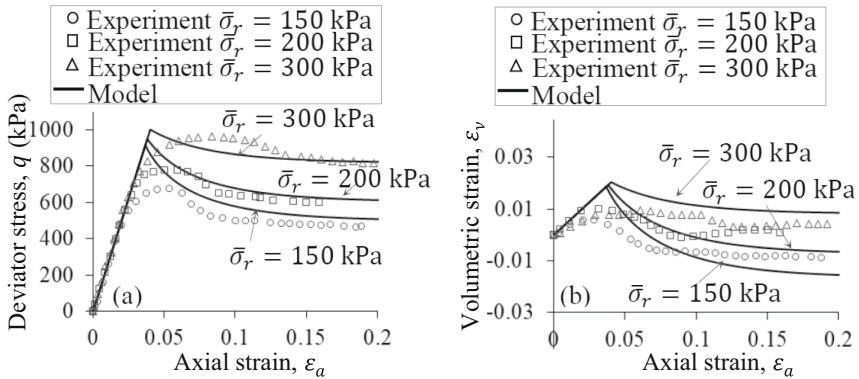


Fig. 4. Validation with an undrained triaxial compression test on Kaolin soil at the initial suction of $s_0 = 300$ kPa (after [15]) **a** $\epsilon_a : q$ **b** $\epsilon_a : \epsilon_v$

A parametric study is performed to investigate the effects of coupling between saturation and volumetric deformation upon yielding on bifurcation, through different values of parameter β ($\beta = 0; 0.5; 0.9$). In this example, we use the same constants as adopted

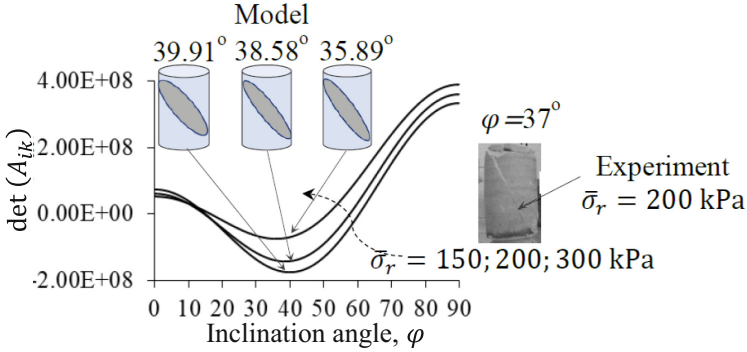


Fig. 5. Validation with the measured orientation of shear band in the undrained triaxial compression test on Kaolin soil at $s_0 = 300$ kPa based on $\varphi : \det(A_{ik})$ at the bifurcation point (after [15])

earlier for the example of the undrained triaxial shear test on compacted Kaolin soil [15]. It can be found that $\beta \neq 0$ allows the proposed bifurcation criterion to capture the wetting-drying difference (e.g. reflected in $-\dot{S}_r^p$) induced by the loading-unloading process (e.g. reflected in $\dot{\epsilon}_v^p$) and vice versa due to its presence in the flow rules (see Eqs. (4) and (6)). Furthermore, Fig. 6 shows that the decrease in β leads to the increase in the orientation of shear band φ because the irreversible change of saturation degree is observed to be stronger at a higher β . The sensitivity of the bifurcation response to β can also be clarified through its contribution to generating the effect of saturation degree on the plastic dilatancy ratio $\dot{\epsilon}_v^p / \dot{\epsilon}_s^p$ which significantly affects the dilation as seen in the $\epsilon_a : \epsilon_v$ and $\epsilon_a : q$ results in Fig. 6a. These features reflect hydromechanical mechanisms of the interactions between grain contact sliding and capillary irreversibility at the grain scale, confirming an advance of our bifurcation theory in comparison with existing ones for partially saturated soils. Nevertheless, it is acknowledged that the effect of β on the onset of shear band is not strong in this example due to the loading condition despite its appearance in the formulation.

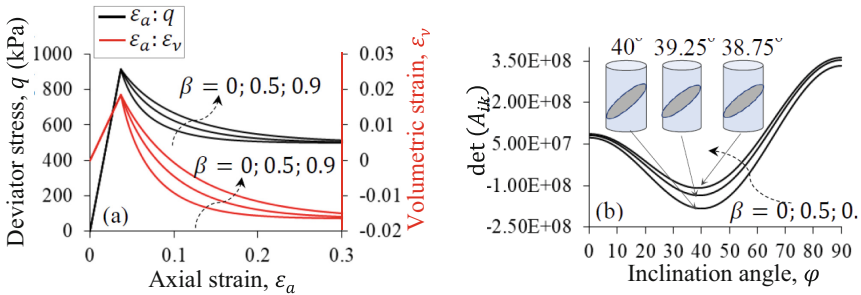


Fig. 6. Effects of different values of β on the model responses **a** $\epsilon_a : q$ and $\epsilon_a : \epsilon_v$ **b** $\varphi : \det(A_{ik})$ at bifurcation point

4 Conclusion

This study focuses on the development of a criterion for detecting the onset and orientation of the localisation band under the effects of the coupling between mechanical and hydraulic yielding responses in different loading and saturation regimes, based on the classical bifurcation theory [12] and the constitutive model for unsaturated soils by [11]. The use of a single yield surface dependent on both stress and suction and two flow rules for the irreversible rates of strain and saturation degree allows better descriptions of hydro-mechanical coupling in partially saturated soils. In particular tangent stiffness with cross-coupling terms is used in the bifurcation criterion to provide the path-dependent nature of SWCC, without the need of a separate water retention curve. The potentials of the model in predicting both onset and orientation of localisation band under different levels of stress and suction can be seen in numerical examples. Nevertheless, the effects of the thickness of the localisation band in the post-localisation regime are not considered in the proposed formulation yet, hindering it from correctly reproducing the size-dependent responses [7]. This will be addressed in our future works.

Acknowledgments. The authors gratefully acknowledge support from the Australian Research Council via Discovery Projects FT140100408, FT200100884, DP170103793, and DP190102779.

References

1. Alabdullah, J.: Testing unsaturated soil for plane strain conditions: a new double-wall biaxial device. *Lehrstuhl für Grundbau. Boden-und Felsmechanik* (2010)
2. Borja, R.I.: Cam-Clay plasticity. Part V: a mathematical framework for three-phase deformation and strain localization analyses of partially saturated porous media. *Comput. Methods Appl. Mech. Eng.* **193**, 48–51, 5301–5338 (2004)
3. Cruz, J.A., Hoyos, L.R., Lizcano, A.: Unsaturated soil response under plane strain conditions using a servo/suction-controlled biaxial apparatus. In *Unsaturated Soils: Research and Applications*, pp. 31–38. Springer (2012)
4. Higo, Y., Oka, F., Kimoto, S., Sanagawa, T., Matsushima, Y.: Study of strain localization and microstructural changes in partially saturated sand during triaxial tests using microfocus X-ray CT. *Soils Found.* **51**(1), 95–111 (2011)
5. Higo, Y., Oka, F., Sato, T., Matsushima, Y., Kimoto, S.: Investigation of localized deformation in partially saturated sand under triaxial compression using microfocus X-ray CT with digital image correlation. *Soils Found.* **53**(2), 181–198 (2013)
6. Maleki, M., Bayat, M.: Experimental evaluation of mechanical behavior of unsaturated silty sand under constant water content condition. *Eng. Geol.* **141**, 45–56 (2012)
7. Nguyen, G.D., Bui, H.H.: A thermodynamics-and mechanism-based framework for constitutive models with evolving thickness of localisation band. *Int. J. Solids Struct.* **187**, 100–120 (2020)
8. Nuth, M., Laloui, L.: Advances in modelling hysteretic water retention curve in deformable soils. *Comput. Geotech.* **35**(6), 835–844 (2008)
9. Perić, D., Zhao, G., Khalili, N.: Strain localization in unsaturated elastic-plastic materials subjected to plane strain compression. *J. Eng. Mech.* **140**(7), 04014050 (2014)
10. Patil, U.D., Puppala, A.J., Hoyos, L.R., Pedarla, A.: Modeling critical-state shear strength behavior of compacted silty sand via suction-controlled triaxial testing. *Eng. Geol.* **231**, 21–33 (2017)

11. Phan, D.G., Nguyen, G.D., Bui, H.H., Bennett, T.: Constitutive modelling of partially saturated soils: Hydro-mechanical coupling in a generic thermodynamics-based formulation. *Int. J. Plast.* **136** (2021)
12. Rudnicki, J.W., Rice, J.: Conditions for the localization of deformation in pressure-sensitive dilatant materials. *J. Mech. Phys. Solids* **23**(6), 371–394 (1975)
13. Schiava, R., Etse, G.: Constitutive modeling and discontinuous bifurcation assessment in unsaturated soils (2006)
14. Song, X., Wang, K., Ye, M.: Localized failure in unsaturated soils under non-isothermal conditions. *Acta Geotech.* **13**(1), 73–85 (2017). <https://doi.org/10.1007/s11440-017-0534-4>
15. Thu, T.M.: Shear Strength and Volume Change Relationship for an Unsaturated Soil (2006)



Identification of Creep-Quake Cycles in Calcareous Sands

Leonardo Crespo-Parraga^(✉), François Guillard, and Itai Einav

The University of Sydney, Camperdown, NSW, Australia
leonardo.crespoparraga@sydney.edu.au

Abstract. Degradation processes in porous media concern numerous industries. In geomaterials, these processes are capable of triggering localised instabilities which may result in the collapse events, as has been observed with the formation of sinkholes and the collapse of rock salt mines. Previous studies have identified periodic creep-quake collapse patterns in porous materials under simultaneous compression and degradation. However, the possibility of the development of this particular collapse pattern in geomaterials is yet to be explored. Here, we reproduce the creep-quake cycle patterns in two different calcareous sands and present the physical mechanism that underpins it. Our experiments show that this mechanism results in sudden localized collapse events, loud acoustic emissions, and drops in the servo-controlled load used to compress the sand samples. We then explore the behavioural change of the sand when subjected to different degradation rates and different applied stresses. Finally, we explore the parametric limits of applied stresses and degradation rates within which calcareous sand undergoes creep-quake cycles. Our results show that this collapse mechanism can emerge in geomaterials that are simultaneously subjected to sufficient compression and a non-uniform degradation field.

Keywords: Calcareous sand · Acetic acid · Creep-quake cycles

1 Introduction

The chemical dissolution of geomaterials is a common diagenetic process found in nature. The effects of these processes may result in the damage of man-made or natural structures, such as leakage and structural instability in tailing dams [1, 2], sinkhole formation [3], damage to underground CO₂ storage systems [4], and submarine landslides [5]. The consequences of such events may include environmental pollution, human injuries, and loss of lives. This highlights the importance of developing an accurate understanding of the behaviour of geomaterials under acid degradation. In recent years, a novel collapse mechanism was identified experimentally in uniaxially loaded, partially soaked puffed rice [6]. The mechanism consists of localised cyclic collapse events, named ‘ricequakes’, that initiated within the partially saturated material and were interluded by periods of accelerated creep deformation. The discovery of these ‘creep-quake’ cycles motivated our investigation of this distinct collapse pattern in other porous media. Specifically, we

consider the effect of chemical dissolution processes in calcareous sands under load, which can be closely related to the conditions under which the puffed rice exhibited creep-quake cycles. In this paper, we describe how the creep-quake collapse pattern emerges in these geomaterials using an array of experiments performed on two different calcareous sand samples. The sand samples were both loaded uniaxially and chemically degraded from the bottom, simultaneously. Additionally, we show the effects of stress and degradation rates on the behaviour of the calcareous sands, with which we discuss the creep-quake cycle mechanism and how it emerges in this material.

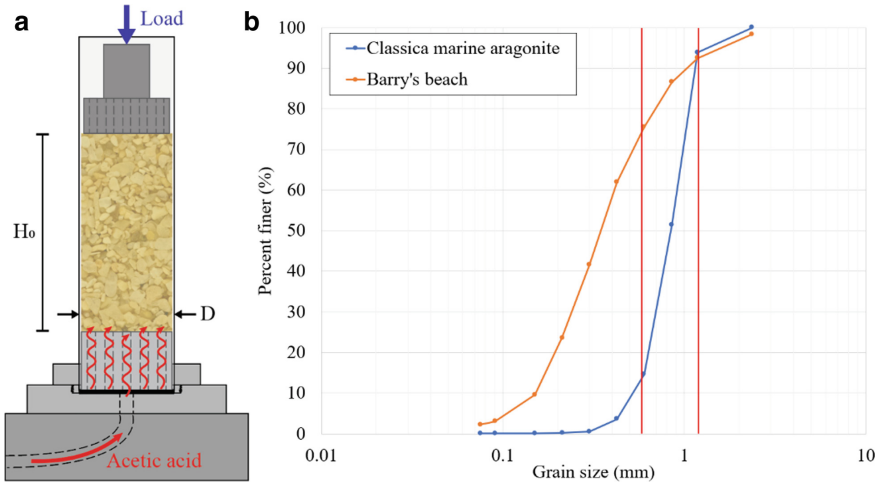


Fig. 1. **a** Experimental set-up. **b** Sieve analysis of two different calcareous sands. The red vertical lines show the limits at which the grain size distribution was capped to make the experimental samples

2 Methodology

The experimental set-up used across all the experiments is depicted in Fig. 1a. It consisted of a cylindrical sand sample with a diameter (D) of 34.2 mm and an initial height (H_0) of 100 mm in an acrylic tube. The samples sat between two porous plates that allowed fluid flow through them, with the bottom plate being static and the top plate acting as a loading piston connected to a Tinus Olsen H5KS loading frame. The tube wall was sealed at the bottom with an aluminium base, with an inlet tube that allowed for liquid injection.

The preparation of the samples involved initially filling the test apparatus with water, then pluviating the sand into the tube until reaching the desired initial height. This was done in order to reach a loose initial sample density. The samples were then compressed uniaxially by the loading frame at a constant strain rate of 5 mm/min until the target load was reached. At this point, the loading mode was switched to stress control, and the servo-controller maintained that target load throughout the experiment. It is noted that

due to the nature of using a servo-controller, there was a constant target stress applied on the sand samples. As will be discussed later in the paper, this resulted in drops to the stress applied whenever a quake occurred. However, the stiffness of the machine used allowed for the recovery time of those stress drops to be significantly faster than the frequency of the quake events. Therefore, its effects on our experimental results are considered to be minimal.



Fig. 2. Macroscopic photograph of the two sands **a** Classica marine aragonite **b** Barry's beach sand. The photographs were taken on sieved samples. Hence, the grain sizes are between 0.6 and 1.18 mm

Once the load was stable, the acidic solution was injected from under the bottom plate at a constant flow rate with a peristaltic pump connected to an acid reservoir. Although the injection rate of the acetic acid varied across experiments, it was kept constant for the duration of each experiment. Once the solution had travel through the height of the sample, it overflowed from the top of the tube onto a collection bucket for disposal. As the acid flowed through the samples, its hydrogen ions concentration decreased as it chemically reacted with the calcium carbonate of the sand. Consequently, the solution exiting the samples was significantly less acidic than the injected one. The macroscopic photographs in Fig. 2 were taken with a Hirox microscope, while the photographs of the experiments were acquired with a Nikon D3300 camera placed in front of the set-up. The experiment photographs were taken at a rate of one frame every five seconds and they were used to produce the sand spatiotemporal graphs shown in Fig. 3.

Two different types of calcareous sand samples were used: 'Classica marine aragonite' and 'Barry's beach' Sand. The Classica marine aragonite was purchased as an aquarium supply. This sand was an ideal material to react with acid and explore creep-quake cycles in geomaterials, since it is commonly used as a pH buffer in aquarium tanks. The sand is characterised by round coarse grains of approximately 1 mm in diameter (Fig. 1b). In contrast, the Barry's beach sand samples were obtained from south Victoria, Australia. This sand has been previously studied and its engineering properties are detailed in literature [7]. In comparison to the Classica marine aragonite, the Barry's beach sand has a larger content of fines, which is clearly visible in its sieve analysis. It is further noted that the Barry's beach sand coarse grains were significantly more angular than the typically more spherical grains of the Classica marine aragonite, as can be seen in the macroscopic photographs in Fig. 2. The two sands were stored in a cool dry place and were sieved prior to each experiment in order to remove grains coarser

than 1.18 mm or finer than 0.6 mm. The red vertical lines in Fig. 1 show the fraction of the sand samples taken to make the experimental samples.

The acid solution used to dissolve the calcareous sand samples was purchased as ‘Coles white vinegar’ and as ‘Coles double strength vinegar’ from a local supermarket. The vinegar purchased is an aqueous acetic acid solutions with a concentration of 4 and 8% acetic acid by weight, corresponding to an initial pH 2.6 and 2.4, respectively. Double strength vinegar was the used across all the experiments on the Classica marine aragonite, while single strength vinegar was used for the Barry’s beach sand experiments, as the Barry’s beach sand was found to react to the vinegar at significantly faster rates.

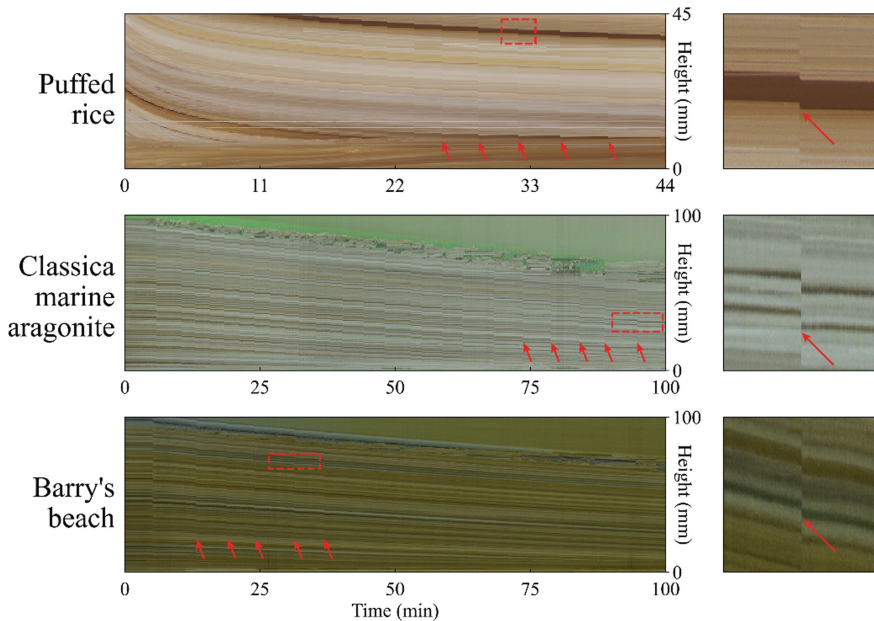


Fig. 3. Spatiotemporal plots for experiments on three different materials. Left column: full spatiotemporal plot, right column: zoom in of one quake event (red delimited area in spatiotemporal plots). From top to bottom: puffed rice [6], Classica marine aragonite, and Barry’s beach sand. The two sand experiments had an initial height of 100 mm, an injection flow rate of 10 mL/min, and a compressive stress of 4.35 MPa. On each spatiotemporal plot, five quake events are signaled by a red arrow to ease their observation. In these plots, quakes appear as discontinuities in the downward pixel pattern

3 Results

Similar to the effect of water saturation in puffed rice, we found that the chemical degradation process in the sand grains together with the axial compression may generate creep-quake cycles due to the localized degradation of the material. The similarity

between the puffed rice and the calcareous sands collapse pattern is evident in the spatiotemporal plots shown in Fig. 3. The plots were generated by taking a column of pixels in the centre of the samples from the experiment photographs and plotting it (vertical axis) over time (horizontal axis). This imaging technique allows for a static observation of the one-dimensional behaviour of the samples over time and facilitates the identification of creep-quake cycles. In these graphs, creep is seen as the gradual downward trend in the pixels, which is interrupted by a sudden larger downward displacement with every quake. The two cyclical deformation stages are further shown in Fig. 4 as deformation versus time curves. The two sand experiments in Fig. 3 had identical testing parameters, as detailed in the caption, with the exception of the concentration of acetic acid injected, as mentioned in the methodology Sect. 2. In addition to the visible similitude of the creep-quake cycles across these three materials, the quake events in the sand samples were also accompanied by drops in the servo-controlled load used to compress them, as seen in Fig. 5, and distinct acoustic emissions, two features that were highlighted in the original discovery of ricequakes [6].

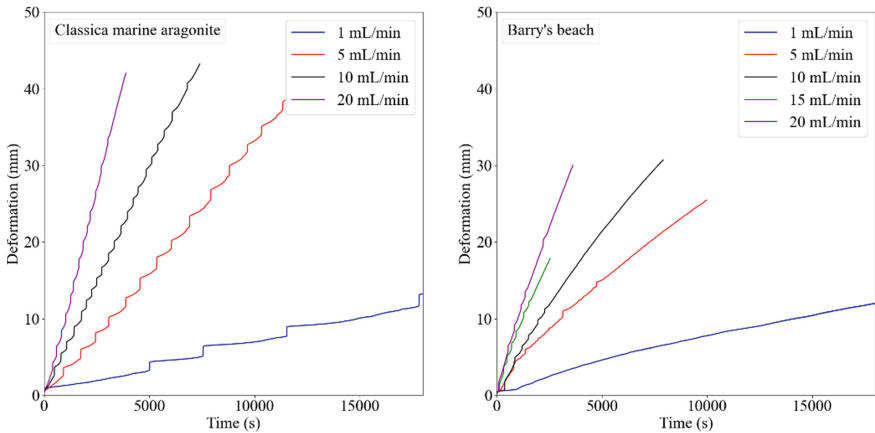


Fig. 4. Deformation versus time curves for two sets of experiments under different acid injection rates: Classica marine aragonite (left) and Barry's beach sand (right)

3.1 Injection Rate Effect

Once creep-quakes cycles were identified in the two sands, the effect of acid injection rate was explored, see Fig. 4. This was achieved with two set of identical experiments where the only parameter varied was the injection rate. The experiments in Fig. 4 consisted of a 100 mm tall sand column under an applied stress of approximately 4.35 MPa (4 kN force). As expected, a lower acid injection rate resulted in a slower rate of deformation of the sand samples. This trend also led to prolonged creep periods, separating the quake events by larger spans of time. In the case of the Classica marine aragonite, this does not prevent quakes from occurring, as they are prevalent throughout the four different experiments all the way until the experiment was stopped. However, the Barry's beach sand samples do

not exhibit creep-quake cycles at lower reaction rates, and the quakes seem to disappear early instead of being regularly present for the whole duration of the experiment. This feature is also visible in the spatiotemporal graphs in Fig. 3, as there are no more sudden displacements of pixels after approximately 80 min. Furthermore, it is observed that higher injection rates result in creep-quake cycles that are far less discernible from creep alone. This is clearly seen in the 20 mL/min injection rate experiments in both sand samples.

3.2 Loading Magnitude Effect

The effect of load magnitude on the development of creep-quake cycles was further studied with a set of experiments on Barry's beach sand samples. The findings of these experiments are summarised graphically in Fig. 5. These experiments were performed on 100 mm tall sand columns with a 10 mL/min acid injection rate and with different applied loads. This shows that quakes can only occur when sufficient confining load is applied. At low load magnitudes, creep-quake cycles come to a halt and degradation accelerated creep is the sole mechanism through which the sand deforms. However, there is no clear effect between load magnitude and quake frequency. A similar trend was observed in the Classica marine aragonite samples, although not presented in this figure for conciseness.

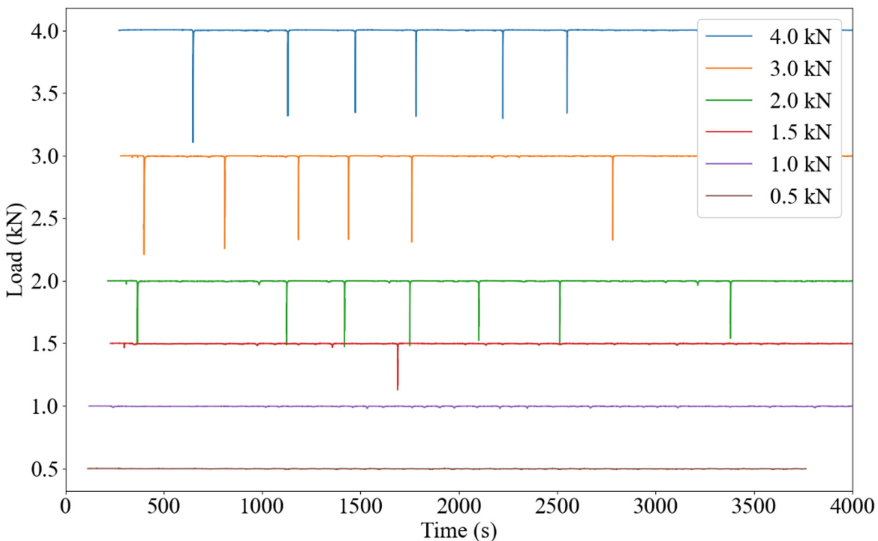


Fig. 5. Measured load versus time curves for a set of experiments on Barry's beach sand with varying applied target load

4 Discussion

In line with the effects of partial saturation in puffed rice, the acetic acid degrades the calcareous sands mostly at the bottom of the samples. As the acid travels through the

material, its concentration of hydrogen ions available to react with the calcium carbonate in the sand decays. This results in reaction rates within the material which reduce with distance from the bottom base plate. The field of degradation that the sand experiences is estimated to have significantly faster reaction rates at the bottom of the samples.

The creep periods in the samples are a result of the mass reduction caused by the acetic acid reacting with the sand grains. This reaction makes the sand grains smaller and may lead to their rearrangement, resulting in the accelerated creep deformation we observe in our experiments. Quakes, however, are the result of an instability within the granular structure. This instability arises from a localised increase in porosity and decrease in strength of the granular medium and ultimately, a quake occurs when the region can no longer withstand the compressive stress applied. When a sand grain within a highly degraded region of the sample (close to the bottom plate) breaks or dislodges into available space (pores), it may overload the granular structure, thus triggering a local collapse event (a quake). The non-homogeneity of dissolution along the loading direction is key to the development of recurring creep-quake cycles. This interpretation is supported by Fig. 4, where we see how faster injection rates result in less distinct creep-quake cycles. This is likely caused by a homogenisation of the degradation field. Faster injection rates result in a larger concentration of hydrogen ions further away from the bottom of the sample, causing a more uniform degradation of the samples in comparison to the slower injection rates. This can be seen in the similarity between the 15 and 20 mL/min injection rates experiments. At these faster rates, the sample deformation is no longer limited by the distribution of hydrogen ions within the material, but instead by the chemical kinetics of the reaction. Hence, the results of our experiments point towards two required ingredients for creep-quake cycles to emerge in sands exposed to acidic degradation. Firstly, a non-homogeneous degradation field which results in a localised zone of weakness and higher porosity due to the grains loss of mass, consequently generating quakes. Second, sufficient load is required for these cycles to occur, as demonstrated in Fig. 5. Without sufficient pressure, the breakage or rearrangement of grains within a highly degraded zone does not appear to result in sudden collapse. The lower stress allows the granular structure to rearrange and slowly re-stabilise while constantly degrading.

The difference in creep-quake cycles duration between the two sands is explained by the morphology of their grains. While the angular nature of the Barry's beach sand grains causes a faster consumption rate of the sand due to their larger surface area, it also reduces the porosity of the sand column, generating less space for grains to dislodge or break into. Therefore creep-quake cycles in Barry's beach sand come to a halt earlier than they do in Classica Marine Aragonite. When exposed to the experimental conditions for long enough, Classica Marine Aragonite also stop undergoing creep-quake cycles.

An additional distinction appears when comparing the collapse patterns of the puffed rice and the two sand samples. Ricequakes are characterised by a growth in creep duration over time [6]. Visibly (Figs. 4 and 5), this is not a characteristic of the collapse patterns of the two sand samples. We explain this difference with the accumulation of inert material at the bottom of the cereal samples and the lack of renewal of degrading agent in that case. In the puffed rice experiments, a known volume of water was injected at the start of the experiments and it was not renewed. As time progressed, the collapsed cereal mass

at the bottom of the tube increased and this widened the distance between the base of the tube and the undegraded (and therefore susceptible to collapse) grains. This results in the undegraded grains saturating at a slower rate as time progresses and causes the growing creep periods observed in [6]. In contrast, the acid solution was constantly renewed in the sand experiments and the sand grains continued to degrade even after a quake has occurred, as they continually weakened and reduced in size. This difference in how the degrading agent and the samples interact explains why growing creep periods are not observed in the sand experiments.

5 Conclusion

In conclusion, we have shown that the mechanism of creep-collapse cycles originally found in puffed rice [6], ‘ricequakes’, can emerge in geomaterials under acidic degradation, using two distinct calcareous sands. One-dimensional experiments were performed in which we applied compressive load and a non-uniform chemical degradation field to the sand specimens, simultaneously. We observed that changing the degrading field has a direct effect in the creep-quake behaviour of the sands, making the collapse patterns less pronounced as the high degradation front broadens. These observations ultimately point to the fact that in order for creep-quake cycles to emerge in geomaterials under chemical degradation, the materials has to experience sufficient compressive stress, as well as a non-uniform degradation field.

References

1. Alonso, E.E., Gens, A.: Aznalcóllar dam failure. Part 1: field observations and material properties. *Géotechnique* **56**(3), 165–183 (2006)
2. Lottermoser, B., Ashley, P.: Tailings dam seepage at the rehabilitated Mary Kathleen uranium mine, Australia. *J. Geochem. Explor.* **85**(3), 119–137 (2005)
3. Waltham, T., Bell, F.G., Culshaw, M.G., Knez, M., Slabe, T.: Sinkholes and Subsidence: Karst and Cavernous Rocks in Engineering and Construction, vol. 382. Springer, Berlin (2005)
4. Espinoza, D., Kim, S., Santamarina, J.: CO₂ geological storage—Geotechnical implications. *KSCE J. Civ. Eng.* **15**(4), 707–719 (2011)
5. Urgeles, R., Camerlenghi, A.: Submarine landslides of the Mediterranean Sea: trigger mechanisms, dynamics, and frequency-magnitude distribution. *J. Geophys. Res. Earth Surf.* **118**(4), 2600–2618 (2013)
6. Einav, I., Guillard, F.: Tracking time with ricequakes in partially soaked brittle porous media. *Sci. Adv.* **4**(10), eaat6961 (2018)
7. Hull, T., Poulos, H., Alehossein, H.: The static behaviour of various calcareous sediments. In: *Engineering for Calcareous Sediments*, pp. 87–96 (2021)



Liesegang Patterns Interpreted as a Chemo-Hydrromechanical Instability

Chong Liu¹ , Manman Hu¹  , and Klaus Regenauer-Lieb² 

¹ Department of Civil Engineering, The University of Hong Kong, Pokfulam, Hong Kong
chongliu@connect.hku.hk, mmhu@hku.hk

² WA School of Mines: Minerals, Energy and Chemical Engineering, Curtin University, Curtin,
Bentley, WA 6102, Australia
klaus@curtin.edu.au

Abstract. Patterns in nature form through bifurcations triggered by Multiphysics feedbacks that involve chemical, hydraulic, mechanical, and thermal processes. A generic approach has been developed based on a nonlocal reaction-diffusion equation where patterns grow as a result of travelling dissipative waves. Here we present a simplified analysis on the formation of vastly different patterns (e.g., Liesegang stripes and dendritic precipitation) in Solnhofen limestone that are traditionally interpreted to result from the same group of chemical precipitation reactions. The transition from stripes to dendritic growth in the same formation suggests a commonality that is not yet captured or understood by the classical chemical feedback models. We propose that mechanical processes drive the patterns. The objective of this study is therefore to identify a set of characteristic diffusion coefficients and reaction processes that generate pressure waves which can encompass chemical and hydrromechanical feedback process driving the selection between the two-types of instabilities.

Keywords: Solnhofen limestone · Liesegang rings · Phase field

1 Introduction

Patterns are formed in reaction-diffusion systems that are far from the thermodynamics equilibrium, which are frequently encountered in many disciplines, such as animal patterns in biology, electrochemical deposition in chemistry, rock textures in geology. In this study, we focus on a particular pattern emerging in Solnhofen limestone where the surface is often stained by black or red-brown as shown in Fig. 1a (investigations on the transition to Fig. 1b are ongoing). Here we approach the pattern forming process by a more general Thermo-Hydro-Mechanical-Chemical (THMC) process defining cross-diffusion as the phenomenon where a gradient of one generalised thermodynamic force of species C_j drives another generalised thermodynamic flux of species C_i , described by

$$\frac{\partial C_i}{\partial t} = \tilde{D}_{ii} \nabla^2 C_i + \sum_{j \neq i} \tilde{D}_{ij} \nabla^2 C_j + r_i \quad (1)$$

The species j is identified as the cross-diffusion species other than the species i . Introducing a fully populated ($N \times N$) diffusion matrix \tilde{D}_{ij} , Eq. (1) can (using explicit summation instead of Einstein convention) also be written as

$$\frac{\partial C_i}{\partial t} = \sum_{k=1}^N \tilde{D}_{ik} \nabla^2 C_k + r_i \quad (2)$$

whereby the classical (self-)diffusive length scale of each THMC process is defined by $\sqrt{4\tilde{D}_{ii}t}$. The cross-diffusion approach introduces also a new meso-scale coupling length scale that can provide a link between the large-scale self-diffusion length scales of the THMC processes.

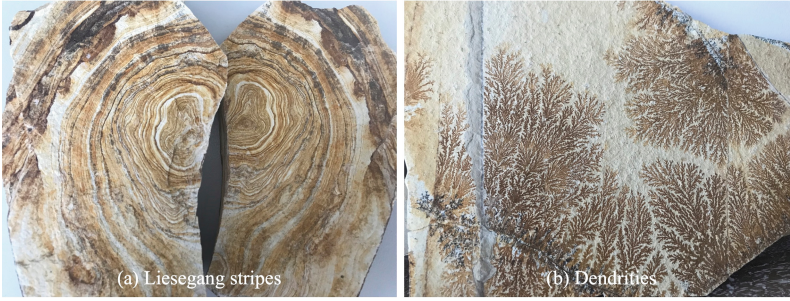


Fig. 1. Patterns in Solnhofen limestone: **a** Liesegang stripes versus **b** Dendrites

The traditional explanation of the formation of Liesegang patterns and dendritic growth suggests a chemical reaction [1, 2] where metallic ions (iron or manganese) penetrate into the rock surface and then oxidize into their respective oxide. The corresponding reaction-diffusion system can be generalised as a chemical reaction: $A + B \rightarrow C$. In this system, an external aqueous electrolyte A diffuses into the gel-like host and reacts to the inner electrolyte B , thereby generating the product concentration of the solid C in the wake of a moving diffusion front. The production C enables to form the rhythmic precipitated patterns of iron-oxides in Fig. 1a but the transition from the quasistationary rhythmic pattern to the dynamic dendritic growth pattern is not captured by the approach.

In this contribution we first visit the common arguments for the rhythmic striped pattern and identify a possible transition to a rhythmic spotted pattern. The formation of the stripe pattern can be understood by the concept introduced by Wilhelm Ostwald in the late nineteenth century, for chemical systems thus valid for chemical length scales at submicroscopic scale. The common explanation refers to a pre-nucleation supersaturation model that forms the origin of the pattern. In this model, the pre-nucleation process forms the seed; However, the length scale of the diffusive mass transfer eventually forming the periodic precipitation bands after its concentration C exceeds a certain value cannot be a chemical diffusion length and must involve a THMC process at a larger scale such as a hydrous or mechanical transport process.

The traditional model also cannot interpret several experimental findings, such as gravity-dominated Liesegang stripes. To alleviate this limitation, Hedges and Henley

suggested a sol coagulation theory [3]. The sol coagulation models divide the formation of the distinct precipitation into two steps. First, the colloidal sol is created, but invisible to the naked eye. With the colloidal sol increasing at certain areas, the visible precipitation bands then emerge when ion concentration strength approaches the critical coagulation limit. Although both the supersaturation and sol coagulation theory are able to reproduce empirical laws observed in experiments, a shared drawback is the determination of the threshold of the concentration of the generated product.

To address this problem, a more recent theory, called phase separation model, has been proposed to simulate the formation of Liesegang patterns. In this model, the patterns form as a result of spinodal decomposition of the product extending a spin-1/2 kinetic Ising model with coarse-grained dynamics [4, 5]. More specifically, when the product concentration is initially in a stable or metastable state, the diffusion front transforms in between the spinodal points, leading to instability and pattern formation. The phase separation method is capable of modeling irregular patterns, such as helices, and the transition between bands and spots after introducing noise effects [6]. Due to its robustness and efficiency, this model has been widely used to simulate the Liesegang family patterns in many fields. Herein, we adopt the phase separation concept and extend to investigate the diverse pattern formation in Solnhofen limestone.

2 Phase Separation in a Chemo-Hydromechanical Sense

We start with considering a simple scenario of phase separation, that is, two reagents A and B diffuse and react generating a product C in the wake of the moving diffusion front: $A_{(aq)} + B_{(aq)} \rightarrow C_{(s)}$. The corresponding reaction-diffusion equations for the reagents can be expressed as

$$\begin{aligned}\frac{\partial a}{\partial t} &= D_a \Delta a - \kappa ab \\ \frac{\partial b}{\partial t} &= D_b \Delta b - \kappa ab\end{aligned}\quad (3)$$

where a and b are concentrations of two reagents A and B , κ is the reaction rate, and D_a and D_b are the self-diffusion coefficients. We assume $D_a = D_b = D$ for simplicity.

It is phenomenologically observed that the reaction production C can automatically segregate into two distinct phases, i.e., low- and high-concentration phases [5]. The contrast in concentration leads to the rhythmic precipitation patterns in the system. The dynamics of the production C can be captured by the Cahn-Hilliard equation:

$$\frac{\partial c}{\partial t} = -\nabla \cdot (\lambda_0 \nabla \mu) + \kappa ab + \eta_{c0} \quad (4)$$

where λ_0 is the diffusive mobility, κab represents the production rate of C particles by the reaction front, and η_{c0} denotes noise effects, such as the inhomogeneous reagents and thermal fluctuations. μ is the total free energy density (here defined as a generalized thermodynamic potential) that drives the phase separation, which consists of two components: the bulk free energy density $f_{,c}$ and interfacial energy density $\sigma_0 \Delta c$ as

$$\mu = -f_{,c} + \sigma_0 \Delta c \quad (5)$$

in which σ_0 is the gradient parameter related to the sharpness of the interfaces. For the sake of simplicity, we use a Landau-Ginzburg type free energy f with two minima corresponding to c_l and c_h and the maximum to $\bar{c} = (c_l + c_h)/2$.

$$f = -\frac{\varepsilon}{2}(c - \bar{c})^2 + \frac{\gamma}{4}(c - \bar{c})^4 \quad (6)$$

where ε and γ are system-dependent parameters and $\sqrt{\varepsilon/\gamma}$ determines the minima of the bulk free energy f . Note that both ε and γ need to be greater than zero for inducing phase separation in the system.

Hence, the generalized chemical potential defining the material reservoir can be written as

$$\mu = \varepsilon(c - \bar{c}) - \gamma(c - \bar{c})^3 + \sigma_0 \Delta c \quad (7)$$

The dimensionless treatment for the system regarding the concentration, time, and length scales is

$$\hat{c} = \frac{c_h - c_l}{2}, \tau = \frac{1}{\kappa \hat{c}}, l = \sqrt{\frac{D}{\kappa \hat{c}}} \text{ and } m = \frac{c - \bar{c}}{\hat{c}} \approx \frac{c}{\hat{c}} - 1 \quad (8)$$

The final set of nondimensional governing equations similar to [7] reads

$$\begin{aligned} \frac{\partial a}{\partial t} &= D_a \Delta a - \kappa ab \\ \frac{\partial b}{\partial t} &= D_b \Delta b - \kappa ab \\ \frac{\partial m}{\partial t} &= -\nabla \cdot (\lambda \nabla \mu) + \kappa ab + \eta_c \\ \mu &= \varepsilon m - \gamma m^3 + \sigma \Delta m \end{aligned} \quad (9)$$

where $\lambda = \lambda_0 \varepsilon / D$, $\sigma = \sigma_0 \kappa \hat{c} / D \varepsilon$, and $\eta_c = \eta_{c0} / \kappa \hat{c}^2$ are rescaled parameters.

The corresponding boundary conditions (BCs) can be decomposed into essential and natural boundaries. The essential boundary conditions contain $a = \bar{a}$, $b = \bar{b}$, $m = \bar{m}$, and $\mu = \bar{\mu}$ on the related boundaries, and the natural boundary conditions include $\nabla a \cdot \mathbf{n} = j_a$, $\nabla b \cdot \mathbf{n} = j_b$, $\nabla m \cdot \mathbf{n} = j_m$, and $\nabla \mu \cdot \mathbf{n} = j_\mu$ where \mathbf{n} is the unit outer normal vector.

In addition, the initial conditions (ICs) are

$$a|_{t=0} = a_0, b|_{t=0} = b_0, m|_{t=0} = m_0, \text{ and } \mu|_{t=0} = \mu_0 \quad (10)$$

An open-source high-performance phase-field code, PRISMS-PF [8] based on one finite element library of deal.II, is used to solve Eq. (9) with the corresponding BCs and ICs. This PRISMS-PF library supports adaptive mesh refinement, massively parallel, and matrix-free finite element simulation, which allows for future extensions of this study to a 3D scenario. The PRISMS-PF uses an explicit scheme for time discretization. Although the explicit method only has first-order accuracy and limits to satisfy Courant-Friedrichs-Lewy (CFL) condition, it is simple to implement and computes fast during each time step. The formulation of associated weak forms for the PRISMS-PF implementation is presented in a different manuscript (in prep).

3 Simulation Results

We first apply the phase separation model presented in Sec. 2 for the numerical simulation of Liesegang ring pattern forming and compare our numerical results with empirical laws derived from a variety of experimental observations [4], such as the timing law, the spacing law, the width law, etc.

The model setup considers a 2D circular domain with a round cavity in the center as shown in Fig. 2a. The radius of the exterior and inner boundary is $R_{outer} = 100$ and $R_{inner} = 12.5$, respectively. The size ratio of the inner and outer radius refers to [6]. Dirichlet boundary condition $\bar{a} = 100$ is applied at the internal boundary for the reagent A, while no-flux boundary conditions are imposed for other variables. On the exterior, no-flux boundary conditions are imposed for all variables. The initial conditions are $a_0 = 0$, $b_0 = 1.0$, and $m_0 = -1.0$ for the entire domain. η_c is vanished to ignore the noise effects. The total simulation time is $T = 300$ with the increment time step $\Delta t = 0.001$. Other material parameters include the self-diffusion coefficients $D_a = D_b = 1.0$, the reaction rate $\kappa = 1.0$, the diffusion mobility $\lambda = 1.0$, and the parameters $\varepsilon = 1.0$, $\gamma = 0.4$, and $\sigma = 0.2$. Time evolution of typical Liesegang ring forming is illustrated in Fig. 2b.

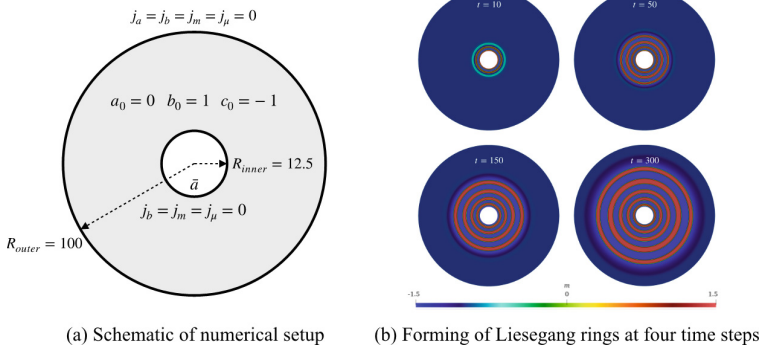


Fig. 2. Verification for the Liesegang rings **a** Schematic of numerical setup and **b** forming of Liesegang rings at four time steps

Our simulation matches the *spacing law* relating the position of two consecutive rings by $\frac{r_{n+1}}{r_n} = 1 + p$, where $1 + p = 1.31$, representing the spacing coefficient as depicted in Fig. 3a. The phenomenological *Matalon-Packter law* $p = F(b_0) + G(b_0) \frac{b_0}{a_0}$, indicating the role of the initial concentrations of the reagents is obtained by fitting the spacing coefficient with an inverse function as shown in Fig. 3b. Furthermore, the linear *width law* between the radius of the ring and its thickness is numerically benchmarked in Fig. 3c. Further, additional patterns have been identified for Liesegang stripes in different rocks where the stripe patterns can transition into isolated spots. Here we show that the presented phase separation mechanism in its simplest form can be used to investigate such transitions, as illustrated in Figs. 4, 5, 6 and 7. The model considers heterogeneous nature of the rocks and contains noise effects in the generalized reaction-diffusion equations.

We find that noise effects and heterogeneity play a vital effect on the formation of the irregular patterns or precipitation rings.

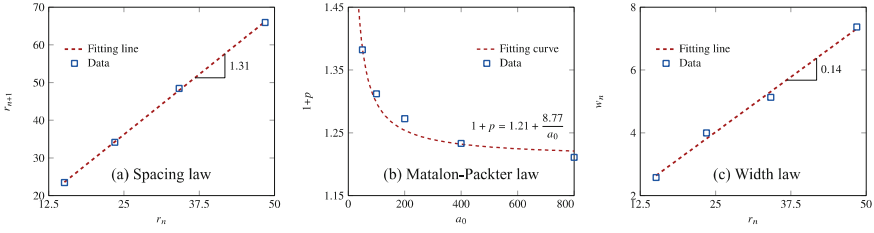


Fig. 3. Numerical verification of three empirical laws **a** The spacing law, **b** the Matalon-Packter law and **c** the width law

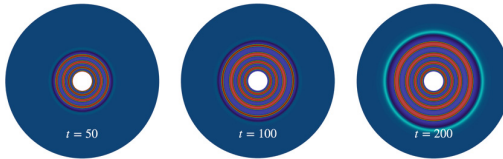


Fig. 4. Ring patterns. The scaled parameters: $\bar{a} = 100, a_0 = 0, b_0 = 0.5, D_a = D_b = 1.0, \kappa = 1.0, \sigma = 0.2, m_0 = -1.5, \lambda = 1.0, \varepsilon = 1.0, \gamma = 0.4,$ and $\eta_c \in [-0.01, 0.01]$

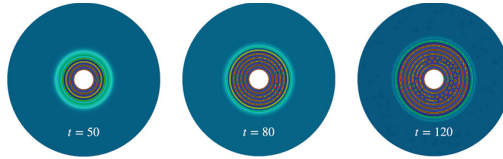


Fig. 5. Patterns combined spots and rings. The scaled parameters: $\bar{a} = 100, a_0 = 0, b_0 = 0.5, D_a = D_b = 1.0, \kappa = 1.0, \sigma = 0.2, m_0 = -1.5, \lambda = 0.3, \varepsilon = 1.0, \gamma = 0.15,$ and $\eta_c \in [-0.01, 0.01]$

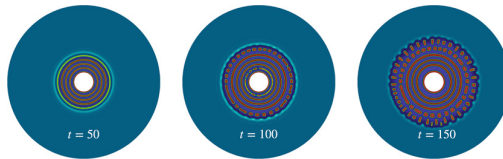


Fig. 6. Patterns transiting from rings to spots. The scaled parameters used for the simulation: $\bar{a} = 100, a_0 = 0, b_0 = 0.5, D_a = D_b = 1.0, \kappa = 1.0, \sigma = 0.2, m_0 = -1.5, \lambda = 0.5, \varepsilon = 1.0, \gamma = 0.15,$ and $\eta_c \in [-0.01, 0.01]$

4 Discussion

In order to identify the possible THMC feedback mechanism we use the diffusive length scale from Eq. (2) as a diagnostic tool as the gradient in concentrations in the equation can

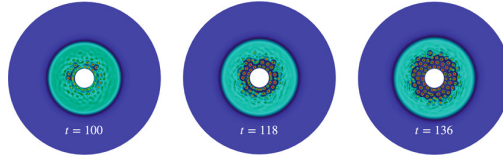


Fig. 7. Spot patterns. The scaled parameter used for the simulation: $\bar{a} = 100$, $a_0 = 0$, $b_0 = 0.5$, $D_a = D_b = 1.0$, $\kappa = 1.0$, $\sigma = 0.2$, $m_0 \in [-1 - 0.01, -1 + 0.01]$, $\lambda = 0.15$, $\varepsilon = 1.0$, $\gamma = 0.15$, and $\eta_c = 0$

be understood as chemical, hydraulic, mechanic or thermal pressure waves. Instead of solving the fully populated 4×4 diffusion matrix we emphasise that there exists a scale separation between THMC diffusion length scales and a chemical pre-nucleation process may simplify to a hydro-mechanically coupled process where the chemical reaction process is subsumed in the fluid pressure term allowing pattern formation at larger than submicroscopic chemical length scale. Such hydro-mechanical pressure waves have been identified in compacting saturated porous media [9].

4.1 Hydro-Mechanical Pressure Waves

Rhythmic patterns with a similar length scale (cm-dm scale) to the above described Liesegang patterns have been identified in compacting clay rich semi-consolidated rocks in the Whakatika Formation (New Zealand) [9]. In the case of the subduction setting for the Whakatika Formation at the Hikurangi margin a mechanical compaction process is clearly the driving mechanism of the pattern forming process. This pattern has been interpreted as a rhythmic quasi-stationary pressure wave which can be characterised by a simplified Eq. (2) without cross-diffusion terms. The cnoidal wave formulation reads as

$$\Delta u - \lambda(1 + u)^m + \mu e^{\beta u} = 0 \quad (11)$$

A detailed review on the cnoidal wave patterning can be found in [10]. An automatically adaptive stabilized finite element scheme [11] can be employed to simulate the cnoidal waves described by Eq. (11).

The hydronechanical pattern can explain the morphological origin of compaction bands as evident from thin-section images of grain crushing field spanning from the centre of the compaction bands (see Fig. 4 in [9]). This simplified cnoidal wave equation as a pioneering attempt is certainly not rich enough to reproduce the patterns observed in nature. The spacing and width relationships were found only in special cases to be perfectly periodic and like the Liesegang patterns request additional terms in the reaction-diffusion equation to match the observations. We suggest here that the above described spinodal decomposition model provides the necessary extension of the THMC Eq. (2) can deliver the correct length scales for the observed Liesegang patterns and the observed compaction bands in the New Zealand case. Equation (2) is agnostic of the mechanism of rock densification and it remains to be debated whether the solid precipitation of iron-oxide in the Liesegang case is comparable to the densification through grain-crushing in the poorly consolidated claystone case.

5 Conclusion

We have presented in this work an ongoing study for investigating the transition from a quasistatic pattern forming process (Liesegang pattern) to a dynamic growth pattern (dendrites) and conclude that mechanical pressure most likely controls the longest wavelength diffusion length scale. Ongoing work incorporates solutions for dendritic pattern forming processes which will be used to enrich Eq. (2) by specific reaction terms capable of changing the pattern style to dendritic growth. The overall aim of the study is to provide a complete set of reaction-cross-diffusion equations that can be used to invert for the coefficients from observations in nature thus providing extra information about the hidden nature of the pattern forming processes.

References

1. Chopard, B., Herrmann, H.J., Vicsek, T.: Structure and growth mechanism of mineral dendrites. *Nature* **353**, 409–412 (1991)
2. Msharrafieh, M., Al-Ghoul, M., Zaknoun, F., El-Rassy, H., El-Joubeily, S., Sultan, R.: Simulation of geochemical banding I: acidization-precipitation experiments in a ferruginous limestone rock. *Chem. Geol.* **440**, 42–49 (2016)
3. Hedges, E.S., Henley, R.V.: CCCLX.—The formation of Liesegang rings as a periodic coagulation phenomenon. *J. Chem. Soc.*, pp. 2714–2726 (1928)
4. Rácz, Z.: Formation of Liesegang patterns. *Phys. A* **274**, 50–59 (1999)
5. Antal, T., Droz, M., Magnin, J., Rácz, Z.: Formation of Liesegang patterns: a spinodal decomposition scenario. *Phys. Rev. Lett.* **15**, 2880 (1999)
6. Dayeh, M., Ammar, M., Al-Ghoul, M.: Transition from rings to spots in a precipitation reaction–diffusion system. *RSC Adv.* **4**, 795–801 (1961)
7. Thomas, S., Lagzi, I., Molnár, F., Jr., Rácz, Z.: Probability of the emergence of helical precipitation patterns in the wake of reaction-diffusion fronts. *Phys. Rev. Lett.* **110**, 078303 (2013)
8. PRISMS-PF: Version 2.2, 2021
9. Hu, M., Schrank, C., Regenauer-Lieb, K.: Cross-diffusion waves in hydro-poro-mechanics. *J. Mech. Phys. Solids* **135**, 103632 (2020)
10. Hobbs, B., Ord, A.: Failure modes in fluid saturated rocks: deformation processes and mode-switching. *Geol. Mag.*, pp. 1–18 (2022)
11. Cier, R.J., Poulet, T., Rojas, S., Veveakis, M., Calo, V.M.: Automatically adaptive stabilized finite elements and continuation analysis for compaction banding in geomaterials. *Int. J. Numer. Meth. Eng.* **122**, 6234–6252 (2021)



Cross-Scale Dynamic Interactions in Compacting Porous Geomaterials as a Trigger to Instabilities

Qingpei Sun¹ , Manman Hu¹  , and Klaus Regenauer-Lieb² 

¹ Department of Civil Engineering, The University of Hong Kong, Pokfulam, Hong Kong
qpsun@connect.hku.hk, mmhu@hku.hk

² WA School of Mines: Minerals, Energy and Chemical Engineering, Curtin University, Curtin,
Bentley, WA 6102, Australia
klaus@curtin.edu.au

Abstract. We present an approach to model material bifurcations derived from the dynamic interplay of at least two coupled reaction-diffusion processes during compaction of porous media. Our new approach introduces nonlocal terms that describe the coupling between scales through mutual cross-diffusivities and regularize the ill-posedness of the reaction-self-diffusion system. Applying bifurcation theory, we suggest that geological patterns can be interpreted as physical representations of two classes of well-known instabilities, i.e., Turing instability, Hopf bifurcation, and a new class of complex soliton-like waves. The new class appears for small fluid release reactions rates which may, with negligible self-diffusion, lead to an extreme focusing of wave intensity into a short sharp earthquake-like event. Here we investigate the phenomenon of episodic tremor and slip instability of time-periodic slip events recorded in subduction zones. It is shown that the instability is a Hopf bifurcation and our inversion of the recorded events conclusively shows that episodic fluid release from serpentinite dehydration is the cause for the sudden slip events as postulated earlier. Our analysis further allows derivation of chemical reaction rates under geodynamic loading conditions opening the path for physics/chemistry-based forecasting of catastrophic instabilities in nature.

Keywords: Geological pattern · Reaction-cross-diffusion · Bifurcation

1 Introduction

Pattern formations are ubiquitous in natural systems, ranging from animal markings to rhythmic metamorphic banding among others, in both the living and the inorganic world [1, 2]. Potential mechanisms underpinning these patterns are the reaction-diffusion instabilities in the coarse-grained single-continuum system [3], which is characterized by the large-scale thermodynamics averaged behavior whereas the small-scale dynamics are neglected [4, 5].

In this study, we propose a new microphysics-based approach which couples the microscale cross-constituent interplays to the large-scale dynamic behavior, in the context of the hydro-mechanically coupled porous media. The approach is able to recover

different types of instabilities in geological scenarios, via tight coupling of the solid matrix pressure with the dissipation of the pore fluid pressure.

2 Reaction-Cross-Diffusion Model in Compacting Geomaterials

For the compacting saturated porous geomaterials, they could be regarded as a dual-continuum system which features a global scale REV and a local scale REV. The mass and energy transfer at the macroscale level can be characterized by the familiar self-diffusion processes while the counterpart at the microscale level is controlled by surface interactions between the solid and fluid phase, resulting in an interfacial domain defined by cross-diffusion length scales [6]. Here, to model the equivalent poro-mechanical coupled feedbacks, we encapsulate both the macro- and micro-physics processes into a thermodynamic consistent framework, deriving a minimum set of two reaction-cross-diffusion equations in terms of the normalized solid viscous-plastic overstress $\tilde{p}_s = \bar{p}_s/p_{\text{ref}}$ and pore fluid pressure $\tilde{p}_f = p_f/p_{\text{ref}}$ together with the normalization $\tilde{x} = x/l_0$, $\tilde{t} = \dot{\epsilon}_0 t$

$$\frac{\partial \tilde{p}_s}{\partial \tilde{t}} = \tilde{D}_M \frac{\partial^2 \tilde{p}_s}{\partial \tilde{x}^2} + \tilde{d}_H \frac{\partial^2 \tilde{p}_f}{\partial \tilde{x}^2} + \tilde{a}_{11} \tilde{p}_s + \tilde{a}_{12} \tilde{p}_s^2 + \tilde{a}_{13} \tilde{p}_s^3 + \tilde{a}_{14} \tilde{p}_f \quad (1)$$

$$\frac{\partial \tilde{p}_f}{\partial \tilde{t}} = \tilde{d}_M \frac{\partial^2 \tilde{p}_s}{\partial \tilde{x}^2} + \tilde{D}_H \frac{\partial^2 \tilde{p}_f}{\partial \tilde{x}^2} + \tilde{a}_{21} \tilde{p}_s + \tilde{a}_{22} \tilde{p}_f \quad (2)$$

where $\tilde{D}_M = \frac{D_M}{l_0^2 \dot{\epsilon}_0}$, $\tilde{d}_H = \frac{d_H}{l_0^2 \dot{\epsilon}_0}$, $\tilde{a}_{11} = \frac{a_{11}}{\dot{\epsilon}_0}$, $\tilde{a}_{12} = \frac{a_{12} p_{\text{ref}}}{\dot{\epsilon}_0}$, $\tilde{a}_{13} = \frac{a_{13} p_{\text{ref}}^2}{\dot{\epsilon}_0}$, $\tilde{a}_{14} = \frac{a_{14}}{\dot{\epsilon}_0}$, $\tilde{d}_M = \frac{d_M}{l_0^2 \dot{\epsilon}_0}$, $\tilde{D}_H = \frac{D_H}{l_0^2 \dot{\epsilon}_0}$, $\tilde{a}_{21} = \frac{a_{21}}{\dot{\epsilon}_0}$, $\tilde{a}_{22} = \frac{a_{22}}{\dot{\epsilon}_0}$. Here, p_{ref} is the reference pressure while l_0 and $\dot{\epsilon}_0$ are the reference length scale and strain rate respectively. Note that the nonlinear terms in the right-hand side of Eq. (1) are associated with the rheological behaviors of the solid matrix (3rd order power law adopted here to characterize the nonlinear creep [6, 7]) while the remaining linear reaction terms represent the first-order fluid/solid pressure generation source arising from mineral dehydration and rehydration [8].

3 Results

3.1 Linear Stability Analysis

Given that the analytical solutions to Eqs. (1) and (2) are not tractable, we herein conduct linear stability analysis to characterize the system response under small perturbations near its steady state. The linearized perturbation evolution equations spell out as

$$\frac{\partial \tilde{p}_s^*}{\partial \tilde{t}} = \tilde{D}_M \frac{\partial^2 \tilde{p}_s^*}{\partial \tilde{x}^2} + \tilde{d}_H \frac{\partial^2 \tilde{p}_f^*}{\partial \tilde{x}^2} + \tilde{a}_{11} \tilde{p}_s^* + \tilde{a}_{14} \tilde{p}_f^* \quad (3)$$

$$\frac{\partial \tilde{p}_f^*}{\partial \tilde{t}} = \tilde{d}_M \frac{\partial^2 \tilde{p}_s^*}{\partial \tilde{x}^2} + \tilde{D}_H \frac{\partial^2 \tilde{p}_f^*}{\partial \tilde{x}^2} + \tilde{a}_{21} \tilde{p}_s^* + \tilde{a}_{22} \tilde{p}_f^* \quad (4)$$

Based on the space Fourier transform, the above perturbations \tilde{p}_s^* and \tilde{p}_f^* can be further expressed in the following form

$$\tilde{p}_s^* = \tilde{p}_s^* \exp(ik\tilde{x} + s_k\tilde{t}) \quad (5)$$

$$\tilde{p}_f^* = \tilde{p}_f^* \exp(ik\tilde{x} + s_k\tilde{t}) \quad (6)$$

where k denotes the wavenumber while s_k is the perturbation growth rate. By substituting Eqs. (5) and (6) into Eqs. (3) and (4), the following determinant needs to vanish so as to ensure non-trivial solutions to the perturbation equations.

$$\det \begin{vmatrix} s_k + k^2\tilde{D}_M - \tilde{a}_{11} & k^2\tilde{d}_H - \tilde{a}_{14} \\ k^2\tilde{d}_M - \tilde{a}_{21} & s_k + k^2\tilde{D}_H - \tilde{a}_{22} \end{vmatrix} = 0 \quad (7)$$

Expanding the above criterion, we arrive at a characteristic equation for s_k ,

$$s_k^2 - \text{tr}_k s_k + \Delta_k = 0 \quad (8)$$

$$\text{tr}_k = (\tilde{a}_{11} + \tilde{a}_{22}) - k^2(\tilde{D}_M + \tilde{D}_H)$$

$$\Delta_k = \tilde{a}_{11}\tilde{a}_{22} - \tilde{a}_{14}\tilde{a}_{21} + k^4(\tilde{D}_M\tilde{D}_H - \tilde{d}_M\tilde{d}_H) - k^2(\tilde{a}_{11}\tilde{D}_H + \tilde{a}_{22}\tilde{D}_M - \tilde{a}_{21}\tilde{d}_H - \tilde{a}_{14}\tilde{d}_M)$$

Hence, the solution of Eq. (8) gives

$$s_k = \frac{\text{tr}_k \pm \sqrt{\text{tr}_k^2 - 4\Delta_k}}{2} \quad (9)$$

Based on the bifurcation theory, the system may encounter three types of instability, depending on the value of s_k i.e. the dispersion relationship as described in Eq. (9).

3.1.1 Turing Instability

The Turing scenario corresponds to the change of a stable node to an unstable saddle in the phase space and its dispersion relationship is shown in Fig. 1a. It is found that there exists a critical wave number k_{cr} with the maximum perturbation growth rate. Hence, the wavelength of Turing pattern is an intrinsic characteristic determined by $\lambda = 2\pi/k_{cr}$. The 1-D Turing pattern (for the solid matrix) in the temporal-spatial domain is plotted in Fig. 1b, which shows that the Turing pattern is periodic in space and does not change over time (i.e., a standing wave) after being triggered by initial perturbations applied on the left boundary.

3.1.2 Hopf Bifurcation

A Hopf bifurcation takes place when the phase diagram of the system turns from a stable focus to an unstable one, featuring an imaginary perturbation growth rate with a nonnegative real part (Fig. 2a). The spatial-temporal plot of a Hopf bifurcation is shown in Fig. 2b. One finds that the entire system quickly enters a periodic oscillation mode after initial perturbations, giving rise to a characteristic frequency for the system behavior $f = 1/T$.

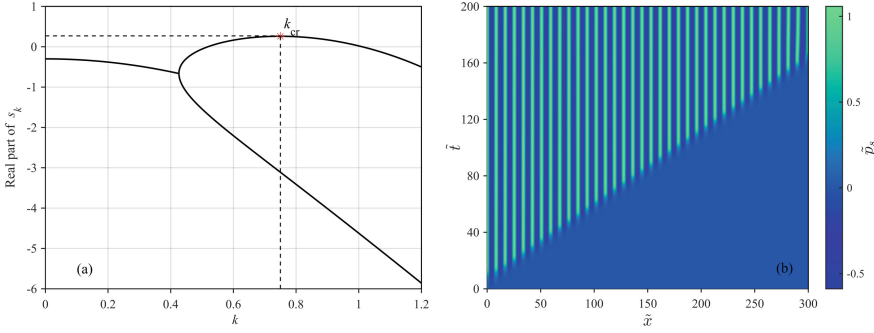


Fig. 1. Results of Turing instability: **a** dispersion relationship **b** temporal-spatial evolution (obtained from finite difference simulation)

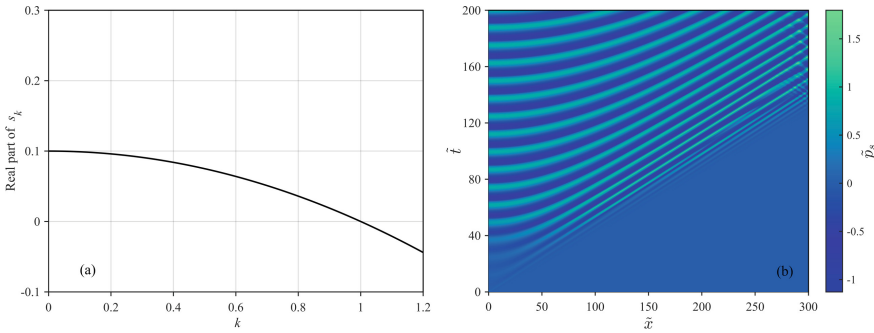


Fig. 2. Results of Hopf instability **a** dispersion relationship, **b** temporal-spatial evolution

3.1.3 Cross-Diffusion Soliton-Like Waves

In addition to Turing and Hopf instabilities, a new class of soliton-like waves is identified in the reaction-cross-diffusion system. This scenario is different from the above-mentioned ones in that the instability only occurs when the cross-diffusional coupling effect is significant (and reaction coefficients are small) in Eq. (2). Note that the initial perturbation on the boundary also needs to exceed a certain threshold in order to provoke this type of wave instability, as the system remains stable (negative real part of s_k in Fig. 3) under small perturbations in this case. The spatial-temporal plot in Fig. 3b indicates that the wave propagates with a constant velocity (similar to classical solitons) which does not reflect on the boundaries.

The above theoretical and numerical investigations reveal three different types of instabilities, while the remainder of this paper focuses on the type (II) Hopf bifurcation and its application for interpreting episodic tremor and slip (ETS) events.

3.2 ETS Events as a Hopf Bifurcation of the Reaction-Cross-Diffusion Model

During the subduction of oceanic slabs below continental ones, an interfacial localization zone is formed, where various thermo-hydro-mechanical-chemo processes take place.

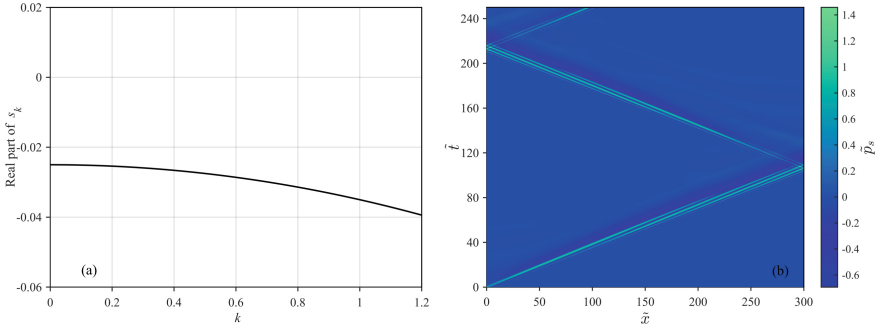


Fig. 3. Results of cross-diffusion soliton-like wave **a** dispersion relationship, **b** temporal-spatial evolution

Of critical importance is the dehydration of serpentinite minerals at deeper regions of the localization zone, which results in complex fluid-solid interactions and promotes ETS events energetically. Here, to model ETS sequences (blue dots in Fig. 4, with data obtained from [9]) at the Cascadia subduction zone, we assume the overburden behaves like a rigid block and the displacement at the effective boundary of the localization zone is determined by integrating the viscous-plastic strain rate $u = \int_{t_0}^{t_1} \int_{x_0}^{x_1} \dot{\epsilon}_{vp} dx dt$. A power law rheology $\dot{\epsilon}_{vp} = \dot{\epsilon}_0 \times \left(\alpha_1 (\bar{p}_s/p_{ref})^2 + \alpha_2 (\bar{p}_s/p_{ref})^3 \right)$ is utilized here to characterize the solid strain rate, where $\dot{\epsilon}_0$ and p_{ref} are the reference strain rate and pressure while α_1 and α_2 are coefficients. Note that the rheological law has been encapsulated in Eq. (1) via the relationship $\alpha_1 = -[(1 - \phi)\beta_s + \phi\beta_f]a_{12}p_{ref}^2/\dot{\epsilon}_0$, and $\alpha_2 = -[(1 - \phi)\beta_s + \phi\beta_f]a_{13}p_{ref}^3/\dot{\epsilon}_0$, derived from the mixture theory [8], where ϕ is the porosity, β_s and β_f the compressibility of solid skeleton and pore fluid respectively. By substituting the above relations into the rheological law, the displacement can be expressed in terms of normalized quantities

$$u = \frac{p_{ref}d[(1 - \phi)\beta_s + \phi\beta_f]}{2} \int_{\tilde{t}_0}^{\tilde{t}_1} \int_{-1}^1 \left(-\tilde{a}_{12}\tilde{p}_s^2 - \tilde{a}_{13}\tilde{p}_s^3 \right) d\tilde{x}d\tilde{t} \quad (10)$$

where half of the localization zone thickness $d/2$ is chosen as the reference length scale.

Based on Eqs. (1), (2) and (10) the displacements obtained from the model can be used to understand the ETS signals recorded by the GPS network, and the quantitative fitting in the physical as well as the spectral domains are presented in the left and right column of Fig. 4, respectively. It can be found from the top panel of Fig. 4 that by matching the dominant frequency component, the model results within the Hopf bifurcation regime can capture the overall ETS sequences, while there exist certain discrepancies at the occurrence of small tremor activities (like at the year of 2008 and 2010). Given this, we further adjust the nonlinear coefficients (e.g. \tilde{a}_{12}), to investigate their influence on the displacement and spectrum characteristics, and to explore the possibility of correlation improvement by varying the nonlinear rheological parameters. Notable results are shown in the bottom panel of Fig. 4, where we have found that the amplitude of the minor frequency increases as \tilde{a}_{12} grows from 0.35 to 0.78 and this frequency variation has led to

a higher correlation coefficient (0.74) with two characteristic humps in one displacement cycle.

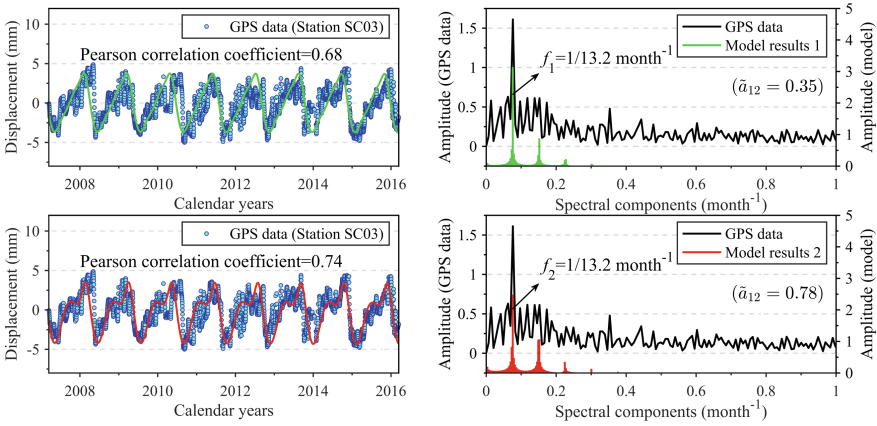


Fig. 4. ETS sequence recorded by the GPS network [9] at the Cascadia subduction zone modelled by poromechanical reaction-cross-diffusion equation for serpentinite dehydration. Two sets of fitting are shown in the real (left) and spectral (right) domain

It is worth noting that the recurrence interval of ETS events at the Cascadia subduction zone is usually around 13–15 months depending on the GPS station, and very insignificant changes are observed over time for a specific GPS observation station. Hence, it is plausible that we use constant parameters (autonomous system) during the fitting procedure and do not consider the nonautonomous case. The model parameters with the best obtained fitting performance against GPS recordings are summarized in Table 1, which shows that our new approach can not only invert the basic material and rheological parameters from the ETS sequences, but also allow to derivate the mineral reaction rates at geodynamic loading conditions.

Table 1. Parameters with the best fitting performance in Fig. 4

Parameter	Value	Units	Parameter	Value	Units
κ	5×10^{-23}	m^2	α_1	-0.07	-
ϕ	0.04	-	α_2	0.1	-
μ_f	10^{-5}	$\text{Pa}\cdot\text{s}$	a_{11}	1.6×10^{-8}	s^{-1}
$\beta_s + \beta_f$	10^{-7}	Pa^{-1}	a_{14}	-3.2×10^{-7}	s^{-1}
$\dot{\epsilon}_0$	2×10^{-7}	s^{-1}	a_{21}	1.1×10^{-7}	s^{-1}
d	10^{-1}	m	a_{22}	2.4×10^{-8}	s^{-1}
p_{ref}	2	MPa			

4 Conclusion

In this work, we present a micro-physics enriched approach to model material bifurcations in compacting porous media. The theoretical and numerical analysis indicates that there exist three types of instabilities in the reaction-cross-diffusion system, namely Turing instability (featuring an intrinsic wavelength), Hopf bifurcation (embracing a characteristic frequency), and a new class of soliton-like waves (propagating with constant velocities). The Hopf bifurcation solution has been employed to interpret the GPS data of episodic tremor and slip events at subduction zones, and the parameters inverted from fitting can be used to determine the chemical reaction rates and the rheological parameters of the creep regime under geodynamic loading conditions, which may shed light on physics/chemistry-based forecasting of catastrophic instabilities in nature.

References

1. Ball, P.: Pattern formation in nature: physical constraints and self-organising characteristics. *Archit. Des.* **82**(2), 22–27 (2012)
2. Hobbs, B.E., Ord, A., Regenauer-Lieb, K.: The thermodynamics of deformed metamorphic rocks: a review. *J. Struct. Geol.* **33**(5), 758–818 (2011)
3. Turing, A.M.: The chemical basis of morphogenesis. *Bull. Math. Biol.* **52**(1), 153–197 (1990)
4. Regenauer-Lieb, K., Hu, M., Schrank, C., et al.: Cross-diffusion waves resulting from multiscale, multi-physics instabilities: theory. *Solid Earth.* **12**(4), 869–883 (2021)
5. Regenauer-Lieb, K., Hu, M., Schrank, C., et al.: Cross-diffusion waves resulting from multiscale, multiphysics instabilities: application to earthquakes. *Solid Earth.* **12**(8), 1829–1849 (2021)
6. Hu, M., Schrank, C., Regenauer-Lieb, K.: Cross-diffusion waves in hydro- poro-mechanics. *J. Mech. Phys. Solids.* **135** (2020)
7. Alevizos, S., Poulet, T., Sari, M., et al.: A framework for fracture network formation in overpressurised impermeable shale: deformability versus diagenesis. *Rock Mech. Rock Eng.* **50**(3), 689–703 (2017)
8. Hu, M., Sun, Q., Schrank, C., et al.: Cross-scale dynamic interactions in compacting porous media as a trigger to pattern formation. *Geophys. J. Int.* **230**(2), 1280–1291 (2022)
9. NASA: Jet Propulsion Laboratory. <https://sideshow.jpl.nasa.gov/post/series.html> (2022)



Instability of Granular Soil Under Conventional Triaxial and Constant Stress Paths

N. Benahmed¹(✉), J. Zuo², and A. Wautier¹

¹ INRAE, RECOVER Research Unit, Aix Marseille University, 3275 Route de Cézanne, 40061, 13182 Aix-en-Provence Cedex 5, CS, France
nadia.benahmed@inrae.fr

² Formerly at Ecole Centrale de Nantes, Nantes, France

Abstract. The concept of bifurcation domain has emerged in the context of the study of the mechanical stability of soils, and more generally of geomaterials. This domain constitutes a zone in which the failure of a material is possible but conditioned by the application of a particular mechanical stress and the use of a well-chosen control mode. The definition of failure modes in the bifurcation domain is more general than that used in a classic elastoplastic formalism with hardening (reaching the plastic limit surface). This study aims to highlight the existence of the bifurcation domain characterized by the instability line defined in undrained triaxial test. The conditional failure of a granular sample was investigated with the use of triaxial tests either in strain or stress control modes in one hand, and by applying different incremental loads after a first phase of drained triaxial loading in the other hand. An emphasis was put in particular on constant deviatoric loading path with successive steps of creep phase before and after crossing the instability line defined by the conventional undrained compression tests.

Keywords: Conventional undrained triaxial tests · Constant stress path · Bifurcation · Instability line

1 Introduction

Because of their non-associated plastic behavior, the failure modes of granular materials are more diverse than those related to associated plasticity (Darve et al. 2004; Wan et al. 2017). Indeed, the non-respect of the normality rule for the plastic strain, necessary to account for the volumetric behavior of granular materials, results in the existence of failure modes strictly before reaching the plastic limit surface. Such failure modes are well illustrated by the static liquefaction of loose sand observed in undrained triaxial tests. In such tests, the deviatoric stress shows a non-monotonic evolution, with a peak stress reached strictly below the maximum yield surface as defined from drained triaxial tests. In (q, p') diagrams, the peak stresses obtained for different initial confining pressures align on a straight line known as the “instability line” (Lade 1993; Benahmed 2001; Dong et al. 2016).

From a theoretical point of view, this instability line connects with the concept of bifurcation domain. This domain constitutes a set of mechanical states for which conditional failure exists (Wan et al. 2017). A material in its bifurcation domain will effectively fail if it is loaded (i) in some particular directions and (ii) for some particular modes of control. Formally, the bifurcation domain is defined from the vanishing of the second-order work W_2 (Hill 1958) for some incremental loading directions:

$$\exists(\mathbf{d}\sigma, \mathbf{d}\epsilon) \text{ linked by the constitutive behavior, such that } W_2 = \mathbf{d}\sigma : \mathbf{d}\epsilon < 0$$

For an undrained evolution, the second-order work simplifies as $W_2 = dq d\epsilon_d$, where $d\epsilon_d$ is the incremental deviatoric strain, which is always positive and proportional to the axial strain in an undrained triaxial test. As a result, the instability line, defined as $dq = 0$ in the experiments, corresponds also to $W_2 = 0$. Therefore, the instability line belongs to the bifurcation domain (Darve et al. 2004). It is usually assumed that this line corresponds indeed to the frontier of the bifurcation domain (or at least lies very close to it).

Conditional failure in the bifurcation domain is well established from a theoretical point of view (Nova, 1994; Nicot et al., 2009; Wan et al. 2017), and has been tested numerically several times (Sibille et al., 2008; Wautier et al. 2018). However much less results exist on the experimental side (Gajo et al. 2000; Daouadji et al. 2011; Dong et al. 2016). In this study, we intend to explore the bifurcation domain from an experimental point of view with use of constant deviatoric stress loading paths. The vanishing of the second-order work along such paths is detected and the controllability of the tested material is challenged by keeping constant the stress state strictly inside the bifurcation domain under stress control.

The experimental campaign (conducted on loose specimen of Hostun sand) consists in three series of tests. A first series of drained triaxial tests enabled to obtain the maximum plastic yield surface of the material. A second series of undrained triaxial tests provided the instability line. Finally, the bifurcation domain is explored along constant deviatoric stress paths preceded by an initial drained triaxial loading.

2 Experimental Procedure

2.1 Material Characteristics and Specimen Preparation

The material used is Hostun silica sand HN31, which is a fine and uniform sand with angular to sub angular grain shape. It has a medium diameter $D_{50} = 0.35$ mm, and a coefficient of uniformity $C_u = 1.57$. Its minimum and maximum void ratio are equal to 0.656 and 1, respectively. The grain size distribution of the soil is shown in Fig. 1.

To obtain loose specimens with good control of density, moist tamping method was used to prepare all the specimens in this study (Benahmed 2004). First, predetermined amount of sand to achieve the target density was divided into seven equal parts; each part was mixed thoroughly with 3% of de-aired water to get loose structure due to capillary cohesion. Subsequently, the moist sand was placed carefully by spoon in a split mold layer by layer; each of them compacted at 20 mm thick with a graduated hand tamper. The height and the diameter of the specimens were 140 mm and 70 mm respectively. The initial relative density was equal to $D_r = 10\%$

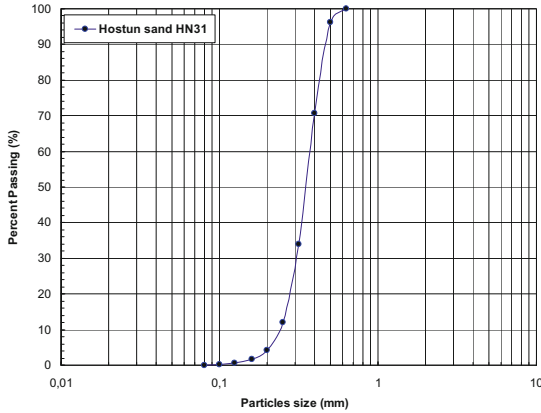


Fig. 1. Grain size distribution curve of Hostun sand.

2.2 Triaxial Procedure

The triaxial experiments were carried out using a fully computer controlled Triaxial System from Wykeham Farrance. The axial load was monitored by an internal submersible load transducer, while the axial displacement was measured by an LVDT mounted on the top platen. The volume variation was collected by an automatic volume change device. After filling the triaxial cell and consolidating the specimens under 100 kPa, the saturation stage was performed by flushing first CO₂ under a pressure of 20 kPa for 30 min, followed by de-aired water for a volume of about three times the specimen volume. Back pressure ranging from 200 to 400 kPa was then applied to ensure the full saturation of the specimens with a Skempton coefficient B higher than 0.96. Finally, for the specimens to be sheared under higher confining pressure, the latter was increased to the desired confining stress.

3 Results and Discussion

Nine drained and undrained triaxial tests and five constant deviatoric stress path tests at different consolidation pressures were performed. The shearing process was strain controlled with an axial strain rate of 1% per minute for the conventional triaxial tests and stress controlled for the constant deviatoric stress path. Details of the tests are given in Table 1.

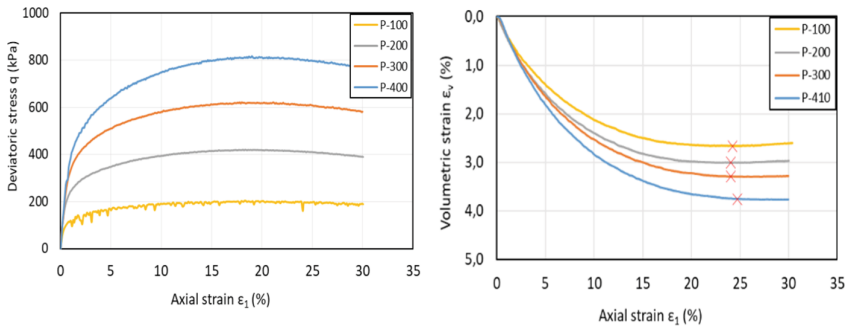
3.1 Conventional Drained and Undrained Triaxial Tests

Figures 2 and 3 show the obtained results of the drained and undrained triaxial tests in terms of deviatoric stress and volumetric strain versus axial strain for drained tests and in terms of deviatoric stress versus axial strain and effective mean stress path for undrained tests. These two series of tests enable to determine the instability line (IL) and the plastic limit surface (FL) in Cambridge plane (p' , q), as shown in Fig. 4.

Table 1. Details of isotropically consolidated triaxial tests performed in this study

Test name	P'_c (kPa)	e_c	ID_c	Shearing method
DMC-Dr10-P100	100	0.982	0.05	Drained
DMC-Dr10-P200	200	0.964	0.10	Drained
DMC-Dr10-P300	300	0.959	0.12	Drained
DMC-Dr10-P400	410	0.961	0.11	Drained
UMC-Dr10-P65	65	0.990	0.03	Undrained
UMC-Dr10-P100	100	0.997	0.01	Undrained
UMC-Dr10-P215	215	0.968	0.09	Undrained
UMC-Dr10-P350	350	0.973	0.08	Undrained
UMC-Dr10-P400	400	0.965	0.10	Undrained
CSD-Dr10-P100-0.54	100	0.967	0.07	Constant q
CSD-Dr10-P200-0.54	200	0.949	0.15	Constant q
CSD-Dr10-P300-0.54	300	0.958	0.12	Constant q
CSD-Dr10-P400-0.54A	400	0.953	0.14	Constant q
CSD-Dr10-P300-M4	300	0.963	0.11	Constant q

e_c void ratio after consolidation; ID_c density index after consolidation; P'_c confining pressure..

**Fig. 2.** Drained compression tests. Deviatoric stress and volumetric strain versus axial strain.

The plastic limit surface determined in drained and undrained tests are very similar and corresponds to a Mohr-Coulomb yield surface with slope around 1.2. Such slope corresponds to a friction angle $\varphi' = 30.2^\circ$. As for the instability line, the slope is equal to 0.79 that corresponds to a mobilized friction angle of 20.4° . These values are in agreement with those obtained by Benahmed (2001) on the same material (Hostun sand).

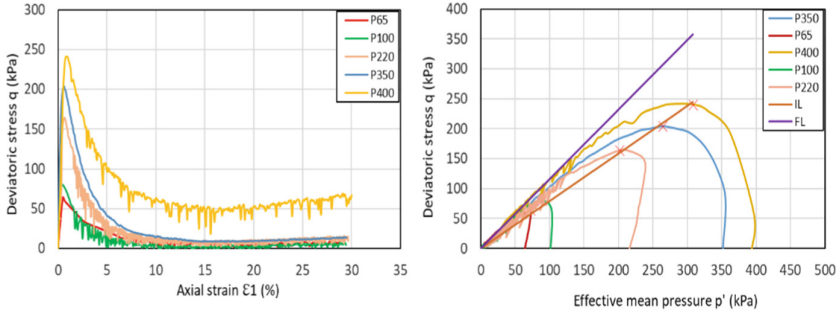


Fig. 3. Undrained compression tests. Deviatoric stress versus axial strain and effective stress path. The red crosses corresponds to the vanishing of the second-order work.

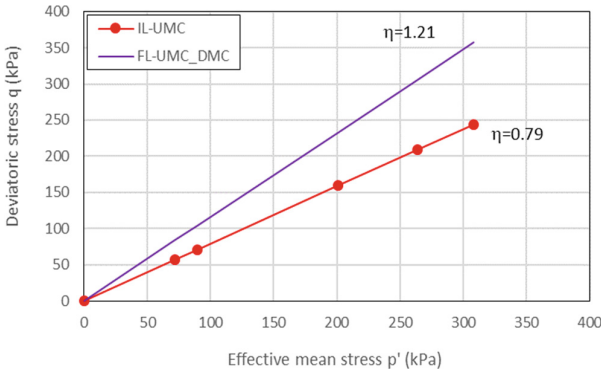


Fig. 4. The instability line (IL-UMC) and the plastic limit surface (FL-UMC-DMC) for drained and undrained conventional triaxial tests.

3.2 Constant Deviatoric Stress Test and Controllability Analysis

From previous experimental studies (Gajo et al. 2000; Chu et al. 1993; Dong et al. 2016) and numerical studies (Darve et al. 2004; Sibille et al. 2008) it is known that the constant deviatoric stress path is an adverse loading path for materials in the bifurcation domain. This loading direction often belongs to the instability cone (the set of loading directions for which $W_2 < 0$). In practical applications, this loading path is consecutive to a sudden surge in pore water pressure, which can be the consequence of water infiltration during heavy rainfall, a flooding event for a dike or a dam for instance.

In order to assess the material stability against such loading paths from an experimental point of view, mixed loading paths were performed on Hostun sand. First, the specimens were consolidated at pressure of 100, 200, 300 and 400 kPa (see Table 1). Then, they were sheared under a drained compression until reaching a stress ratio $\eta = \frac{q}{p'} = 0.54$ corresponding to two thirds of the stress ratio on the instability line. Afterwards, the deviatoric stress was kept constant and the mean effective stress was reduced by increasing pore water pressure at the rate of 20 kPa/min. Figure 5 shows the constant deviatoric stress paths observed until failure for the four specimens consolidated under 100, 200,

300 and 400 kPa. Along a constant q loading path, the second-order work criterion reads $W_2 = dp'd\varepsilon_v$, where dp' is the incremental variation of the mean effective stress and $d\varepsilon_v$ is the incremental volumetric strain. As a result, for a decreasing mean effective pressure, the second-order work vanished when a change from dilatancy ($d\varepsilon_v < 0$) to contractancy ($d\varepsilon_v > 0$) is observed. This point is marked with a red cross in Fig. 5a, b. It corresponds to the moment where the constant q loading path enters the instability cone of the material. It is interesting to underline the fact that this occurs for a stress ratio $\eta_{IL-CSD} \simeq 0.93$, which is strictly between the instability line stress ratio determined in UMC tests $\eta_{IL-UMC} = 0.79$ and the plastic limit stress ratio $\eta_{FL} = 1.21$ shown in Fig. 4. $\eta_{IL-UMC} < \eta_{IL-CSD}$ is consistent with results obtained by Dong et al. (2004) and Sibille (2006).

The difference between the two instability lines can be explained:

- By the fact that for the same stress ratio, the microstructures are different in UMC and CSD tests due to hysteresis. As a consequence, the microstructure obtained for CSD loading paths helps keep the material stable for higher stress ratios than for UMC loading paths;
- By the fact that the CSD loading direction does not belong to the cone of instability (the set of loading directions able to trigger underlying mechanical instability) for $\eta_{IL-UMC} < \eta < \eta_{IL-CSD}$. In that case, the material is unstable for $\eta_{IL-UMC} < \eta < \eta_{IL-CSD}$ but one has to impose a loading path different from the CSD to observe the effective failure.

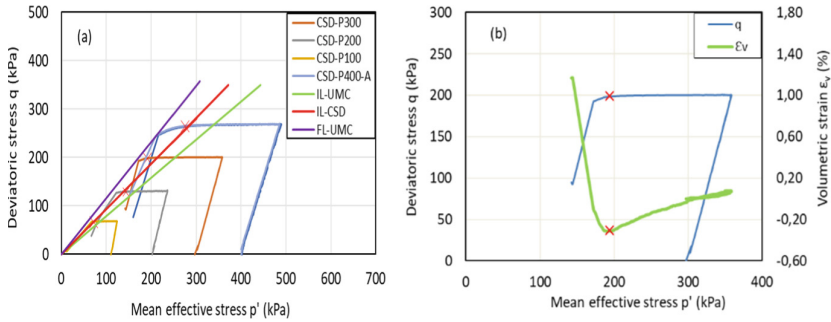


Fig. 5. (a) Constant deviatoric stress paths after an initial drained triaxial loading. (b) Zoom of volumetric strain for test CSD-Dr10-P300-0.54. The red cross corresponds to the vanishing of the second-order work on the loading path considered.

Shortly after the vanishing of the second order work, instability occurs. This is visible in Fig. 5 through a simultaneous decrease in p' and q . Such a decrease in q corresponds to a loss of controllability (Nova 1994), since it is supposed to be constant on the loading path considered. Contrary to undrained triaxial loadings, the test is fully stress controlled here, which enable instability to occur through an inertial transition from a quasi-static to a dynamic regime when W_2 vanished (Wautier et al. 2018).

3.3 Constant Deviatoric Stress Test with Creep Stages

In order to investigate further the loss of controllability that can occur inside the bifurcation domain, an additional constant deviatoric path was conducted, and paused several times during the test (“CSD-Dr10-P300-M4” in Table 1). During the pause, the stress state was kept constant by controlling the pore water pressure in the sample and the axial stress applied through the vertical piston (full stress control). The whole test procedure is illustrated in Fig. 6.

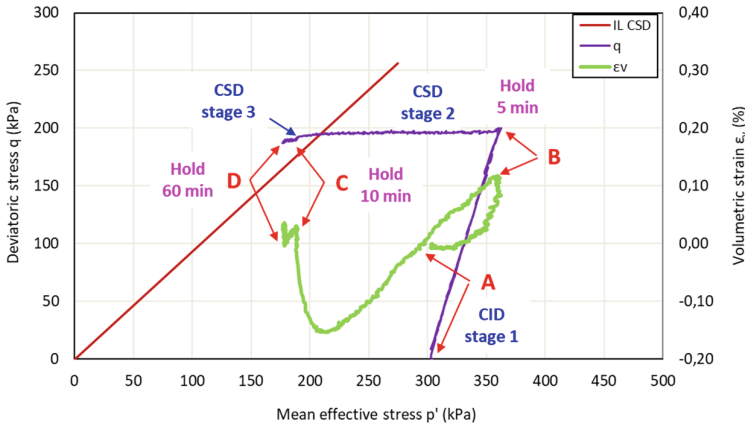


Fig. 6. Drained triaxial loading followed by a constant deviatoric stress test with three stress controlled pauses. Sample “CSD-Dr10-P300-M4” in Table 1.

The first pause of 5 min at point B was performed to verify that the controllability of the sample is ensured when the stress state is out of the bifurcation domain (not shown here). Then, the second pause of 10 min at point C, and the third pause of 60 min at point D were performed after the vanishing of the second-order work along q constant direction (i.e. inside the bifurcation domain when the q constant loading direction belongs to the instability cone). The time responses of the sample during these two pauses are shown in Figs. 7 and 8. As it can be seen, some delayed deformation is observed when p' is stopped from decreasing with a slight increase in axial strain ϵ_a and in volumetric strain ϵ_v (i.e. a slight contractancy). However, the rate of this delayed deformation, which can be interpreted as creep, decreases with time and stabilize after 10 to 15 min for ϵ_v . If the stress state is kept constant long enough, it can be observed in Fig. 8 that the volumetric strain decreases for $t > 40$ min (the sample dilates again preventing any acceleration in the creep rate).

Surprisingly, no complete loss of controllability was observed during the pauses at points C and D, despite the fact that (i) a full stress control mode is used in the bifurcation domain (ii) for a loading direction in the instability cone. According to the definition of the bifurcation domain, conditions (i) and (ii) should have been sufficient to trigger material failure from a theoretical point of view for rate independent materials. In the present case, the delayed deformation observed in Fig. 8 shows that the underlying microstructure reorganizations enable to restabilize the sample as the volumetric strain

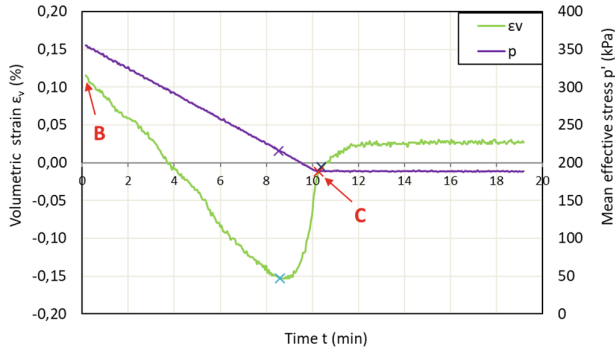


Fig. 7. Time evolution of the mean effective pressure and the volumetric strain along the q constant loading path from point B to C, and the consecutive pause of 10 min at constant stress (after the red cross). Sample “CSD-Dr10-P300-M4” in Table 1.

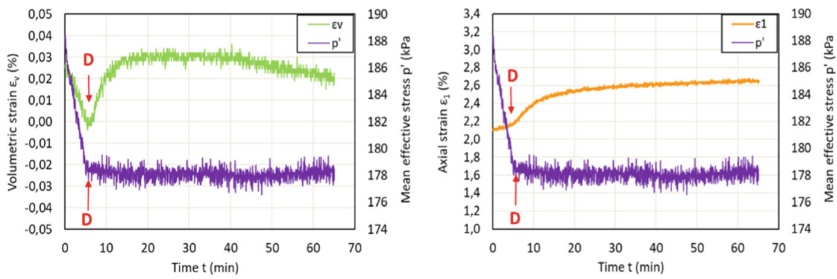


Fig. 8. Time evolution of the mean effective pressure, the volumetric strain and the axial strain along the q constant loading path from point C to D, and the consecutive pause of 60 min at constant stress (after $t = 5$ min). Sample “CSD-Dr10-P300-M4” in Table 1.

changes from contractancy to dilatancy. It should be underlined that these reorganizations need time to develop. The larger η , the longer it takes to the microstructure to restabilize (approximately 2 min at point C and 15 min at point D), which is probably be the reason why no restabilization is observed along CSD loading paths with a constant rate of decrease in p' (the sample continues to contract). The competition between macro and micro characteristic times can be further highlighted by varying the rate of decrease in p' which affects the moment where the second-order work vanishes. For a slower decreasing rate in p' , η_{IL-CSD} was found to increase (not shown here). Consequently, the existence of creep effects when approaching the maximum plastic surface makes the definition of a bifurcation domain not unique. Incremental constitutive relationships are no longer sufficient to describe the material response. A finite and sufficiently rapid perturbation is needed to lead to effective failure, which is consistent with reported results in the literature (Echersley 1990; Sasitharan et al. 1993; Gajo et al. 2000; Wautier et al. 2018).

4 Conclusion

An experimental study was conducted on loose samples of Hostun sand in order to explore its mechanical behavior in its bifurcation domain. Based on drained and undrained triaxial tests, the bifurcation domain was estimated as lying in between the instability line obtained in undrained compression and the plastic limit surface obtained in drained compression. Then the mechanical stability and controllability of loose specimen was investigated along constant deviatoric stress loading paths.

It was shown that the second-order work vanishes along such loading paths strictly inside the bifurcation domain. This vanishing of the second-order work is followed by specimen failure, but only after a finite size additional perturbation of the stress state. Just after reaching the instability point (i.e. when the constant q loading direction enters the instability cone), if the loading was stopped and the stress state kept constant, creep will occur, but no effective failure of the specimen occurs as the volumetric deformations change from contraction to dilation. This behavior can be interpreted as a sign of re-stabilization in the sense of the second-order work criterion. The creep can also lead to a little decrease in deviatoric stress, depending whether it develop into the third stage and lead to failure of the specimen. Additional tests with longer pauses are needed to verify this point.

References

- Benahmed, N., et al.: *Structure initiale et propriétés de liquéfaction statique d'un sable*. C. R. Mécanique **332** (2004)
- Benahmed, N.: *Comportement mécanique d'un sable sous cisaillement monotone et cyclique: application aux phénomènes de liquéfaction et mobilité cyclique*. Marne-la-vallée: Doctoral dissertation, ENPC
- Chu, J., Lo, S.-C., Lee, I.: Instability of granular soils under strain path testing. J. Geotech. Eng. **119**(5), 874–892 (1993)
- Daouadji, A., Darve, F., Al Gali, H., Hicher, P.Y., Laouafa, F., Lignon, S., Wan, R.: Diffuse failure in geomaterials: experiments, theory and modelling. Int. J. Numer. Anal. Methods Geomech. **35**(16) (2011)
- Darve, F., Servant, G., Laouafa, F., Khoa, H.D.: Failure in geomaterials: continuous and discrete analyses. Comput. Methods Appl. Mech. Eng. **193**(27–29), 3057–3085 (2004)
- Dong, Q., et al.: Drained instability in loose granular material. Int. J. Geomech. **16**(2), 04015043 (2016)
- Eckersley, D.: Instrumented laboratory flowslides. Geotechnique **40**(3), 489–502 (1990)
- Gajo, A., Piffer, L., De Polo, F.: Analysis of certain factors affecting the unstable behaviour of saturated loose sand. Mech. of Cohesive-Frictional Mater. **5**(3), 215–237 (2000)
- Hill, R.: A general theory of uniqueness and stability in elastic-plastic solids. J. Mech. Phys. Solids **6**(3), 236–249 (1958)
- Lade, P.: Initiation of static instability in the submarine Nerlerk Berm. Can. Geotech. J. **30**(6), 895–904 (1993)
- Nicot, F., Sibille, L., Darve, F.: Bifurcation in granular materials: an attempt for a unified framework. Int. J. Solids Struct. **46**(22–23), 3938–3947 (2009)
- Nova, R.: Controllability of the incremental response of soil specimens subjected to arbitrary loading programmes. J. Mech. Behav. Mater. **5**(2), 193–202 (1994)

- Sasitharan, S., Robertson, P., Sego, D., Morgenstern, N.: Collapse behavior of sand. *Can. Geotech. J.* **30**(4), 569–577 (1993)
- Sibille, L. (2006). *Modélisations discrètes de la rupture dans les milieux granulaires*. Grenoble, INP Grenoble
- Sibille, L., Donzé, F.V., Nicot, F., Chareyre, B., Darve, F.: From bifurcation to failure in a granular material: a DEM analysis. *Acta Geotech.* **3**(1), 15 (2008)
- Wan, R., Nicot, F., Darve, F.: *Failure in Geomaterials: A Contemporary Treatise*. Elsevier (2017)
- Wautier, A., Bonelli, S., Nicot, F.: Micro-inertia origin of instabilities in granular materials. *Int. J. Numer. Anal. Meth. Geomech.* **42**(9), 1037–1056 (2018)

Fracturing, Failure and Seismicity



Influence of Crystalline Structure on Strength Anisotropy of Silica Sand

Wadi H. Imseeh¹✉, Khalid A. Alshibli¹, Peter Kenesei², and Hemant Sharma²

¹ Department of Civil and Environmental Engineering, University of Tennessee, 325 John Tickle Building, Knoxville, TN 37996, USA

wimseeh@vols.utk.edu, alshibli@utk.edu

² Advanced Photon Source, Argonne National Laboratory, Lemont, IL 60439, USA
{kenesei, hsharma}@aps.anl.gov

Abstract. There is limited literature focused on experimentally investigating the influence of the crystalline structure of particles on the constitutive anisotropy of silica sand. This paper assesses the influence of quartz crystal structure on the constitutive response of synthetic silica cubes and natural silica sand particles using 3D x-ray diffraction (3DXRD), synchrotron micro-computed tomography (SMT), and 3D finite element (FE) analysis. The results of unconfined uniaxial compression experiments on synthetic silica cubes exposed constitutive anisotropy that was caused by the crystal structure of quartz. The 3D finite element (FE) analysis was validated to accurately model the crystal-based constitutive anisotropy in silica particles using the results of the silica cube experiments. Then 3D FE analysis was conducted to study how the change in crystal local orientation of individual sand particles can fundamentally produce anisotropy in the constitutive response of natural sand particles. Both the experiments and 3D FE analysis showed that the crystal structure of quartz essentially causes a directional anisotropy in the constitutive behavior of silica sand particles.

1 Introduction

Particle-scale properties have long been recognized to have a major influence on the constitutive behavior of sand at micro-, meso- and macro-scales. At the micro-scale, sand particle mineralogy and morphology (represented by surface texture, roundness, and sphericity) are the most important properties to be considered when studying the strength and fracture behavior of sand. Contact network/ fabric is the main parameter at the meso- and macro-scales. Sand anisotropy is commonly attributed to fabric anisotropy and only in recent years advances in 3D x-ray diffraction (3DXRD) enabled researchers to experimentally measure the lattice strain and lattice structure of synthetic and natural silica sand in a non-destructive manner (Amirrahmat et al. 2020; Cil et al. 2017; Hall and Wright 2015; Hurley et al. 2018).

The discrete element method (DEM) has been widely used to model the behavior of granular materials. Yet, the assumption of rigid particles in DEM fails to properly model the influence of the crystal structure of sand particles since it does not allow the user to implement the proper constitutive model, especially when modeling the failure of

sand. 3D finite element (FE) method has emerged in recent years as a powerful approach to model sand fracture by meshing 3D images of sand particles that were acquired using SMT and implementing proper continuum constitutive models assuming isotropic material behavior (Druckrey and Alshibli 2015; Imseeh and Alshibli 2017; Thakur and Penumadu 2020; Turner et al. 2019; Wei et al. 2019).

In this paper, Lattice strains for synthetic silica cubes subjected to unconfined uniaxial compression were experimentally measured and compared the evolution of lattice strain versus compression when the cubes are loaded in different directions with respect to their crystal planes. The simple geometry of the cube eliminates the effect of particle-scale morphology and isolates the influence of crystalline-scale properties on the constitutive behavior of silica particles. The stress-strain response of the silica cube permits assessing the agreement among the experimental constitutive behavior, calculated closed-form solution, and simulated 3D FE analysis. This paper answers a fundamental question about the effect of crystal orientation within individual sand particles on their constitutive behavior; a scale that has not been investigated by other researchers. Although the paper may not have an immediate practical application in the civil engineering field, it offers an original contribution that can be incorporated into constitutive models to predict the contact force network and fracture of granular materials with potential impacts on engineered granular materials and in applications that can take advantage of controlling the orientation of crystals to achieve specific performance outcomes.

2 Experiments on Synthetic Silica Cubes

The mineralogy of sand particles is mainly inherited from the parent rock sources and weathering conditions (Pettijohn et al. 1972) and quartz is the most common mineral in sands. The unit cell of crystal quartz is silicon oxide tetrahedra (SiO_4) with each oxygen atom shared between two tetrahedra. This composition gives quartz an overall chemical formula of silicon dioxide (SiO_2), commonly known as silica. In crystallography, crystal quartz is known to possess a hexagonal lattice system, trigonal crystal system, and rhombohedral unit cell (Dušek et al. 2001; Nikitin et al. 2007). The trigonal crystal system of quartz, whether right- or left-handed, is spanned by a local coordinate system of four axes: a_1 , a_2 , a_3 , c . The three a axes correspond to the a lattice parameter, span the hexagonal lattice plane, intersect at 60° angles, and are commonly referred to as the a —axis for simplification. The c —axis runs perpendicular to the lattice hexagonal plane and corresponds to the c lattice parameter, which is 1.1 times the length of a or b . This paper will refer to the crystal local orientations using the Miller-Bravais four-index system ($a_1 a_2 a_3 c$), in which parentheses and brackets respectively describe the crystal local planes and axes.

Synthetic silica cubes with a side length of 1 mm were selected to perform the unconfined uniaxial compression experiments to study the influence of crystal orientation and compare the evolution of lattice strain versus compressive load when the cubes are loaded in different directions with respect to its crystal planes. The simple geometry of the cube eliminates the effect of particle-scale morphology and isolates the influence of crystalline-scale properties on the constitutive behavior of silica particles. The crystal parameters of the synthetic silica cubes and silica sand were identified using powder

x-ray diffraction. Laue x-ray diffraction technique was used to identify the orientation of crystal planes with respect to the scanned face of the cube and revealed that the cube faces are perfectly aligned with $(2 \ -1 \ -1 \ 0)$, $(0 \ 1 \ -1 \ 0)$, and $(0 \ 0 \ 0 \ 1)$ crystal local planes. Cube faces aligned with the $(2 \ -1 \ -1 \ 0)$ and $(0 \ 0 \ 0 \ 1)$ crystal local planes (a -axis and c -axis; respectively) were colored differently with sharpie markers. The cubes were later subjected to unconfined uniaxial compression against the differently colored faces while collecting in-situ SMT and 3DXRD scans at the advanced photon source (APS).

A special compression apparatus transparent to x-ray was mounted on the stage of the x-ray beamline 1-ID, APS, Argonne National Laboratory (ANL), Illinois, USA. Two experiments were conducted on two cubes that were loaded against differently marked faces corresponding to the $(2 \ -1 \ -1 \ 0)$ and $(0 \ 0 \ 0 \ 1)$ crystal planes while acquiring in-situ SMT and 3DXRD scans. Uniaxial compression was paused at pre-determined uniaxial load steps of 0, 300, 600, 900, and 1200 N to acquire SMT scans followed by 3DXRD. SMT scans were acquired using a 1.6 mm (width) x 1.2 mm (height) beam while rotating the apparatus over at angular increments and 0.5 s exposure time. This procedure produced 1800 radiographs per scan that were reconstructed into 3D slice-structured images with an excellent spatial resolution of $0.98 \ \mu\text{m}/\text{pixel}$. 3DXRD scans were collected using a 1.6 mm (width) x 0.2 mm (height) beam during another 360° rotation of the apparatus at 0.2° angular increments and 0.3 s exposure time. The height of the 3DXRD beam was intentionally reduced to 0.2 mm to improve the accuracy of the measurements and to scan the entire cube by five vertically stacked layers.

3 3D FE Analysis of the Silica Cube Experiments

SMT scans offered visualization of the cube's microstructure to check for potential initial defects and the absence of crack evolution during compression since the scope of the cube experiments is to experimentally evaluate the elastic constitutive behavior of silica particles. 3DXRD scans were analyzed using Microstructural Imaging Diffraction Analysis Software (MIDAS) that was developed by APS staff (Park et al. 2015; Sharma et al. 2012). Lattice strains in the form of a symmetric second-order tenor (ϵ) expressed in the global coordinate system and a positive sign convention represents compression. Figure 1a. Displays the evolution of uniaxial compression using central vertical slices across the SMT scans for the two cubes where the superimposed color represents the major principal strain in the cube's crystal lattice as quantified by 3DXRD measurements. At the same global uniaxial compressive load, the cube loaded against $(2 \ -1 \ -1 \ 0)$ crystal plane (Fig. 1b.) exhibited a significantly higher major principal lattice strain than the cube loaded against $(0 \ 0 \ 0 \ 1)$ crystal plane Fig. 1b. Hereinafter, the terms "weak cube" (less stiff) and "strong cube" (stiffer) refer to the cube loaded against $(2 \ -1 \ -1 \ 0)$ and $(0 \ 0 \ 0 \ 1)$ crystal plane, respectively. Later, the term "isotropic cube" will also be introduced to describe 3D FE analysis for an isotropic approximation of the silica cube constitutive behavior. Crystal quartz possesses trigonal symmetry (point group 32) and six independent elastic constants ($C_{11}, C_{12}, C_{13}, C_{14}, C_{33}, C_{44}$)($C_{11}, C_{12}, C_{13}, C_{14}, C_{33}, C_{44}$):

$$[\sigma] = [C][\epsilon] \quad (1)$$

$$\begin{bmatrix} \sigma_1 \\ \sigma_2 \\ \sigma_3 \\ \sigma_4 \\ \sigma_5 \\ \sigma_6 \end{bmatrix} = \begin{bmatrix} C_{11} & C_{12} & C_{13} & C_{14} & 0 & 0 \\ C_{12} & C_{11} & C_{13} & -C_{14} & 0 & 0 \\ C_{13} & C_{13} & C_{33} & 0 & 0 & 0 \\ C_{14} & -C_{14} & 0 & C_{44} & 0 & 0 \\ 0 & 0 & 0 & 0 & C_{44} & C_{14} \\ 0 & 0 & 0 & 0 & C_{14} & \frac{1}{2}(C_{11} - C_{12}) \end{bmatrix} \begin{bmatrix} \varepsilon_1 \\ \varepsilon_2 \\ \varepsilon_3 \\ \varepsilon_4 \\ \varepsilon_5 \\ \varepsilon_6 \end{bmatrix} \quad (2)$$

where $[\sigma]$, $[\varepsilon]$, and $[C]$ denote the stress, strain, and elastic-stiffness tensors; respectively, expressed in conventional Voigt notation. The quartz elastic constants reported in Heyliger et al. (2003) based on experimental measurements (Table 1) were used in this paper to calculate stresses from lattice strains using Eq. 2. The constitutive relationship defined by Eq. 2 was scripted into a FORTRAN user subroutine to numerically model silica material in ABAQUS FE code. In another user-subroutine, $[C]$ in Eq. 2 was replaced by the isotropic approximation $[C]_{iso}$ (Eq. 3) to compare the isotropic with the anisotropic behavior:

$$[C]_{iso} = \frac{E}{(1+\nu)(1-2\nu)} \begin{bmatrix} 1-\nu & \nu & \nu & 0 & 0 & 0 \\ \nu & 1-\nu & \nu & 0 & 0 & 0 \\ \nu & \nu & 1-\nu & 0 & 0 & 0 \\ 0 & 0 & 0 & \frac{1-2\nu}{2} & 0 & 0 \\ 0 & 0 & 0 & 0 & \frac{1-2\nu}{2} & 0 \\ 0 & 0 & 0 & 0 & 0 & \frac{1-2\nu}{2} \end{bmatrix} \quad (3)$$

where $E = 99.45 \text{ GPa}$ and $\nu = 0.06$ are the modulus of elasticity and Poisson's ratio calculated by Voigt-Reuss-Hill averaging based on the values listed in Table 1. Since the latter material model is isotropic, $[C]_{iso}$ is invariant for all orthogonal coordinate systems. Therefore, the rotational stress/strain transformations are redundant and were eliminated from the user-subroutine algorithm.

Table 1. Elastic constants of crystal quartz (Heyliger et al. 2003)

Elastic constant	C_{11}	C_{12}	C_{13}	C_{14}	C_{33}	C_{44}
Value: GPa	87.26	6.57	11.95	-17.18	105.8	57.15

The material user-subroutines were executed in ABAQUS to model the constitutive response of the silica cube under unconfined uniaxial compression. The silica cube was modeled by a 20-noded hexahedral element that performed the stress-strain FE calculations (call the material user-subroutine) at 27 integration points using quadratic shape functions. The hexahedral element measured 0.5 mm in side length and plane symmetry boundary conditions were appropriately assigned for the nodes across the X-Z, Y-Z, and X-Y faces. The FE calculations were conducted via the static implicit solver in ABAQUS, which simulated the uniaxial compression using 1×10^{-4} mm compressive displacement increments assigned to the nodes across the top face of the hexahedral

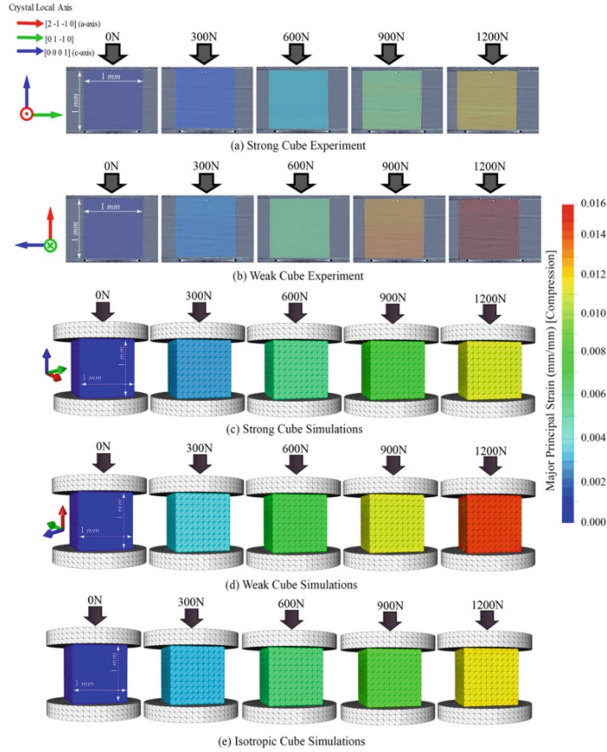


Fig. 1. In-situ SMT scans illustrating the lattice strain measured using 3DXRD for (a) Strong, and (b) Weak cubes that were loaded in unconfined uniaxial compression against opposite crystal planes; 3D FE simulations of the (c) Strong and (d) Weak cube experiments assuming anisotropic linear elastic behavior, and (e) assuming isotropic linear elastic behavior.

element. The incremental uniaxial displacement was halved and doubled in preliminary trials and its effect on the FE analysis was found to be negligible. Three trial simulations were conducted on the hexahedral element with the same boundary conditions. Two of the trials modeled the strong (Fig. 1c) and weak (Fig. 1d) silica cubes using the anisotropic material user-subroutine. The third trial (Fig. 1e) modeled the constitutive behavior of the silica cube elements using the isotropic user-subroutine Eq. (3).

The regular geometry of the cube made it easy to calculate the closed-form solution using the theory of linear elasticity. Figure 2. Displays the relationship between the uniaxial compressive load and the major principal strain of the cube using solid lines for experimental data, dotted lines for simulated data, and dashed lines for calculated data. The FE simulated responses overlay their corresponding dotted lines (closed-form solution) in Fig. 2. With a difference in slope $< 1\%$. The experimental responses include filled-circle markers that represent the cube's global uniaxial compressive load versus major principal strains of the crystal lattice per 3DXRD measurements. At each load step, multiple filled-circle markers appear because of the vertical stacking procedure in 3DXRD scanning that provided five lattice strain measurements per load step. Solid

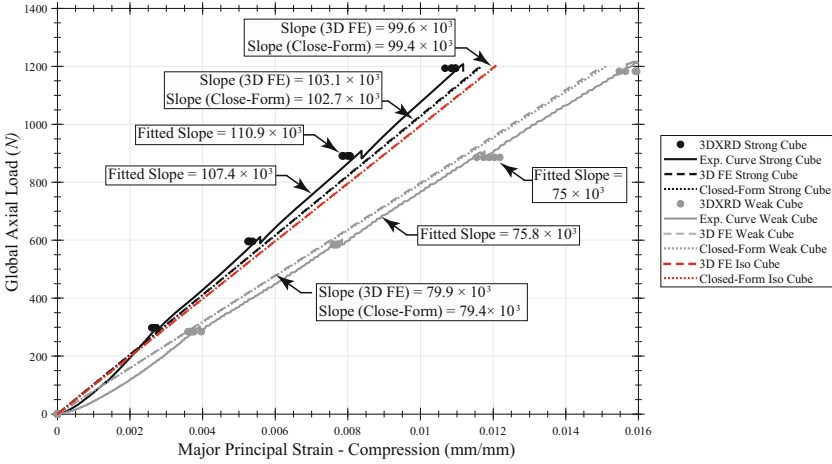


Fig. 2. Summary of experimental and FE results of the experiments on silica cubes.

lines represent the uniaxial load (N) versus displacement (mm) relationships as recorded by the data acquisition system of the compression apparatus. Recall that the solid lines in Fig. 2. Also represent the cube’s global uniaxial stress (MPa) versus strain since the cube side length is 1 mm. The red color denotes the data (e.g., points, lines, and curves) related to the isotropic cube, while the black and grey colors represent the strong and weak cube’s data, respectively. The constitutive response of the strong cube in Fig. 2. is stiffer (slope = 103.1×10^3) than the weak cube (slope = 79.9×10^3), which is in agreement with the experimental observations in Fig. 1a. The red line (slope = 79.9×10^3) represents the simulation that executed the isotropic user-subroutine and has a closer response to the strong cube line than the weak.

A close agreement can be seen between the solid lines and filled-circle markers in Fig. 2. ($<4\%$ difference in slope), which confirms the capability of MIDAS to analyze and measure lattice strains of the scanned cubes under 3DXRD. This agreement fundamentally demonstrates that the crystal lattice strain of the cube has accurately manifested the global uniaxial strain measured at its top face. Overall, Fig. 2. Shows an excellent agreement among the experimental (solid line, and circular points), 3D FE (dashed line), and closed form (dotted line) constitutive behavior for the strong (black) as well as the weak cube (grey). Since the solid black and grey curves in Fig. 2. Divert more from one another than the dashed/dotted lines, it can be concluded that the experimental response manifests a bit higher degree of constitutive anisotropy than what is captured by the 3D FE simulations and strong-form solutions. Finally, the red lines in Fig. 2. Represent the isotropic approximation of crystal quartz constitutive behavior, which appears to overestimate the stiffness since the red lines are closer to the black lines (strong cube) than the grey (weak cube).

4 FE Simulations of Sand Single Particle Fracture

Unlike the simple cube geometry, natural sand particles have complex morphologies that make it very difficult to establish a closed-form solution or experimentally control the loading direction of a sand particle with respect to its crystal planes. To assess the constitutive anisotropy of natural silica sand particles, the authors have upgraded their 3D FE simulation capabilities via coding development in ABAQUS in order to model natural sand. The new FE simulations seek to model sand particles using 3D FE particles that closely match the morphology of natural sand. Subsequently, element strains of the 3D FE particles were converted to stresses via the isotropic or anisotropic material user-subroutine that were presented earlier (Eqs. 2 and 3). A numerical contact model was adopted to simulate the transmission of stresses at contact interactions between the 3D FE meshes (sand particles). ABAQUS general contact module was used to model the particle-to-particle, particle-to-platen, and particle-to-mold interactions. Surface elements of ABAQUS assembly parts (e.g., sand particles, loading platens, and confining mold) were extracted into individual element sets and were included in the domain of the general contact module. Contacts were detected using a node-into-face penetration mechanism for the element sets included in the domain of the general contact module. When elements came into contact, shear and normal forces were transmitted across the contact interface to resist node-into-face, node-into-rigid surface, and edge-into-edge penetration. The default hard contact model in ABAQUS was used to relate normal contact forces to penetration distance. Briefly, the element bulk stiffness was automatically scaled by ABAQUS at the normal to contact interface in which the effect of contact deformation on the time increment is minimal: allowed penetration is neglected in most of the simulations. A frictional contact model was also adopted from ABAQUS to simulate the tangential force transmission at contact interfaces using a friction coefficient of $\tan 23^\circ = 0.42$; a typical value for the true angle of friction of silica sand (Rowe 1962). Accordingly, ABAQUS performed a slip-stick check at the beginning of every time increment for the penetrating nodes at the contact interfaces between meshed parts to simulate their relative sliding (Imseeh and Alshibli 2021).

A frictional failure surface similar to Drucker–Prager yield criterion that activates the onset of fracture at the element material point was adopted. A tension cutoff limit was introduced to the failure criterion in which von Mises stress yield stress (σ_{vf}) remained constant when the hydrostatic mean stress in tension extended beyond the cutoff limit. The cutoff limit eliminated numerical instabilities associated with the failure near the stress state of hydrostatic tension ($\sigma_{vf} \rightarrow 0$) (for more details, see Imseeh and Alshibli 2021). Continuum damage mechanics is the principal framework that governs the numerical modeling of fracture in brittle materials such as sand particles. The framework postulates the sudden collapse in the stress-strain behavior at fracture through progressive degradation in the stiffness associated with the material point, assuming the damaged and undamaged states have equivalent strains (Lemaitre and Chaboche 1978). One way to model the amount of degradation in stiffness is by using a scalar damage parameter (d) that ranges between 0 and 1. A value of $d = 0$ represents an undamaged section whereas a value of $d = 1$ indicates a fully damaged section. We used the damage model adopted by (Imseeh and Alshibli 2021) that permitted degradation of the bulk modulus only when volume change was tensile and degradation of the shear modulus regardless

of whether the volume change was tensile or compressive. The damage approach was anisotropic in the sense of different degradation in the stiffness of the material point under tensile versus compressive loading, and appropriately modeled the constitutive damage in brittle materials such as silica sand particles.

The material user-subroutines were developed and implemented in ABAQUS FE software using FORTRAN scripts to simulate the constitutive and fracture behaviors of natural silica sand particles. The FE simulations operate on 3D meshes of linear tetrahedral elements that closely resemble the morphology of natural sand particles. The explicit dynamic solver in ABAQUS was used to conduct the FE simulations. The assumption of nodal lumped masses in this specific solver produced a diagonal mass matrix (M), which was used to balance the equation of motion. The explicit central-difference time integration rule was then used to advance the nodal kinematic state (nodal displacement, velocity, and acceleration) over time. The key advantage of this solver is the use of explicit balance equations and the fast inversion of M (diagonal) versus the Newton–Raphson procedure, which is executed at every time increment of the static implicit solver to iterated equilibrium. Although the explicit dynamic solver was originally designated for problems with impact loading (i.e., high strain rate), the use of uniform mass-scaling limited the speed of stress wave propagation, allowing for the utilization of the explicit dynamic solver in quasi-static analyses. Moreover, the mass-scaling offered the advantage of drastically reducing the simulation runtime by increasing the size of the minimum stable time increment.

3D FE simulations were carried out to simulate the fracture of two ASTM 20–30 Ottawa sand particles (99.9% silica sand) loaded using unconfined compression. Both particles had almost the same equivalent diameter of ~ 0.850 mm with a difference of less than 0.005 mm. The particle in the processed SMT image at the initial state (unloaded) was projected on 2D planes at a specific angle, and the distance between the outermost tangents of projections was calculated to represent the 3D Feret diameter of that angle. Multiple 3D Feret diameters were computed with a sampling of 31 angles regularly spaced in 3D space around the upper part of a unit sphere. The equivalent diameter was computed as the diameter of a sphere with equal volume to the sand particle. For baseline analyses to compare results, simulations of the single particle compression experiment were also executed on a sphere with a diameter of 0.850 mm (\sim equivalent diameter of the sand particles). Figure 3. Presents the 3D volume rendering of the SMT images for the two single particle compression experiments and their corresponding FE simulation, as well as the analogous simulations conducted on the sphere. “Particle-1” and “Particle-2” refer to the two single particle compression experiments, whereas the simulations of the sphere are denoted as “Sphere-Eq”. For each particle (both sand and the spherical particle), three simulations were conducted and given the labels “Isotropic”, “Strong”, and “Weak”. In the Isotropic case, the simulations executed the material user subroutine that assumed isotropic linear approximation of silica constitutive behavior (Eq. 3). On the other hand, the Strong (when the particle was loaded against its crystal c -axis) and Weak (when the particle was loaded against its crystal a -axis) simulations executed the material user-subroutine that was developed using the anisotropic linear model for silica mineral (Eq. 2).

Figure 3d presents the evolution curves of vertical compressive load (F_Z) versus displacement (U_Z) of the top loading platen. U_Z presents the movement of the top platen and F_Z is the summation of reaction forces acting against the platen. It can be seen from Fig. 3d that the numerical prediction of the experimental curves (solid lines) improved when the material user-subroutine implemented the anisotropic linear elastic model of silica mineral (Strong and Weak curves), in comparison to the isotropic approximation (isotropic curves). When comparing the F_Z versus U_Z responses for individual particles (set of curves with the same color), the Strong curves (dashed line) display a stiffer response compared to the Weak (double dashed line) and Isotropic curves (dotted line), respectively. The latter remark aroused from aligning the loading direction in the Strong simulations with the stiff crystal c-axis. Figure 3d also demonstrates a significant variation in the $U_Z - F_Z$ responses between Particle-1 and Particle-2. Relative to the response of Sphere-Eq, Particle-2 fractured at about half F_Z whereas Particle-1 at almost $0.25 U_Z$. Both Particles were selected from Ottawa ASTM 20–30 sand, which is a standard natural sand that has been widely used in geotechnical testing and is known for having silica constituent (more than 99.9% as well as a uniform grain size distribution). Similar variation in $U_Z - F_Z$ response was also reported by Cil et al. (2013) for 87 particles of the same sand that were tested using the same testing apparatus. Then, 3D FE simulations were conducted to investigate the variation in the fracture and constitutive behaviors between Particles 1 and 2. Referring to Fig. 3, it can be seen that Particle-2 exhibited soft contact with the loading platens that caused the particle to rotate slightly between $F_Z = 0$ and $F_Z = 20$ N. Conversely, Particle-1 lacked this rotation due to its firm contact with the two loading platens. The difference in the nature of particle-to-platen contacts explains the long stretch in the blue curves in Fig. 3d relative to the red curves.

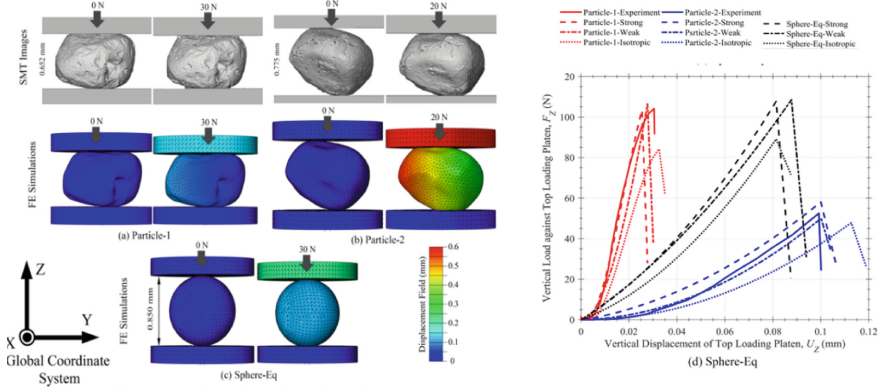


Fig. 3. In-situ SMT scans and 3D FE simulation of single-particle crushing experiments on (a) Particle-1; (b) Particle-2 of ASTM 20–30 Ottawa sand; (c) 3D FE simulations of Sphere-Eq (a sphere with equivalent diameter to the ASTM 20–30 Ottawa sand); and (d) load-displacement curves for the experiments and simulations at the top loading platen.

Figure 4 displays the distribution of σ_v within both particles and Sphere-Eq at fracture. For Particle-1 (Fig. 4a), it can be seen that fracture patterns in the three FE simulations (Strong, Weak, and Isotropic) mainly occurred near a surface depression obvious from the SMT image that penetrated through the micro-structure of Particle-1. Such material imperfections are well-known to exist in natural sand particles and create weak points in the particle micro-structure that give rise to fracture onset. Particle-2 and Sphere-Eq were free of micro-structural imperfections (based on SMT image of particle-2) and exhibited different fracture modes in the strong simulations when compared to weak simulations. The latter finding clearly challenged the isotropic FE simulations, which falsely presume the same fracture and constitutive behaviors for two particles with identical morphology and particle-to-plate interaction. Differences in the constitutive and fracture behaviors of identical particles can fundamentally arise from properties beyond the micro-scale and exist at the crystal scale-level of silica sand. The X-Y views of fractured particles in Fig. 4 clearly illustrate a broader spread of red area in Sphere-Eq and Particle-1 than Particle-2. This red area represents the highly stressed region within the particle that interacted with the top loading platen. The difference in the particle-to-plate interaction area can explain the fracture of Particle-2 at a much lower F_Z in Fig. 3d relative to Particle-1 and Sphere-Eq. Namely, F_Z in Particle-2 acted on a smaller region that caused high-stress concentrations within the particle, and thus Particle-2 fractured at a low F_Z . Another observation from Fig. 4c is the shattering fracture manifested by the Isotropic simulations of Sphere-Eq. Such behavior was attributed to the regularity in the sphere geometry accompanied by the presumed isotropy in the constitutive response.

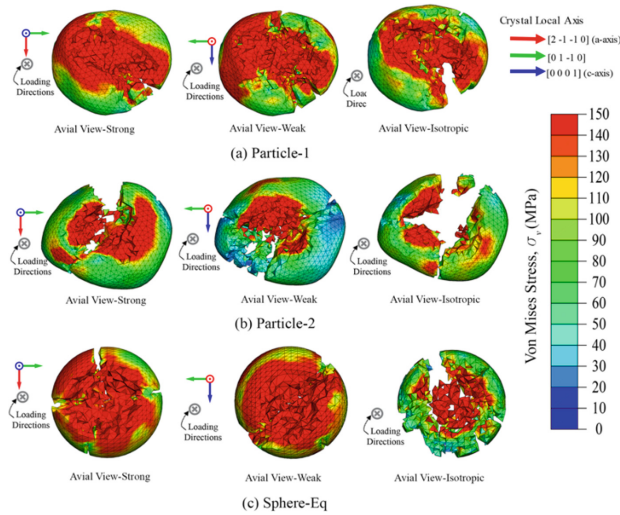


Fig. 4. Fracture patterns for (a) Particle-1; (b) Particle-2; and (c) Sphere-Eq assuming anisotropic and isotropic linear elastic behaviors.

5 Conclusions

The influence of quartz crystal structure on the constitutive response of natural and synthetic silica particles was examined using rich 3D experimental measurements quantified by combined in-situ SMT and 3DXRD scanning as well as numerical 3D FE analysis. The crystal structure of quartz essentially produces directional anisotropy in the constitutive behavior of silica particles. On the scale of a single silica $(1 \text{ mm})^3$ cube subjected to unconfined uniaxial compression, major principal lattice strain experimentally manifested ~ 1.3 stiffer response when the cube was loaded against the face aligned with $(0 \ 0 \ 0 \ 1)$ versus $(2 \ -1 \ -1 \ 0)$ crystal plane. 3D FE analysis can numerically model the constitutive anisotropy in silica particles by implementing crystal-based material sub-routines and accurately simulated the significant difference in the evolution of the major principal lattice strain for the silica cube when loaded against opposite crystal planes. At the particle-scale, natural silica sand particles exhibit significant stiffer constitutive behavior when their major principal stress direction is aligned with the $[0 \ 0 \ 0 \ 1]$ crystal local axis compared to $[2 \ -1 \ -1 \ 0]$.

Acknowledgments. The work in this paper is funded by the National Science Foundation (NSF) Grant No. CMMI-1362510. Any opinions, findings, conclusions, and recommendations expressed in this paper are those of the authors and do not necessarily reflect the views of NSF. This paper has used resources of the Joint Institute for Advanced Materials (JIAM), x-ray diffraction facility located at the University of Tennessee, Knoxville, TN and the Advanced Photon Source (APS), a U.S. Department of Energy (DOE) Office of Science User Facility operated for the DOE Office of Science by Argonne National Laboratory (ANL) under Contract No. DE-AC02-06CH11357. We would also like to thank Zaher A. Jarrar and Andrew M. Druckrey of the University of Tennessee for contributing to the experimental work at APS.

References

- Amirrahmat, S., Imseeh, W.H., Alshibli, K.A., Kenesei, P., Jarrar, Z.A., Sharma, H.: 3D experimental measurements of evolution of force chains in natural silica sand. *J. Geotech. Geoenviron. Eng.* **146**(5), 04020027 (2020)
- Cil, M., Alshibli, K., McDowell, G., Li, H.: Discussion: 3D assessment of fracture of sand particles using discrete element method. *Géotech. Lett* **3**(3), 13–15 (2013)
- Cil, M.B., Alshibli, K.A., Kenesei, P.: 3D Experimental measurement of lattice strain and fracture behavior of sand particles using synchrotron X-ray diffraction and tomography. *J. Geotech. Geoenviron. Eng.* **143**(9) (2017)
- Druckrey, A.M., Alshibli, K.A.: 3D finite element modeling of sand particle fracture based on in situ X-Ray synchrotron imaging. *Int. J. Numer. Anal. Methods Geomech.*, (2015)
- Dušek, M., Petříček, V., Wunschel, M., Dinnebier, R., Van Smaalen, S.: Refinement of modulated structures against X-ray powder diffraction data with JANA2000. *J. Appl. Crystallogr.* **34**(3), 398–404 (2001)
- Hall, S.A., Wright, J.: Three-dimensional experimental granular mechanics. *Geotech. Lett.* **5**, 236 (2015)
- Heyliger, P., Ledbetter, H., Kim, S.: Elastic constants of natural quartz. *J. Acoust. Soc. Am* **114**, 644 (2003)

- Hurley, R.C., Herbold, E.B., Pagan, D.C.: Characterization of the crystal structure, kinematics, stresses and rotations in angular granular quartz during compaction. *J. Appl. Crystallogr.* **51**(4), 1021–1034 (2018)
- Imseeh, W.H., Alshibli, K.A.: 3D Analysis of force chains in sand using finite element method. In *3rd International Conference on Tomography of Materials and Structures Lund, Sweden* (2017)
- Imseeh, W.H., Alshibli, K.A.: Influence of micro-and crystalline-scale properties on the fracture of silica sand particles using 3D finite-element analysis. *Int. J. Geomech.* **21**(9), 04021154 (2021)
- Lemaitre, J., Chaboche, J.-L.: Aspect phénoménologique de la rupture par endommagement. *J. Méc. Appl.*, **2**(3) (1978)
- Nikitin, A., Markova, G., Balagurov, A., Vasin, R., Alekseeva, O.: Investigation of the structure and properties of quartz in the α - β transition range by neutron diffraction and mechanical spectroscopy. *Crystallogr. Rep.* **52**(3), 428–435 (2007)
- Park, J.-S., et al.: High-energy synchrotron x-ray techniques for studying irradiated materials. *J. Mater. Res.* **30**(9), 1380–1391 (2015). <https://doi.org/10.1557/jmr.2015.50>
- Pettijohn, F.J., Potter, P.E., Siever, R.: Introduction and source materials. *Sand and Sandstone*, Springer, pp. 1–23 (1972)
- Rowe, P.W.: The stress-dilatancy relation for static equilibrium of an assembly of particles in contact. *Proc. Royal Soc. London. Series A. Math. Phys. Sci.* **269**(1339), 500–527 (1962)
- Sharma, H., Huizenga, R.M., Offerman, S.E.: A fast methodology to determine the characteristics of thousands of grains using three-dimensional X-ray diffraction. I. Overlapping diffraction peaks and parameters of the experimental setup. *J. Appl. Crystallogr.* **45**(4), 693–704 (2012)
- Thakur, M.M., Penumadu, D.: Triaxial compression in sands using FDEM and micro-X-ray computed tomography. *Comput. Geotech.* **124**, 103638 (2020)
- Turner, A.K., Sharma, A., Penumadu, D., Herbold, E.B.: Finite element analyses of single particle crushing tests incorporating computed tomography imaging and damage mechanics. *Comput. Geotech.* **115**, 103158 (2019)
- Wei, D., Zhao, B., Dias-da-Costa, D., Gan, Y.: An FDEM study of particle breakage under rotational point loading. *Eng. Fract. Mech.* **212**, 221–237 (2019)



The Role of Seismic Slip Velocity in the Evolution of Shear Band Thickness

Alexandros Stathas^(✉) and Ioannis Stefanou

Institut de Recherche en Génie Civil et Mécanique (UMR CNRS 6183),
Ecole Centrale de Nantes, Nantes, France
ioannis.stefanou@ec-nantes.fr

Abstract. aut]Stathas, Alexandrosaut]Stefanou, IoannisIn this paper we investigate the role of seismic slip velocity in the thickness evolution of a fault's principal slip zone (PSZ) during coseismic slip. The PSZ of a fault can be modelled as a shear band of evolving thickness (see [33]). The PSZ thickness is associated with energy dissipation and apparent frictional softening during earthquakes. We use numerical non-linear analyses that take into account the granular size and the main Thermo-Hydro-Mechanical (THM) couplings that take place during coseismic slip. The material inside the PSZ where the shear band occurs, is modelled using Cosserat theory under small deformations, which introduces an internal length scale to the problem [17]. Temperature and pressure diffusion introduce further internal length scales to the system and enhance softening depending on applied seismic slip velocity. Going beyond existing numerical analyses [16, 18], we introduce a three step procedure which includes consolidation, slow shear of 1 mm/s and then fast shear of 1 m/s for a shear displacement of 5 mm at each step. The effect of boundary fluxes is considered and a shear traction envelope for the different cases is produced. Next we subject the system to large shear displacements up to 1 m under different slip rates. We find that velocity increase leads to softening increase and localization thickness decrease. For large displacements we observe a steady state response that seems to include a limit cycle and travelling waves of strain localization.

Keywords: Strain localization · THM-couplings · Travelling instability · Cosserat · Finite elements

1 Introduction

In this paper we investigate the role of seismic slip velocity in the evolution of shear strain localization width inside the fault gouge of a mature fault. The fault gouge is a region of ultracataclastic granular material inside the fault with thickness of some millimetres that accommodates the majority of the seismic slip (see [8, 22, 29]). Inside the fault gouge, the seismic slip is commonly accompanied by a localization of shear strain- rate into a narrow thin zone, the Principal Slip Zone (PSZ). The PSZ is a zone of finite thickness of some hundreds of

micro meters (see [21]). Strain localization and the formation of shear bands in fault zones is very important as it affects shear heating and pore pressure increase during seismic slip. As a result they determine the post peak, softening behaviour of faults, which is responsible for earthquake nucleation, the dissipated energy and the energy radiated to the surface [1, 8].

The shear strength of the fault is dependent on various mechanical and physico-chemical mechanisms [19, 28, 29]. Here we investigate the mechanism of thermal pressurization of pore fluid in fluid saturated faults in particular, in order to capture its effect on the evolution of shear strength during coseismic slip. Thermal pressurization happens as a consequence of the different expansivities of fluid and the surrounding rock inside the fault gouge and has been shown to play an important role in the weakening of fault zones [9, 20, 34]. As slip progresses, temperature increases due to frictional dissipation. Then the confined pore fluid inside the fault, which tends to expand more than the rock for the same temperature increase, increases its pressure, leading to a decrease in the effective Terzaghi mean stress, and therefore, to a reduction of the fault's available shear strength. The thickness of the PSZ is essential for the quantification of plastic work, giving rise to the temperature increase inside the fault and consequently to the apparent softening behaviour.

Experimental evidence in faults (see [14, 22]) has shown, that the PSZ has a finite width and it does not collapse into a mathematical plane. This behaviour cannot be captured by the use of a Classical Cauchy continuum in numerical analyses, because it has been shown that such a continuum localizes on a mathematical plane when strain softening is present [13]. This makes the numerical analyses mesh dependent, leading to wrong estimates for the dissipated energy during coseismic slip. Different approaches have been tested to avoid mesh dependency of the numerical solution. These include the use of a strain softening strain-rate hardening material law (see [35]) and the use of higher order continua [2, 4, 12, 16]. We have shown mathematically and numerically in [24] that the first approach involving the use of elasto viscoplasticity does not regularize the mesh dependency of the numerical results.

In this paper we make use of Cosserat continua for the description of the fault gouge material for the calculation of PSZ thickness. Cosserat continua are a special class of micromorphic continua whose material particles can be considered to have six degrees of freedom in 3D space comprised of three translations u_i and three rotations ω_i , $i = 1, \dots, 3$. Due to the existence of a material length, R , present in the material equations, localization width does not collapse to zero as in a classical Cauchy continuum.

Using Cosserat continuum for describing strain localization during coseismic slip, we solve the nonlinear problem for large displacements with the help of the FE software Numerical Geolab [25]. Going beyond existing results [16, 17], we obtain the stress-strain post peak response of the fault for a wide range of seismic slips and seismic slip velocities, the evolution of localization width during shearing of the layer and the apparent rate dependency of the system due to THM couplings even for a rate independent mechanical behaviour.

2 Kinematics of the Cosserat Continuum and Balance Equations

We consider a set of rigid particles in the Cosserat continuum each one described by the position of its center of mass. In a first order theory, the displacement of each point inside the rigid particle can be described by making use of every point's distance from the particle's center of mass χ'_i and its micro-rotation ω_i , which is common to all points inside the particle [6, 26]. Due to the rigid particle assumption and making use of the external product and tensor theorem of algebra, ω_i represents the vectorial form of the external product tensor ω_{ij} . Where the relationship between the micro-rotation vector ω_i and the tensor of rotation ω_{ij} is given as $\omega_i = -\epsilon_{ijk}\omega_{ij}$ with ϵ_{ijk} to be the Levi-Civita symbol. Following the Einstein summation, the displacement field at each point of the particle can be given as:

$$u'_i = u_i + \omega_{ij}\chi'_j \quad (1)$$

2.1 Cosserat Kinematics

We continue by introducing the kinematic fields of the deformation tensor γ_{ij} . We define its symmetric part $\gamma_{(ij)}$ as the macroscopic strain ε_{ij} while its anti-symmetric part $\gamma_{[ij]}$ is the difference between macroscopic rotation Ω_{ij} and the microscopic rotation tensor ω_{ij} . We also take into account the gradient of the microscopic rotation tensor, the curvature tensor κ_{ij} .

$$\gamma_{ij} = \gamma_{(ij)} + \gamma_{[ij]} = u_{i,j} - \omega_{ij} = u_{i,j} + \epsilon_{ijk}\omega_k \quad (2)$$

$$\gamma_{(ij)} = \varepsilon_{ij} = \frac{1}{2} (u'_{i,j} + u'_{j,i}) \quad (3)$$

$$\gamma_{[ij]} = \frac{1}{2} (u'_{i,j} - u'_{j,i}) = \frac{1}{2} (u_{i,j} - u_{j,i}) - \omega_{ij} = \Omega_{ij} - \omega_{ij} \quad (4)$$

$$\kappa_{ij} = \omega_{i,j} \quad (5)$$

2.2 Linear and Angular Momentum Balance Equations

As is the case with Cosserat strains γ_{ij} the Cosserat stress tensor τ_{ij} is also not symmetric. The gradient of micro rotations introduces also Cosserat moments or Couple stresses μ_{ij} to the balance equations. In contrast to Cauchy continua, τ_{ij} can be decomposed into a symmetric, $\tau_{(ij)} = \sigma_{ij}$, and a non-zero antisymmetric $\tau_{[ij]}$ part. The balance equations can then be written as:

$$\tau_{ij,j} - \rho \frac{\partial^2 u_i}{\partial t^2} = 0 \quad (6)$$

$$\mu_{ij,j} - \epsilon_{ijk}\tau_{jk} - \rho I \frac{\partial^2 \omega_i}{\partial t^2} = 0 \quad (7)$$

where ρ and I are, respectively, the density and microinertia considered isotropic here, while ϵ_{ijk} is the Levi-Civita permutation tensor.

2.3 Energy Balance Equation

Conservation of energy in a quasi-static transformation (we neglect the convective derivative) where the material yields producing heat in the form of plastic dissipation, assuming Fourier's law is expressed as:

$$\rho C \frac{\partial T}{\partial t} = \dot{W}^p + k_T T_{,ii} \quad (8)$$

$$\rho C \left(\frac{\partial T}{\partial t} - c_{th} T_{,ii} \right) = \sigma_{ij} \dot{\varepsilon}_{ij}^p + \tau_{[ij]} \dot{\gamma}_{[ij]}^p + \mu_{ij} \dot{\kappa}_{ij}^p \quad (9)$$

where $c_{th} = \frac{k_T}{\rho C}$, k_T are defined as the thermal diffusivity and thermal conductivity of the medium respectively. The quantities under $(\dot{})^p$ indicate the plastic part of the rate of symmetric, antisymmetric strain and curvature tensors respectively.

2.4 Mass Balance Equation

In the case of porous media as the one discussed here, the medium consists of both a fluid phase and a solid phase (insoluble to the fluid) which we consider to communicate perfectly in whole. Meaning no effects of tortuosity and no distinction between principal and secondary pore fluid network will be taken into account. The two phases communicate with each other by acting forces to one another due to different deformation properties [3, 15, 27]. Finally the local form of the mixture mass balance equation is given according to Rattetz et al. [16]:

$$\frac{\partial p}{\partial t} = c_{hy} p_{i,i} + \frac{\lambda^*}{\beta^*} \frac{\partial T}{\partial t} - \frac{1}{\beta^*} \frac{\partial \varepsilon_v}{\partial t} \quad (10)$$

where $c_{hy} = \frac{\chi}{\eta^f \beta^*}$ is the hydraulic diffusivity expressed with the help of the porosity of the solid skeleton χ and the pore fluid viscosity η^f , while $\beta^* = n\beta^f + (1-n)\beta^s$, $\lambda^* = n\lambda^f + (1-n)\lambda^s$ are the mixture's compressibility and expansivity respectively [32].

3 Cosserat Elastoplastic Constitutive Relations

In what follows the Terzaghi theory of effective stress is assumed to hold true. That is, the effective stress τ'_{ij} found at the Gauss points by use of the relation $\tau_{ij} = \tau'_{ij} - p\delta_{ij}$ for $\tau_{ij}, \tau'_{ij} > 0$ in tension and $p > 0$ in compression. No reference to the grain compressibility as well as the existence of a double porosity network is being taken into account.

3.1 Cosserat Elasticity

The general constitutive equations for a centrosymmetric Cosserat material relating stresses and Cosserat moments to Cosserat strains and curvatures are given by Vardoulakis [33]:

$$\tau_{ij} = K\gamma_{kk}^e \delta_{ij} + 2G \left(\varepsilon_{ij}^e - \frac{1}{3}\gamma_{kk}^e \delta_{ij} \right) + 2G_c \gamma_{[ij]}^e \quad (11)$$

$$\mu_{ij} = L\kappa_{kk}^e \delta_{ij} + 2M \left(\kappa_{(ij)}^e - \frac{1}{3}\kappa_{kk}^e \delta_{ij} \right) + 2M_c \kappa_{[ij]}^e \quad (12)$$

We notice that additionally to the elastic moduli used by the Cauchy media (K, G) denoting isotropic compression and shear moduli respectively, four additional constants are added G_c, L, M, M_c referring to the anti-symmetric part of Cosserat deviatoric stresses, the spherical part of Cosserat moments, the symmetric and anti-symmetric deviatoric parts of the Cosserat moments respectively.

3.2 Thermo-elasto-Plastic Constitutive Relationship

The development of the thermo-elasto-plastic constitutive relations that follow is based on [30]. Since we follow a small strain approach, the strain rate and the curvature rate tensor can be decomposed into its elastic plastic and thermal parts. Large displacements are then taken into account through an updated Lagrangian approach. In what follows we make the assumption that the curvature tensor stays unaffected by a change of temperature. Therefore strain rate and curvature rate tensors are decomposed as [10]:

$$\begin{aligned} \dot{\gamma}_{ij} &= \dot{\gamma}_{ij}^e + \dot{\gamma}_{ij}^p + \dot{\gamma}_{ij}^{th} \\ \dot{\kappa}_{ij} &= \dot{\kappa}_{ij}^e + \dot{\kappa}_{ij}^p \end{aligned} \quad (13)$$

Thermal strain rates can be expressed as $\dot{\gamma}_{ij}^{th} = \alpha \dot{T} \delta_{ij}$, where α is the thermal expansion coefficient. For the calculation of the plastic strain rate we first define a Drucker-Prager yield function $F = F(\tau_{ij}, \sigma_{ij}, \gamma^p, \varepsilon_v^p)$ which we assume to be dependent on the first and second stress tensor invariants, and the deviatoric and spherical parts of the accumulated plastic strain tensor ($\gamma^p, \varepsilon_v^p$). Analytical derivation of the derived relationships for the specific material is given in [17]. A more complete approach in a thermodynamical framework that takes into account grain breakage and the consequent evolution of the internal lengths can be found in [2].

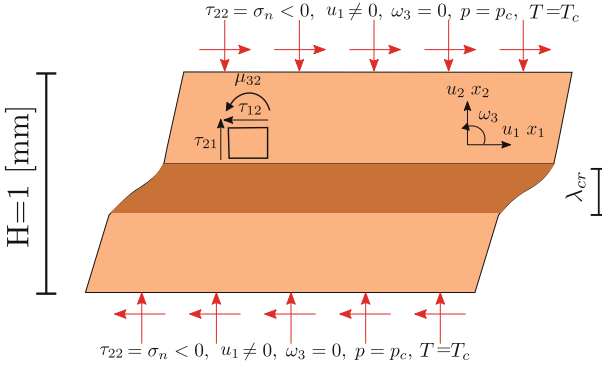


Fig. 1. 1D shearing of a Cosserat layer under constant vertical normal stress, under isothermal ($T = 0$) and drained conditions ($p = p_c$) corresponding to a mature saturated gouge layer.

4 Shearing of a Mature Fault Under Variable Slip Velocities

In this paper, we consider the shearing of a Cosserat layer with different slip velocities. The analysis is done in two steps with a slow slip velocity at the start and a fast slip at the second step. A 1D model of a Cosserat layer was used where shear displacement was applied to the surface of the layer while rotations were blocked at both ends, (see Fig. 1). The layer was discretized using 80 mixed type finite elements, with quadratic shape functions for the displacement field u_i and linear shape functions for the rotations ω_i . Furthermore, reduced integration scheme was used for displacement field. These element parameters were taken as a result of an investigation of different shape functions and number of Gauss points that was performed in previous work [23]. The mesh characteristics are summarized in Table 2. The Cosserat material properties used to describe a mature fault in the seismogenic zone are summarized in Table 3 where a high value for the Drucker-Prager friction coefficient μ has been used and path averaged values for λ^* , β^* were considered as proposed in [19] (Table 1).

The value of the Drucker-Prager friction coefficient is taken equal to $\mu = 0.5$. For the mature fault gouge geomaterial the friction coefficient corresponds to a friction angle $\phi = 21^\circ$ when we match the Drucker-Prager to the Mohr-Coulomb yield criterion in a compression triaxial test. Thus, the predicted yield limit for the fault friction during simple shear of the fault gouge is realistic. The dilatancy coefficient in the plastic potential of our analyses is set to $\beta = 0$. This corresponds to a mature fault gouge, which has reached the critical state, and thus only shear deformation along the fault plane can occur.

To illustrate the role of seismic slip velocity in the post peak behaviour of the fault we apply two different shear programs to the model at hand. First we implement a three step procedure described in 4.2 which includes qualitatively, consolidation of the layer to the stresses and pressure at a depth representative

Table 1. Loading program for the analyses performed using the three step procedure.

STEP		Slip δ mm	Slip velocity $\dot{\delta}$ m/s		
0	Consolidation	–	–		
1	Shear	5	0.01		
2	Shear	5	0.01	0.1	1.0

Table 2. Mesh properties of the problem.

	u_i	ω_i
Element type	Quadratic	Linear
Integration scheme	Reduced	Full
Number of elements	80	

of the seismogenic zone (~ 7 km), followed by slow shear of the layer and then by fast shear for a shear slip of 10 mm at each stage. The second program in Sect. 4.3 involves initial consolidation and then shear with constant slip velocity ranging from as slow as 0.01–1.0 m/s for a total of 100 mm of seismic slip.

Table 3. Material parameters of a mature fault at the seismogenic depth [see 17, 19].

Parameters	Values	Properties	Parameters	Values	Properties
K	20×10^3	MPa	μ	0.5	–
G	10×10^3	MPa	β	0	–
G_c	5×10^3	MPa	λ^*	13.45×10^{-5}	$/^\circ\text{C}$
L	10^3	MPa mm ²	β^*	8.2×10^{-5}	MPa ⁻¹
M	1.5	MPa mm ²	ρC	2.8	MPa/ $^\circ\text{C}$
M_c	1.5	MPa mm ²	c_{hy}	12.0	mm ² /s ²
R	0.01	mm	c_{th}	1.0	mm ² /s ²
σ_n	200	MPa	α_s	10^{-5}	$/^\circ\text{C}$
p_0	66.67	MPa	χ	12×10^{-15}	m ²

4.1 The Question of Large Displacements

Before we begin describing the loading programs used in the analyses, we need to address the question of large deformations since our analyses reach displacements far greater than the 1D model's geometrical dimensions. Our application involves pure shearing of the layer and therefore the displacement derivatives with respect to x_2 axes are neglected. We notice that the displacement parallel

to the vertical direction is close to zero ($u_1 = 0$). This is because no additional loading occurs in the vertical direction during shearing and from the plastic potential we have that for a mature fault the dilatancy angle is zero ($\beta = 0$). Thus only the thermal expansion remains. We consider the thermal expansion and compressibility coefficients to be very small so that in the observed temperature and pressure range their effects are minimal. Therefore the deformation gradient tensor F can be written as:

$$F = \begin{bmatrix} \frac{\partial x_1}{\partial X_1} & \frac{\partial x_1}{\partial X_2} \\ \frac{\partial x_2}{\partial X_1} & \frac{\partial x_2}{\partial X_2} \end{bmatrix} = \begin{bmatrix} 1 + \frac{\partial u_1}{\partial X_1} & \frac{\partial u_1}{\partial X_2} \\ \frac{\partial u_2}{\partial X_1} & 1 + \frac{\partial u_2}{\partial X_2} \end{bmatrix} \approx \begin{bmatrix} 1 & 0 \\ \frac{\partial u_1}{\partial X_1} & 1 \end{bmatrix} \quad (14)$$

From the above one can deduce that $\det F = 1$. Therefore no volume change takes place during shearing. This conclusion is supported also by the numerical findings in which the volumetric strain is adequately small $\varepsilon_v < 0.005$. To account for any effects that large displacements may introduce to our model we have also run a series of analyses based on an Arbitrary Lagrangian Eulerian (ALE) method where at every iteration we update the new mesh position. The change in the mesh is kept at every converged increment otherwise the cumulative change is discarded and the procedure starts a new.

4.2 Three Step Shearing Procedure

During this procedure the layer is first consolidated by applying a hydrostatic total stress of σ_n and water pressure p_c . Following this the layer is sheared with varying slip velocity $\dot{\delta}$ in two steps. At each step a target displacement δ of 5 mm at each end is reached for a total of 10 mm at the end of the analysis. The shear velocity $\dot{\delta}$ at the first step is 0.01 m/s while for the final step different analyses were run in which shear velocity varies ranging from 0.01 to 1 m/s. The details of the loading program are presented in Table 1. In the left part of Fig. 2 we compare the different τ, δ responses for the different velocities applied at the final step of the analyses. In the right part of Fig. 2 the profiles of strain localization rate $\dot{\lambda}$ over the layer's height are plotted. We observe that the increase of slip velocity $\dot{\delta}$ has a weakening effect on the $\tau - \delta$ diagram as observed also by Rattetz et al. [16, 17]. This happens due to the fact that a faster increase in the heat production term of Eq. 9 leads to an increase in the thermal pressurization term of Eq. 10 which increases pressure and due to the application of Terzaghi principle $\sigma^{eff} = \sigma_n + p$, ($p > 0$ water pressure, $\sigma^{eff}, \sigma_n > 0$ in tension), pressure drops faster intensifying the weakening.

The increase of slip velocity leads also to narrower localization zones, which are in agreement with the steeper post-peak response observed in τ, δ diagrams. We observe though that the model does not present an increase in apparent shear stress τ due to the velocity stepping, as it would be expected from a rate and state friction model [5]. Adopting rate and state friction as a reference, this means that our model misses some necessary physics at the microscale.

Finally, we investigate the influence of the boundary conditions of pressure and temperature to the behaviour of the problem. In the left part of Fig. 3 we present the $\tau - \delta$ curves, for slip velocity at the final step of the analysis of $\dot{\delta} = 1$ m/s, for Adiabatic-Undrained, Isothermal-Drained, Isothermal-Undrained, Adiabatic-Drained conditions. We observe that undrained boundary conditions influence the response the most as they tend to follow on the solution of uniform adiabatic undrained shear [9] for small slip velocities $\dot{\delta} = 0.01$ m/s. The difference at the peak strength between drained and undrained conditions has to do with the frequency our algorithm saves the output as well as the time increment used by the analysis. In the right part of Fig. 3 we present the plastic strain-rate profiles $\dot{\lambda}$ for different boundary conditions applied at the end of the analysis. We observe that for the given seismic slip of 10 mm, localization width is dependent on the seismic slip velocity applied and not on the boundary conditions.

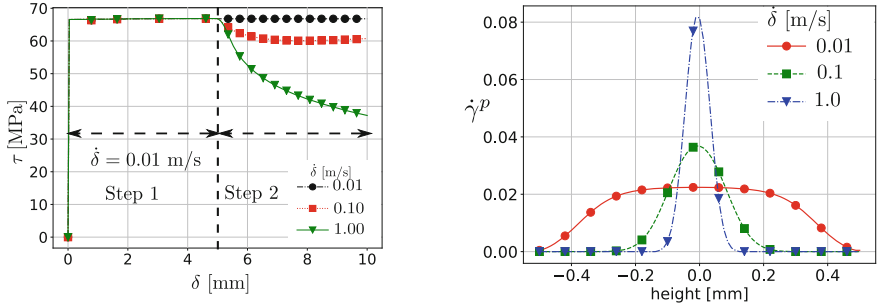


Fig. 2. Left: $\tau - \delta$ response of the layer for different slip velocities $\dot{\delta}$ applied (velocity stepping). We observe that as the shearing rate increases, the softening behaviour becomes more pronounced as a result of smaller localization widths due to the smaller characteristic diffusion time. Right: Profiles of strain localization rate inside the layer for different slip velocities $\dot{\delta}$ applied at the end of the analysis. Higher shearing velocities correspond to more localized plastic strain rate $\dot{\gamma}^p$ profiles.

4.3 Two Step Shearing Procedure

To better illustrate the dependence of the fault behaviour to the velocity of seismic slip $\dot{\delta}$, we run a second part of analyses for the case of isothermal drained conditions in which the intermediate part of slow shear velocity has been omitted and the fault model is immediately subjected to fast slip velocity rates after initial consolidation. Furthermore, the target seismic displacement δ has been increased to 100.0 mm. We aim that way to examine in more detail the fault's response under displacement scales commonly observed in nature. Table 4 summarizes the two step shearing procedure followed.

In the left part of Fig. 4 we present the shear stress with seismic slip on top of the layer $\tau - \delta$ response for different values of seismic slip velocity $\dot{\delta}$. It can

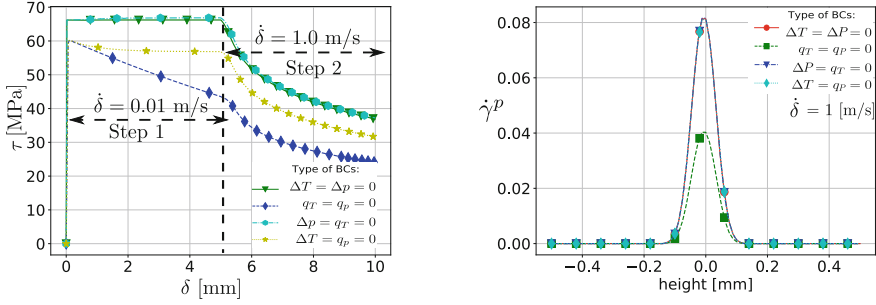


Fig. 3. Left: $\tau - \delta$ response of the layer for different boundary conditions applied. An envelope is created between Isothermal drained ($\Delta T = \Delta P = 0$) and Adiabatic-Undrained ($q_T = q_p = 0$) conditions. At the slow slip part of the analysis in the case of adiabatic undrained boundary conditions, thermal pressurization is present from the beginning. In this case, the initial stress at the start of the fast shear is lower and thus the stress drop is smaller. Right: Profiles of strain localization rate inside the layer for different boundary conditions. Since Cosserat material parameters and coseismic slip velocity $\dot{\delta}$ remain the same in all cases, the localization width does not change.

Table 4. Loading program for the analyses performed using the two step procedure.

Step	Height H mm	Slip δ mm	Slip velocity $\dot{\delta}$ m/s
0 Consolidation	1	–	–
1 Shear		100.0	{0.01, 0.05, 0.1, 0.25, 0.50, 0.75, 0.90, 1.0}
0 Consolidation	1	–	–
1 Shear		1000.0	1.0
0 Consolidation	1	–	–
1 Shear		1000.0	0.5
0 Consolidation	2	–	–
1 Shear		1000.0	0.5

be clearly seen from the results that two behaviours are present depending on the shear velocity. If the slip velocity is small then the layer accommodates the heat produced from the plastic work during yielding of the material and both heat and pressure diffuse efficiently away from the yielding zone which has a comparatively large localization width l_{loc} as shown in the right part of Fig. 4. As slip velocity increases the post peak softening response is seen in larger parts of the analysis before eventually diffusion dominates and peak shear strength is restored. However, shear strength is only partially restored for the analyses of large shear velocities. The right part of Fig. 4 shows the evolution of the shear band width for the different seismic slip velocities. In order to estimate the localization width in each case a curve according to Eq. (15) described in [19]

was selected for fitting.

$$\dot{\lambda} = A + \frac{B}{\sqrt{1\pi D}} \exp \left[-\frac{1}{2} \left(\frac{y - C}{D} \right)^2 \right]$$

$$l_{loc} = 2\sqrt{2 \ln(2) D} \quad (15)$$

It is clear that large velocities lead to narrower localization widths l_{loc} . We observe that for large velocities localization width is not monotonously decreasing, but rather it exhibits some noise as shearing progresses. This has to do with the fact that the instability exhibited here by the material is a travelling instability. This can be seen in the τ, δ response where a periodic increase and loss of strength is observed in the post peak response for all velocities above 0.01 m/s. This jerky behaviour can be responsible for higher frequency instabilities during seismic slip and enhance the frequency content of an earthquake event (see [31]).

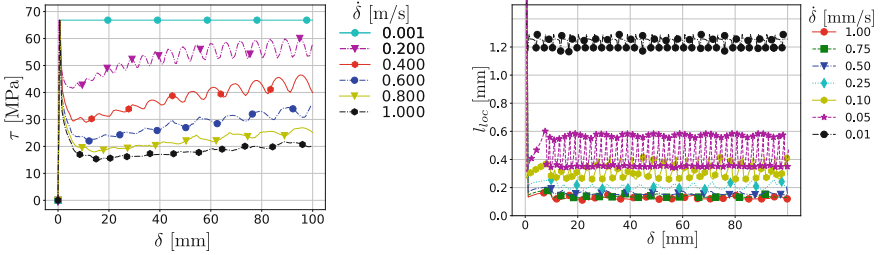


Fig. 4. Left: $\tau - \delta$ response of the layer for different velocities. Isothermal, drained boundary conditions $\Delta T = \Delta P = 0$ are applied. Frictional strength regain is observed due to the diffusion at the boundaries. The frictional response presents oscillations due to the travelling plastic strain rate instability. A smaller residual friction value is achieved. Right: $l_{loc} - \delta$ response of the localization width inside the layer for different boundary shear velocities applied at the boundaries. We notice that the localization width is oscillating for the small to intermediate range of shear velocities $\dot{\delta} = 0.01 - 0.25$ m/s. This is due to the interaction between the diffusion lengths of pressure and temperature.

4.4 Application with Seismic Slip $\delta = 1$ m and Seismic Slip Velocity $\dot{\delta} = 1$ m/s

In order for the observed oscillations to fully develop in amplitude for the analyses with high slip rate $\dot{\delta}$ we apply a very large shear displacement. Figure 5 presents the τ, δ response for a slip velocity $\dot{\delta}$ of 1 m/s and an applied slip $\delta = 1$ m. As can be seen from the above analysis the shear strength of the layer is eventually oscillating around a new residual strength value which is smaller than the original peak strength. The right part of Fig. 6 shows the profiles of plastic strain

rate $\dot{\lambda}$, and accumulated plastic strain γ^p at the end of the analysis. It is clear that the shear band travels across the material since the accumulated plastic strain profile is bigger in width than the localization width of the instability. This is one major difference compared to small slip rates, which our analyses under large displacements allowed to highlight, where the layer regains all of its peak strength in the steady state as shown in Fig. 4. Finally the left part of Fig. 6 presents the profiles of Temperature T and pressure p at the end of the analysis. We observe that the temperature reached is much higher than the one required for the onset of melting for the minerals present in the seismogenic zone [19]. This has to do with the relatively high Drucker-Prager friction coefficient μ used in our analyses. A moderate value of $\mu=0.25$ would roughly halve the temperature observed. This does not preclude though other mechanisms, such as chemical effects [28,30], that might become dominant after thermal pressurization becomes impossible.

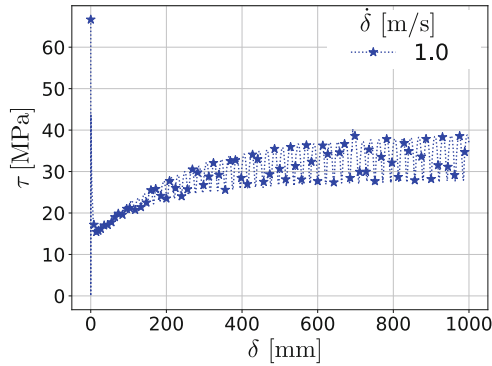


Fig. 5. Evolution of τ_{21} with slip distance δ . We observe that after sufficient time has passed the oscillations have stabilized in amplitude and frequency partially recovering the layer's initial shear strength.

5 Conclusions

In this paper the effect of slip velocity during shearing of a fault was investigated taking large displacements into account. Shear strength τ was plotted against coseismic slip displacement on top of the fault gouge layer δ for a large range of slip velocities $\dot{\delta}$ and target displacements. Although the slips applied are enormous compared to the size of the model, because shear is applied without significant changes in the normal strains of the model $\varepsilon_v < 5 * 10^{-3}$, the Jacobian of the deformation is close to unity. Therefore, the influence of large displacements leading to geometry changes is expected to be negligible. From the results of Sects. 4.2 and 4.3 it is clear that THM couplings induce softening

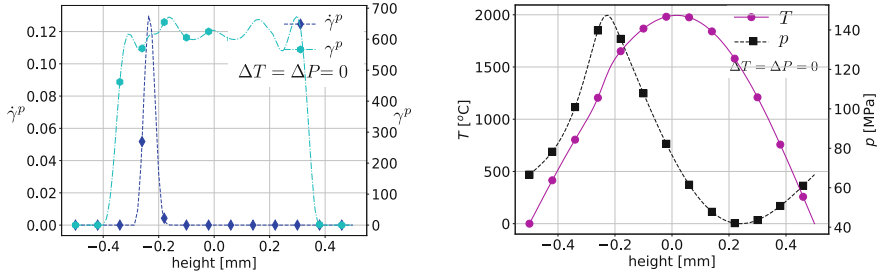


Fig. 6. Left: Profiles of shear strain rate and accumulated plastic shear strain $\dot{\gamma}^p, \gamma^p$ at the end of the analysis for applied slip $\delta = 1$ m and slip rate $\dot{\delta} = 1$ m/s. Since the two profiles differ, we conclude that the localization oscillates inside the layer. Localization does not travel the whole of the layer due to the boundary conditions applied. Right: Profiles of pressure and temperature p, T at the end of the analysis for applied slip $\delta = 1$ m and slip rate $\dot{\delta} = 1$ m/s. Diffusion at the boundaries leads to extremely high values of temperature $T = 2000$ °C.

to the model. This softening is not of a mechanical source, rather it is produced by the pressure increase in the fault gouge due to thermal pressurization of the material. The softening branch in the material is steeper for higher slip velocities [16, 17]. This effect can also be seen in the localization width, where higher velocities lead to narrower localization as expected by the τ, δ response.

Using an adaptive Lagrangian Eulerian (ALE) method that updates the mesh position at each converged increment, we have increased the induced seismic slip δ to values observed in nature. Thus, we show that the softening branch is only present at the start of the slip, while the localization instability region travels across the fault layer. This increases the effects of diffusion, therefore, increasing the strength of the fault. The fault friction, τ , oscillates around a residual value, which is dependent on the slip velocity. This indicates the existence of a limit cycle due to thermal pressurization effects. This jerky behaviour is similar to the Portevin Le Chatelier (PLC) phenomenon (see [7, 11]). This type of instability can enhance the frequency content of earthquakes due to instabilities of small length scales (see [31]).

Acknowledgments. The two authors would like to acknowledge the support of the European Research Council (ERC) under the European Union’s Horizon 2020 research and innovation program (Grant agreement no. 757848 CoQuake).

References

1. Andrews, D.J.: Rupture dynamics with energy loss outside the slip zone. *J. Geophys. Res. Solid Earth* **110**(1), 1–14 (2005). ISSN 21699356. 10.1029/2004JB003191
2. Collins-Craft, N.A., Stefanou, I., Sulem, J., Einav, I.: A cosserat breakage mechanics model for brittle granular media. *J. Mech. Phys. Solids*, p. 103975 (2020)
3. Coussy, O.: Poromechanics. Wiley (2004). <https://doi.org/10.1002/9780470710388>

4. de Borst, R., Sluys, L.J.: Localisation in a Cosserat continuum under static and dynamic loading conditions. *Comput. Methods Appl. Mech. Eng.* **90**(1–3), 805–827 (1991). ISSN 00457825. [https://doi.org/10.1016/0045-7825\(91\)90185-9](https://doi.org/10.1016/0045-7825(91)90185-9)
5. Dieterich, J.H.: Earthquake nucleation on faults with rate-and state-dependent strength. *Tectonophysics* **211**(1–4), 115–134 (1992). [https://doi.org/10.1016/0040-1951\(92\)90055-B](https://doi.org/10.1016/0040-1951(92)90055-B)
6. Godio, M., Stefanou, I., Sab, K., Sulem, J.: Multisurface plasticity for cosserat materials: plate element implementation and validation. *Int. J. Numer. Methods Eng.* **108**(5), 456–484 (2016). <https://doi.org/10.1002/nme.5219>
7. Hähner, P., Ziegenbein, A., Rizzi, E., Neuhäuser, H.: Spatiotemporal analysis of Portevin-Le Chatelier deformation bands: theory, simulation, and experiment. *Phys. Rev. B Condens Matter Mater. Phys.* **65**(13), 1–20 (2002). ISSN 1550235X. <https://doi.org/10.1103/PhysRevB.65.134109>
8. Kanamori, H., Brodsky, E.E.: The physics of earthquakes. *Rep. Progr. Phys.* **67**(8), 1429–1496 (2004). ISSN 00344885. <https://doi.org/10.1088/0034-4885/67/8/R03>
9. Lachenbruch, A.H.: Frictional heating, fluid pressure, and the resistance to fault motion. *J. Geophys. Res. Solid Earth* **85**(B11), 6097–6112 (1980). <https://doi.org/10.1029/JB085iB11p06097>
10. Lemaitre, J., Chaboche, J.-L., Benallal, A., Desmorat, R.: *Mécanique des matériaux solides-3e éd.* Dunod (2020)
11. Mazière, M., Besson, J., Forest, S., Tanguy, B., Chalons, H., Vogel, F.: Numerical aspects in the finite element simulation of the Portevin-Le Chatelier effect. *Comput. Methods Appl. Mech. Eng.* (2010). ISSN 00457825. <https://doi.org/10.1016/j.cma.2009.11.004>
12. Mühlhaus, H.-B., Vardoulakis, I.: The thickness of shear bands in granular materials. *Géotechnique* **38**(2), 331 (1988). ISSN 0016-8505. <https://doi.org/10.1680/geot.1988.38.2.331b>
13. Needleman, A.: Material rate dependence and mesh sensitivity in localization problems. *Comput. Methods Appl. Mech. Eng.* **67**(1), 69–85 (1988). [https://doi.org/10.1016/0045-7825\(88\)90069-2](https://doi.org/10.1016/0045-7825(88)90069-2)
14. Nicchio, M.A., Nogueira, F.C., Balsamo, F., Souza, J.A., Carvalho, B.R., Bezerra, F.H.: Development of cataclastic foliation in deformation bands in feldspar-rich conglomerates of the rio do peixe basin, ne Brazil. *J. Struct. Geol.* **107**, 132–141 (2018). <https://doi.org/10.1016/j.jsg.2017.12.013>
15. Puzrin, A., Houlsby, G.: On the thermodynamics of porous continua. Report No OUEL, 2235 (01) (2001). https://doi.org/10.1007/978-3-540-35724-7_3
16. Rattetz, H., Stefanou, I., Sulem, J.: The importance of Thermo-Hydro-Mechanical couplings and microstructure to strain localization in 3D continua with application to seismic faults. Part I: theory and linear stability analysis. *J. Mech. Phys. Solids* **115**, 54–76 (2018a). ISSN 00225096. <https://doi.org/10.1016/j.jmps.2018.03.004>
<https://doi.org/10.1016/j.jmps.2018.03.004>
17. Rattetz, H., Stefanou, I., Sulem, J., Veveakis, M., Poulet, T.: The importance of Thermo-Hydro-Mechanical couplings and microstructure to strain localization in 3D continua with application to seismic faults. Part II: numerical implementation and post-bifurcation analysis. *J. Mech. Phys. Solids* (2018b). ISSN 00225096. <https://doi.org/10.1016/j.jmps.2018.03.003>
18. Rattetz, H., Stefanou, I., Sulem, J., Veveakis, M., Poulet, T.: Numerical analysis of strain localization in rocks with thermo-hydro-mechanical couplings using cosserat continuum. *Rock Mech. Rock Eng.* **51**(10), 3295–3311 (2018)
19. Rice, J.R.: Heating and weakening of faults during earthquake slip. *J. Geophys. Res. Solid Earth* **111**(B5) (2006). <https://doi.org/10.1029/2005JB004006>

20. Rice, J.R., Rudnicki, J.W., Platt, J.D.: Stability and localization of rapid shear in fluid-saturated fault gouge: 1. Linearized stability analysis. *J. Geophys. Res. Solid Earth* **119**(5), 4311–4333 (2014). <https://doi.org/10.1002/2013JB010710>
21. Sibson, R.: Fault rocks and fault mechanisms. *J. Geol. Soc.* **133**(3), 191–213 (1977)
22. Sibson, R.H.: Thickness of the seismic slip zone. *Bull. Seismol. Soc. Am.* **93**(3), 1169–1178 (2003). ISSN 0037-1106. <https://doi.org/10.1785/0120020061>. <https://doi.org/10.1785/0120020061>
23. Stathas, A., Stefanou, I.: Elastoplastic response of a cosserat continuum layer for application in fault mechanics. In: 12th HSTAM International Congress on Mechanics Thessaloniki, Greece, 22–25 Sept. 2019 (2019)
24. Stathas, A., Stefanou, I.: The role of viscous regularization in dynamical problems, strain localization and mesh dependency. *Comput. Methods Appl. Mech. Eng.* **388**, 114185 (2022)
25. Stefanou, I.: Numerical geolab (2021). <https://www.coquake.eu/>. Nantes, FR
26. Stefanou, I., Sulem, J., Vardoulakis, I.: Homogenization of interlocking masonry structures using a generalized differential expansion technique. *Int. J. Solids Struct.* **47**(11–12), 1522–1536 (2010). <https://doi.org/10.1016/j.ijsolstr.2010.02.011>
27. Stefanou, I., Sulem, J., Rattetz, H.: Cosserat approach to localization in geomaterials (2016). https://doi.org/10.1007/978-3-319-22977-5_10-1
28. Sulem, J., Famin, V.: Thermal decomposition of carbonates in fault zones: Slip-weakening and temperature-limiting effects. *J. Geophys. Res. Solid Earth* **114**(3), 1–14 (2009). ISSN 21699356. <https://doi.org/10.1029/2008jb006004>
29. Sulem, J., Stefanou, I.: Thermal and chemical effects in shear and compaction bands. *Geomech. Energy Environ.* **6**, 4–21 (2016). ISSN 23523808. <https://doi.org/10.1016/j.gete.2015.12.004>. <http://dx.doi.org/10.1016/j.gete.2015.12.004>
30. Sulem, J., Stefanou, I., Veveakis, E.: Stability analysis of undrained adiabatic shearing of a rock layer with cosserat microstructure. *Granular Matter* **13**(3), 261–268 (2011). <https://doi.org/10.1007/s10035-010-0244-1>
31. Tsai, V.C., Hirth, G.: Elastic impact consequences for high-frequency earthquake ground motion. *Geophys. Res. Lett.* **47**(5), 1–8 (2020). ISSN 19448007. <https://doi.org/10.1029/2019GL086302>
32. Vardoulakis, I.: Dynamic stability analysis of undrained simple shear on water-saturated granular soils. *Int. J. Numer. Anal. Methods Geomech.* **10**(2), 177–190 (1986). <https://doi.org/10.1002/nag.1610100206>
33. Cosserat Continuum Mechanics. LNACM, vol. 87. Springer, Cham (2019). <https://doi.org/10.1007/978-3-319-95156-0>
34. Viesca, R.C., Garagash, D.I.: Ubiquitous weakening of faults due to thermal pressurization. *Nat. Geosci.* **8**(11), 875–879 (2015). <https://doi.org/10.1038/ngeo2554>
35. Wang, W., Sluys, L., De Borst, R.: Viscoplasticity for instabilities due to strain softening and strain-rate softening. *Int. J. Numer. Methods Eng.* **40**(20), 3839–3864 (1997). [https://doi.org/10.1002/\(SICI\)1097-0207\(19971030\)40:20<3839::AID-NME245>3.0.CO;2-6](https://doi.org/10.1002/(SICI)1097-0207(19971030)40:20<3839::AID-NME245>3.0.CO;2-6)



Modelling of Hydraulic Fracturing in Rocks in Non-isothermal Conditions Using Coupled DEM/CFD Approach with Two-Phase Fluid Flow Model

M. Krzaczek^(✉), M. Nitka, and J. Tejchman

Gdańsk University of Technology, Gdańsk, Poland
marek.krzaczek@pg.edu.pl

Abstract. Shale rock is a strongly heterogeneous, discontinuous, and porous material. Under non-isothermal conditions, the movement of fluid in the pore and capillary system is strongly coupled with heat transfer. The process of the hydraulic fracture strongly depends on the rock saturation degree. An innovative DEM-based thermo-hydro-mechanical model was developed to track in detail the liquid/gas fractions in pores and cracks with respect to their different geometry, size, location, and temperature. A coarse 2D mesh was generated to create a fluid flow network and to solve the energy conservation equation. Finally, the importance of a fully coupled thermo-hydromechanical model is illustrated by the simulation of cold fluid injection during hydraulic fracturing in a rock matrix with different degrees of water saturation.

Keywords: Hydraulic fracturing · DEM-CFD · Heat transfer

1 Introduction

Most of physical phenomena in engineering problems occur under non-isothermal conditions. More-over, even if the physical system is initially in a state of thermodynamic equilibrium, the physical phenomena or chemical reactions that occur may lead to local temperature changes and, consequently, to heat transfer. Therefore, understanding heat transfer in particulate systems is of great interest to many scientific disciplines and engineering applications such as environmental science, chemical and food processing, geomechanics, and geological engineering. The need to take into account the effect of heat transfer becomes critical in the analysis of many multi-field problems in porous and fractured materials. Complex thermo-hydro-mechanical (THM) processes, including heat transfer, fluid flow, and material deformation occur simultaneously and are affected by many non-linear processes.

The most common approach in THM models is the continuous medium phenomena approach, which is based on a mathematical framework linking sets of equations to describe the laws of thermodynamics, solid mechanics, and hydraulics, e.g. the finite element implementations of such concepts [1–6]. Nonetheless, even though attractive

for macro-scale applications, continuum modeling approaches based on the finite element method (FEM) or the finite volume method (FVM) suffer critical computational and continuity limitations when applied to discontinuous and highly deformable media such as packed or fluidized beds and granular or fractured porous materials. In porous media with low porosity (less than about 15%), such as rocks, classical methods lead to huge problems with generating sufficiently fine mesh [7]. The problem increases when simulating the crack initiation and propagation process in porous materials with low porosity (e.g. shale rocks).

On the other hand, discrete approaches like, for instance, the discrete element method (DEM) [8] or the finite-discrete element method (FDEM) prove successful at modeling the behavior of these discrete systems. FDEM method was used by [9] to formulate a thermo-mechanical model for simulating thermal cracking of rock and by Yan et al. [10] to develop a 2D coupled thermal-hydro-mechanical model for describing rock hydraulic fracturing. The strength of DEM in modeling particulate systems opened up recent efforts to extend its predictive capabilities to meso- and micro-scale THM processes. Different approaches have been used to couple DEM with fluid flow and heat transfer models. Direct numerical simulations (DNS) can be used to couple TH processes with DEM. To solve governing equations, DNS models can use different numerical methods (e.g. FEM, FVM). Deen et al. [11] proposed immersed boundary implementation that does not require using any effective diameter of spherical discrete element. The method was dedicated to THM processes in dense fluid-particle systems. However, the proposed method was limited to invariant geometries, their topologies and relatively high porosity (porosity greater than that of rocks). In practice, DNS-DEM models are restricted to systems comprised of a smaller number of particles than CFD. Another approach is based on the lattice Boltzmann method (LBM) [12, 13]. LBM relies strongly on the accurate representation of solid-fluid boundaries which is difficult both numerically and computationally and leads to the same limitations as with DNS-DEM models.

To study THM processes with DEM in very dense fluid-particle systems with very low porosity (even below 5%) such as rocks, fluid flow and heat transfer models should be simplified to reduce computational costs and avoid numerical limitations. Most of the recently available DEM-based THM models separate the fluid flow in the reservoirs (pores, macropores, pre-existing cracks, etc.) and flow between the reservoirs. The assumption is that the fluid in the reservoirs is compressible while the fluid flowing between the reservoirs is incompressible. This concept of simplification was first introduced and developed in [14–16]. In most cases, a Poiseuille flow model in pipes or between two parallel plates is adopted to estimate mass flow rates. The pressure in the pores is calculated directly from the assumed equation of state [15, 16] or the solution of the Stokes equation [17, 18]. All models assume a single-phase fluid flow of a pure liquid or mixture. Tomac and Gutierrez [19] solved the energy conservation equation for each cell (reservoir) volume. The adopted energy conservation equation corresponded to the energy transport in the laminar flow of an incompressible fluid. Caulk et al. [20] proposed a more advanced DEM-based THM model. They proposed a 3D model based on the framework of the pore-scale finite volume (PFV) scheme initially proposed by Chareyre et al. [21] and extended by Scholtès et al. [22] for up-scaling compressible viscous flow and oriented toward dense grain packing applications.

The goal of the current paper is to demonstrate the DEM-based pore-scale thermal-hydro-mechanical model of two-phase fluid flow coupled with heat transfer in porous materials of very low porosity (e.g. rocks). Calculations were carried out with a 3D DEM model coupled with a 2D CFD and 2D heat transfer model that combined solid mechanics with fluid mechanics and heat transfer at the meso-scale. Previously, our coupled DEM/CFD model was successfully used to describe a hydraulic fracturing process in rocks with one- or two-phase laminar viscous two-phase fluid flow composed of a liquid and gas [23, 24].

The innovative elements of our DEM-based THM mesoscopic approach for modelling fluid flow and heat transfer as compared to other existing models in the literature are: the detailed tracking of water/gas fractions in pores regarding their varying geometry, size and location; an algorithm for automatic meshing and remeshing domains of solids and fluids to capture changes in geometry and their topology; the use of a coarse mesh of solid and liquid domains to generate a virtual fluid flow network (VPN) and solve energy conservation equation; adoption of the corrected Peng-Robinson equation of state for both fluid phases to study supercritical fluid flow (necessary for the study of THM processes in the hydrofracturing process); FVM was used to solve the energy conservation equation on a very coarse mesh of cells in both domains.

The current paper is structured as follows. After the introductory Sect. 1, a mathematical model of the DEM-based coupled thermal-hydro-mechanical approach is presented. Section 3 investigates gas-phase content influence on hydraulic fracture initiation and propagation. Finally, some concluding remarks are offered in Sect. 4.

2 Thermo-hydro-mechanical Model

The novel concept of the model is based on the assumption that two different domains coexist in a physical system: the 3D discrete (solid) domain and the 2D continuous (fluid) domain. Originally, the solid domain consists of one layer of 3D spherical elements while the fluid domain is two-dimensional (Fig. 1a).

Spheres are arranged in such a way that their gravity centres are located on a mid-plane (2D surface). The spheres are projected onto the plane to form circles (Fig. 1b). After projection, both the domains are discretized into a very coarse grid of cells (triangles) (Fig. 1b). Consequently, the equations of motion of discrete elements are solved in the 3D discrete domain and the equations of fluid flow are solved in the 2D fluid continuous domain (red colour in Fig. 1b) and heat transfer equations are solved in the 2D fluid and solid continuous domains (red and black colours in Fig. 1b).

2.1 DEM for Cohesive-Frictional Materials

DEM calculations were performed with the 3D spherical explicit discrete element open code YADE [25]. The method allows for a small overlap between two contacted bodies (the so-called soft-particle model). Thus, an arbitrary micro-porosity can be obtained in DEM wherein particles interact with each other during translational and rotational motions through a contact law and Newton's 2nd law of motion using an explicit time-stepping scheme [8]. In the model, a cohesive bond is assumed at the grain contact

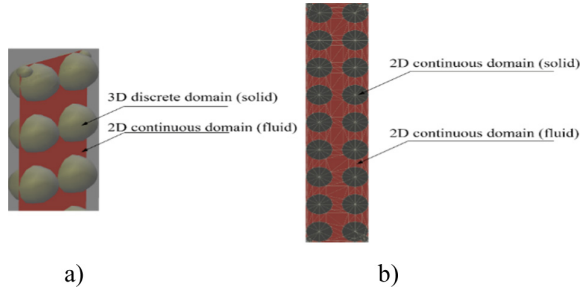


Fig. 1. Two domains coexisting in one physical system: (a) co-existing domains before projection and discretization, (b) solid and fluid domains after discrete elements projection and discretization (fluid domain in red colour and solid domain in black colour)

exhibiting brittle failure under the critical normal tensile load. The shear cohesion failure initiates contact slip and sliding obeying the Coulomb friction law under normal compression. Damage occurs if a cohesive joint between spheres disappears after reaching a critical threshold. If any contact between spheres after failure re-appears, the cohesion does not appear more. A simple local non-viscous damping is used [8] to accelerate convergence in quasi-static analyses. The material softening is not considered in the DEM model. The DEM model and its calibration were described in detail in [26, 27].

2.2 Fluid Flow Model

The general concept of a fluid flow algorithm using DEM was adopted from [14–16]. However, the model in the current paper [23, 24] significantly differs from this general concept. The pores, cracks and pre-existing cracks store now not only pressures but also phase fractions, fluids densities, energy, and temperature. An immiscible fluid was assumed in the multiphase fluid flow regime. The numerical algorithm can be divided into 5 main stages:

- (a) estimating the mass flow rate for each phase of fluid flowing through the cell faces (in channels surrounding VP) by employing continuity and momentum equations,
- (b) computing the phase fractions and their densities in VP by employing equations of state and continuity,
- (c) computing pressure in VP by employing the equation of state,
- (d) solving energy conservation equation in fluid and solids,
- (e) updating material properties.

This algorithm is repeated for each VP in VPN and each solid cell (stage ‘d’) using an explicit formulation.

2.3 Heat Transfer in Fluid

A homogeneous heat transfer model in multiphase fluid flow is assumed. For simplicity, incompressible and homogeneous fluid is assumed. The viscous dissipation of

energy is neglected. The energy conservation equation is shared among the phases in a homogeneous model, and is expressed in integral form:

$$\int_V \frac{\partial}{\partial t} (\rho_{eff} E) \cdot dV + \oint \nabla \cdot (\rho_{eff} \vec{v} E) \cdot d\vec{A} = \oint (\lambda_{eff} \nabla T) \cdot d\vec{A} + \int_V S_h, \quad (1)$$

where ρ_{eff} is the effective fluid density [kg/m^3], E is the total energy [J], t is time [s], v is the velocity [m/s], T is the temperature [K], λ_{eff} is the effective thermal conductivity of fluid [$\text{W}/(\text{mK})$] and S_h denotes the energy sources. Assuming an incompressible and laminar flow of a homogeneous fluid, the enthalpy h equation of state is:

$$h = \int_{T_{ref}}^T c_p dT, \quad (2)$$

where T_{ref} is the reference temperature [K] and c_p is specific heat in constant pressure [$\text{J}/(\text{kg}\cdot\text{K})$]. The effective fluid properties and velocity are computed by volume averaging over the phases. If the time derivative is discretized using backward differences and assuming that the total energy E is equal to the enthalpy h and applying the enthalpy h equation of state to Eq. 1, the energy conservation equation can be expressed in terms of temperature T :

$$\begin{aligned} T^{n+1} = T_{ref} + \frac{c_{p,eff}^n (T^n - T_{ref})}{c_{p,eff}^{n+1}} + \frac{\Delta t}{V \rho^n c_{p,eff}^{n+1}} \sum_f^{N_{faces}} \lambda_{eff} \nabla T_f^n \cdot \vec{A}_f \\ - \frac{\Delta t}{V \rho^n c_{p,eff}^{n+1}} \sum_f^{N_{faces}} \rho_f^n \vec{v}_f^n c_{p,eff}^n (T_f^n - T_{ref}) \cdot \vec{A}_f + \frac{\Delta t}{\rho^{n+1} c_{p,eff}^{n+1}} S_h, \end{aligned} \quad (3)$$

where N_{faces} is the number of faces enclosing the cell, T_f is the value of T on the face f , $\rho_f v_f \bullet A_f$ is the mass flux through the face f , A_f is the area vector of the face f , ∇T_f is the gradient of T at the face f , V is the cell volume and S_h is related to the internal enthalpy source of diffusive energy [W/m^3] of heat transferred by diffusion along the channel S2S. The FVM method is used to solve the energy conservation equation (Eq. 3).

2.4 Heat Transfer in Solids

Assuming no convective energy transfer, no internal heat sources and constant density ρ_s , in solid regions, the energy conservation equation has the following integral form:

$$\rho_s \int_V \frac{\partial E}{\partial t} \cdot dV = \oint (\lambda_s \nabla T) \cdot d\vec{A}, \quad (4)$$

where E is the total energy and is equal to enthalpy h , ρ_s is the density of solid [kg/m^3], λ_s is the solid thermal conductivity [$\text{W}/(\text{mK})$], T_{ref} is the reference temperature and c_p

is the specific heat in constant pressure. Equation 4 is applied to each cell (triangle) in the solid domain. The discretization of Eq. 4 yields for a given cell

$$T^{n+1} = T^n + \frac{\Delta t}{V \rho_s c_p} \sum_f^{N_{faces}} \lambda_s \nabla T_f^n \cdot \vec{A}_f. \quad (5)$$

The FVM method is used to solve Eq. 5.

3 Model Validation

The DEM-based THM model was validated by comparing the numerical findings with the analytical solution for the classic 1D heat transfer problem (diffusion) in the cohesive granular bar specimen

$$\frac{\partial T}{\partial t} = \alpha_{eqv} \frac{\partial^2 T}{\partial x^2}, \quad (6)$$

where α_{eqv} is the effective thermal diffusivity [m²/s] and t is the time [s]. The initial and boundary conditions for the analytical solution of the 1D heat equation are as follows

$$T(x, 0) = 323.16[K] \quad x \in (0, L). \quad (7)$$

$$T(0, t) = T(L, t) = 293.16[K] \quad t \geq 0, \quad (8)$$

where L is the length of the bar. The calculations were performed using a bonded granular bar specimen with a random distribution of spheres (Fig. 2a). The effective thermal diffusivity α_{eqv} was calculated for the volume-averaged phase properties. The initial and boundary conditions are shown in Fig. 2b (the bar specimen was cooled down by 30 K). The effective thermal diffusivity and boundary conditions imitated heat transfer by diffusion only in the equivalent solid bar, made of a fictitious homogeneous material with effective thermal properties. The single-phase flow of water was assumed. The numerical results agree with the analytical solution. After 400 s of cooling, the largest difference between numerical and analytical values was 0.52 K (Fig. 3).

4 Gas-Phase Content Influence on Hydraulic Fracture Initiation and Propagation

Our DEM-based THM mesoscopic approach to fluid flow and heat transfer modeling can recreate shale rock with faults, pre-existing fractures, bedding layers, etc. The model enables the reconstruction of real samples of shale rocks on the basis of microcomputer tomography (micro-CT). However, for simplicity and clarity, a small 30 × 30 mm specimen imitating shale rock matrix was chosen to investigate the effect of the initial gas-phase content on the initiation and propagation of the hydraulic fracture under non-isothermal conditions.

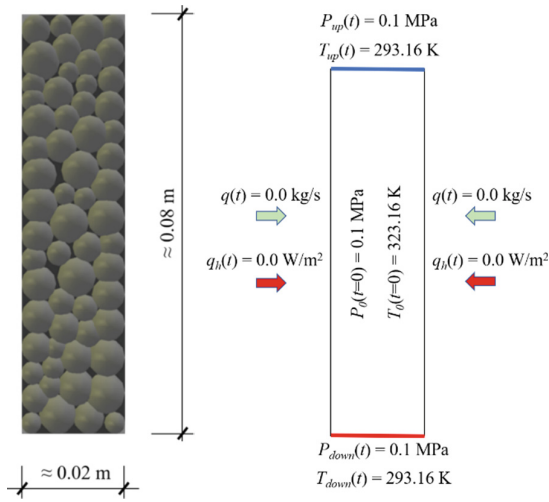


Fig. 2. Bonded granular specimen imitating shale rock: (a) specimen, (b) boundary and initial conditions

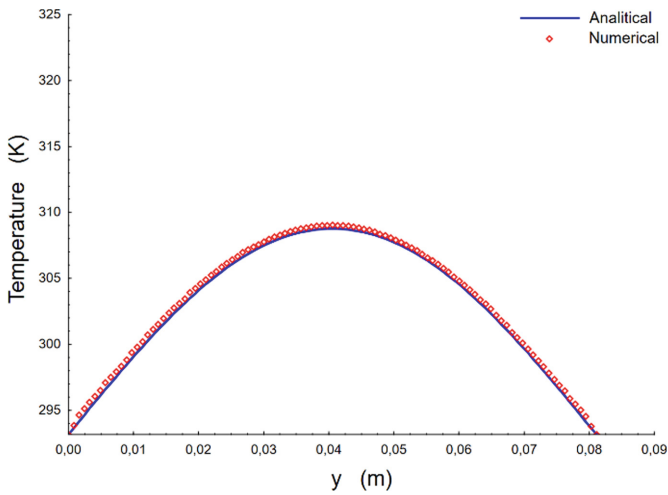


Fig. 3. Temperature along the vertical center line of the sample of the cohesive granular bar in Fig. 2a after 400 s of cooling

The specimen porosity was 5%. The fluid injection point was located in the middle of the lower boundary. Four cases with different contents of the gas phase were considered: (a) 0% of gas, (b) 20% of gas, (c) 40% of gas and (d) 60% of gas. It was assumed that the fluid was heated in the wellbore from 293.16 K to 323.16 K before being injected into the rock. The initial rock temperature was assumed to be 343.16 K, and the initial pressure was 20 MPa (Fig. 4). The pressure of the fluid being injected was 90 MPa. The rock matrix (discrete elements) heat transfer coefficient was assumed at the level of

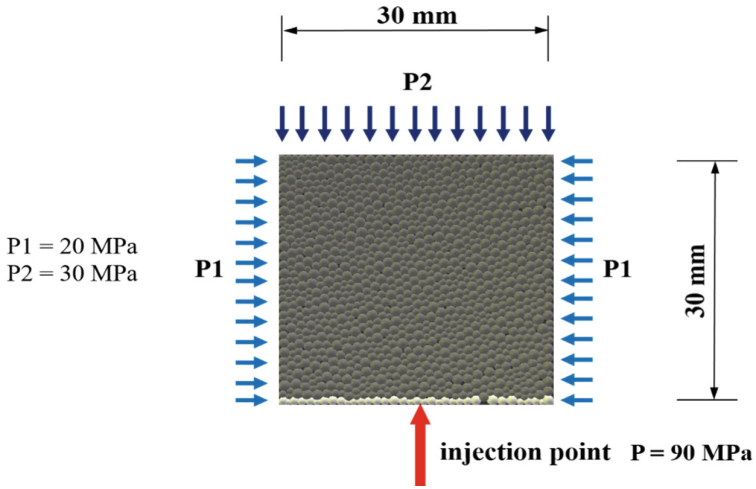


Fig. 4. Bonded granular specimen imitating shale rock with boundary and initial conditions

3.5 W/(m • K), while the gas phase heat transfer coefficient was 0.0262 W/(m • K) and the liquid phase heat transfer coefficient was 0.6 W/(m • K). The spheres were not fixed, except for the spheres along the lower boundary. They were fixed (zero displacement and rotation) in the vertical direction. The DEM-THM model was calibrated according to the procedure presented in [24]. The permeability of the rock specimen was $2.04 \cdot 10^{-17} \text{ m}^2$.

Initial Gas Content 0%

In the case 'a', the initial gas content was 0%. The rock specimen was fully saturated and there was only single-phase fluid flow. The cold fluid was injected into the injection point. The hydraulic fracture initiated and propagated for 1.8 ms to reach the upper boundary of the specimen (Fig. 5a). It can be observed that the injection fluid heats up to the initial temperature of the specimen very quickly and very close to the injection point. Such rapid heating of the fluid is due to the fact that the rock specimen is completely filled in with water, which is an almost incompressible fluid. Therefore, a very small amount of injected water was necessary to penetrate the specimen and increase the fluid pressure above the rock strength limit. As a consequence, the injected water heated up very quickly to the initial temperature (343.16 K) of the rock specimen (Fig. 5b).

Initial Gas Content 20%

In the case 'b', the initial gas content was 20%. The rock specimen was partially filled with water and partially with gas (humid air). There was a two-phase fluid flow in the specimen. The hydraulic fracture initiated and propagated for 9.6 ms to reach the upper boundary of the specimen (Fig. 6). In contrast to the case 'a', an increase in fluid pressure was due to compression of the gas phase by increasing the water content. More water had to be injected to increase the fluid pressure above the rock's strength limit. This resulted in an increase in advection as compared to the case 'a'. The fluid temperature increased to 338.9 K at the top of the hydraulic fracture. The shape of the hydraulic fracture was different than in the case 'a'. A small branching of a hydraulic fracture was formed.

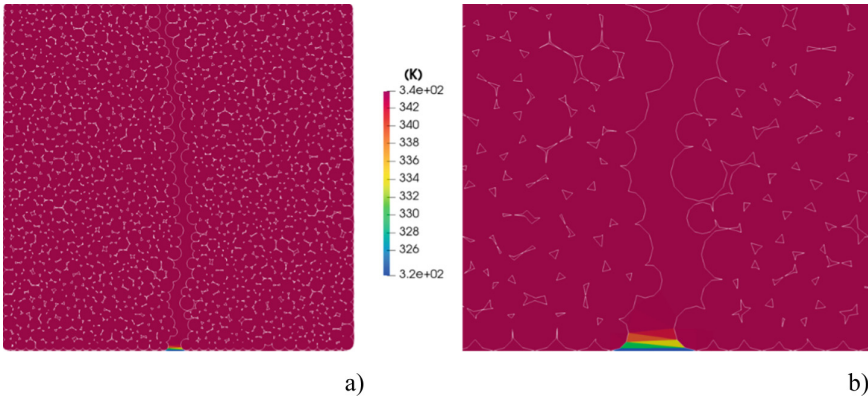


Fig. 5. Temperature distribution in bonded granular rock specimen after 1.8 ms: (a) entire specimen and (b) vicinity of injection point

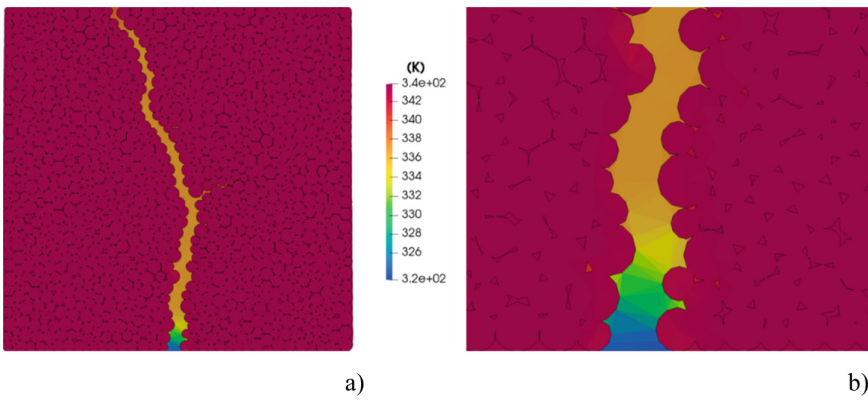


Fig. 6. Temperature distribution in bonded granular rock specimen after 9.6 ms: (a) entire specimen and (b) vicinity of injection point

Initial Gas Content 40%

The rock specimen was partially filled with water and partially with gas (humid air). There was a two-phase fluid flow in the specimen. The hydraulic fracture initiated and propagated for 18.1 ms to reach the upper boundary of the specimen (Fig. 7). As in the case ‘b’, an increase in fluid pressure was caused by compression of the gas phase by increasing the water content. The fluid temperature increased to 332.4 K at the top of the hydraulic fracture and was 6.5 K lower than in the case ‘b’.

In contrast to the case ‘b’, the shape of the hydraulic fracture was different and there was no branching. The fluid temperature in the vicinity of the injection point was lower than in the case ‘b’. The longer hydraulic fracture propagation time and the lower fluid temperature resulted in significant cooling of the rock specimen in contact with the fluid

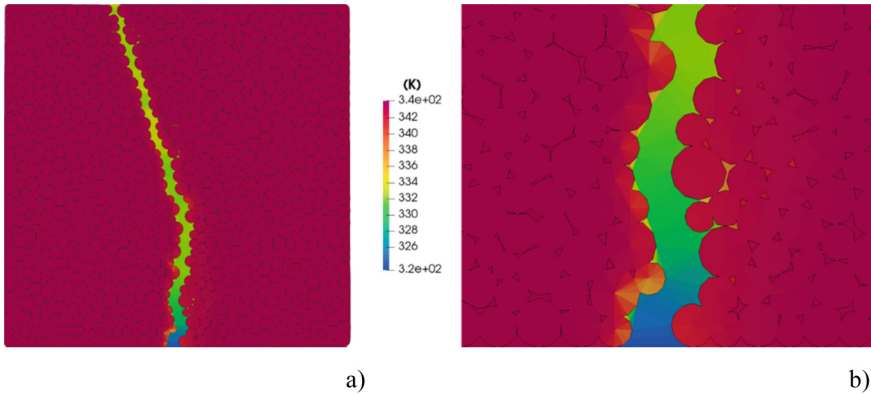


Fig. 7. Temperature distribution in bonded granular rock specimen after 18.1 ms: (a) entire specimen and (b) vicinity of injection point

in the hydraulic fracture in the vicinity of the injection point. The temperature of the rock specimen in the vicinity of the injection point dropped by 6.1 K.

Initial Gas Content 60%

The rock specimen was partially filled in with water and partially with gas (humid air). There was a two-phase fluid flow in the specimen. The hydraulic fracture initiated and propagated for 24.8 ms to reach the upper boundary of the specimen (Fig. 8). An increase in fluid pressure was again caused by compression of the gas phase by increasing the water content. The fluid temperature increased to 338.1 K at the top of the hydraulic fracture and was 5.7 K higher than in the case 'c'. In contrast to the cases 'b' and 'c', the length of the hydraulic fracture filled with a fluid of relatively low temperature (not exceeding 327.8 K) reached about 45% of its total length. Then, the temperature of the fluid quickly increased up to 337.2 K to reach 338.1 K at the top of the hydraulic fracture. The longer hydraulic fracture propagation time and the lower fluid temperature resulted in significant cooling of the rock specimen in contact with the fluid in the hydraulic fracture at the vicinity of the injection point. The temperature of the rock specimen near the injection point dropped by 8.3 K which was 2.2 K more than in the case 'c'.

5 Conclusions

The paper presents a novel DEM-based pore-scale thermal-hydro-mechanical model of two-phase fluid flow coupled with heat transfer in porous materials of very low porosity (shale rocks). The hydraulic fracturing process was tested in a cohesive granular specimen with an initial porosity of 5% for various saturation degrees. The results of the limited numerical research allowed the following preliminary conclusions to be drawn:

- the more gas phase in the rock specimen, the slower the hydraulic fracture propagates,
- the more gas phase in the rock matrix, the more intense the heat exchange between the fluid and the rock matrix,

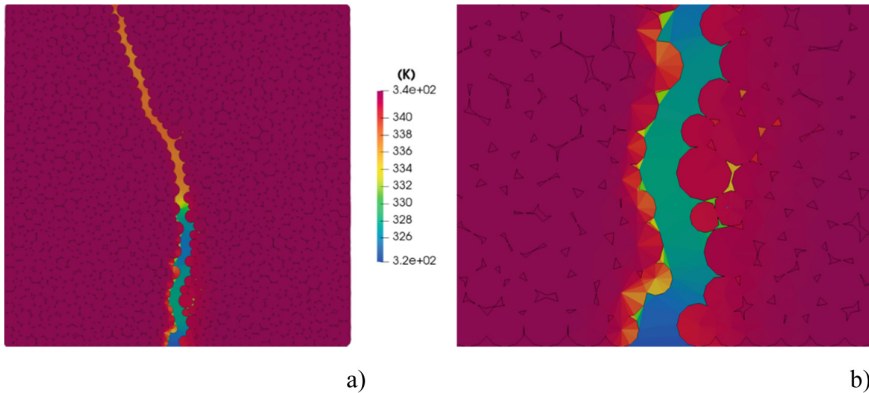


Fig. 8. Temperature distribution in bonded granular rock specimen after 24.8 ms: (a) entire specimen and (b) vicinity of injection point

- in the initially saturated rock specimens, the heat transfer effect is insignificant and may be neglected, while in the matrix of unsaturated rock, the heat transfer effect is very important and cannot be ignored.

Acknowledgements. The present study was supported by the research project “Fracture propagation in rocks during hydro-fracking—experiments and discrete element method coupled with fluid flow and heat transport” (years 2019–2022) financed by the National Science Centre (NCN) (UMO-2018/29/B/ST8/00255).

References

1. Olivella, S., Gens, A., Carrera, J., Alonso, E.: Numerical formulation for a simulator (code bright) for the coupled analysis of saline media. *Eng. Comput.* **13**(7), 87–112 (1996)
2. Kolditz, O., Bauer, S., Bilke, L., Böttcher, N., Delfs, J.O., Fischer, T., Görke, U.J., Kalbacher, T., Kosakowski, G., McDermott, C.I., Park, C.H., Radu, F., Rink, K., Shao, H., Shao, H.B., Sun, F., Sun, Y.Y., Singh, A.K., Taron, J., Walther, M., Wang, W., Watanabe, N., Wu, Y., Xie, M., Xu, W., Zehner, B.: Opegeosys: an open-source initiative for numerical simulation of thermo-hydro-mechanical/chemical (thm/c) processes in porous media. *Environ. Earth Sci.* **67**(2), 589–599 (2012)
3. Zareidarmiyani, A., Salarirad, H., Vilarrasa, V., Kim, K.-I., Lee, J., Min, K.-B.: Comparison of numerical codes for coupled thermo-hydro-mechanical simulations of fractured media. *J. Rock Mech. Geotech. Eng.* **12**, 850–865 (2020)
4. Rühaak, W., Sass, I.: Applied thermo-hydro-mechanical coupled modeling of geothermal prospecting in the Northern Upper Rhine Graben. In: *Proceedings, Thirty-Eighth Workshop on Geothermal Reservoir Engineering*. Stanford University, Stanford, California (2013)
5. Selvadurai, A.P.S., Suvorov, A.P., Selvadurai, P.A.: Thermo-hydro-mechanical processes in fractured rock formations during a glacial advance. *Geosci. Model Dev.* **8**, 2167–2185 (2015)
6. Yan, C., Xie, X., Ren, Y., Ke, W., Wang, G.: A FDEM-based 2D coupled thermal-hydro-mechanical model for multiphysical simulation of rock fracturing. *Int. J. Rock Mech. Min. Sci.* **149**, 104964 (2022)

7. Abdi, R., Krzaczek, M., Tejchman, J.: Comparative study of high-pressure fluid flow in densely packed granules using a 3D CFD model in a continuous medium and a simplified 2D DEM-CFD approach. *Granular Matter* **24**(1), 1–25 (2021). <https://doi.org/10.1007/s10035-021-01179-2>
8. Cundall, P., Strack, O.: A discrete numerical model for granular assemblies. *Géotechnique* **29**(1), 47–65 (1979)
9. Yan, C., Zheng, H.: A coupled thermo-mechanical model based on the combined finite-discrete element method for simulating thermal cracking of rock. *Int. J. Rock Mech. Min. Sci.* **91**, 170–178 (2017)
10. Li, T., Tang, C., Rutqvist, J., Hu, M.: TOUGH-RFPA: Coupled thermal-hydraulic-mechanical rock failure process analysis with application to deep geothermal wells. *Int. J. Rock Mech. Min. Sci.* **142**, 104726 (2021)
11. Deen, N.G., Kriebitzsch, S.H., van der Hoef, M.A., Kuipers, J.: Direct numerical simulation of flow and heat transfer in dense fluid–particle systems. *Chem. Eng. Sci.* **81**, 329–344 (2012)
12. Chen, Z., Jin, X., Wang, M.: A new thermo-mechanical coupled DEM model with non-spherical grains for thermally induced damage of rocks. *J. Mech. Phys. Solids* **116**, 54–69 (2018)
13. Yang, B., Chen, S., Liu, K.: Direct numerical simulations of particle sedimentation with heat transfer using the lattice boltzmann method. *Int. J. Heat Mass Transf.* **104**, 419–437 (2017)
14. Cundall, P.: *Fluid Formulation for PFC2D*. Itasca Consulting Group, Minneapolis, Minnesota (2000)
15. Hazzard, J.F., Young, R.P., Oates, S.J.: Numerical modeling of seismicity induced by fluid injection in a fractured reservoir. In: *Proceedings of the 5th North American Rock Mechanics Symposium, Mining and Tunnel Innovation and Opportunity*, pp. 1023–1030. Toronto, Canada, 7–10 July 2002
16. Al-Busaidi, A., Hazzard, J.F., Young, R.P.: Distinct element modeling of hydraulically fractured Lac du Bonnet granite. *J. Geophys. Res.* **110**, B06302. <https://doi.org/10.1029/2004JB003297>
17. Catalano, E., Chareyre, B., Barthélémy, E.: Pore-scale modeling of fluid–particles interaction and emerging poromechanical effects. *Int. J. Numer. Anal. Meth. Geomech.* **38**, 51–71 (2014)
18. Papachristos, E., Scholtès, L., Donzé, F.V., Chareyre, B.: Intensity and volumetric characterizations of hydraulically driven fractures by hydro-mechanical simulations. *Int. J. Rock Mech. Min. Sci.* **93**, 163–178 (2017)
19. Tomac, I., Gutierrez, M.: Coupled hydro-thermo-mechanical modeling of hydraulic fracturing in quasi-brittle rocks using BPM-DEM. *J. Rock Mech. Geotech. Eng.* **9**, 92–104 (2017)
20. Caulk, R., Sholtès, L., Krzaczek, M., Chareyre, B.: A pore-scale thermo–hydro-mechanical model for particulate systems. *Comput. Methods Appl. Mech. Eng.* **372**, 113292 (2020)
21. Chareyre, B., Cortis, A., Catalano, E., Barthélemy, E.: Pore-scale modeling of viscous flow and induced forces in dense sphere packings. *Transp. Porous Media* **94**(2), 595–615 (2012)
22. Scholtès, L., Chareyre, B., Michallet, H., Catalano, E., Marzougui, D.: Modeling wave-induced pore pressure and effective stress in a granular seabed. *Continuum Mech. Thermodyn.* **27**(1–2), 305–323 (2014). <https://doi.org/10.1007/s00161-014-0377-2>
23. Krzaczek, M., Nitka, M., Kozicki, J., Tejchman, J.: Simulations of hydro-fracking in rock mass at meso-scale using fully coupled DEM/CFD approach. *Acta Geotech.* **15**(2), 297–324 (2019). <https://doi.org/10.1007/s11440-019-00799-6>
24. Krzaczek, M., Nitka, M., Tejchman, J.: Effect of gas content in macro-pores on hydraulic fracturing in rocks using a fully coupled DEM/CFD approach. *Int. J. Numer. Anal. Meth. Geomech.* **45**(2), 234–264 (2021)
25. Kozicki, J., Donzé, F.V.: A new open-source software developer for numerical simulations using discrete modeling methods. *Comput. Methods Appl. Mech. Eng.* **197**, 4429–4443 (2008)

26. Suchorzewski, J., Tejchman, J., Nitka, M.: Discrete element method simulations of fracture in concrete under uniaxial compression based on its real internal structure. *Int. J. Damage Mech* **27**(4), 578–607 (2018)
27. Nitka, M., Tejchman, J.: Modelling of concrete behaviour in uniaxial compression and tension with DEM. *Granular Matter* **17**(1), 145–164 (2015)



A Mechanism of Unstable Growth of Hydraulic Fractures in Laboratory Experiments

Arcady V. Dyskin¹(✉), Elena Pasternak², and Junxian He¹

¹ Department of Civil, Environmental and Mining Engineering, University of Western Australia, 35 Stirling Hwy, Crawley, WA 6009, Australia
arcady.dyskin@uwa.edu.au

² Department of Mechanical Engineering, University of Western Australia, 35 Stirling Hwy, Crawley, WA 6009, Australia

Abstract. Development of hydraulic fracture in lab tests is accompanied by a significant pressure drop in fracturing fluid. This is not normally observed in the field. The pressure drop suggests the presence of a stage of unstable fracture growth in the laboratory samples. The paper shows that unstable fracture growth is produced by interaction between the fracture and free sample surfaces that are parallel to the fracture. This is another difference from the field situation on top of the scale difference, since in the field the presence of a nearby free surfaces parallel and close to the hydraulic fractures is a rare occurrence. This finding is important in analysing the results of laboratory experiments and developing methods of their upscaling.

Keywords: Pressure drop · Free surface effect · Critical crack size · Microscopic length · Bridges

1 Introduction

Pressure monitoring of fracturing fluid in the process of hydraulic fracture propagation in the field shows at most a slight pressure drop (not exceeding the recorded pressure fluctuations) corresponding to the time of hydraulic fracture initiation (e.g. [1, 2]). Opposite to this, the laboratory experiments on hydraulic fracturing show considerable pressure drop at the fracture initiation [3, 4] (in some cases almost to zero pressure, [5–9] as also shown in the experiments described below).

While small pressure drops at the time of onset of the field hydraulic fracture can be attributed to the difference between the pressure required to initiate the fracture and the pressure needed to maintain the fracture growth, the considerable pressure drops observed in the laboratory experiments require the presence of an unstable stage of fracture propagation. Unstable fracture propagation, that is propagation under reduced pressure, requires considerable increase of the stress intensity factor with fracture size, R . If one assumes that the hydraulic fracture propagates under the pressure p of fracturing fluid applied to the whole fracture surface, then the growth will be unstable as the stress intensity factor $K_I \propto p\sqrt{R}$ increases as a square root of the crack size. However, the

almost instantaneous pressure drop measured at the pump suggests that the fractures have grown faster than the fracturing fluid could fill the fracture. (This would not be the case in the field as the hydraulic fractures there are large enough to ensure their filling with the fracturing fluid.) Therefore, the unstable fracture growth is produced by the pressure concentrated at the fracture area of the order of the borehole diameter. In the simplest case when the fracture is modelled as a 2D crack this corresponds to the situation of the crack growing under the action of a pair of concentrated forces of magnitude $F = 2al/L$, where a is the borehole radius, l is the length of the pressurised part of the borehole (between packers), L is the sample length. Such a loading leads to the stress intensity factor $K_I \propto p/\sqrt{R}$ decreasing as a square root of the crack size.

This paper investigates the above mechanism of fracture growth instability assuming that the unstable fracture growth is induced by interaction of the fracture with the sample free surfaces that are parallel to the fracture. (The other pairs of the sample faces are assumed to produce little effect on the fracture propagation.)

2 Unstable Fracture Growth in Laboratory Experiments

Two tests [10] were conducted on 100 mm cubic samples of mortar (cement:sand:water = 1:1:0.4). The sand particle sizes were under 0.15 mm. The properties of mortar samples are: density $\rho = 2.3 \text{ g/cm}^3$, Young's modulus (dynamic) $E = 27.9 \text{ GPa}$, dynamic Poisson's ratio $\nu = 0.19$.

The experiments and equipment are shown in Fig. 1 [10]. Silicon oil of 97.77 cp viscosity was used as fracturing fluid; it was pumped using a GDS high pressure pump with volume control. Figure 2a shows schematics of the fracture-produced loading, a model of borehole of radius $a = 2 \text{ mm}$ and working (fracture-produced) length of $l = 30 \text{ mm}$. Sample size is $L = 100 \text{ mm}$. The produced hydraulic fracture is indicated by a circle (broken line). The pressure changes with time are shown in Fig. 2b, c. The sample was also pre-loaded vertically (z -axis, Figs. 1b, 2a) with steel loading platens to ensure that the fracture propagates vertically. During the tests the acoustic emission was recorded by the AE sensors hosted by the upper loading platen, Fig. 1b. The accumulated number of pulses is plotted in Fig. 2b, c. The displacement was measured on the face parallel to the crack using the DIC with Phantom stereo-vision high speed cameras, Fig. 1a.

Hydraulic fracture growth proceeds with local interruptions and overlapping resulting in formation of bridges distributed across the whole fracture and constricting the fracture opening [8, 9]. The effective stiffness k of the system of bridges relating stress that opens the fracture and fracture surface displacement, $\sigma = k\Delta u/2$, where Δu is the average fracture opening can be estimated from the displacement measurements as follows. Since the stage is considered when the fracture almost traverses the sample, the average displacement related to the average fracture opening, $\Delta u/2$ is approximately equal to the average displacement of the sample surface. The average opening stress σ is taken as approximately equal to the peak borehole pressure since the fracturing fluid moves inside the fracture. The effective bridge stiffness produces a characteristic length [8–10], so-called constriction length $\lambda = E/k$, where E is the Young's modulus of the sample material (mortar).

The peak pressure, the (average) fracture opening at the peak as well as the estimated effective bridge stiffnesses and the constriction lengths are summarised in Table 1. It is seen that the constriction length is almost 2 orders of magnitude greater than the sample size, which suggests that the effect of bridges can be neglected, and the fracture can be modelled as a conventional crack with non-interacting faces.

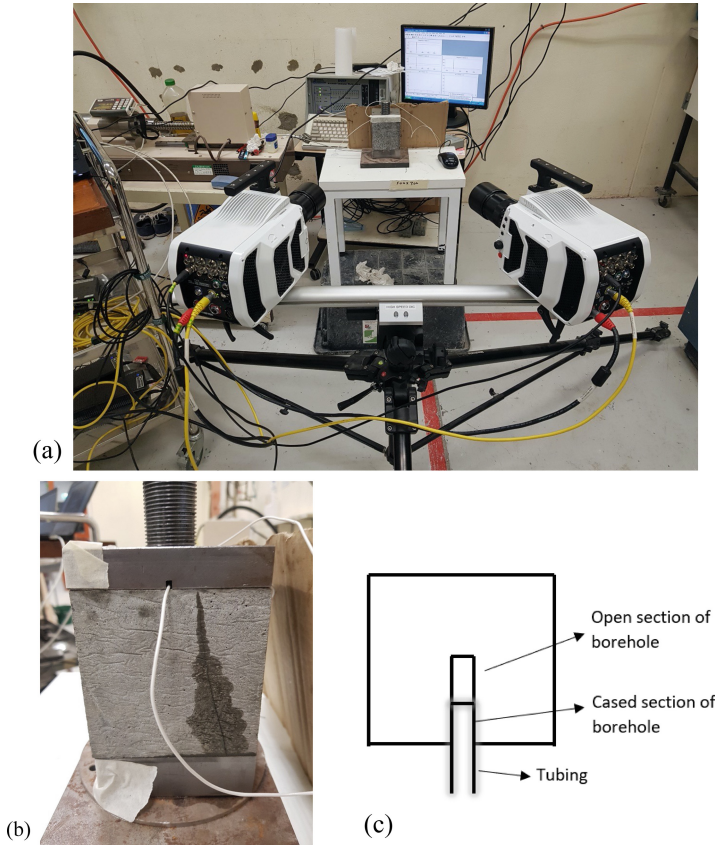


Fig. 1. Laboratory experiments on hydraulic fracture [10]: (a) Experimental set-up; (b) tested sample with a hydraulic fracture between two vertical loading platens; the upper loading platen also hosts the AE sensors; (c) schematics of the model of borehole.

3 Mechanism of Unstable Fracture Growth in Laboratory Experiments

In the above experiments the size, $2R$, of the produced fractures is of the order of the sample size, $L = 100$ mm, Figs. 1b, 2a. This is much greater than the borehole radius $a = 2$ mm. This suggests a simplified way of modelling the fracture growth by considering

Table 1. Parameters of the test samples and the inferred bridge characteristics.

Test	Peak fluid pressure, p , MPa	Fracture opening, Δu , mm	Stiffness of the bridges, k , GPa/m	Young's modulus of the sample, E , GPa	Constriction length, λ , m
1	12.1	0.44	8.8	27.9	3.2
2	15.2	0.26	13.6	27.9	2.55

it as a 2D crack opened at the centre by a pair of 2D concentrated forces F (such a crack is shown in Fig. 3a) representing the opening action of the pressurised borehole.

$$F = 2pa \frac{l}{L} \quad (1)$$

Here p is the peak pressure in the borehole, a is the borehole radius, l is the pressurised part of the borehole, L is the sample size. In this 2D modelling the total force $2pal$ is referred to the whole sample thickness, L .

The unstable growth of such a crack can be produced by interaction with a free surface parallel to the crack [11, 12]; as soon as the crack length reaches a critical value (corresponds to the minimum of the stress intensity factor) the stress intensity starts increasing with the crack size and the crack growth becomes unstable.

In the case under consideration the fracture is located at the centre of the sample, therefore the closest configuration would be the crack located at the centre of a free strip with free surfaces, Fig. 3a. For this configuration the stress intensity factor reads:

$$K_I = \frac{F}{\sqrt{\pi R}} \frac{f(s)}{(1-s)^{3/2}}, \quad s = \frac{2R}{2R+L} \quad (2)$$

Function $f(s)$ is tabulated in [13]. It is also shown to have two simple asymptotics: $f(s) \sim (1-s)^{3/2}$ as $s \rightarrow 0$ and $f(s) \sim \sqrt{3\pi}s^{3/2}/2$ as $s \rightarrow 1$. This allows putting forward the following approximation that incorporates these two asymptotics:

$$f(s) \approx (1-s)^{\frac{3}{2}} + \frac{\sqrt{3\pi}}{2} s^{3/2} \quad (3)$$

Comparison of Eq. (3) with the numerical values given by [13] shows that the average relative error over 7 points is 4%.

Dependence (2), (3) is shown in Fig. 3b. It is seen that as R increases the stress intensity factor reaches minimum and then increases. The critical crack size, R_{cr} , obviously corresponds to the minimum, $dK_I/dR = 0$. This gives:

$$R_{cr} = 0.237 L, \quad K_I^{min} = 8.72 \frac{apl}{\sqrt{2\pi}L^{3/2}} \quad (4)$$

The unstable fracture propagation commences when the pressure p is such that

$$K_I^{min} = K_{Ic} \quad (5)$$

where K_{Ic} is the fracture toughness of the material.

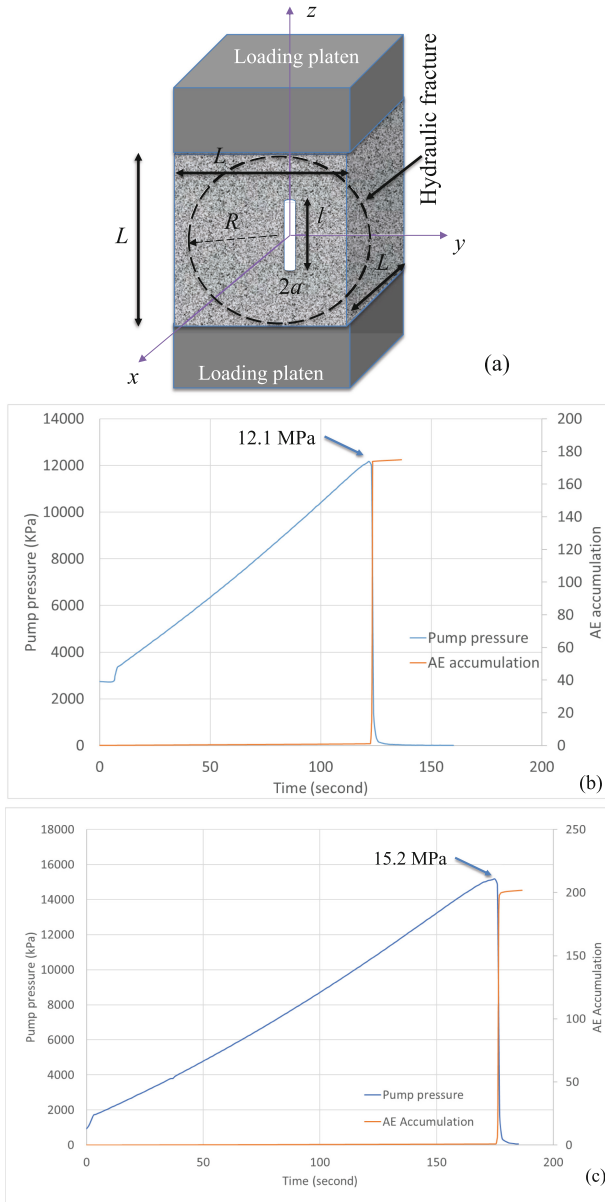


Fig. 2. Results of laboratory experiments on hydraulic fracture (of radius R) in a cubic sample of size $L = 100$ mm [10]: (a) schematics of the fracture-produced loading in the experiment; only pressurised part of the borehole is shown (length $l = 30$ mm, diameter $2a = 4$ mm); the acoustic emission sensors are located between the upper loading platen and the sample; (b) results of test 1; (c) results of test 2, pump pressure (kPa) and total number of AE events versus time (s).

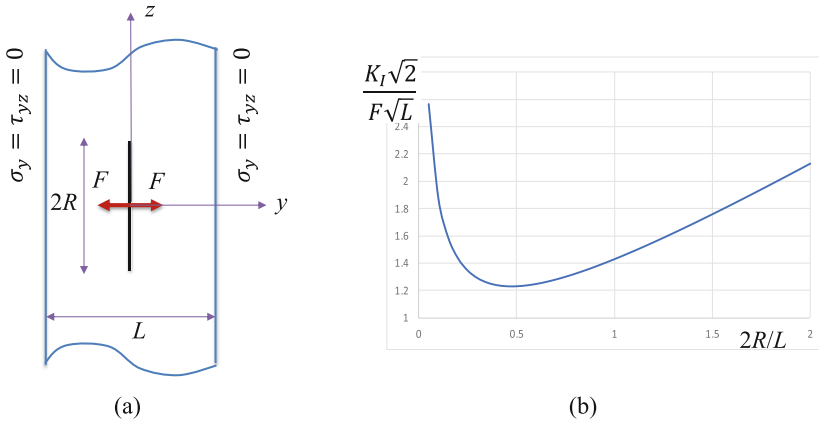


Fig. 3. Unstable fracture growth due to interaction of with free surfaces: (a) crack at the centre of a strip with free surfaces; (b) normalised stress intensity factor versus the normalised crack size.

4 Discussion

1. The obtained criterion of unstable fracture propagation (4), (5) can be interpreted by introducing a characteristic microscopic fracture length l_m which is the minimum size of the fracturing element. In the case of crack propagation it is an equivalent of the process zone length, but instead of considering the non-linear processes within this zone (which might well be material specific) we will use a simplified approach [14–16] by considering the magnitude of the singular stress at distance l_m from the crack tip, Fig. 4, and equating it to the minimum tensile strength σ_t to express the criterion of fracture propagation. (In [14] the non-singular terms were also taken into account which lead to the expression of the scale effect in fracture toughness; in the simplified model considered in this paper only singular terms are used.)

Subsequently, the criterion of unstable fracture propagation (4), (5) expressed in terms of the minimum tensile strength σ_t reads:

$$\frac{K_I^{min}}{\sqrt{2\pi l_m}} = \sigma_t \tag{6}$$

The fracture starts from the borehole pressurised to pressure p , at the point with the minimum strength, which is σ_t . Given that the stress concentration at the borehole surface is p , one finds that $\sigma_t = p$. From here, using criterion (6) one can estimate the characteristic microscopic length $l_m \sim 7 \cdot 10^{-3}$ mm. This is close to the lower limit of Portland cement grain sizes, $10^{-3} - 10^{-1}$ mm (e.g., [17]). This suggests that fracturing of mortar involves the scale of cement grains (that is the smallest scale) while the presence of heterogeneities of larges sizes leads to complex fracture surface geometry at the microscale. In particular, the fracture becomes patchy with local overlapping and formation of bridges distributed all over the fracture, Fig. 5 [10].

- The above approach ignores the effect of the other pairs of sample surfaces. The pair of surfaces subjected to vertical load is in contact with the loading platens and hence cannot be free due to the contact friction. The other pair of surfaces that is normal to the fracture is not included because the model is two dimensional. A planned 3D modelling will be directed towards investigating the effect of fracture geometry and interaction with all sample surfaces.

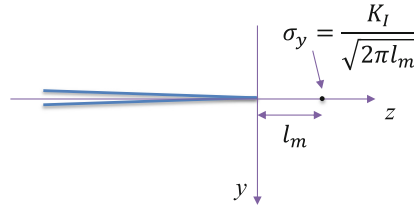


Fig. 4. The concept of crack growth criterion based on the introduction of characteristic microscopic length l_m . The coordinate frame corresponds to that of Fig. 3a.

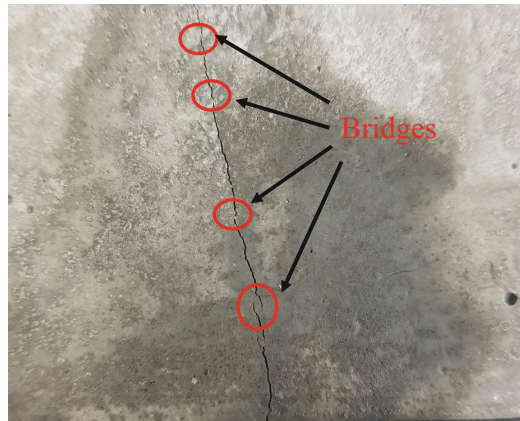


Fig. 5. Bridges (local interruptions and overlapping) observed on the fracture trace [10].

5 Conclusions

Laboratory experiments on hydraulic fracture are often used to investigate fracking in the field. It is conventionally accepted that the major distinction between the laboratory experiments and the field situation is the scale difference, which is to be addressed by upscaling. This paper demonstrates that there exists another important difference—the presence of the sample free surfaces in the laboratory tests, which are not normally present in the field. (The faults or joints do not represent free surfaces as their faces are in contact due to in situ compressive stresses.)

Interaction between the growing fracture and the free surfaces oriented parallel to the fracture turns initially stable fracture growth into unstable well before the fracturing fluid is able to fill the fracture and thus ensures the continuation of fracture growth. This leads to the sharp drop of the pressure not observed in the field.

The analysis also shows that fractures in mortar samples grow by breaking microscopic elements at the cement grain scale. This produces patchy fracturing leading to local overlapping and formation of distributed bridges [8–10].

Acknowledgement. AVD and EP acknowledge the support of the Australian Research Council through projects DP190103260 and LE17170100079.

References

1. Jeffrey, R.G., Bungler, A.P., Lecampion, B., Zhang, X., Chen, Z.R., van As, A. Allison, D.P. de Beer, W., Dudley, J.W., Siebrits, E., Thiercelin, M., Mainguy, M.: Measuring hydraulic fracture growth in naturally fractured rock. *SPE* 124919, 1–19 (2009)
2. Zhang, Y., Zhang, J., Yuan, B., Yin, S.: In-situ stresses controlling hydraulic fracture propagation and fracture breakdown pressure. *J. Petrol. Sci. Eng.* **164**, 164–173 (2018)
3. Hayashi, K., Haimson, B.C.: Characteristics of shut-in curves in hydraulic fracturing stress measurements and determination of in situ minimum compressive stress. *J. Geophys. Res.* **96**(B11), 18311–18321 (1991)
4. Ning, L., Shicheng, Z., Yushi, Z., Xinfang, M., Shan, W., Yinuo, Z.: Experimental analysis of hydraulic fracture growth and acoustic emission response in a layered formation. *Rock Mech. Rock Eng.* **51**, 1047–1062 (2018)
5. AlTammam, M.J., Sharma, M.M., Manchanda, R.: The effect of pore pressure on hydraulic fracture growth: an experimental study. *Rock Mech. Rock Eng.* **51**, 2709–2732 (2018)
6. Hampton, J.C., Hu, D., Matzar, L., Gutierrez, M.: Cumulative volumetric deformation of a hydraulic fracture using acoustic emission and micro-CT imaging. *ARMA* 14-7041 (2014)
7. Bungler, A.P., Kear, J., Dyskin, A.V., Pasternak, E.: Interpreting post-injection acoustic emission in laboratory hydraulic fracturing experiments. *Proc. ARMA* 14-6973 (2014)
8. Dyskin, A.V., Pasternak, E., He, J., Lebedev, M., Gurevich, B.: The role of bridge cracks in hydraulic fracturing. In: *Proceedings of the 10th International Conference on Structural Integrity and Failure (SIF2016)*. Adelaide, Australia, Paper #6 (2016)
9. He, J., Pasternak, E., Dyskin, A.V.: Bridges outside fracture process zone: their existence and effect. *Eng. Fract. Mech.* **225**, 106453 (2020)
10. He, J., Pasternak, E., Dyskin, A.V.: Monitoring of hydraulic fracture using photogrammetry and acoustic emission. Abstract and presentation for seminar series: *Mechanics of Rocks and Structural Materials*. University of Western Australia, 23 July (2020)
11. Dyskin, A.V., Germanovich, L.N.: Model of rockburst caused by cracks growing near free surface. In: *Rockbursts and Seismicity in Mines*, vol. 93, pp. 169–175 (1993)
12. Germanovich, L.N., Dyskin, A.V.: Fracture mechanisms and instability of openings in compression. *Int. J. Rock Mech. Min. Sci.* **37**(1), 263–284 (2000)
13. Tada, H., Paris, P.C., Irwin, R.I.: *The Stress Analysis of Cracks Handbook*, 2nd edn. Paris Production Inc., St Luis, Missouri (1985)
14. Dyskin, A.V.: Crack growth criteria incorporating non-singular stresses: Size effect in apparent fracture toughness. *Int. J. Fracture* **83**, 191–206 (1997)
15. Dyskin, A.V., Pasternak, E.: Asymptotic analysis of fracture propagation in materials with rotating particles. *Eng. Fract. Mech.* **150**, 1–18 (2015)

16. Dyskin, A.V., Pasternak, E., Esin, M.: Multiscale rotational mechanism of fracture propagation in geomaterials. *Phil. Mag.* **95**(28–30), 3167–3191 (2015)
17. Ferraris, C.F., Hackley, V.A., Avilés, A.I.: Measurement of particle size distribution in Portland cement powder: analysis of ASTM Round Robin studies. *Cem. Concr. Aggregates* **26**(2), 1–11 (2004)



Asymptotic Modelling of Fractures with Constricted Opening

Elena Pasternak¹(✉) and Arcady V. Dyskin²

¹ Department of Mechanical Engineering, University of Western Australia, 35 Stirling Hwy, Crawley, WA 6009, Australia

elena.pasternak@uwa.edu.au

² Department of Civil, Environmental and Mining Engineering, University of Western Australia, 35 Stirling Hwy, Crawley, WA 6009, Australia

Abstract. Fractures in geomaterials do not grow as a continuous surface as they are affected by local interruptions and overlapping. These form bridges which being distributed all over the fracture constrict its opening. The effect of the distributed bridges is modelled by an equivalent Winkler layer whose stiffness represents the total bridge stiffness per unit area of the fracture. The paper develops approximate expressions for the stress intensity factors and volume (area in 2D) of fracture opening under uniform tensile load based on interpolating between the asymptotics of small and large fractures. A case of growth of a fracture with constricted opening under displacement-control loading is analysed. The presented results can be important in modelling of fracture propagation in heterogenous materials.

Keywords: Cracks · Bridges · Winkler layer · Interpolation between asymptotics · Displacement-control loading

1 Introduction

Tensile fractures growing in geomaterials (e.g., hydraulic fractures) are usually depicted as forming a continuous surface, however in reality they are affected by local interruptions and overlapping [1–4] distributed all over the fracture surface, Fig. 1a. These work as bridges connecting the opposite faces of the fracture, Fig. 1b and hence restrict their opening, which is reflected in the term *Fractures with constricted opening* [5, 6].

The interruptions and overlappings, Fig. 1c, are observed in 2D images (surface or cross-sections) of extensively propagating fractures [5–7]. These features are short compared to the fracture length (or length of the fracture trace) and distributed all over the fracture, rather than just in the process zone. In real 3D situations the interruptions and overlappings should also be local, i.e., have all dimensions small compared to the fracture dimensions, Fig. 2. (Local fracture surface interruptions can also be seen in observations [8].) Therefore, these features do not interrupt the fracture path (as one could conclude from 2D pictures) but form bridges locally connecting the opposite

surfaces of the fracture, Fig. 2. Each bridge works as a small pillar or beam (in the case of overlapping) exerting a force F resisting the fracture opening at the bridge location. The bridge can be characterised by stiffness S_0 (in N/m) relating force F and fracture opening Δu at the bridge location: $F = S_0 \Delta u$. Apparently, the action of bridges that leads to a very complex fracture width (rather than the surface roughness as assumed in [9]).

In order to simplify the modelling, we concentrate on the average effect of bridges. The combined effect of the multitude of distributed (and randomly located) bridges can be modelled on average by relating the total bridge force per unit area of the fracture surface and the average fracture opening. This leads to representing the bridges as a Winkler layer with effective stiffness k (in Pa/m) connecting the average stress and opening:

$$\sigma = k \Delta u, \quad k = N \langle S_0 \rangle \tag{1}$$

where N is the number of bridges per unit area of fracture surface, $\langle S_0 \rangle$ is the average bridge stiffness.

Therefore a fracture with (randomly) distributed bridges can be modelled as a crack with Winkler layer between the opposite surfaces (or crack with linear links) [5, 8–13].

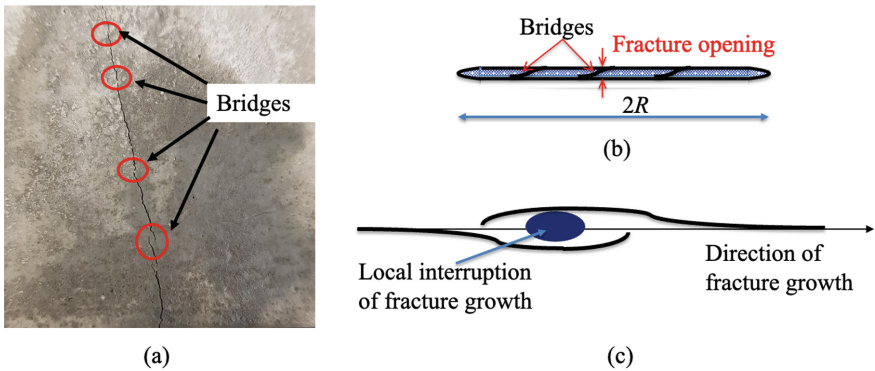


Fig. 1. Bridges observed on the surface or cross-sections: (a) observations in one of our tests [5–7]; (b) the effect of bridges on the fracture opening; $2R$ is the crack length; (c) mechanism of overlapping.

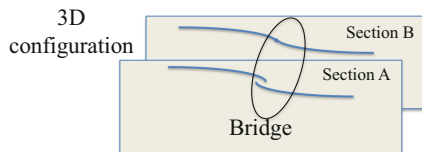


Fig. 2. Formation of bridges in 3D.

Numerical solutions for elastic isotropic problem of a crack with Winkler layer were proposed in [8, 9] (in 3D) and [10, 11] (in 2D). Analytical solutions exist for very large

cracks whose dimensions exceed a characteristic length (constriction length) introduced in [5–8]:

$$\lambda = \frac{E}{1 - \nu^2} k^{-1} \approx E/k \quad (2)$$

Here E , ν are the Young's modulus and Poisson's ratio of the surrounding (isotropic) material. Two asymptotics are known for the case of uniform load: large cracks, when the crack size $R \gg \lambda$ and small cracks, $R \ll \lambda$. The later are just conventional cracks without surface interaction.

In this paper we develop approximate expressions for the Mode I stress intensity factor and the volume (area in 2D) of crack opening under uniform tensile load based on interpolation between the asymptotics of small and large cracks. Using these approximations, the growth of fractures with constricted opening (cracks with Winkler layer) under displacement-controlled loading is analysed.

2 Crack with Winkler Layer Under Uniform Tension. Approximate Expressions for K_I and Volume (Area) of Opening

Here we present the known asymptotics of large and small cracks, then develop interpolating formulas and compare them with numerical solutions found in the literature. We assume that the crack is loaded by uniform tensile stress p . We consider a disc-like crack and a 2D straight crack.

2.1 3D Case: A Disc-Like Crack

In the asymptotics of cracks of large radius $R \gg \lambda$ the main asymptotic terms (in the limiting transition $R/\lambda \rightarrow \infty$) for Mode I stress intensity factor K_I and the volume of crack opening V have the following form [10]

$$K_I = p\sqrt{\lambda}, \quad V = 2\pi \frac{1 - \nu^2}{E} \lambda R^2 p \quad (3)$$

Here p is the uniform tensile stress applied to the crack. On the other hand, in the asymptotics of cracks of small radius $R \ll \lambda$ the main asymptotic terms (in the limiting transition $R/\lambda \rightarrow 0$) for Mode I stress intensity factor K_I and the volume of crack opening V have the corresponding expressions for the conventional disc-like crack, e.g. [14]:

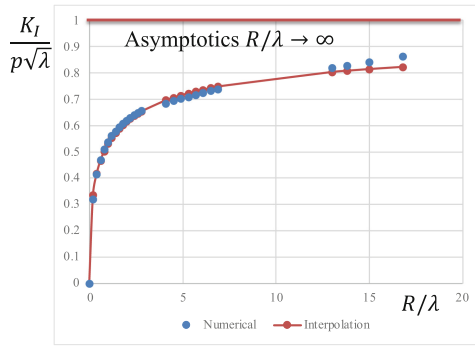
$$K_I = 2p\sqrt{R/\pi}, \quad V = \frac{16}{3} \frac{1 - \nu^2}{E} R^3 p \quad (4)$$

We propose the following interpolating formulae for finite radii: $0 < R/\lambda < \infty$

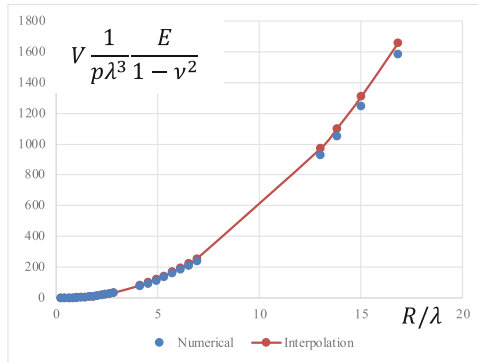
$$K_I = \frac{2p\sqrt{R/\pi}}{1 + 2\sqrt{R/\pi\lambda}}, \quad V = \pi \frac{1 - \nu^2}{E} \frac{\lambda R^2}{1 + \frac{3\pi}{16} \frac{\lambda}{R}} p \quad (5)$$

It can readily be seen that when $R \gg \lambda$ Eqs. (5) have Eqs. (3) as the main asymptotic terms and when $R \ll \lambda$ Eqs. (5) have Eqs. (4) as the main asymptotic terms.

Figure 3 shows comparison of interpolating formulae (5) with numerical solutions [10] obtained by solving the corresponding integral equations by approximating the unknown function with a finite linear combination of an orthonormal basis. It is seen that the accuracy of the interpolations is quite high, which justifies the use of Eq. (5) as the main tool for investigating propagation of disc-like fractures with constricted opening. It is also seen that the asymptotic formula $K_I = p\sqrt{\lambda}$ starts working only at very large crack radii.



(a)



(b)

Fig. 3. Comparison of interpolating formulae (5) with numerical solution [10]: (a) stress intensity factor; the horizontal line refers to asymptotics $K_I = p\sqrt{\lambda}$; (b) volume of fracture opening.

2.2 2D Cracks

Now we consider the 2D crack model, a straight crack of length $2R$, Fig. 1b. In the asymptotics of cracks of large length, $R \gg \lambda$ the main asymptotic terms (in the limiting

transition $R/\lambda \rightarrow \infty$) for Mode I stress intensity factor K_I and the area of crack opening A have the following form [12]

$$K_I = p\sqrt{\lambda}, A = 2R\Delta u_\infty = \frac{4}{E'}\lambda Rp \tag{6}$$

where $\Delta u_\infty = 2p\lambda/E'$ is the limiting crack opening displacement at $R/\lambda \rightarrow \infty$ [8] and $E' = E$ for plane stress and $E' = E/(1 - \nu^2)$ for plane strain.

In the asymptotics of cracks of small length $R \ll \lambda$ the main asymptotic terms (in the limiting transition $R/\lambda \rightarrow 0$) for Mode I stress intensity factor K_I and the area of crack opening A have the corresponding expressions for the 2D crack, e.g. [14]:

$$K_I = p\sqrt{\pi R}, A = \frac{2\pi}{E'}R^2p \tag{7}$$

We developed the following interpolating formulae for finite lengths: $0 < R/\lambda < \infty$

$$K_I = \frac{p\sqrt{\pi R}}{1 + \sqrt{\pi R/\lambda}}, A = \frac{4\pi p}{E'} \frac{R^2}{2 + \frac{\pi R}{\lambda}} \tag{8}$$

Figure 4 shows comparison of interpolating formula for the stress intensity factor (8) with numerical solution [12]. It is seen that the accuracy of the interpolations is not as high as in 3D, especially in the interval $0.1 < R/\lambda < 5$. More work is required to understand the underlying reasons for the reduction in accuracy.

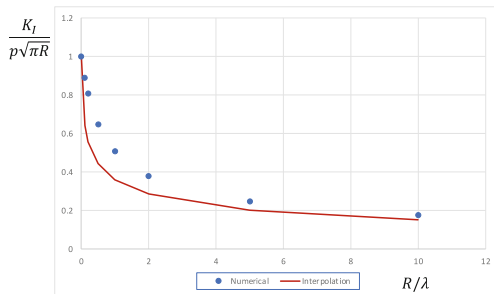


Fig. 4. Comparison of interpolating formulae (8) for the stress intensity factor with numerical solution [12].

3 Disc-Like Crack Under Displacement-Controlled Loading

So far the crack characteristics were considered under stress-controlled loading. In this case we can see that as the crack increases its size the stress intensity factor increases. It means that if some stress magnitude p satisfies the condition of crack growth, $K_I = K_{Ic}$, where $K_{Ic} = const$ is the material fracture toughness (e.g. [14]), the crack growth will never stop. This is the case of unstable crack growth. A different situation can occur under

the displacement-controlled loading since the crack growth increases the compliance of the body with the crack such that the crack growth can lead to stress decrease thus affecting the crack growth. In order to analyse this situation, we consider a sample of height H and square base $L \times L$ with a disc-like crack parallel to the base, Fig. 5a. We fix the lower end of the sample and apply displacement u_0 to its upper end.

The average stress reduction under displacement-controlled loading due to the presence of the crack can be estimated taking into account the fact that under stress p the average displacement will consist of displacement of the upper end of the sample without the crack plus the crack opening volume per unit volume of the sample. Therefore, taking into account the second equation of (5) and neglecting, for the sake of simplicity, the crack interaction with the sample boundaries one obtains:

$$u_0 = \frac{H}{E} \left[1 + \pi \frac{1 - \nu^2}{HL^2} \frac{\lambda R^2}{1 + \frac{3\pi \lambda}{16 R}} \right] p \quad (9)$$

From here stress p can be expressed through u_0

$$p = u_0 \frac{E}{H} \left[1 + \pi \frac{1 - \nu^2}{HL^2} \frac{\lambda R^2}{1 + \frac{3\pi \lambda}{16 R}} \right]^{-1} \quad (10)$$

And finally, using the first Eq. (5)

$$K_I = 2u_0 \frac{E}{H} \frac{\sqrt{R/\pi}}{1 + 2\sqrt{R/\pi}\lambda} \left[1 + \pi \frac{1 - \nu^2}{HL^2} \frac{\lambda R^2}{1 + \frac{3\pi \lambda}{16 R}} \right]^{-1} \quad (11)$$

Figure 5b-d show dependence of the normalised stress intensity factor of the normalized crack radius for different normalised sample heights and different constriction lengths. It is seen that for very short sample, $H = 0.1L$, Fig. 5b, the displacement-controlled loading has the highest manifestation: the stress intensity factor increases only up to certain crack radii and then it starts decreasing. This means that the unstable crack growth is limited, turning into the situation when the load (displacement) needs to be increased in order to continue crack growth (stable crack growth). A similar type of behavior corresponds to the case of cubic sample, $H = L$, Fig. 5c, albeit the stress intensity factor decrease is not that strong as in the first case. Opposite to this, for very tall sample, $H = 10L$, Fig. 5d the stress intensity factor only increases, indicating that this case is close to the stress-controlled loading. It should be emphasised that the crack interaction with the sample surfaces could alter the pictures presented in Fig. 5b-d.

4 Conclusions

Rock heterogeneity, non-uniform breakage of microscopic elements of the geomaterial as well as microscopic non-uniformity in the stress field lead to local deviations from planar fracture growth. This produces patchy fracturing leading to local overlapping and formation of bridges distributed all over the fracture (rather than just in the process

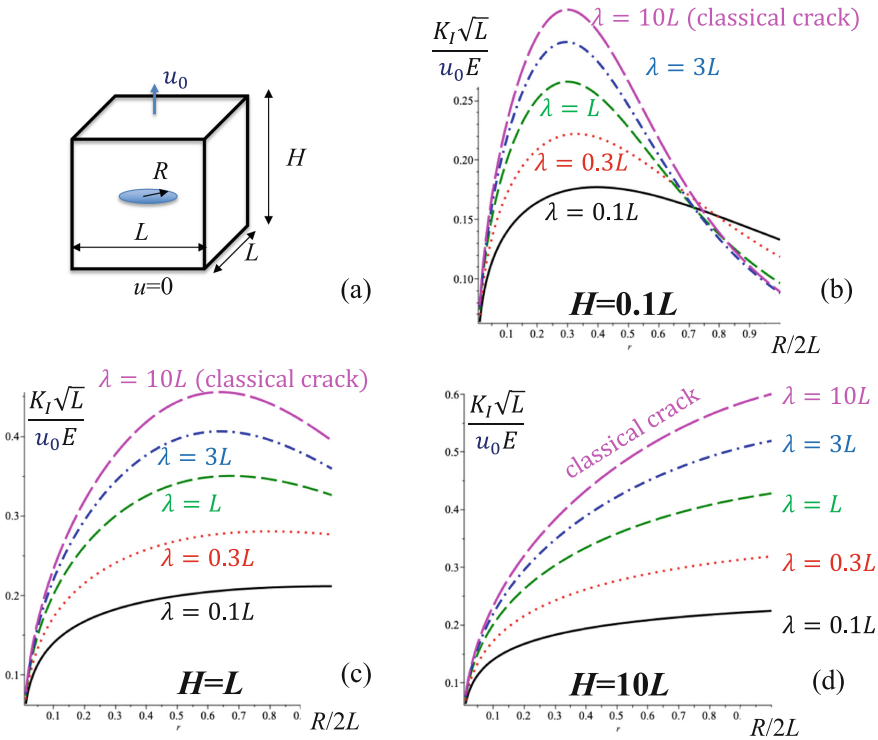


Fig. 5. Displacement-controlled loading: (a) sample with a disc-like crack tensioned by displacement u_0 ; (b) sample height $H = 0.1L$; (c) sample height $H = L$; (d) sample height $H = 10L$.

zone). Distributed bridges constrict the fracture opening and reduce the Mode I stress intensity factor.

The effect of bridges can be modelled on average by introducing effective bridge layer stiffness which relates applied stress and average crack opening. Since the effective stiffness has units of Pa/m, the Young’s modulus divided by the stiffness gives a characteristic length which we call the *constriction length*. The effect of bridges is only important when the fracture size is comparable with or greater than the constriction length; in smaller fractures the effect of distributed bridges can be neglected.

Fracture with bridges can be modelled as a crack with Winkler layer whose stiffness is equal to the effective bridge stiffness. Analytical solutions for Mode I stress intensity factor and volume of fracture opening can only be found in asymptotics of either very large crack or very small (and hence conventional) crack. Interpolating formulae for the stress intensity factor and crack opening volume have been developed that give good accuracy when compared with numerical solutions.

In stress-controlled loading the fracture propagation is always unstable. In displacement-controlled loading the fracture initially grows unstably and then turns to stable growth. The constriction (bridges) shifts the transition towards larger cracks and increases the displacement needed for the transition.

The presented results are important in analysing the results of observation of hydraulic fracture growth. Furthermore, after extending these results to Mode II and III stress intensity factor it will make it possible to treat asperities as bridges in shear fractures.

Acknowledgements. AVD and EP acknowledge the support of the Australian Research Council through project DP190103260.

References

1. Marshall, D.B., Swain, M.V.: Crack resistance curves in magnesia-partially-stabilized. *J. Am. Ceramic Soc.* **71**(6), 399–407 (1988)
2. Huggins, P., Waiterson, J., Walsh, J.J., Childs, C.: Relay zone geometry and displacement transfer between normal faults recorded in coal-mine plans. *J. Struct. Geol.* **17**(12), 1741–1755 (1995)
3. Jeffrey, R.G., Bungler, A.P., Lecampion, B., Zhang, X., Chen, Z.R., van As, A.A., de Beer, D.P.W., Dudley, J.W., Siebrits, E., Thiercelin, M., Mainguy, M.: Measuring hydraulic fracture growth in naturally fractured rock. *SPE 124919*, 1–19 (2009)
4. Hampton, J.C., Hu, D., Matzar, L., Gutierrez, M.: Cumulative volumetric deformation of a hydraulic fracture using acoustic emission and micro-CT imaging. *ARMA 14-7041* (2014)
5. Dyskin, A.V., Pasternak, E., He, J., Lebedev, M., Gurevich, B.: The role of bridge cracks in hydraulic fracturing. In: *Proceedings of the 10th International Conference on Structural Integrity and Failure (SIF2016)*, Adelaide, Australia, Paper #6 (2016)
6. He, J., Pasternak, E., Dyskin, A.V.: Bridges outside fracture process zone: their existence and effect. *Eng. Fract. Mech.* **225**, 106453 (2020)
7. He, J., Pasternak, E., Dyskin, A.V.: Monitoring of hydraulic fracture using photogrammetry and acoustic emission. Abstract and presentation for seminar series: *Mechanics of Rocks and Structural Materials*. University of Western Australia (2020)
8. Li, Q., Xing, H., Liu, J., Liu, X.: A review on hydraulic fracturing of unconventional reservoir. *Petroleum* **1**(1), 8–15 (2015)
9. Ali Daneshy, A.: Pressure Variations Inside the Hydraulic Fracture and Their Impact on Fracture Propagation, Conductivity, and Screenout, pp. 107–111. *SPE Production & Operations* (2007)
10. Shifrin, E.I.: Plane-normal separation crack for the case of linear linkages between its surfaces. *Mech. Solids* **17**(3), 70–76 (1982)
11. Shifrin, E.I.: The I-mode crack whose sides interact according to a linear law. *Mech. Solids* **23**(5), 91–97 (1988)
12. Rose, L.R.F.: Crack reinforcement by distributed springs. *J. Mech. Phys. Solids* **35**(4), 383–405 (1987)
13. Movchan, A.B., Willis, J.R.: Asymptotic analysis of the reinforcement of a brittle crack by bridging fibers. *J. Mech. Appl. Math.* **46**(Pt 2), 331–350 (1993)
14. Tada, H., Paris, P.C., Irwin, R.I.: *The Stress Analysis of Cracks Handbook*, 2nd edn. Paris Production Inc., St Luis, Missouri (1985)



An Experimental Study on Silt Desiccation Cracking with Different Basal Constraints and Various Humidity

Ruoyu Chen^(✉), Winston Lindqwister, Tomasz Hueckel, and Manolis Veveakis

Duke University, Durham, NC 27705, USA
ruoyu.chen@duke.edu

Abstract. This paper presents the desiccation failure process of geomaterials under controlled environmental conditions. The experiment material, granite powder silt, was tested in a controlled atmospheric chamber that ensures temperature consistency and provides humidity control. A polytetrafluoroethylene (PTFE) mold was used in the setup stages to make sure the samples have the same dimensions. The shrinkage of the silt slabs was subject to different sets of frictional constraints, including a flat PTFE plate, a plate with a 45-degree constraint, and a plate with a 90-degree constraint, to analyze the influence of boundary conditions on the air-entry desiccation cracks. The humidity was kept constant during each experiment and different humidities were applied in the series of experiments to find the role of the evaporation rates (ER) on desiccation cracking. Data including the cracks onsets, crack morphology, mass changes, and the atmospheric conditions during the drying process were recorded and collected while the patterns of cracks, crack onsets with different bottom boundary conditions, and different evaporation rates were calculated and discussed.

Keywords: Desiccation · Evaporation · Boundary conditions

1 Introduction

Desiccation is one of the premier problems in geomechanics engineering. The initiation and propagation of cracks may cause catastrophic damage including failure in structural foundations or leakages of pollutants, such as those in nuclear waste disposal [1–3].

Previous researchers have shown that natural environmental conditions (humidity, temperature, and the wet-dry cycles) have impacts on the desiccation of geomaterials, with shrinkage due to dehydration believed to be the main factor leading to crack formation. Tang indicated that cracks initiate faster when temperatures increase, which is believed to be tied to an increase in the evaporation rate [4, 5]. A time decrease in the initiation cracks with respect to increasing relative humidity is found by previous researchers [6–9].

On the other hand, the boundary conditions that physically constrain the geomaterial can contribute to failure as well [10, 11]. Corte proposed the constraints on shrinkage that causes the tensile stress to exceed the soil strength is an important parameter of the

proliferation of desiccation cracks [12]. Several types of bottom boundary conditions have been used and analyzed. Peron has compared desiccation processes of PTFE plates with 90-degree constraints and pointed out that the time of onset of cracking is quite similar to the time of the sample reaching its shrinkage limit [10]. Zeng and Lakshmikantha showed that cracks can initiate from both the top and bottom surfaces of soil as well as within the soil, and concluded that the cause of top surface cracks is desiccation while the bottom cracks are generated by sample curling or syneresis [2, 13].

The shape and dimension also contribute to the geometry and initialization of desiccation cracks [14, 15]. The experimental results from Prat prove a larger surface area leads to a lower crack stress threshold while Lakshmikantha discusses a negative relation between samples thickness and stress threshold [13, 16]. For the controlled shape and dimension samples, though the stress threshold for desiccation failure is fixed, the onsets of cracks with different basal constraints under constant atmosphere conditions are various motivated by these pioneering works and acknowledging the discussion of the separate influence of atmospheric conditions and soil basal conditions, further exploration needs to be done to examine the combined influence on cracks from these factors. Based on the morphology, mass changes, and onset data, the relation between evaporation rate and relative humidity is determined and the crack initiation process on various constraints is discussed.

2 Experiment Methodology

The geomaterial used in these experiments is granite silt powder, with physical properties listed in Table 1. The granite silt powder was mixed with distilled water and fully stirred with a spatula into a paste. The container was struck on the table several times to remove the trapped air in the paste and left undistributed for 30 min to get a relatively homogeneous water content inside the mixture paste.

Table 1. Physical properties of soil material used in these experiments.

Characteristic	Specific gravity	Liquid limit (%)	Plastic limit (%)	Young's modulus (Mpa)	Shear modulus (Mpa)	Poisson's ratio
Values	2.89	25.02	17.15	8.60	3.30	0.286

A mold (with inner dimensions of length 150 mm, width 50 mm, and height 14 mm) was used to shape the samples in the setup. The inside of the mold was covered by PTFE strips and coated with lubricating oil, which helped to reduce the deformation due to friction when removing the mold. The desired constraints were fixed with mold then the mold was fulfilled with prepared material to form the fixed shape samples. After the rectangular sample was prepared in the mold, black paint was sprayed on the sample surface to increase the contrast for more accurate figures analysis results. Three different basal constraint platforms, the flat PTFE covering with a thin film of lubricating oil, the

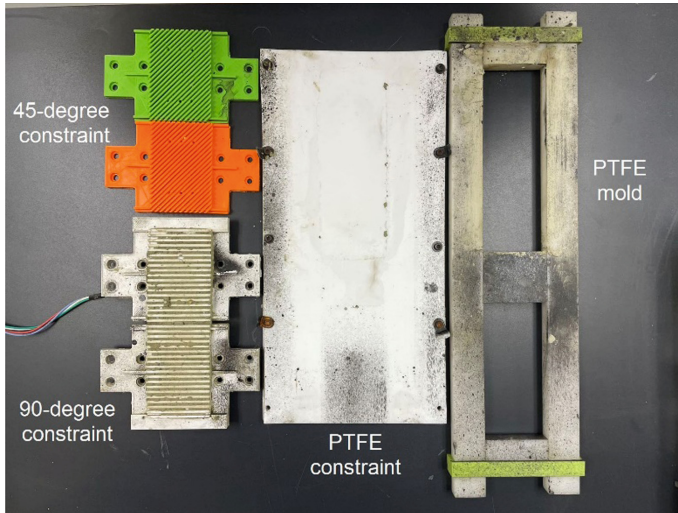


Fig. 1. The PTFE mold and three different constraint platforms. The upper left orange-green platform is the 45-degree constraint; the bottom left white platform is the 90-degree constraint with cables connecting to a force sensor; the middle white platform is the flat PTFE constraint; the right workpiece is the PTFE mold.

90-degree angular constraint platform, and the 45-degree angular constraint platform was used in these test (Fig. 1).

The temperature conditions in the experiment were set to 25 ± 2 °C. The initial moisture content of the sample was measured via the RAD WAG MA 50/1.R moisture analyzer while the temperature was set to 120 °C during the measurement. The initial moisture content of the silt samples tested in the experiments was $25 \pm 1\%$ except for two groups. A precision mass balance, Adventurer Pro AV812C, with a readability of 0.01 g, was installed beneath the platform during the experiment after Exp.18a to record sample mass changes, which correlates with water loss, every 10s during the dehydration periods. Two Canon EOS 4000D cameras were fixed on the aluminum framework in the atmospheric chamber to capture the surface photos to analyze the cracks' appearance and shrinkage at 30 or 60 s intervals.

As shown in Fig. 2, four temperature and humidity sensors were installed in the chamber to record the environmental atmospheric conditions and help the humidifier to maintain a constant relative humidity (RH). The values of three sensors, except sensor A located next to the sample, were shown on the panel and the average relative humidity values are compared with the expected values. When a low expected humidity was set on the panel, the fans located at the silica gel and the entrance of the tube activate if the atmospheric humidity in the chamber was higher than the desired value, thus lowering the relative humidity. When a higher humidity was required, the humidifier in the water tank activated in conjunction with the fans at the water tank and entrance of the tube. The left sensor A, which was next to the sample, monitors and records the atmospheric temperature and relative humidity through an Arduino board. One force sensor was installed beneath the platform to measure the total stress variations during the

desiccation process. Though the numerical results from the stress sensor were subject to bias due to the friction between the platform and framework, the stress peaks that appear at failure are reliable as a qualitative measure to determine the onset start time.

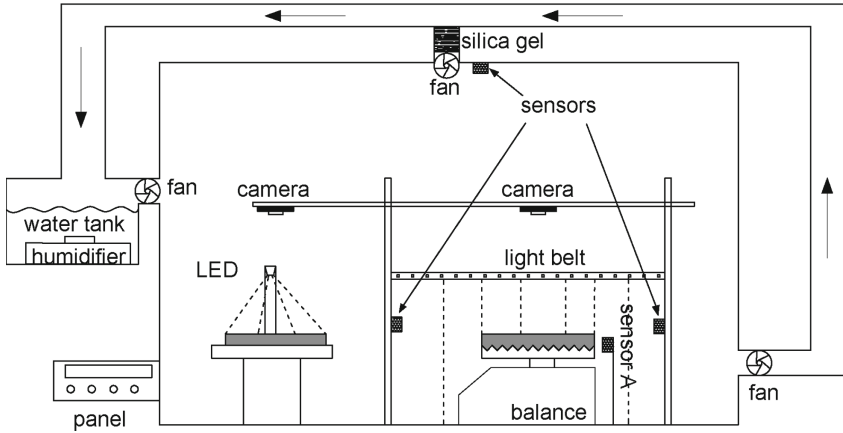


Fig. 2. The atmospheric chamber with humidity controllers; the left sample lies on the PTFE plate and the right sample lies on the platform with constraints; the panel is used to control and monitor the humidity based on three sensors minus the one next to the sample.

3 Results

3.1 Morphology

The details of the experiment, including experiment ID, initial moisture content, and temperature, are shown in the appendix. The top surface of the samples was captured and the patterns of the first (second or third) cracks were recorded. Figure 3(a) and (b) are the initial and final stages in test 25b, which ran for 1180 min. The vertical strain (along the shorter edge on the top surface) was 6% while the horizontal strain (along the longer edge on the top surface) was 3%. Though the samples were free to shrink on the platform, strain deviations along samples thickness are easily observed, which results in the sample shape changing from rectangle to trapezoid.

Figure 3(c) shows the curl at the corners which was another typical observation of stress difference. As shown in Fig. 4, the stress, σ_{xx} , from the evaporation decreases along the thickness while the σ_{xz} comes from the evaporation on the side edge is balanced to each other. Based on the left corner, the torque can be easily calculated and forces the left part of the sample to rotate clockwise and causes the curl at the corner. For the right part of the sample, an inverse direction of torque can be found. The consequence of the curling is that the gravity will provide additional shear stress that will cause a shear failure, which is beyond the research interest in this experimental study. Previous researchers choose to increase the ratio of length over width or choose a circular mold to reduce the influence of side edges in the experiment or simulation [10].

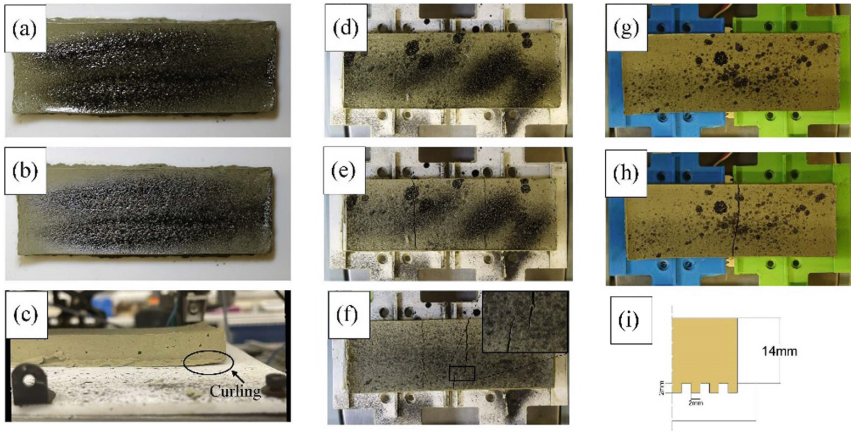


Fig. 3. Typical shape changes under various constraints. (a) The initial stage of test 25b; (b) The final stage of test 25b, 1180 min after starting; (c) The curl at the bottom corner; (d) The initial stage of test 31a; (e) The final stage of test 31a which, 1132 min after starting; (f) The discontinuous cracks in test 34a caused by an air bubble on the sample side; (g) The initial stage of test 23a; (h) The final stage of test 23a, 748 min after starting; (i) The dimension of curves on the basal constraints.

The number of cracks observed from photos at the end of the desiccation experiment varied from 0 to 3. The PTFE support tests had zero instances of cracks over all experiments, which accounted for all instances of no cracks. Meanwhile, cracks consistently appeared for tests with 90 and 45-degree constraints. Figure 3(d), and (e) are the initial and final stages of test 31a with the 90-degree constraint. Two cracks are easily recognized on the top surface parallel with the shorter edge of the sample (vertical to the main axis). Figure 3(g), (h) come from test 23a with the 45-degree constraint, with the sample cracking evenly into two parts. The cracks in all tests have the same directionality of being parallel to the short edge and symmetrically distributed on the silt sample surface.

3.2 Moisture Content Changes

There are three (some researchers combine the second and third stages) typical evaporation rate stages in the desiccation process: a constant rate of evaporation in the first stage, the evaporation rate decreases in the second stage, and the rate approximately equal to zero, and remaining water content is the residual water content in the sample in the third stage [6, 17, 18]. As the interest in this paper is in the onset of the initiation of the first cracks, the experiments stopped in the second stage and remained far away from the residual water stage.

The initial moisture contents were measured by the moisture analyzer and the following moisture content values were calculated based on the recorded mass following Eq. 1

$$MC = \frac{M_t - M_s}{M_t} \quad (1)$$

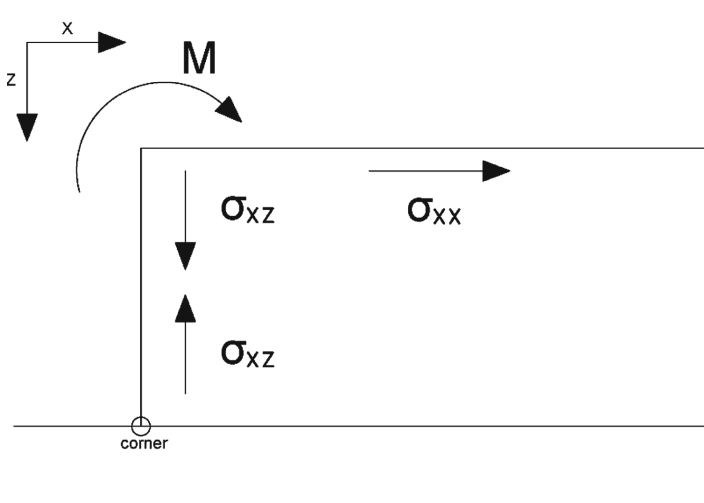


Fig. 4. A sketch of curling at the corner in Exp 25b.

where M_t is the total mass of samples recorded by the balance and M_s is the mass of soil calculated from the initial total mass and initial moisture content.

Figure 5 presents the moisture content changes under different RH settings with both kinds of constraints. Most of the moisture content rate of change decreased when the relative humidity increased as the evaporation process is driven by the water content gradient. However, the result from test 20a showed a higher evaporation velocity compared with test 28a which has lower relative humidity (50%). This abnormal case was caused by a 4 °C temperature difference between these two test groups.

The mass change in test 33a shown in Fig. 5(a) clearly shows two stages and the evolution from a constant velocity stage to a slower velocity stage. The evaporation rate with different constraints is the same once they are under the same environmental conditions.

3.3 Crack Onsets

The crack initiation is restored with the help of the stress sensor at the bottom of the platform. The propagation dynamics is beyond the research interest in this paper, but the stress plots show a sharp rebound during the fracture process caused by the invasion of gas as the sample reaches its crack onset threshold [19]. The stress in Fig. 6 is normalized by dividing the max absolute stress values in the process while the negative values represent the compression in the shrinkage stage. The normalized stress sharply increases at 655 min, which indicates a failure in the sample.

Figure 6 shows the relation between the relative humidity and the first crack appearance time while the upper subfigure represents the stress in the mid of the sample. The negative value means the compression and the total stress exist an increment till the air entry appears. At the air entry point, the suction experienced a sharp decrement, which is known as the Haines jump, which is treated as the onset of cracks. The first crack time

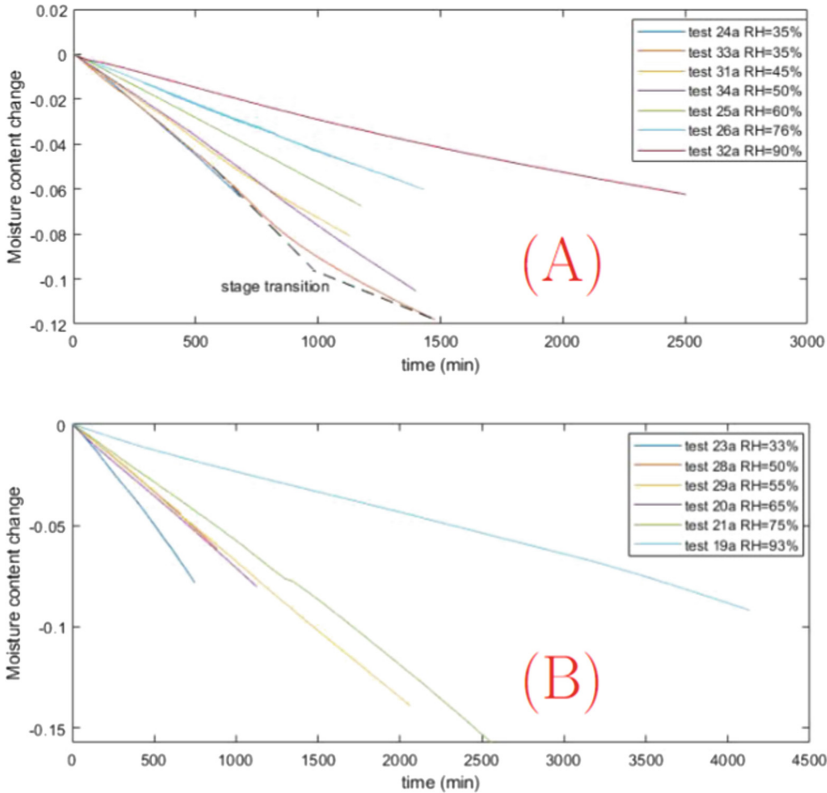


Fig. 5. Moisture contents changes, calculated as the difference between initial moisture content and the moisture content during the test. (a) Evaporation with the 90-degree constraint; (b) Evaporation with the 45-degree constraints; The noise present in test 21a is caused by an apparatus malfunction, but the moisture content rate of change has the same slope before and after the malfunction.

in test 23a (45-degree constraint, humidity of 33%) and test 33a (90-degree constraint, humidity of 35%) was 39300s and 40700s. The first crack time in test 28a (45-degree constraint, humidity of 50%) and test 34a (90-degree constraint, humidity of 50%) was 44910s and 42200s. The onsets of different constraints show up at nearly the same time in the low humidity conditions. Test 21a (45-degree constraint, humidity of 75%) had its first crack at 69780s while test 26a (90-degree constraint, humidity of 76%) had its first crack at 76920s. The time difference increases when the humidity becomes higher and the 90-degree constraint tests tended to have earlier times of failure than the 45-degree constraint tests.

4 Conclusions

This paper discusses laboratory experiments in an atmosphere chamber with variable RH on geomaterials subject to various basal constraints. These results were proceeded

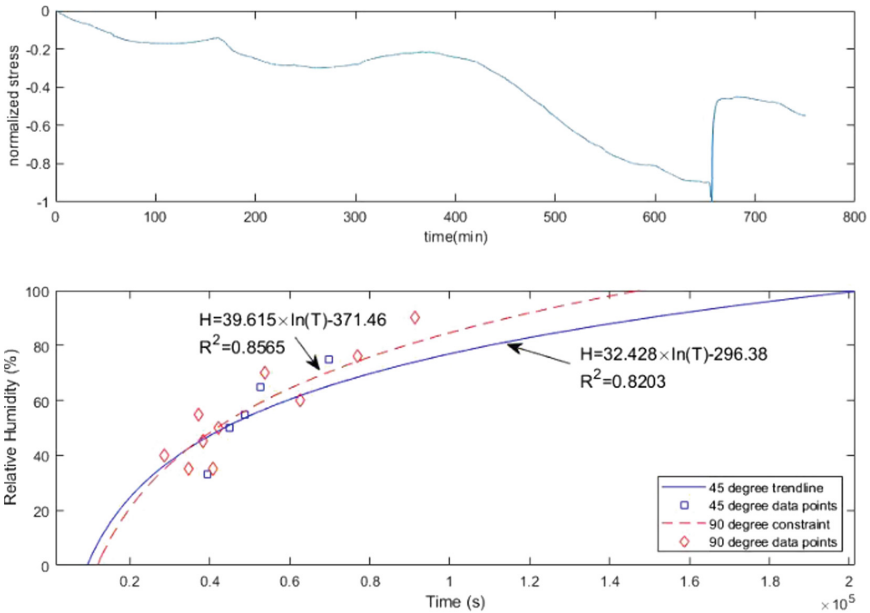


Fig. 6. Crack onsets; The upper figure is the normalized stress change with time in test 23a, a stress rebound appearing at 655 min was the sign of crack onset; The lower figure is the crack onset data and tendency lines with different humidity and constraints.

to analyze the influence of environmental conditions on material desiccation, with the main findings summarized as follows:

1. The pattern of cracks was different between the PTFE flat plate and constraint platforms. No cracks were found in the PTFE experiments while cracks that were parallel to the short edge appeared when there were basal constraints.
2. The curling at the corner is a result of the torque caused by the stress from different moisture content distributions inside the sample. This curling can cause shear stress that will also influence sample failure.
3. The cracks initiate in the constant evaporation rate stages when most of the free water evaporates and air entry happens. In this stage, the total compression increases till the air entry which causes suction decrement.
4. The onsets increase when RH increases and were relatively the same with different basal constraints at low RH, where the moisture content gradient was the predominant contributor towards failure. At high RH, cracks in the 90-degree group appeared earlier than that in the 45-degree group, which is the influence of the basal strain constraints.

Appendix

See Table 2.

Table 2. Desiccation test summary

Exp ID	Initial moisture content (%)	Relative humidity (%)	Temperature (°C)	Initial porosity (%)	Photos interval (s)	Constraints
15*	25.9	94	24	—	60	90-degree constraint
16**	26.5	70	24	—	60	90-degree constraint
17*	25.8	55	24	—	60	90-degree constraint
18*	26	40	25	—	60	90-degree constraint
19a	25.4	93	25	57.4746	60	45-degree constraint
19b	25.4	93	25	57.4746	60	PTFE with lubricant
20a	25.1	65	27	57.0125	60	45-degree constraint
20b	25.1	65	27	57.0125	60	PTFE with lubricant
21a	26.2	75	27	59.5201	60	45-degree constraint
21b	26.2	75	27	59.5201	60	PTFE with lubricant
23a	25.1	33	26	55.1577	60	45-degree constraint
23b	25.1	33	26	55.1577	60	PTFE with lubricant
24a	25.5	35	24	53.6896	60	90-degree constraint
24b	25.5	35	24	53.6896	60	PTFE with lubricant
25a	24.8	60	25	53.7324	60	90-degree constraint
25b	24.8	60	25	53.7324	60	PTFE with lubricant
26a	25	76	24	53.9641	60	90-degree constraint

(continued)

Table 2. (continued)

Exp ID	Initial moisture content (%)	Relative humidity (%)	Temperature (°C)	Initial porosity (%)	Photos interval (s)	Constraints
26b	25	76	24	53.9641	60	PTFE with lubricant
28a	25.9	50	23	56.5372	30	45-degree constraint
28b	25.9	50	23	56.5372	30	PTFE with lubricant
29a	25.7	55	24	55.9573	30	45-degree constraint
29b	25.7	55	24	55.9573	30	PTFE with lubricant
31a	24.7	45	24	52.865	60	90-degree constraint
31b	24.7	45	24	52.865	60	PTFE with lubricant
32a**	23.5	90	24	51.6679	60	90-degree constraint
32b**	23.5	90	24	51.6679	60	PTFE with lubricant
33a	25.7	35	26	53.8115	60	90-degree constraint
33b	25.7	35	26	53.8115	60	PTFE with lubricant
34a	24.6	50	24	50.9749	60	90-degree constraint
34b	24.6	50	24	50.9749	60	PTFE with lubricant

*The sensitive balance was not installed in these tests.

**The initial moisture contents are beyond the expected range but results are used and discussed.



References

1. Kodikara, J.: Desiccation. In: Bobrowsky P.T., Marker B. (eds.) Encyclopedia of Engineering Geology. Encyclopedia of Earth Sciences Series. Springer, Cham (2020). https://doi.org/10.1007/978-3-319-73568-9_87
2. Zeng, H., Tang, C.-S., Cheng, Q., Zhu, C., Yin, L.-Y., Shi, B.: Drought-induced soil desiccation cracking behavior with consideration of basal friction and layer thickness (2020). <https://doi.org/10.1029/2019WR026948>
3. J.P. Gourc, S. Camp, B.V.S. Viswanadham, S. Rajesh, Deformation behavior of clay cap barriers of hazardous waste containment systems: Full-scale and centrifuge tests, Geotext. Geomembr.
4. Tang, C.S., Cui, Y.J., Tang, A.M., Shi, B.: Experiment evidence on the temperature dependence of desiccation cracking behavior of clayey soils. Eng. Geol. **114**(3–4), 261–266 (2010)

5. Tang, C.-S., Zhu, C., Cheng, Q., Zeng, H., Xu, J.-J., Tian, B.-G., Shi, B.: Desiccation cracking of soils: a review of investigation approaches, underlying mechanisms, and influencing factors. *Earth-Sci. Rev.*
6. Ward, W.G., Fredlund, D.G., Barbour, S.L.: Coupled soil-atmosphere modelling for soil evaporation. *Can. Geotech. J.*
7. Rodríguez, R., Sánchez, M., Ledesma, A., Lloret, A.: Experimental and numerical analysis of desiccation of a mining waste. *Can. Geotech. J.*
8. Nahlawi, H., Kodikara, J.K.: Laboratory experiments on desiccation cracking of thin soil layers. *Geotech. Geol. Eng.*
9. Uday, K.V., Singh, D.N.: Investigation on cracking characteristics of fine-grained soils under varied environmental conditions. *Drying Technol.* **31**(11), 1255–1266 (2013). <https://doi.org/10.1080/07373937.2013.785433>
10. Peron, H., Laloui, L., Hueckel, T., Hu, L.B.: Desiccation cracking of soils. *Eur. J. Environ. Civ. Eng.* **13**(7–8), 869–888 (2009)
11. Hueckel, T.A.: Water–mineral interaction in hygromechanics of clays exposed to environmental loads: a mixture-theory approach. *Can. Geotech. J.* **29**(6), 1071–1086 (1992). <https://doi.org/10.1139/t92-124>
12. Corte, A., Higashi, A.: Experimental research on desiccation cracks in soil (No. CRREL-RR-66 Final Rpt.) (1964)
13. Lakshmikantha, R.M., Prat Catalán, P., Ledesma Villalba, A.: Boundary effects in the desiccation of soil layers with controlled environmental conditions. *Geotech. Test. J.* **41**(4), 675–697 (2018).
14. Prat, P.C., Ledesma, A., Lakshmikantha, M.R.: Size effect in the cracking of drying soil. In: *Fracture of Nano and Engineering Materials and Structures* (pp. 1373–1374). Springer, Dordrecht (2006)
15. Bažant, Z.P.: Size effect in blunt fracture: Concrete, rock, metal. *J. Eng. Mech.* **110**(4), 518–535 (1984). [https://doi.org/10.1061/\(ASCE\)0733-9399\(1984\)110:4\(518\)](https://doi.org/10.1061/(ASCE)0733-9399(1984)110:4(518))
16. Prat, P., Ledesma, A., Lakshmikhanta, M.R., Levatti, H.U., Tapia, J.: Fracture mechanics for crack propagation in drying soils. In: *12th International Conference on Computer Methods and Advances in Geomechanics 2008*. Leibniz Information Centre for Science and Technology University Library (TIB) (2008)
17. Haines, W.B.: The volume-changes associated with variations of water content in soil. *J. Agric. Sci.* **13**(3), 296–310 (1923)
18. Tang, C.S., Shi, B., Liu, C., Suo, W.B., Gao, L.: Experimental characterization of shrinkage and desiccation cracking in thin clay layer. *Appl. Clay Sci.* **52**(1–2), 69–77 (2011)
19. Shin, H., Santamarina, J.C.: Open-mode discontinuities in soils. *Geotech. Lett.* **1**(4), 95–99 (2011)



Modeling Fault Rupture Through Layered Geomaterials with SPH

Enrique M. del Castillo¹ , Alomir H. Fávero Neto² , and Ronaldo I. Borja¹

¹ Department of Civil and Environmental Engineering, Stanford University, 473 Via Ortega, Stanford, CA 94305, USA
emdc@stanford.edu

² Department of Civil and Environmental Engineering, Bucknell University, 1 Dent Drive, Lewisburg, PA 17837, USA

Abstract. Shallow-lying faults that propagate and rupture at the surface during earthquakes cause significant deformation and damage, putting nearby structures and utilities at risk. Modeling fault propagation and the associated large deformations is tractable for continuum meshfree numerical methods, such as Smoothed Particle Hydrodynamics (SPH), as they avoid mesh entanglement or distortion seen for example in the Finite Element Method. SPH is particularly advantageous since strain localization and kinematic discontinuities, which are two fundamental attributes of faulting, arise naturally without the need for additional enhancements or formulations. Some of our previous work used SPH to show that both normal and reverse faults rotate with increasing slip, passing from Roscoe to Arthur to Coulomb orientations as they propagate. Our results suggest that these three orientations may be stages in the fault development process, helping to explain the varying fault orientations observed in field outcrops. Here, we summarize and expand upon these results, considering how soil inhomogeneity influences fault orientation and propagation path, as well as the width of the fault damage zone.

Keywords: Fault rupture · Layered geomaterials · Smoothed particle hydrodynamics

1 Introduction

The rupture of shallow normal or reverse faults below the surface (blind faults), results in the propagation of a band of localized strain upwards towards the surface, forming a scarp. Often these blind faults lie within strong and rigid bedrock, with soil, loose sands, or alluvium above. A mechanically similar albeit larger scale problem is that of faulting in rigid basement rock overlain by sedimentary cover, where slip in the basement rock fault causes propagation of localized strain into the sedimentary cover, as well as associated fault-propagation folding. These localized bands of strain, or shear bands, can be considered faults whenever they are accompanied by a kinematic discontinuity or when lateral slip accumulates between two previously continuous layers across the band.

An essential question regarding strain localization is that of the orientation or angle taken by shear bands or faults as they nucleate and propagate in geomaterials. The work of Coulomb defined the fault orientation with respect to the maximum principal stress σ_1 as,

$$\Theta_C = 45^\circ \pm (\varphi/2) \quad (1)$$

where φ is the internal angle of friction, such that the Coulomb failure criterion is satisfied on a fault of that orientation. Widely applied to the interpretation of faulting and regional tectonics through Andersonian faulting theory, much controversy persists by the fact that faults found in nature are often not oriented at the Coulomb angle, and instead may lie closer to either the Roscoe angle $\Theta_R = 45^\circ \pm (\psi/2)$, defined with respect to the maximum principal incremental strain, or the Arthur angle $\Theta_A = 45^\circ \pm (\varphi + \psi)/4$, where ψ is the dilatancy angle.

While considerable computational and experimental studies have been performed regarding shear band orientations under relatively simple boundary conditions (for example, under plane-strain compression), only recently has the orientation of shear bands in geomaterials under more complex boundary conditions, such as in reverse or normal fault propagation through geomaterials, been considered [1–3]. Despite its importance in helping predict the fault scarp location and the full extension of the surface damage zone, the temporal evolution of the fault or shear band rupture orientation at the surface, including after the initial surface rupture, has been mostly overlooked. Furthermore, empirical failure surfaces, such as those using logarithmic spirals, have been proposed for a fixed amount of fault slip or offset, usually that required for the initial surface rupture, and use the orientation angle observed at the initial surface rupture. Consequently, the accuracy of these empirical failure surfaces rapidly deteriorates with greater accumulated slip or offset on the blind fault.

In our previous work [1] using numerical simulations of perfectly plastic soil, we showed that shear bands undergo a rotation from Roscoe to Arthur to Coulomb angles in both normal and reverse fault systems, as slip is accumulated on the fault in the bedrock. These results suggest that the shear band rotation is not merely a product of strain softening behavior, but at least in part a result of the boundary conditions and problem geometry. In addition, most previous studies have focused on discerning and modeling fault propagation and rupture in homogenous single layered soil or rock, which is not representative of field conditions, where faults cut across heterogenous and layered geomaterials. We seek to remedy this shortcoming by considering models of stratified soils consisting of layers of loose sand (S) or “soft rock” (RC, meaning rock) a laboratory analogue corresponding to a weak sandstone rock, as proposed by Hung et al. [2]. In particular, we analyze the temporal evolution of shear band orientations in these single and multi-layered geomaterial assemblages that may be perfectly plastic or that undergo strain-softening behavior.

2 Smoothed Particle Hydrodynamics and Computational Methods

This study and our previous work make use of Smoothed Particle Hydrodynamics (SPH), a meshfree continuum method, to conduct numerical simulations of fault propagation

and rupture simulations. SPH solves the strong form of the mechanical boundary value problem, and the continuum domain is discretized into a collection of so-called domain particles possessing continuum properties, which are found for a specific particle using a convolution integral over a given integration domain with a smoothing or weighting function. The size of this integration domain is specified by the smoothing length, which is a numerical characteristic length scale leading SPH to have non-local properties if it is maintained fixed as the discretization changes [1, 4]. Dirichlet boundary conditions are imposed using the formulation of Adami et al. [5], where solid boundaries are discretized into so-called boundary particles which are either fixed or moved with a prescribed velocity and possess constant properties except for stress which is evolved. These boundary particles help avoid penetration of the boundaries by domain particles. SPH is well suited for simulating slope failure [6, 7] and the propagation of faults in soil [1, 8], due to its meshfree nature and because strain localization arises naturally without the need for additional theory or enhancements to the method. Our previous work [1, 8] has shown that SPH can replicate the geometry and kinematics of analogue sandbox or centrifuge experiments while easily providing strain, strain rate, and stress field data, which may be otherwise difficult to obtain in analogue experiments.

In our SPH simulations, the loose sand and soft rock are modeled as elastoplastic materials with a non-associative flow rule on the Drucker-Prager yield criterion. To preserve objectivity under large deformations, an objective stress rate, namely, the Jaumann rate is used [9]. An isotropic strain softening response where the internal friction angle and the dilatancy angle are degraded from a peak to a residual value as a function of the octahedral plastic strain, is employed following the method of Anastasopoulos et al. [10], for some of our simulations.

3 Numerical Simulations and Discussion

In total, four different simulations of reverse fault propagation are carried out. All four simulations are conducted in a 50-m-wide (L) and 8-m-high (H) computational domain discretized into 24,000 domain particles surrounded by walls discretized into boundary particles. In all four simulations, a velocity is imparted on one side of the boundary (along the hanging wall side) and is pushed at a rate V , along an angle $\theta = 60^\circ$, which corresponds to the inclination of the reverse fault in the bedrock, to simulate slippage along this fault. All other boundaries are held fixed. The pushing rate V was 0.2 m/min, rendering equivalent strain rates far below the 0.1 s^{-1} threshold above which SPH is known to exhibit rate-dependent behavior. The pushing is applied until the vertical displacement of the hanging side U (or fault throw) reached 68% of the total height H of the model ($U/H = 68\%$). A schematic of the simulation setup and boundary conditions is presented in Fig. 1.

In the first simulation, the entire computational domain consisted of perfectly plastic sand (RC0S10), the second simulation consisted of sand showing isotropic strain softening (RC0S10s), the third simulation consisted of a bottom half of soft rock and a top half of sand, with both materials experiencing isotropic strain softening (RC5S5s), and the fourth divided the domain into a bottom 70% soft rock and upper 30% sand (RC7S3s)

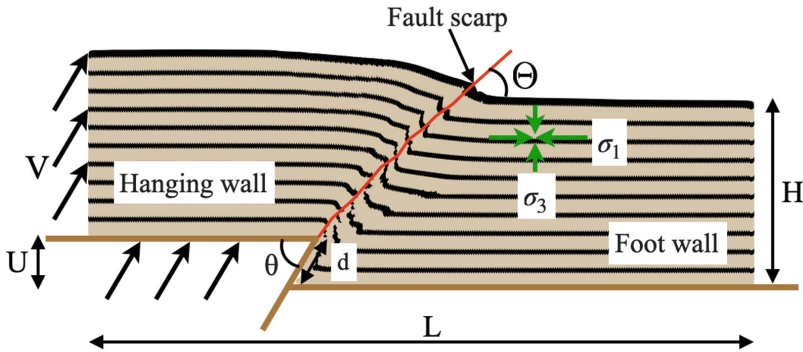


Fig. 1. Boundary value problem setup for the fault propagation simulations, showing the relevant boundary conditions and dimensions. The boundaries are discretized into boundary particles, and the pushing velocity V is applied to the boundary particles along the hanging wall. An example resultant fault is traced in red. The direction of the maximum principal stress σ_1 shown in green is roughly horizontal throughout the top of the foot wall and near the fault scarp. The orientation of the fault tip at the point of surface rupture Θ is measured with respect to the horizontal in this case. The fault slip d equals $U/\sin \theta$.

again with both materials exhibiting strain softening. The values for the material parameters used in the simulations, which are given in Table 1, are taken from the sands and soft rock mixture used in the centrifuge experiments of Hung et al. [2].

Table 1. Simulation parameter values. Key: ρ = material density, c = cohesion, φ_p, ψ_p = ultimate mobilized (peak) friction and dilatancy angles, $\varphi_{res}, \psi_{res}$ = residual friction and dilatancy angles, E = Young’s modulus, ν = Poisson ratio, γ_f^p = plastic octahedral shear strain at the end of softening. For the sand, $\gamma_f^p = 0.022$, whereas for the soft rock, $\gamma_f^p = 0.013$. See Anastasopoulos et al. [10], for details regarding these parameters. In the RC0S10 simulation with perfectly plastic behavior, φ_p and ψ_p were used as the friction and dilatancy angles, respectively.

Material	ρ [g/cm ³]	c [kPa]	φ_p [°]	φ_{res} [°]	ψ_p [°]	ψ_{res} [°]	E [MPa]	ν
Loose sand (S)	1.59	0	37	34.7	12.8	0	20	0.3
Soft rock (RC)	1.57	143	43.6	39.8	37.6	11.4	218.9	0.3

In Fig. 2, colored material marker layers are plotted in the left column and contours of the accumulated plastic strain are plotted in the right column for the four different simulations, RC0S10 (top row), RC0S10s (second row), RC5S5s (third row), and RC7S3s (bottom row). The material marker layers have no mechanical significance and have the purpose of highlighting folding and deformation. In all four simulations, a gently rolling monocline is the main structural feature. The fault folding zone is delimited by a main series of synthetic faults (red) and an antithetic shear band or fault (cyan). In general, all shear bands propagate upwards, and most form from the tip of the fault in the bedrock,

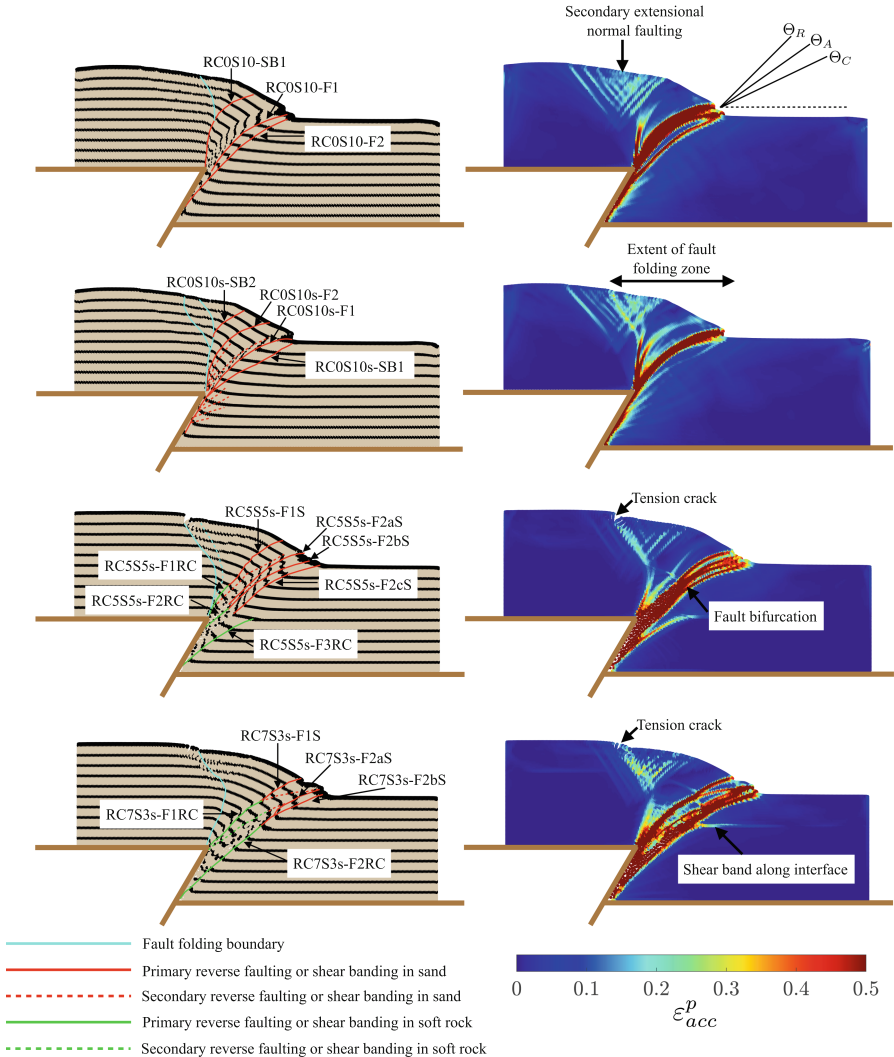


Fig. 2. Snapshots of colored marker layers (left) and accumulated plastic strain (right) at $U/H = 50\%$ for the four different simulations (one in each row). In terms of the nomenclature used, faults observed in the simulation are labeled as -F whereas shear bands as -SB both followed by a corresponding number. For comparison, the theoretical Roscoe, Arthur, and Coulomb orientations are plotted in the top row of the right column using the residual values of the friction and dilatancy angles of the sand.

coalescing with a small area of localization near the surface. Exceptions to this rule occur whenever faults bifurcate, forming from a preexisting fault or band at some intermediate height. In the RC5S5 simulation, the faults refract, locally steepening their orientation as they cross from the stiff soft rock to the compliant sand. The inclination at the fault tip in the sand layer then decreases with respect to the horizontal as propagation continues.

Looking at the temporal evolution of the orientations of the different shear bands or faults measured at their upmost tip, we find that they fully propagate to the top surface and rupture at the Roscoe angle, only to rotate towards Arthur and then Coulomb inclinations with increased fault throw. A rapid decrease in steepness is visible in most faults or shear bands at their tip prior to surface rupture, which happens when the faults/bands are close to the Roscoe orientation. Furthermore, the faults and bands proceed to rapidly leave the Roscoe orientation and stabilize at the Arthur angle from around $U/H = 10$ to 45% depending on the particular shear band or fault, spending a significant proportion of the evolution process at or near the Arthur angle. This behavior is generally visible regardless of the presence of layering or strain softening in the simulation.

The effect of strain softening on fault orientation as seen in simulation RC0S10s is to slightly reduce the longevity of the stable region at the Arthur orientation. In addition, the final orientation of 17° for fault RC0S10-F1s at $U/H = 50\%$ is reasonably close to that measured from the centrifuge experiment of Hung et al. at 14° and is closer than that measured from the RC0S10 simulation without strain softening, which is 22° , likely due to the absence of the strain softening behavior in the latter.

In the RC5S5s and RC7S3s simulations, where layering is added, a rotation of the shear bands and faults is again observed as they propagate in the sand layer but now the greatest period of stability lies mostly around the Coulomb angle, with the Roscoe and Arthur stages being transitory. Furthermore, the faults and shear bands within the soft rock do not follow the typical Roscoe, Arthur, Coulomb rotation, achieving roughly constant orientations at angles at or above the Roscoe prediction. At $U/H = 50\%$, the orientations of fault F2aS and F2bS are both 24° in the centrifuge experiments of Hung et al., whereas in our SPH simulations they are 24 and 25.1° respectively, showing strong agreement. More details, results, and analysis regarding the changing orientations of faults and shear bands in our simulations will be reported in future work.

4 Conclusions

Simulations of reverse fault rupture are performed using SPH models of soft rock and loose sand. Sand layering superimposed over soft rock, as opposed to a homogenous sand medium, changes the number of faults generated as well as their orientation within the simulation model significantly. Nevertheless, a rotation of fault and shear band orientation measured at the upwards fault/band tip, from Roscoe to Arthur to Coulomb inclinations, is omnipresent in all models, including sands modeled as perfectly-plastic, suggesting this rotation is a feature of the boundary conditions, not of strain softening behavior. Future work should consider the factors controlling shear band/fault refraction across different materials, as well as an in-depth exploration of principal stress and strain increment directions within the SPH models, particularly in the vicinity of the propagating faults.

Acknowledgments. This material is supported by the National Science Foundation under Award Number CMMI-1914780. The first author acknowledges the support by the U.S. National Science Foundation (NSF) Graduate Research Fellowship under Grant DGE 1656518, as well as by the Stanford Graduate Fellowship.

References

1. del Castillo, E.M., Fávero Neto, A.H., Borja, R.I.: Fault propagation and surface rupture in geologic materials with a meshfree continuum method. *Acta Geotech.* **16**(8), 2463–2486 (2021). <https://doi.org/10.1007/s11440-021-01233-6>
2. Hung, W.-Y., Soegianto, D.P., Wang, Y.-H., Huang, J.-X.: Reverse fault slip through soft rock and sand strata by centrifuge modeling tests. *Acta Geotech.* **17**, 1–20 (2022). <https://doi.org/10.1007/s11440-021-01447-8>
3. Hazeghian, M., Soroush, A.: DEM-aided study of Coulomb and Roscoe theories for shear band inclination. *Acta Geotech.* (2022). <https://doi.org/10.1007/s11440-022-01475-y>
4. Vignjevic, R., Djordjevic, N., Gemkow, S., De Vuyst, T., Campbell, J.: SPH as a nonlocal regularisation method: solution for instabilities due to strain-softening. *Comput. Methods Appl. Mech. Eng.* **277**, 281–304 (2014). <https://doi.org/10.1016/j.cma.2014.04.010>
5. Adami, S., Hu, X.Y., Adams, N.A.: A generalized wall boundary condition for smoothed particle hydrodynamics. *J. Comput. Phys.* **231**, 7057–7075 (2012). <https://doi.org/10.1016/j.jcp.2012.05.005>
6. Fávero Neto, A.H., Borja, R.I.: Continuum hydrodynamics of dry granular flows employing multiplicative elastoplasticity. *Acta Geotech.* **13**(5), 1027–1040 (2018). <https://doi.org/10.1007/s11440-018-0700-3>
7. Fávero Neto, A.H., Askarinejad, A., Springman, S.M., Borja, R.I.: Simulation of debris flow on an instrumented test slope using an updated Lagrangian continuum particle method. *Acta Geotech.* **15**(10), 2757–2777 (2020). <https://doi.org/10.1007/s11440-020-00957-1>
8. del Castillo, E.M., Fávero Neto, A.H., Borja, R.I.: A continuum meshfree method for sandbox-style numerical modeling of accretionary and doubly vergent wedges. *J. Struct. Geol.* **153**, 104466 (2021). <https://doi.org/10.1016/j.jsg.2021.104466>
9. Borja, R.I.: *Plasticity Modeling and Computation*. Springer, Berlin (2013)
10. Anastasopoulos, I., Gazetas, G., Bransby, M.F., Davies, M.C.R., El Nahas, A.: Fault rupture propagation through sand: finite-element analysis and validation through centrifuge experiments. *J. Geotech. Geoenviron. Eng.* **133**(8), 943–958 (2007)



Progressive Failure in Viscoplastic Materials: The Case of Creeping Landslides

Luca Flessati^(✉) and Claudio di Prisco

Politecnico di Milano, Milano, Italy
luca.flessati@polimi.it

Abstract. In the assessment of rainfall induced landslide hazard, both the comprehension and the theoretical interpretation of the inception phase of unexpected collapses are crucial. In this paper, the case of an infinite long slope is theoretically discussed by assuming the mechanical behaviour of the materials involved to be strain softening elastic-viscoplastic. Rainfall is assumed to induce variations, taking place with time, in the water table level and, consequently, in the effective state of stress. Consequently, accelerations in both strains and displacements, due to the temporal evolution of the perturbation, are not necessarily associated with a system instability or vice versa decelerations are not the signature of a stable system response. In this paper, from a theoretical point of view, the authors apply the controllability theory conceived for a representative elementary volume to a boundary value problem and demonstrate that (i) irreversible strains accumulate, due to the structural hardening, even outside of the shear band, whose thickness is a function of the imposed perturbation, (ii) local instability anticipates the global one, (iii) once assigned the temporal evolution of the perturbation, its frequency does not affect the system response.

Keywords: Progressive failure · Viscoplasticity · Slope stability

1 Introduction

In the scientific literature, the term “creeping landslides” is commonly used to define slow-moving masses along slopes. In many cases, when slopes are not perturbed (i.e. the slope is subject to constant external forces), an almost constant velocity is observed. This is the typical case of masses sliding on predefined (and not spatially evolving) failure surfaces in which the material reached the critical state (“post-failure events”). In other cases (“pre-failure events”), displacements are associated with both progressive accumulation of damage in the material (material softening) along the failure surface and spatial propagation of this latter (structural hardening). In case the system is not perturbed, when structural hardening prevails, the slope progressively decelerates (primary creep), whereas when material softening prevails, a progressive increase in velocity (tertiary creep) is expected. When these two phenomena are balanced, the system evolves at constant rate (secondary creep), but, the microstructure evolves and after a sufficiently long time, a transition toward an unstable response is expected.

In practice slopes are never unperturbed systems and always subject to time-varying perturbations (e.g. rainfall induced cyclic oscillations in water table level), inducing slopes accelerations/decelerations, that do not have to be interpreted as signs of an unstable/stable system response.

In this paper the authors intend to discuss the role of perturbations in affecting the temporal evolution of displacements in an infinite long slope. To this aim, the theory of controllability applied to elastic viscoplastic strain-softening constitutive relationships is employed and discuss the spatial propagation and the temporal evolution of irreversible strains. For the sake of simplicity, here in the following inertia effects, hydro-mechanical coupling and the role of partial saturation are dis-regarded. The condition for the onset of instability in unperturbed cases is firstly discussed, both at the representative element (local) and at the slope (global) scale. Subsequently, a definition of instability, suitable for cyclic perturbations characterized by constant amplitude and period, is introduced.

2 Onset of Instability in Elastic-Viscoplastic Materials

Elastic-viscoplastic constitutive laws cannot be written in an incremental form, implying that standard approaches [1, 2] commonly adopted to study the stability of the material mechanical response subject to a given type of control cannot be employed. For elastic-viscoplastic materials, the onset of instability can be defined by employing the approach proposed in [3], combining Lyapunov theory of stability [4] and controllability theory [2]. According to this approach, under quasi-static mixed stress-strain control conditions, the constitutive relationship can be written as it follows:

$$\dot{\mathbf{X}} = \mathbf{A}\mathbf{X} + \mathbf{F}, \tag{1}$$

where \mathbf{X} and $\dot{\mathbf{X}}$ are the vectors containing the rate and acceleration of the response variables (changing according to the test control), respectively, \mathbf{F} is a forcing term related with the controlled variables and their first- and second-time derivative, whereas matrix \mathbf{A} depends on both constitutive relationship functions and controlled variable rates (\mathbf{Y}).

In case of “generalized creep tests” (i.e. when $\mathbf{Y} = \dot{\mathbf{Y}} = 0$), $\mathbf{F} = 0$ and matrix \mathbf{A} depends only on constitutive relationship functions. For this reason, the eigenvalues of \mathbf{A} ($\lambda_i(\mathbf{A})$) can be employed to study the stability of the material response: instability, defined in terms of the acceleration in the response variables, is obtained when at least one eigenvalue of \mathbf{A} becomes positive. For elastic-viscoplastic materials this condition coincides [3] with:

$$H_{IN} = H - H_\chi < 0 \tag{2}$$

where H and H_χ are the hardening and the controllability [5] modulus, respectively, depending on the constitutive relationship and on the type of control imposed.

By assuming a linear isotropic elastic law, under simple shear conditions, representative for a single layer at depth z of a θ -inclined and h -thick infinite long slope (Fig. 1), \mathbf{Y} , \mathbf{X} and H_χ are [6]:

$$\mathbf{Y} = \left[\dot{\sigma}'_n \quad \dot{\tau}_m \quad \dot{\epsilon}_t = 0 \quad \dot{\epsilon}_y = 0 \right]^T \tag{3}$$

$$X = \left[\dot{\varepsilon}_n \quad \dot{\gamma}_m \quad \dot{\sigma}'_t \quad \dot{\sigma}'_y \right]^T \tag{4}$$

$$H_X = - \frac{\partial f}{\partial \sigma'_t} \frac{E}{1 - \nu^2} \frac{\partial g}{\partial \sigma'_t}, \tag{5}$$

where n and t are the axes normal and parallel to the bedrock (Fig. 1), y the out-of-plane axis, f and g the yield function and the plastic potential, whereas E and ν the Young’s modulus and the Poisson ratio, respectively.

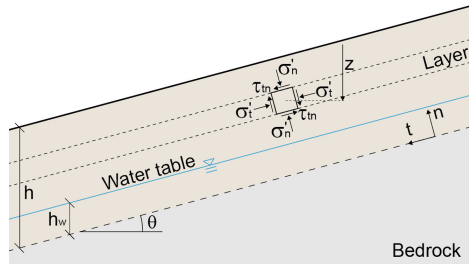


Fig. 1. Layer of an infinite slope under simple shear conditions

3 Controllability Theory Applied to the Detection of Instability in an Elastic-Viscoplastic Infinite Long Slope

In case hydro-mechanical coupling and dynamic effects are disregarded, the approach for the single layer can easily be extended for the entire stratum. For the sake of brevity, only the case of instability induced by the excursion of the water table level (h_w , Fig. 1) will be hereafter discussed.

To generalize the previously mentioned approach to the global system response, the following integrated variables can be introduced:

$$\dot{X}^g = \left[\dot{u}_n \quad \dot{u}_t \quad \dot{\Sigma}_t \quad \dot{\Sigma}_y \right]^T = \left[\int_0^h \dot{\varepsilon}_n dz \quad \int_0^h \dot{\gamma}_m dz \quad \int_0^h \dot{\sigma}'_t dz \quad \int_0^h \dot{\sigma}'_y dz \right]^T \tag{6}$$

Even in this case, the stability can be studied when the system is unperturbed, i.e. when $\dot{h}_w = 0$. Under this assumption, the local response variables can be put in relation

with the global ones as it follows [7]:

$$\dot{X}^g = \begin{bmatrix} \ddot{u}_n \\ \ddot{u}_t \\ \ddot{\Sigma}_t \\ \ddot{\Sigma}_y \end{bmatrix} = \begin{bmatrix} \int_0^h (A_{11}\dot{\epsilon}_n + A_{13}\dot{\sigma}'_t) dz \\ \int_0^h (A_{22}\dot{\gamma}_m + A_{23}\dot{\sigma}'_t) dz \\ \int_0^h A_{33}\dot{\sigma}'_t dz \\ \int_0^h A_{44}\dot{\sigma}'_y dz \end{bmatrix} \quad (7)$$

being A_{ij} the terms (depending on depth) of the local constitutive matrix of Eq. 1. According to [7], Eq. 7 can conveniently be rewritten as:

$$\dot{X}^g = (A^{max} - \Omega)X^g = A^g X, \quad (8)$$

where $A_{ij}^{max} = \max\{A_{ij}\}$ in the whole spatial domain, whereas

$$\Omega = \begin{bmatrix} \Omega_{11} & 0 & \Omega_{13} & 0 \\ 0 & \Omega_{22} & \Omega_{23} & 0 \\ 0 & 0 & \Omega_{33} & 0 \\ 0 & 0 & 0 & \Omega_{44} \end{bmatrix}. \quad (9)$$

The definition of each term in Eq. 9, reported in [7], is hereafter omitted for the sake of brevity. For the sake of clarity, the definition of the term related to shear strain rates is given here below:

$$\Omega_{22} = \frac{\int_0^h (A_{22}^{max} - A_{22})\dot{\gamma}_m dz}{\int_0^h \dot{\gamma}_m dz}. \quad (10)$$

Analogously to what is observed at the representative elementary volume scale, global instability is expected when at least one eigenvalue of A^g becomes positive. Since Ω_{ij} are positive by definition (Eq. 10), condition $\lambda_i(A^g) \geq 0$ (global instability) is necessarily anticipated by condition $\lambda_i(\mathbf{A}^{max}) \geq 0$ (first local instability). In other words, the first local instability is a precursory sign of the global one.

4 Numerical Results

The case of an infinite slope ($\theta = 30^\circ$, $h = 5$ m) constituted of an isotropic strain softening elastic visco-plastic material is hereafter considered. The material is assumed to be characterized by dry and saturated unit weights equal to 16 and 20 kN/m³, respectively. The elastic properties are assumed to be constant along depth. A Mohr-Coulomb yield criterion is considered:

$$f = \sqrt{4\tau_m^2 + (\sigma'_n - \sigma'_t)^2} - (\sigma'_n + \sigma'_t) \sin \phi' - 2c' \quad (11)$$

where c' and ϕ' are cohesion and friction angle, respectively. Cohesion is assumed to be progressively decreasing from an initial value (c'_0) according to the following non-linear softening law:

$$\dot{c}' = -mc'(|\dot{\varepsilon}_n^{vp}| + |\dot{\varepsilon}_t^{vp}| + |\dot{\gamma}_m^{vp}|), \quad (12)$$

where $\dot{\varepsilon}_n^{vp}$, $\dot{\varepsilon}_t^{vp}$ and $\dot{\gamma}_m^{vp}$ are the viscoplastic strain rates, whereas m a non-dimensional parameter defining the material brittleness.

A non-associated flow rule is adopted. In the plastic potential definition, the dilatancy angle ψ substitutes ϕ' and is assumed to decrease with irreversible strains from an initial value ψ_0 :

$$\dot{\psi} = -m\psi(|\dot{\varepsilon}_n^{vp}| + |\dot{\varepsilon}_t^{vp}| + |\dot{\gamma}_m^{vp}|), \quad (13)$$

The viscoplastic strain rates are calculated as it follows:

$$\dot{\varepsilon}_{ij}^{vp} = \eta(f) \frac{\partial g}{\partial \sigma'_{ij}} \quad (14)$$

where η is the fluidity parameter (inverse of viscosity).

The initially dry slope is assumed to be perturbed by an instantaneous increase in the water table level, which is subsequently kept constant ($h_w = h = 5$ m). The slope response is obtained by subdividing the stratum into layers of thickness of 5 cm and by explicitly integrating the constitutive equations under simple shear conditions.

The values of constitutive parameters employed are reported in Table 1.

Table 1. Constitutive parameter values

E (MPa)	ν (-)	ϕ' (°)	m (-)	c_0 (kPa)	ψ_0 (°)	η (kPa ⁻¹ s ⁻¹)
50	0.25	30	10	20	30	$2 \cdot 10^{-7}$

The numerical results are plotted in Fig. 2 in terms of (i) evolution with time (T) of viscoplastic shear strains (Fig. 2a), (ii) evolution with time of viscoplastic shear strain rates (Fig. 2b), (iii) isochrones of shear strain distributions along depth (Fig. 2c), and (iv) evolution with time of displacements along direction t (Fig. 2d). In Fig. 2a–b the results relative to some depth values are omitted for the sake of clarity.

The numerical results clearly put in evidence that initially all the layers are characterized by a progressively decelerating trend (associated with a “structural hardening”), whereas, after a sufficiently long time, deep layers and the whole slope start accelerating (Fig. 2a–b). The first local instability takes place at the bottom of the slope and, subsequently, instability progressively propagates upward, involving more superficial layers.

Irreversibilities develop for $z > 2.75$ m, but only in the subdomain $4.25 \text{ m} < z < 5$ m, identified as the shear band, irreversibilities accumulate with time without stopping (where $\dot{\gamma}_m^{vp} > 0$ for any t value), going progressively to infinite (Fig. 2c). As was discussed

in [7] and in §5, the shear band thickness depends on both material parameter values and perturbation amplitude. In this case, because of the time dependency of the constitutive relationship, the role of microstructure (material characteristic length) is negligible: the material microstructure may in principle influence the distribution in space of irreversible strains, but the material characteristic length is expected to be at least one order of magnitude than shear band thickness.

Initially the slope is decelerating (Fig. 2d), but, after the onset of instability of a sufficiently large number of layers, also the whole slope starts accelerating. The time lag between the first local and the global onset of instability, in this particular case, is approximately equal to 3 days.

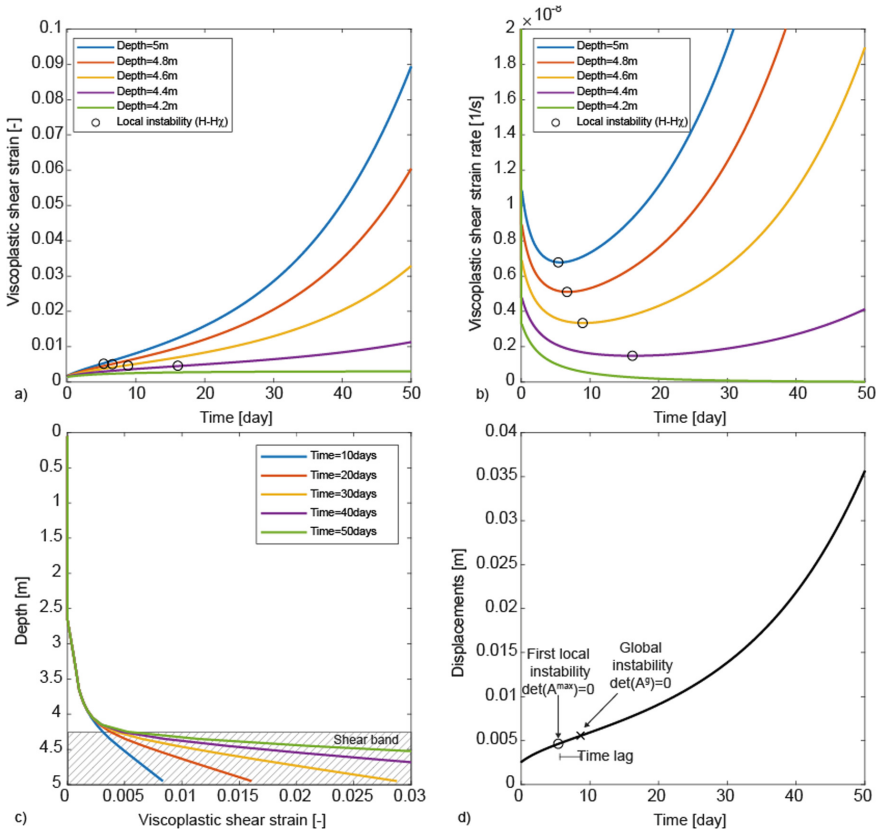


Fig. 2. Numerical generalized creep test results: a) evolution of viscoplastic strain with depth, b) evolution of viscoplastic strain rate with depth, c) isochrones of the profiles of viscoplastic strains with depth and d) evolution of displacements

5 Slope Response Under Cyclic Perturbations

In the previous paragraph, controlled variables were kept constant ($\mathbf{F} = \mathbf{0}$ of Eq. 1). Hereafter, a cyclic variation in the water table level is numerically discussed ($\mathbf{F} \neq \mathbf{0}$ and $\mathbf{A} = \mathbf{A}(\mathbf{Y})$). The single cycle imposed, mimicking the usually observed variations in water table due to rainfall [8], is represented in Fig. 3. Amplitude and frequency of cycles are kept constant with time.

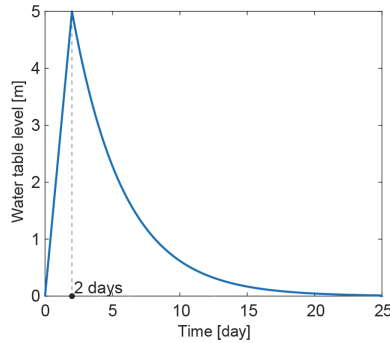


Fig. 3. Evolution with time of the water table level: one cycle

The numerical results (geometry and mechanical properties coincide with those employed in the case discussed in the previous section) are plotted in Fig. 4 in terms of (i) evolution with time of viscoplastic shear strains (Fig. 4a), (ii) isochrones of shear strain distributions along depth (Fig. 4b) and (iii) evolution with time of displacements along direction t (Fig. 4c).

By comparing the results of Fig. 4 with the corresponding ones of Fig. 2 (where the water table level was kept constant but equal to the maximum value cyclically reached), we can state that (i) the local and global mechanical processes take place in significantly longer time periods and (ii) the shear band thickness is smaller. This latter observation confirms what stated in §4 and in [7], that is the shear band thickness is governed even by the imposed perturbation.

In case of cyclic perturbations characterized by constant amplitude and period (ΔT), the stability of the local response can be interpreted by using the single cycle average (irreversible) strain rate:

$$\dot{\gamma}_f = \frac{\int_{\bar{T}}^{\bar{T}+\Delta T} \dot{\gamma}_m dT}{\Delta T} \tag{15}$$

being \bar{T} the starting time of each cycle.

Accordingly, for an assigned cyclic perturbation constant with time: $\ddot{\gamma}_f < 0$ corresponds to stable response, whereas $\ddot{\gamma}_f > 0$ to an unstable one. The change in sign of $\ddot{\gamma}_f$

takes place when:

$$H_{IN\dot{\gamma}} = \frac{1}{\Delta T} \int_{\bar{T}}^{\bar{T}+\Delta T} H_{IN} \frac{\langle f \rangle}{|f|} dT = 0. \quad (16)$$

Analogously, for the global response the average cycle velocity:

$$\dot{u}_{\dot{\gamma}} = \frac{\int_{\bar{T}}^{\bar{T}+\Delta T} \dot{u}_t dT}{\Delta T}. \quad (17)$$

can conveniently be introduced and the stability be defined on the basis of the sign of $\ddot{u}_{\dot{\gamma}}$ ($\ddot{u}_{\dot{\gamma}} < 0$ stable response, whereas $\ddot{u}_{\dot{\gamma}} > 0$ unstable response).

In Fig. 5 the numerical results of Fig. 4a and c are plotted in $\dot{\gamma}_{\dot{\gamma}} - N$ (N stands for number of cycle) and $\dot{u}_{\dot{\gamma}} - N$ planes (Fig. 5a and b, respectively).

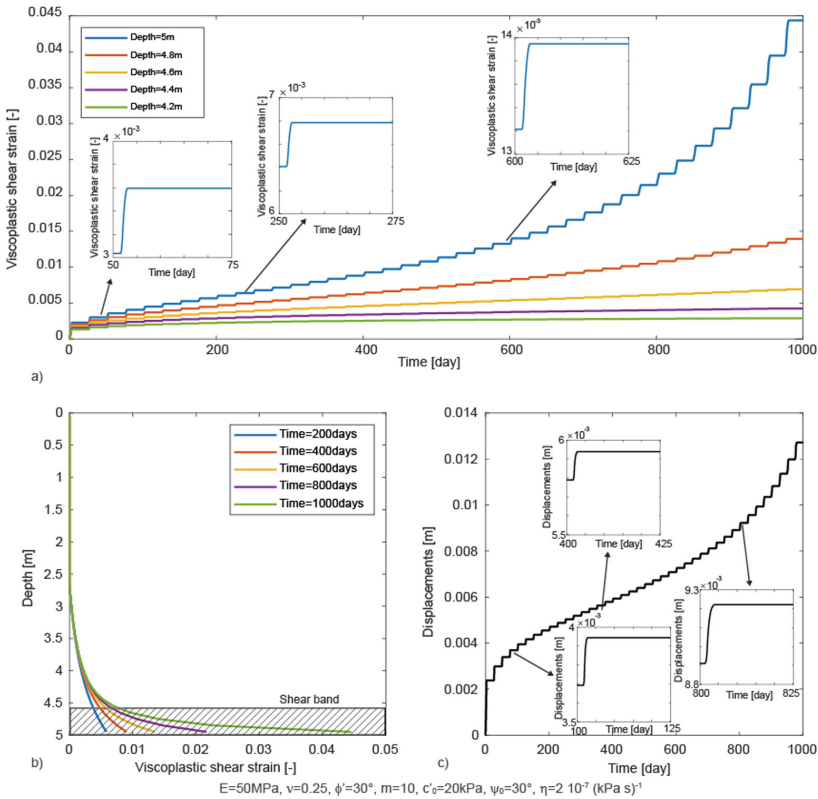


Fig. 4. Numerical results: a) evolution with time of viscoplastic strains, b) isochrones of viscoplastic strain distributions and c) evolution of displacements

Initially, at any depth $\dot{\gamma}_{\dot{\gamma}} < 0$ and $\ddot{u}_{\dot{\gamma}} < 0$. Subsequently (for $N = 8$), at the base of the stratum $\dot{\gamma}_{\dot{\gamma}}$ becomes positive whereas the local response in the rest of the spatial

domain as well as the global response are stable. By further increasing N , local instability progressively propagates upward and after the onset of instability for a sufficiently large number of layers is got, also the global response becomes unstable. Analogously to what was theoretically derived and numerically observed for generalized creeps, a time lag between the development of the first local and the global instability exists. In other words, first local instability is a precursory sign of the global one. This implies that, not only in case of generalized creeps [7], but also when cyclic perturbations are accounted for, local strain rate measurements (e.g. obtained by employing inclinometers) are more effective for early warning systems with respect to ground surface displacement measurements.

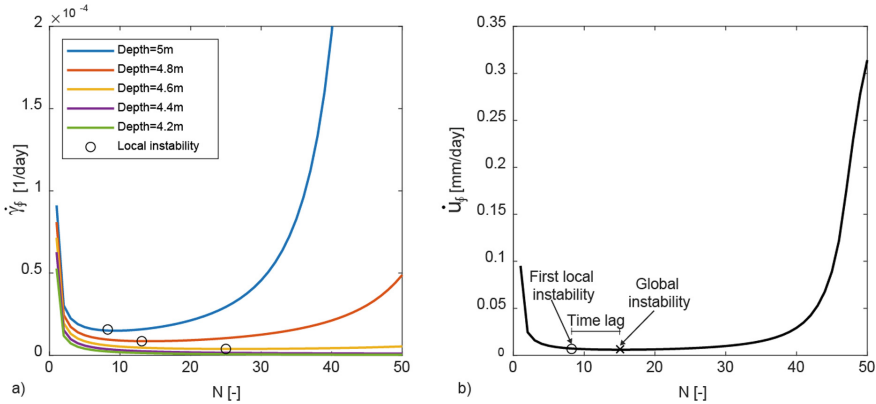


Fig. 5. Numerical results: evolution with N of a) $\dot{\gamma}_f$ and b) \dot{u}_f

The influence of perturbation period is discussed in Fig. 6. The response in terms of displacements (Fig. 6a) is not significantly affected by the perturbation period. On the contrary, by plotting the results in the $\dot{u}_f - N$ (Fig. 6b) plane, a dependence on the number of cycles associated with global instability on the perturbation period is observed: as is shown in Fig. 6, due to the viscoplastic single potential constitutive relationship implemented, the driving variable is time and not the number of cycles. In case a generalized (for instance multi-potential) elastic-plastic constitutive law was adopted, the opposite result would be true.

6 Conclusions

In this paper the authors discussed the onset of instability in case of elastic viscoplastic materials subject to cyclic perturbations. By starting from the definition of local instability for elastic single potential visco-plastic materials extended to infinite long slopes subject to generalized creeps, the authors introduced a instability definition suitable for cyclic perturbations.

This definition is based on the analysis of the response integrated in the cycle period: in case integrated strains/displacement rates increase with time, the response is defined to be unstable. From a practical point of view, this integral measure of instability could be

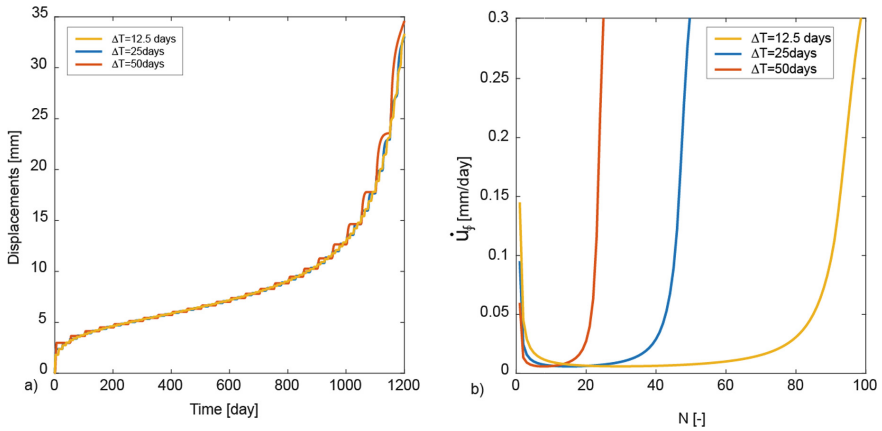


Fig. 6. Numerical results: influence of ΔT on a) γ_m for $z = 5$ m, b) u_t , c) $\dot{\gamma}_f$ for $z = 5$ m and \dot{u}_f

very convenient for interpreting monitoring data. The instability definition, introduced for single cycles mimicking single rainfall events, can also very simply be adapted for larger time periods such as to seasonal oscillations in water table.

Numerical simulation results, obtained by explicitly integrating a strain softening elastic-viscoplastic constitutive relationship under simple shear conditions highlight that even when cyclic perturbations are accounted for, local and global instabilities are not simultaneous: the first local instability always anticipates the global one. Moreover, the results also put in evidence that, even if the constitutive relationship does not account for an internal length, instability takes place in a shear band of finite thickness, not coinciding with the mesh size.

Moreover, the results also put in evidence that, due to the viscoplastic constitutive relationship adopted, instability takes place in a shear band of finite thickness, not coinciding with the mesh size.

The thickness of this shear band, in contrast with what commonly inferred, is a function of both constitutive parameters and imposed perturbation.

References

1. Hill, R.: A general theory of uniqueness and stability in elastic-plastic solids. *J. Mech. Phys. Solids* **6**(3), 236–249 (1958)
2. Nova, R.: Controllability of the incremental response of soil specimens subjected to arbitrary loading programmes. *J. Mech. Behav. Mater.* **5**(2), 193–202 (1994)
3. Pisanò, F., di Prisco, C.: A stability criterion for elasto-viscoplastic constitutive relationships. *Int. J. Numer. Analyt. Methods Geomech.* **40**(1), 141–156 (2016)
4. Lyapunov AM (1892) The general problem of motion stability. *Kharkovskoye Matematicheskoe Obshchestvo* 11
5. Buscarnera, G., Dattola, G., di Prisco, C.: Controllability, uniqueness and existence of the incremental response: a mathematical criterion for elastoplastic constitutive laws. *Int. J. Solids Struct.* **48**(13), 1867–1878 (2011)

6. di Prisco, C., Pisanò, F.: Unstable creeping in geomaterials. In: International Workshop on Bifurcation and Degradation in Geomaterials, pp. 139–145. Springer, Cham (2017)
7. di Prisco, C., Flessati, L.: Progressive failure in elastic–viscoplastic media: from theory to practice. *Géotechnique* **71**(2), 153–169 (2021)
8. Crosta, G.B., di Prisco, C., Frattini, P., Frigerio, G., Castellanza, R., Agliardi, F.: Chasing a complete understanding of the triggering mechanisms of a large rapidly evolving rockslide. *Landslides* **11**(5), 747–764 (2013). <https://doi.org/10.1007/s10346-013-0433-1>



Implication of Different Types of Post-peak Behaviour in Lateral Direction on Failure of Class II Rocks in Uniaxial Compression

H. Wang^{1,2}(✉), B. Jeffcoat-Sacco¹, P. Dight¹, A. V. Dyskin², and E. Pasternak³

¹ Australian Centre for Geomechanics, UWA, Crawley, Australia
hongyu.wang@uwa.edu.au

² Department of Civil, Environmental and Mining Engineering, UWA, Crawley, Australia

³ Department of Mechanical Engineering, UWA, Crawley, Australia

Abstract. The rock samples were tested in uniaxial compression under lateral strain control. The results present Class II stress-strain curves in the axial direction. However, in the lateral direction, two types of post-peak curves were identified. The dilating behaviour (here called Type I) is characterized by the significant irreversible increase of the lateral strain before and after the peak stress. After the peak stress, the lateral strain keeps increasing without obvious axial stress drop over a relatively large lateral strain. For collapsing behaviour (here called Type II), the stress-strain curve presents brittle response in the lateral direction up to the peak stress. After the peak the stress drops immediately, representing an infinitesimal increase in lateral strain. To investigate the implication of both types of behaviour on the ejection of the rock fragments after peak, the uniaxial compression tests using the axial displacement-control method were carried out while capturing the rock failure behaviour with the aid of high-speed cameras. It was found that rocks with Type I dilating behaviour are more likely to have splitting or spallation (the fractures are parallel to the loading direction) failure; while for Type II collapsing behaviour, the inclined fractures are more likely to be induced. These results highlight the importance of investigating the lateral stress-strain curves of rocks.

Keywords: Post-peak · Class II rocks · Lateral strain

1 Introduction

The post-peak tests attempt to obtain the complete stress-strain curves of rocks subjected to compression to investigate the possible macroscopic spontaneous failure [1]. According to a pioneering study by Wawersik and Fairhurst [2], rocks were classified into Class I and Class II based on their failure behaviour in uniaxial compression. The typical stress-strain curve of Class I rock in uniaxial compression is shown in Fig. 1. It is seen that after the peak, the stress gradually decreases, while the (axial) strain steadily increases, until the ultimate failure. As Class I rocks require continued compression of the load frame to progress toward the failure, the post-peak stress-strain curves can be captured relatively

easily. Also, the loading frame must be sufficiently stiff as the energy accumulated in a soft testing machine in the process of loading may induce the unstable and rapid rock failure [3]. For Class II rocks, the stress-strain curve shows snap-back behaviour: as the stress drops after the peak stress, the axial strain also decreases. This indicates that in axial strain control, the failure of Class II rock is unstable or self-sustaining just after the peak stress even if the loading frame is perfectly stiff [2]. Many studies have been conducted attempting to achieve the controlled failure of Class II rocks. The most popular method is the lateral strain control that uses the lateral (circumferential) strain on the rock sample as a feed-back signal to control the movement of the loading platen [4].

In previous studies, most of the researchers focused on the post-peak behaviour in the axial direction, i.e. attempting to identify the Class I or Class II stress-strain curves [5], as shown in Fig. 1. Under compression, however, the lateral strain behaviour of rocks is also important as dangerous rock ejection occurs in directions perpendicular to the applied load. In this paper, we report post-peak tests using the lateral strain control method. We identified two types of post-peak behaviour in the lateral direction of Class II rocks. Also, we investigated the failure process of brittle samples in uniaxial compression tests under axial displacement control, using high-speed video, to capture the fracturing behaviour of both types of Class II rocks under compression.

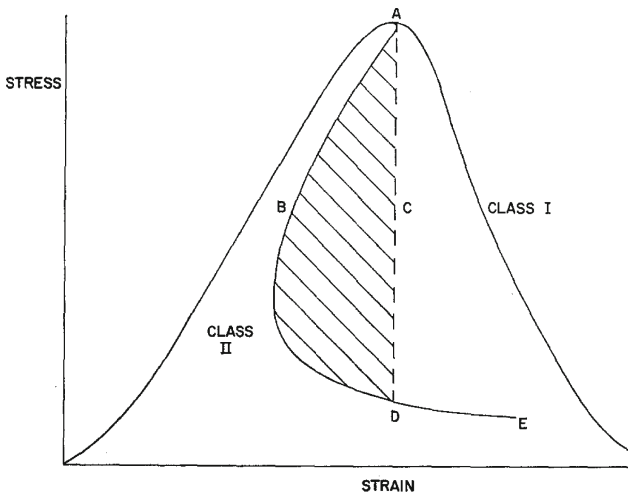


Fig. 1. Classification of stress-strain curves of rocks in uniaxial compression (after [6]).

2 Experimental Set-Up

2.1 Post-peak Test Under Lateral Strain Control

Rock samples are prepared by sub-sampling the rock cores. Samples for post-peak tests and ejection tests were sub-sampled parallel to each other and are from the same cores. The samples have shape of cylinders, with diameter 19 to 21 mm, and length between

38 and 45 mm (Tables 1 and 2). The minimum standard of sample preparation followed the ISRM standard [7].

All post-peak tests were performed using the lateral strain control method. The lateral strain rate adopted for all types of samples were: $1 * 10^{-6}$ 1/s. Two axial extensometers and one lateral extensometer are installed on the sample to monitor the axial and lateral strain during the test, respectively.

Table 1. Basic information of the samples tested in post-peak tests.

Test No	Site	Lithology	Diameter (mm)	Height (mm)	Weight (g)
1	X_E1	Metamorphosed felsic igneous rock	19.20	38.64	34.0
2	C108_B1	Fine-grained monzonite	20.60	42.48	39.4

2.2 Rock Ejection Tests Under Uniaxial Compression Using Axial Displacement Control Method

To investigate the implications of these two types of rock behaviour on the fragmentation and fracture development of rocks under uniaxial compression, we conducted rock ejection tests, that is uniaxial compression tests under axial displacement control. Under this loading, Class II rocks are expected to show sudden failure and possibly ejection at the peak stress, therefore no post-peak data will be captured on the axial load cell.

In the rock ejection test, the sample was first axially loaded at a rate of 0.2 mm/min until the axial stress reached approximately 70% of the expected peak stress. The loading rate was then reduced to 0.05 mm/min in order to minimize actuator-driven platen displacement during the actual period of brittle fracturing which was found to be $\ll 100 \mu\text{s}$. The fragmentation process of the rock ejections was recorded by two Phantom V1212 high speed cameras (Fig. 2).

As the samples were expected to fail violently, a plastic safety shield was used for all tests (as shown in the insert in Fig. 2). In addition, a multi-test jig was used to hold half-bearing platens at the top and bottom of the sample. During the pre-peak stage, the half-bearings limit the possible uneven loading or bending caused by non-parallel sample ends and/or inhomogeneous materials.

3 Experimental Results

In this section, the results from post-peak test under lateral strain control and rock ejection tests under axial displacement control are presented.

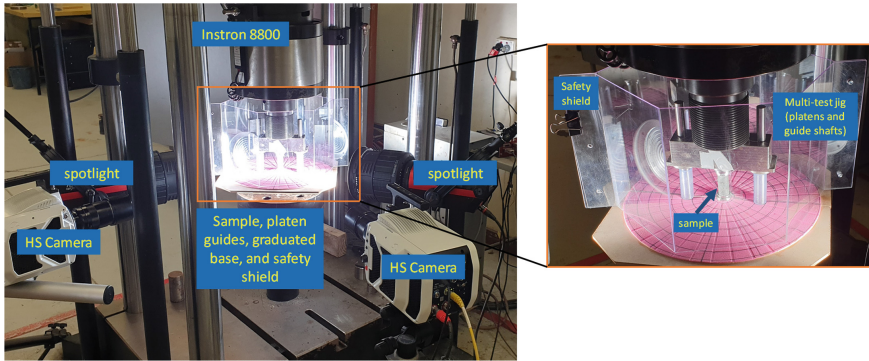


Fig. 2. The set-up of the rock ejection tests under uniaxial compression.

Table 2. Basic information of the samples tested in rock ejection tests.

Test No	Site	Lithology	Diameter (mm)	Height (mm)	Weight (g)
1	X_E3	Metamorphosed felsic igneous rock	19.18	38.66	33.4
2	C108_B2	Fine-grained monzonite	20.62	45.18	42.3

3.1 The Post-peak Test Using Lateral Strain Control Method

Rock sample with dilating post-peak behaviour in lateral direction. The stress-strain curves in test No. 1 (sample X_E1, Fig. 3) are characterized by significant irreversible decrease of the lateral strain before the peak stress; however, the axial irreversible strain is close to zero.

The peak stress of No. 1 (X_E1) is 214 MPa. Near the peak stress, significant lateral deformation occurs, with very little attendant axial deformation. The sample dilates laterally to about -0.55% strain, without much axially shortening. Then it is followed by an axial stress drop, and Class II behaviour in the axial direction. After the first stress drop, the axial stress slightly increases and then decreases again, as the sample again undergoes a large amount of lateral deformation without significant axial deformation. This behaviour is called the dilating or Type I post-peak behaviour.

Rock sample with collapsing post-peak behaviour in lateral direction. For test No. 2 (C108_B1, Fig. 4), the stress-strain curve presents elastic behaviour up to the peak stress in both axial and lateral directions. There is almost no apparent plastic yielding pre-peak stage.

The peak stress is 236 MPa. After the peak stress, the stress drops immediately, presenting a very small lateral strain increase (seen as a straight vertical line in lateral direction), and Class II stress-strain curve in the axial direction. The increase of lateral strain is close to zero in this first axial stress drop after peak. This behaviour is called the collapsing or Type II post-peak behaviour. After the first drop, the axial stress cycles

from 158 MPa to 183 MPa, as the lateral strain increases from 0.19% to 0.31% in several pulses.

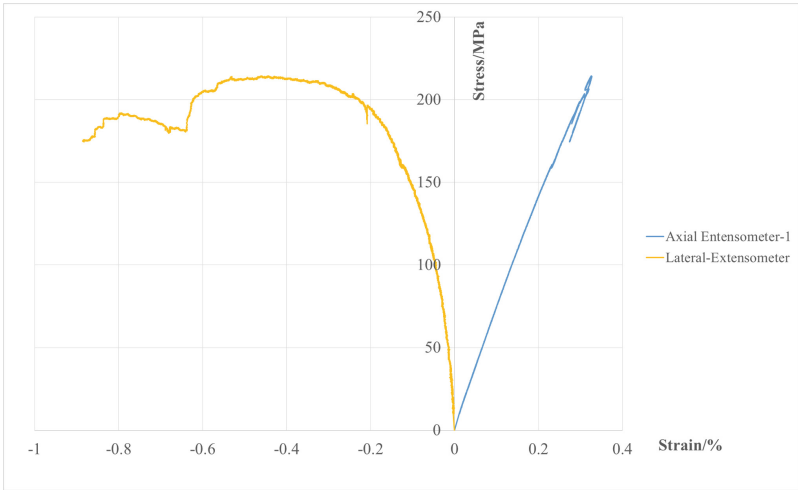


Fig. 3. Axial and lateral stress-strain curves for X_E1.

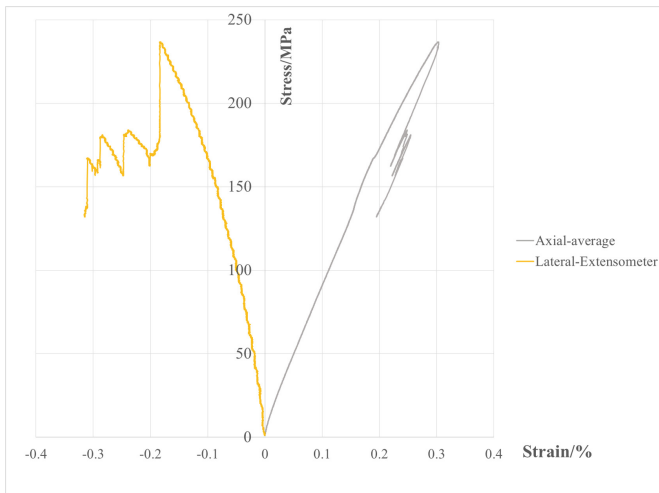


Fig. 4. Stress-strain curves for C108_B2.

3.2 The Rock Ejection Tests

Rock sample with Dilating (Type I) post-peak behaviour in lateral direction. About 1.3 s after the peak stress in rock X_E3, spallation begins at the contact with the upper

platen, in a white alteration infill zone, Fig. 5(a), see the possible mechanism explained in [8]. An axial crack starts growing 2.5 s later, Fig. 5(b), and stabilizes temporarily, without reaching the ends of the sample. About 23 ms later, the crack grows to the top and bottom platens, and opens, and several cracks open to the right of it near the top end of the sample, Fig. 5(c).

Significant ejections from the upper right part of the sample begin 3.4 ms later, Fig. 5(d), as the axial crack opens further. A second axial crack, parallel to the first, opens up 9 ms later, accompanied by more ejection from the top right, Fig. 5(e). After a further 1 ms, a third axial crack opens. The three cracks combine to form a tall wedge with the right half of the sample, while the left half begins to buckle, Fig. 5(f). Failure now proceeds rapidly via buckling and rotation of fragments, Fig. 5(g).

Rock sample C108_B2 with collapsing (Type II) post-peak behaviour in lateral direction. For this sample, the entire failure process appears to occur very rapidly. There is about 0.45 s of plastic “yielding” occurring while the load remains at/near the peak, and nothing visible happens to the sample during this time. This is immediately followed by rapid and precipitous failure. From the first signs of spallation near the top end of the sample, until final buckling of the intact portions of the sample, takes only 448 μ s.

About 421 ms after the peak, spallation initiates in the upper part of the sample, Fig. 6(a). An inclined fracture forms 392 μ s later, along a 60° inclination from the horizontal. A branch grows from it, vertically downward, Fig. 6(b), see the possible mechanism explained in [9]. The two cracks grow quickly ejecting material, and after 56 μ s they form a wedge on the rear-left of the sample. This leaves the front part of the sample to carry most of the load, at which point it begins to buckle, Fig. 6(c). After another 196 μ s, the buckling is obvious, and the platens rotate significantly, Fig. 6(d).

4 Conclusions

Two different types of post-peak behaviour in lateral direction of Class II rocks were identified. The dilating or Type I behaviour is characterized by the significant irreversible lateral strain before and after peak stress. Especially, after the peak stress, the lateral strain keeps increasing without obvious stress drop (sample weakening) within a relatively large lateral strain, and without significant axial deformation. For collapsing or Type II behaviour, the stress-strain curve presents brittle behaviour up to the peak stress in the lateral direction. After the peak stress, the stress drops immediately, presenting an infinitesimal increase in strain in the lateral direction. The rock ejection tests show with the aid of a high-speed camera that rocks with dilating or Type I behaviour is more likely to have splitting or spallation (the fractures are parallel to the loading direction); while inclined fractures are more likely to be induced in rocks with collapsing or Type II behaviour.

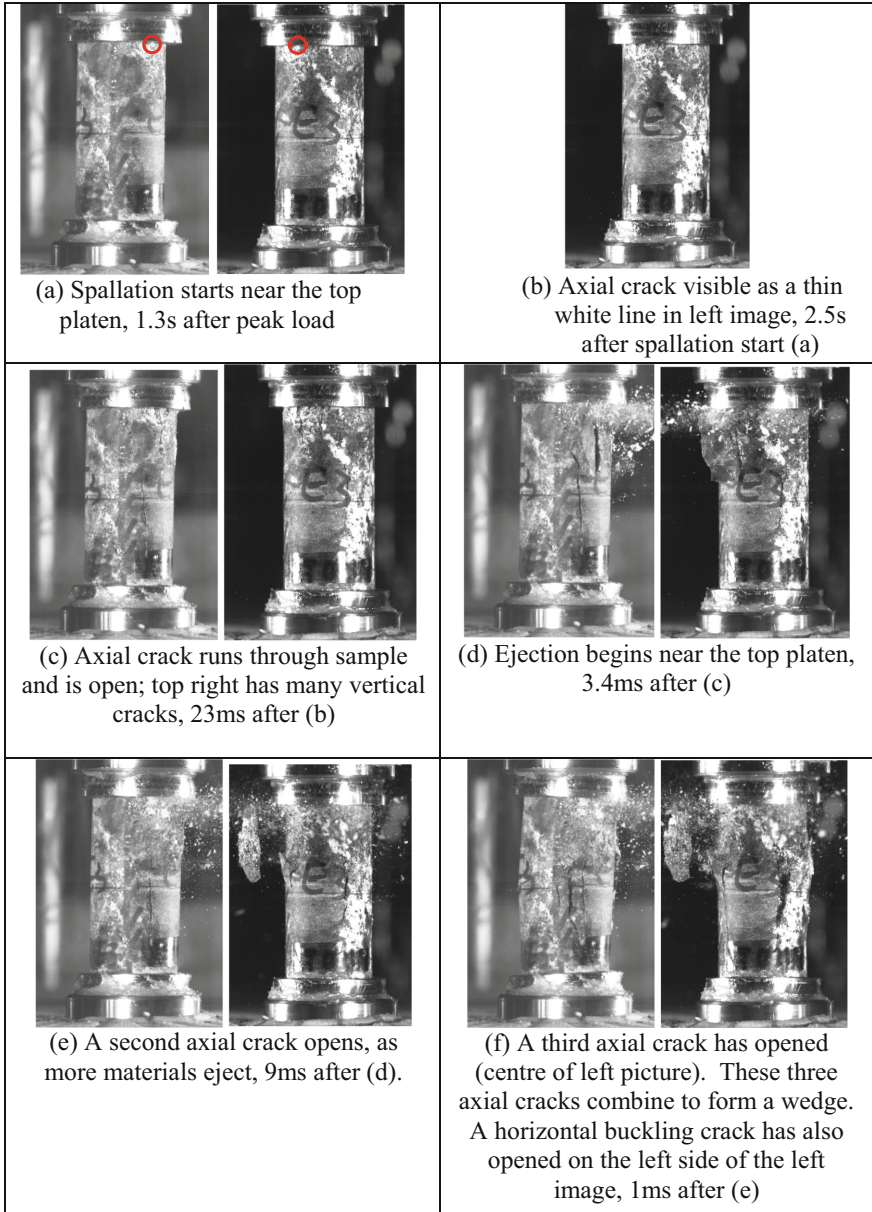


Fig. 5. Stages of the failure process of X_E3.

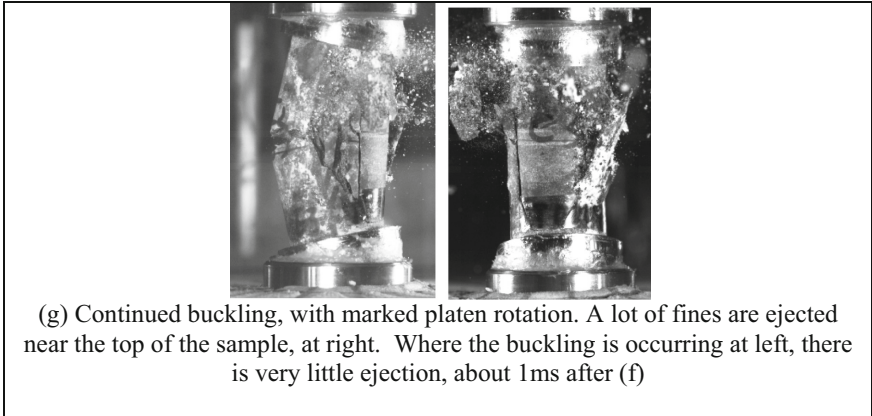


Fig. 5. (continued)

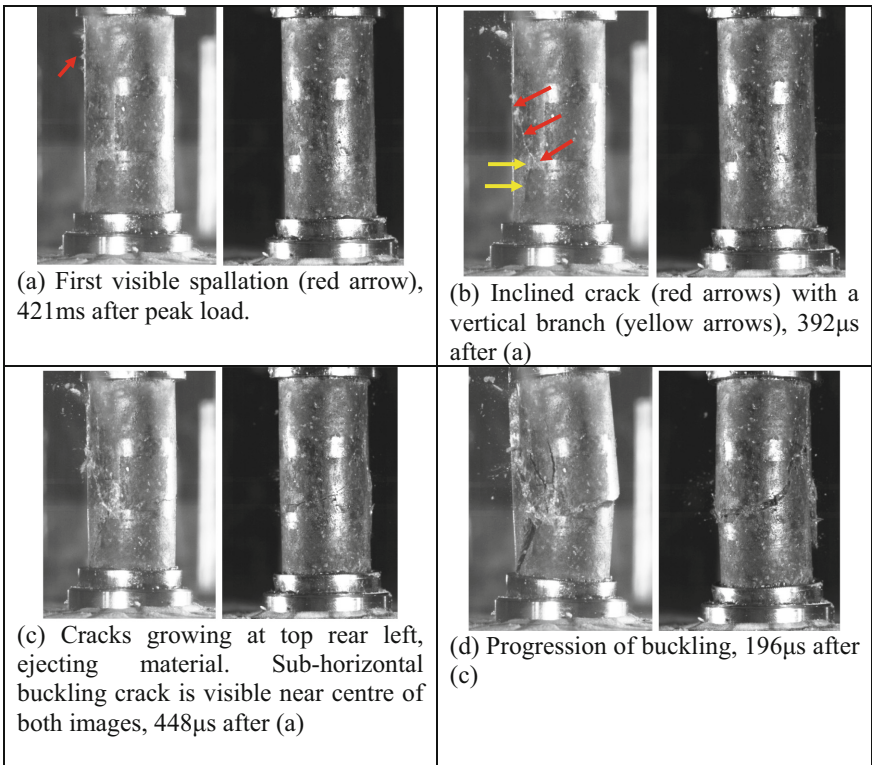


Fig. 6. Photos during failure of C108-B2.

Acknowledgements. The authors acknowledge the support of MRIWA and the sponsors of the research project on strain burst and rock burst. The sponsors are Aeris Tritton Mine, Agnico-Eagle

LaRhonde, AngloGold Ashanti Sunrise Dam, BHP Olympic Dam, BHP Nickel West, Glencore Ernest Henry, Glencore Sudbury, Gold Fields St Ives, Wallaby, Lawlers and Deep South, IamGold Westwood, LKAB, Newcrest Cadia Mine and Northern Star. AVD and EP acknowledge the support of the Australian Research Council through project DP210102224.

References

1. Wawersik, W.R.: Detailed analysis of rock failure in laboratory compression tests. Ph.D. Thesis, University of Minnesota, USA (1968)
2. Wawersik, W.R., Fairhurst, C.: A study of brittle rock fracture in laboratory compression experiments. *Int. J. Rock Mech. Mining Sci. Geomech. Abs.* **7**, 561–575 (1970)
3. Starfield, A.M., Wawersik, W.R.: Pillars as structural components in room-and-pillar mine design. In: *The 10th US Symposium on Rock Mechanics (USRMS): American Rock Mechanics Association* (1968)
4. Hudson, J., Brown, E., Fairhurst, C.: Optimizing the control of rock failure in servo-controlled laboratory tests. *Rock Mech.* **3**, 217–224 (1971)
5. Wang, H., Dyskin, A., Pasternak, E., Dight, P.: Mixed Class I/Class II post-peak curves of mortar models of rock samples. *Theor. Appl. Fract. Mech.*, 103178 (2021)
6. Wawersik, W.R.: Detailed analysis of rock failure in laboratory compression tests (1968)
7. Fairhurst, C.E., Hudson, J.A.: Draft ISRM suggested method for the complete stress-strain curve for intact rock in uniaxial compression. *Int. J. Rock Mech. Min. Sci. Geomech. Abst* **36**, 281–289 (1999)
8. Wang, H., Dyskin, A., Pasternak, E., Dight, P.: Possible mechanism of spallation in rock samples under uniaxial compression. *Eng. Fract. Mech.*, 108577 (2022)
9. Dyskin, A.V., Pasternak, E., Xu, Y.: Negative stiffness, incompressibility, and strain localisation in particulate materials. *Appl. Sci.* **11**, 8751 (2021)



Anomalous Fall-Off in Velocity Power Spectra Caused by Sliding with Asymmetric Friction

Rui X. Wong¹(✉), Elena Pasternak¹, and Arcady V. Dyskin²

¹ Department of Mechanical Engineering, University of Western Australia, 35 Stirling Hwy, Crawley, WA 6009, Australia

ruixiang.wong@research.uwa.edu.au

² Department of Civil, Environmental and Mining Engineering, University of Western Australia, 35 Stirling Hwy, Crawley, WA 6009, Australia

Abstract. Friction resisting sliding over contacted surfaces of faults or shear fractures is usually considered independent of the sliding direction. However, when the rock near sliding surface is anisotropic with a symmetry axis inclined to the sliding direction, normal constraint induces asymmetry, whereby friction forces resisting sliding in opposite directions are different. In this case the applied oscillatory force produces sliding towards the direction with the smallest friction such that macroscopic movement can occur even when the driving force oscillates around zero. Furthermore, friction asymmetry leads to emerging of a critical value of friction in the hard direction: for friction forces lower than the critical value the exponent of the fall-off of the velocity power spectra is near the conventional -1 , while when the friction force reaches the critical value the exponent drops to -2 . This phenomenon can be used for reconstructing the structure of rocks surrounding sliding fractures/faults.

Keywords: Asymmetric friction · Anisotropic friction · Shear fracture sliding

1 Introduction

Anisotropic friction refers to the case where friction magnitude is dependent on sliding directions and can be achieved through surface conditions or material anisotropy. Various materials have been shown to have anisotropic friction: polymers [1], fibre reinforced polymers [2–4], alloys [5] and ceramics [6]. In this study we consider a specific case of anisotropic friction: asymmetric friction when different friction forces resist sliding in opposing directions.

Asymmetric friction has been shown to arise from anisotropy of sliding materials [7] or rocks when an axis of symmetry is inclined to the sliding surface. When constrained in the direction normal to the sliding surface, the material creates a coupling between the normal and shear force. This leads to low friction resisting sliding along the incline, while having high levels of friction when sliding against the incline. This mechanism is entirely dependent on the internal rock structure rather than the surface conditions.

Beeler et al. [8] compared the velocity spectrum recorded in a laboratory to that of natural earthquakes. Triaxial compression tests on Westerly granite and Devil's postpile basalt were conducted. Velocity spectrum was recorded as the sample fractured, as well as the subsequent slip event that occurred over the fractured surface. The velocity spectra during sample fracture yielded a high frequency falloff that approximates the gradient $1/f$ where f is the frequency of the spectra. This result resembles that of natural earthquakes. However during the subsequent slip event over the produced shear fracture surface, the velocity spectra display a falloff that approximates $1/f^2$. This is in contrast to the cases when sliding occurs over a pre-cut slip plane [9, 10]: the slip event had velocity spectra that resemble that of earthquakes. This implies that the fractured surface may introduce a different mechanic that results in the steeper frequency falloff, $1/f^2$.

The triaxial compression leads to fault nucleation and growth (e.g., Reches and Lockner [11]). Under compression, microcracks grow parallel to the major principal compressive stress before the fault (shear fracture) is formed. As the load increases, the density of microcracks increase until an inclined localisation zone is formed. This process zone lengthens and ultimately produces a shear fracture. The random microcracks produce transverse-isotropy with the axis of isotropy inclined to the resulting shear fracture; such a configuration is shown to induce asymmetric friction [7].

This study investigates whether the frequency falloff that approximates $1/f^2$ found during sliding over compressive fractured surface is related to asymmetric friction.

2 Model

To investigate the potential role of asymmetric friction on sliding over fracture due to compression, we consider a simple spring-block model shown in Fig. 1. The model consists of a mass m connected to a harmonically oscillating base through a spring with stiffness k . The sliding between mass m and the base is resisted by friction force f_{fric} . Displacement u_g of the base is taken with respect to a stationary coordinate frame and displacement u_m of the mass m is counted relative to the base. The base harmonically oscillates with amplitude G and driving frequency ω_d .

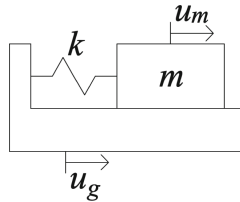


Fig. 1. Spring-block model consisting of mass m that undergoes frictional sliding on a harmonically oscillating base.

The equation of motion of mass m is

$$m\ddot{u}_m = -m\ddot{u}_g - ku_m - f_{fric}(\dot{u}_m, f_m) \quad (1)$$

where

$$\begin{aligned} f_m &= -m\ddot{u}_g - ku_m \\ \ddot{u}_g &= -G \sin(\omega_d t) \end{aligned}$$

As we are interested in the effect of asymmetric friction, the friction model considered here will be rate independent but directionally dependent: f^+ is the friction force that resists sliding in the positive direction and f^- is the friction force that resists sliding in the negative direction. The friction model reads

$$f_{fric}(\dot{u}_m, f_m) = \begin{cases} \min(f_m, f^+), & \dot{u}_m = 0 \text{ and } f_m \geq 0 \\ f^+, & \dot{u}_m > 0 \\ \max(f_m, -f^-), & \dot{u}_m = 0 \text{ and } f_m < 0 \\ -f^-, & \dot{u}_m < 0 \end{cases} \quad (2)$$

The symmetric friction has the same friction force resisting sliding in opposing direction, $f^+ = f^-$. The asymmetric friction has lower friction resisting sliding in the positive direction while higher friction resists sliding in the negative direction, $f^+ < f^-$.

We define normalised time $\tau = \omega_c t$ and normalised displacement $U = \omega_c^2 u / G$, where $\omega_c = \sqrt{k/m}$ is the characteristic frequency. Equations (1) and (2) become

$$U_m'' = -U_g'' - U_m - F_{fric}(U_m', F_m) \quad (3)$$

$$F_{fric}(U_m', F_m) = \begin{cases} \min(|F_m|, F^+), & U_m' = 0 \text{ and } F_m \geq 0 \\ F^+, & U_m' > 0 \\ -\min(|F_m|, F^-), & U_m' = 0 \text{ and } F_m < 0 \\ -F^-, & U_m' < 0 \end{cases} \quad (4)$$

where $U_g'' = -\sin(\beta\tau)$, $\beta = \frac{\omega_d}{\omega_c}$, $F_{fric}(U_m', F_m) = \frac{1}{mG} f_{fric}(\dot{u}_m, f_m)$, $F_m = \frac{1}{mG} f_m$, $F^+ = \frac{1}{mG} f^+$, $F^- = \frac{1}{mG} f^-$.

These equations are solved using MATLAB function ODE23.

3 Results

First consider the motion of a symmetric friction block when subjected to a base that oscillates with driving frequency $\beta = 1.5$. This is similar to the Coulomb friction oscillator considered by H.-K. Hong and C.-S. Liu [12]; however, the displacement of the block in this study is taken with respect to the displacement of the base rather than the stationary coordinate frame. Due to the normalisation, the symmetric friction block will be stationary when the maximum normalised friction force is $F^+ = F^- = 1$. Figure 2 presents the displacement of a block for different symmetric friction cases. The symmetric friction block displaces in both positive and negative directions. As friction force increases, the amplitude of the block's oscillation decreases.

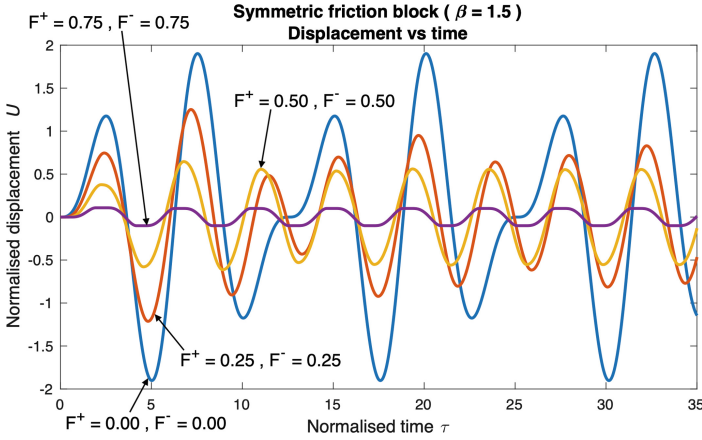


Fig. 2. Displacement of a symmetric friction block when subjected to a driving frequency $\beta = 1.5$. Friction forces are: $F^+ = F^- = 0, 0.25, 0.5, 0.75$.

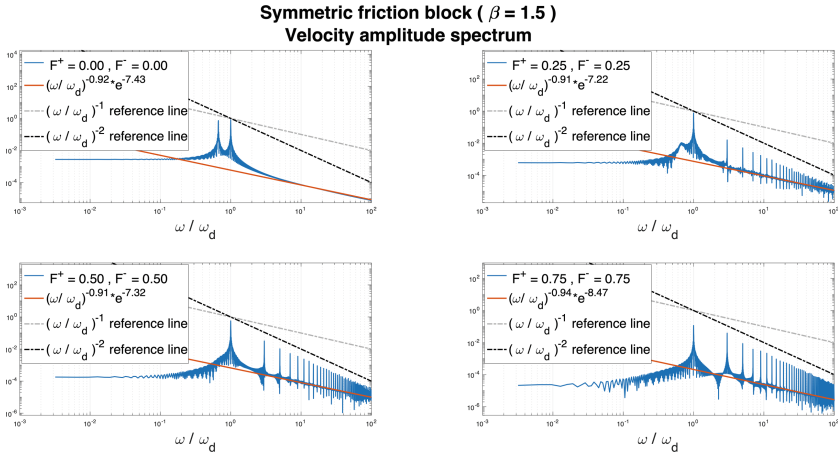


Fig. 3. Velocity amplitude spectra for a symmetric friction block when subjected to a driving frequency $\beta = 1.5$. Friction forces are: $F^+ = F^- = 0, 0.25, 0.5, 0.75$.

Figure 3 presents the amplitude spectra for velocity of the symmetric friction blocks considered in Fig. 2. The lines of best fit for the high frequency falloff as well as the reference lines for $(\omega/\omega_d)^{-1}$ and $(\omega/\omega_d)^{-2}$ are shown in the spectra.

Figure 3 shows that the amplitude spectra for the symmetric friction block have a high frequency falloff of about $(\omega/\omega_d)^{-1}$ for all four cases. Now the falloffs for various driving frequencies β and finer resolution of maximum friction force $F^+ = F^-$ are considered. Figure 4 graphs the exponent of falloff as a function of the symmetric friction force, $F^+ = F^-$.

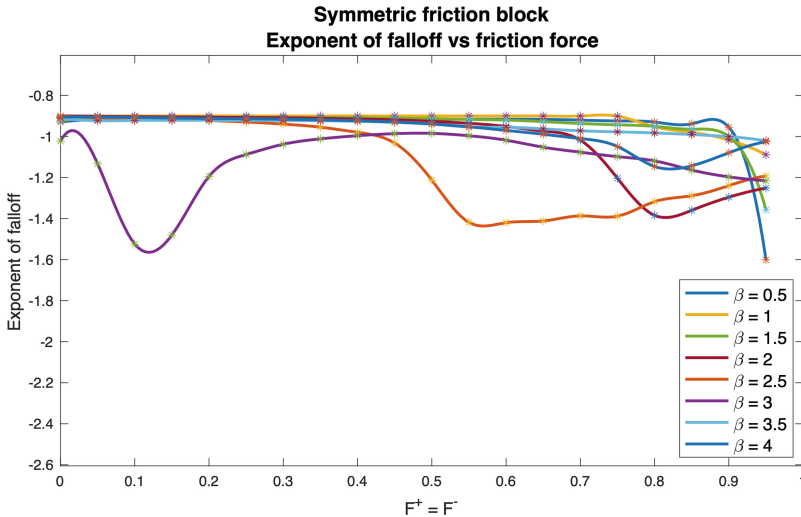


Fig. 4. Exponent of (ω/ω_d) for high frequency falloff in symmetric friction block velocity spectra subjected to $\beta = 0.5, 1, 1.5, 2, 2.5, 3, 3.5, 4$ plotted against maximum friction force.

In Fig. 4, the symmetric friction cases have exponents of falloff that fluctuate about -1 and at certain driving frequencies, the exponent is seen to decrease to around -1.5 at high friction force. The exception is $\beta = 3$ showing a dip in exponent at low friction.

Consider the case of extreme asymmetric friction when the block is frictionless when sliding in the easy direction. This block is subjected to a base that oscillates with driving frequency $\beta = 1.5$. Figure 5 presents the displacement of an asymmetric friction block with different friction in the hard direction.

The asymmetric friction block is seen to have the same movement during initial sliding in the easy direction. During subsequent sliding in the hard direction, the block does not slide as far into the negative displacement. Figure 6 shows the velocity amplitude spectra of the asymmetric friction blocks considered in Fig. 5.

When friction in the hard direction is low ($F^- = 1, 1.5$) the frequency falloff is about $(\omega/\omega_d)^{-1}$, while at high friction in the hard direction the falloff approximates $(\omega/\omega_d)^{-2}$. Figure 7 shows the falloff exponent for various driving frequencies β and magnitudes of friction force in the hard direction F^- .

Figure 7 shows that for all driving frequencies β , there is a threshold value of F^- after which the exponent changes from approximately -1 to -2 . A dip in exponent at low F^- for $\beta = 3$ is also seen here in the asymmetric friction case whose nature is not known and needs further investigation.

4 Conclusion

It is shown that the asymmetric friction works as a switch: there is a critical magnitude of friction in the hard direction, $f_{cr}^- = 2mG$, where m is the block mass, G is the amplitude of the acceleration of the driving oscillation force. When the friction is below f_{cr}^- the

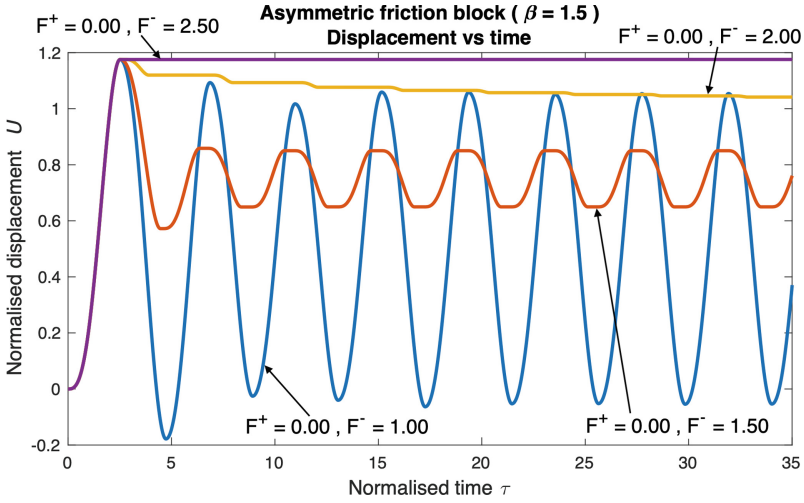


Fig. 5. Displacement of an asymmetric friction block when subjected to a driving frequency $\beta = 1.5$. Friction forces in the easy direction are $F^+ = 0$ and in the hard direction are $F^- = 1, 1.5, 2, 2.5$.

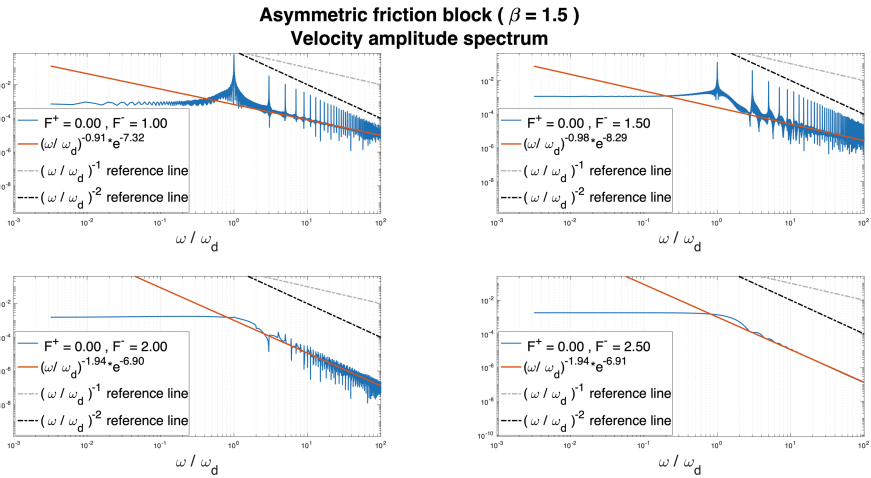


Fig. 6. Velocity amplitude spectra for an asymmetric friction block when subjected to a driving frequency $\beta = 1.5$. Friction forces in the easy direction are $F^+ = 0$ and in the hard direction are $F^- = 1, 1.5, 2, 2.5$.

falloff exponent is -1 . After the friction force increases and crosses the threshold, the exponent drops to -2 . This phenomenon can be used for reconstructing the structure of rocks surrounding sliding fractures/faults.

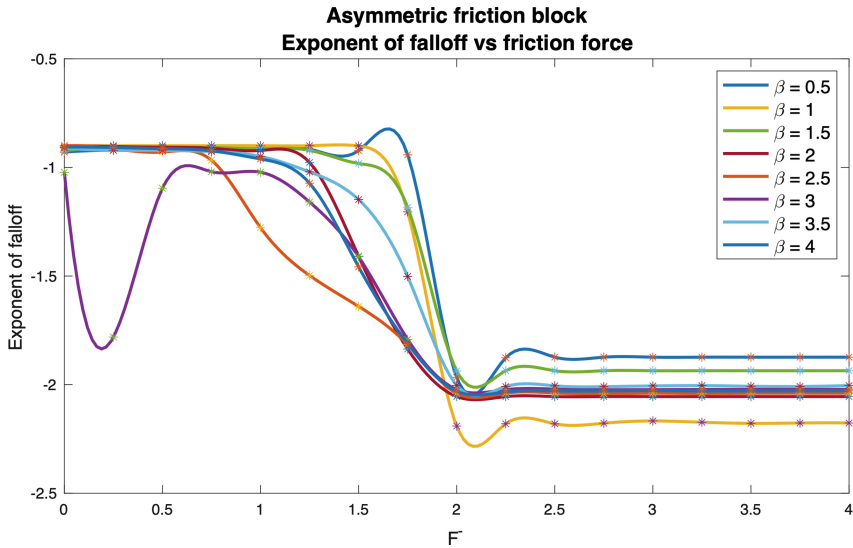


Fig. 7. Exponent of (ω/ω_d) for high frequency falloff in asymmetric friction block velocity spectra subjected to $\beta = 0.5, 1, 1.5, 2, 2.5, 3, 3.5, 4$ plotted against friction in the hard direction.

Acknowledgements. RXW acknowledges the support of the Robert and Maude Gladden Post-graduate Research Scholarship and the Australian Government Research Training Program (RTP) Scholarship. AVD and EP acknowledge the support of the Australian Research Council through project DP190103260.

References




1. Tabor, D., Williams, D.E.W.: The effect of orientation on the friction of polytetrafluoroethylene. *Wear* **4**, 391–400 (1961)
2. Jacobs, O., Friedrich, K., Marom, G., Schulte, K., Wagner, H.D.: Fretting wear performance of glass-, carbon-, and aramid-fibre/epoxy and peek composites. *Wear* **135**, 207–216 (1990)
3. Cirino, M., Friedrich, K., Pipes, R.B.: The effect of fiber orientation on the abrasive wear behavior of polymer composite materials. *Wear* **121**, 127–141 (1988)
4. Chang, H.-W.: Wear characteristics of composites: effect of fiber orientation. *Wear* **85**, 81–91 (1983)
5. Herold-Schmidt, U., Hinsberger, R.: Abrasive wear resistance of anisotropic two phase Fe-Ni-C steels. *Wear* **120**, 151–160 (1987)
6. Kadijk, S.E., Van Groenou, A.B.: Wear anisotropy of MnZn ferrite. Part I: Recorder and sphere-on-tape experiments. Part II: Sliding sphere experiments. Part III: A wear model. *Wear* **139**, 93–148 (1990)
7. Bafekrpour, E., Dyskin, A., Pasternak, E., Molotnikov, A., Estrin, Y.: Internally architected materials with directionally asymmetric friction. *Sci. Rep.* **5**, 10732 (2015)
8. Beeler, N.M., Mclaskey, G.C., Lockner, D., Kilgore, B.: Near-fault velocity spectra from laboratory failures and their relation to natural ground motion. *J. Geophys. Res. Solid Earth* **125** (2020)

9. Schubnel, A., Nielsen, S., Taddeucci, J., Vinciguerra, S., Rao, S.: Photo-acoustic study of subshear and supershear ruptures in the laboratory. *Earth Planet. Sci. Lett.* **308**, 424–432 (2011)
10. Mclaskey, G.C., Lockner, D.A.: Preslip and cascade processes initiating laboratory stick slip. *J. Geophys. Res. Solid Earth* **119**, 6323–6336 (2014)
11. Reches, Z.E., Lockner, D.A.: Nucleation and growth of faults in brittle rocks. *J. Geophys. Res. Solid Earth* **99**, 18159–18173 (1994)
12. Hong, H.-K., Liu, C.S.: Coulomb friction oscillator: Modelling and responses to harmonic loads and base excitations. *J. Sound Vib.* **229**, 1171–1192 (2000)

Deformation Processes



Validity and Stability of Alternative Effective Stress—Specific Volume Relationship for Sands

Tomislav Ivšić¹  and Dunja Perić²  

¹ Faculty of Civil Engineering, University of Zagreb, Kačićeva 26, 10000 Zagerb, Croatia
tomislav.ivsic@grad.unizg.hr

² Department of Civil Engineering, Kansas State University, Manhattan, KS 66506-5000, USA
mailperic@ksu.edu

Abstract. In this study a novel model based on the theory of compressible fluids is used to model the effective stress-specific volume response of granular materials during 1D compression, isotropic compression and critical state. Specifically, a modified Van der Waals equation for real gases is successfully validated against the experimental data obtained from few series of triaxial tests that were conducted over several decades. The proposed equation captures the experimentally observed response throughout the wide range of effective stress including elevated and high pressures. The excellent performance of the model is achieved without introducing any special provisions for grain crushing at elevated and high pressures. Furthermore, features of the proposed isothermal equation of state are further illustrated by presenting it in different coordinate systems along with the experimental data. An additional characteristic of the proposed model is in that it contains thermodynamics-based stability criterion that describes the state of a granular material near the limit of its existence, i.e., in the extreme configuration. The nature of the stability concept is further investigated by presenting the experimental response of sand in triaxial tests observed during the initial stage of the shearing phase. It is found that the observed amount of lateral deformation increases with a decrease in effective confining pressure whereby no lateral deformation is observed initially at high pressures. This indicates that the amount of radial deformation is likely to further increase on approach to zero confining pressure, thus signifying the approach to instability induced collapse.

Keywords: Isothermal equation of state · High pressures · Granular materials

1 Introduction

A granular material, such as sand or gravel, is an assembly of distinct macroscopic particles. These materials exhibit complexities such as instabilities that are associated with transitions from solid like to fluid like state, thus leading physicists toward characterizing the granular material as a new state of matter. The traditional widely used approach to modeling behavior of these materials relies on the use of continuum models that describe their macroscopic behavior while discrete approach, whereby individual

particles and their interactions are modeled, has been gaining popularity primarily in the research community.

Continuum models have traditionally presented pressure-volume in a semi logarithmic diagram that is attributed to Terzaghi and Peck [1], and Scofield and Wroth [2]. Moreover, the classical linear representation in void ratio-log σ' coordinate system remains the most commonly used model in soil mechanics, both for cohesive and cohesion less soils. Recent reviews of compression models [3–5] addresses different classes of models that cover wide stress range. Chong and Santamarina [5] identified some criterions while stating: “Models must be able to fit compressibility data for diverse soils, have physically correct asymptotic values at low stress $\sigma_{ij} \rightarrow 0$ and high stress $\sigma_{ij} \rightarrow \infty$, and involve a small number of physically meaningful parameters (Ockham’s criterion)”. Their brief review includes the classic semilogarithmic and generalized Terzaghi’s model modified to satisfy the asymptotes at low and high stresses, the power function models arising from the log-log presentation, and models using other mathematical functions to provide S-shaped trends like exponential, hyperbolic or arctangent models. Some models include additional features such as grain crushing. For example, Vallejos [4] discussed particle breakage. Russell and Khalili [6] insist on influence of grain crushing on the shape of critical state line (CSL) in a semi-log diagram that is also reflected on a similar shape of the limiting isotropic compression line (LICL). Furthermore, Bauer [7] proposed the exponential model that includes the concept of solid hardness, a pressure at the point of inflection of S-shaped compression curve, thus accounting for grain fragmentation and grain rearrangement in this extended version.

To this end, this study is focused on providing a novel and unified model for macroscopic compression behavior of granular materials that is capable of capturing the material response over extremely wide range of stress without introducing any special provisions for grain crushing. The model is subsequently validated against the relevant experimental data, and the instability criterion that is inherent to the model is also discussed.

2 Proposed Model

2.1 Volume—Pressure Response

Ivšić et al. [8] introduced an alternative model to describe the pressure-volume relationship of granular materials. The model is based on the Van der Waals equation of state or real gases that extends the ideal gas law by accounting for the finite size of molecules of a gas and includes the interaction between the molecules. Ivšić et al. [8] modified Van der Waals equation based on the analogy between the compressible Van der Waals fluid and a sand body that is depicted in Fig. 1.

The corresponding modified or adapted van der Waals equation is given by:

$$\left(p + A/v^2\right)(v - 1) = C \quad (1)$$

where p is pressure, v is specific volume, and A and C are constants that are obtained by fitting the above equation to the relevant experimental data as shown by Ivšić et al. [8], and Ivšić and Gojmerac Ivšić [9]. Equation (1) is suitable for describing any system that

consists of voids and matter as depicted in Fig. 1 whereby the measurable quantities, pressure and volume, are experiencing isothermal conditions. Thus, it also applies to granular assemblies such as sand.

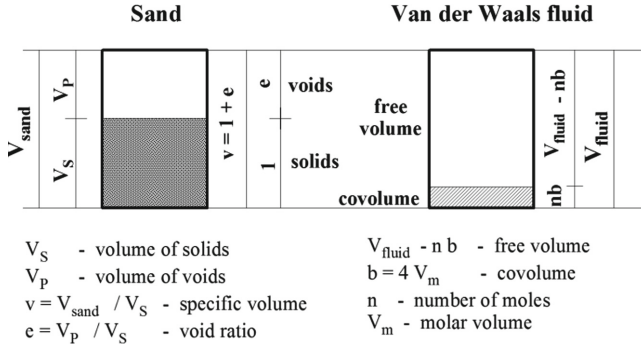


Fig. 1. The continuum idealization of volume relations in sand and van der Waals fluid

The main features of the model presented in [8–10] are:

- the adapted van der Waals equation adequately describes the pressure-volume relationship at critical state of mineral sands over a large range of applied pressures, as well as the pressure-volume relationship in common tests, in which deviator stress is proportional to mean pressure. Moreover, it was demonstrated that the ratio of constants A and C is close to 4 for all tests, which is also expected from theory
- the adapted van der Waals equation adequately describes volume pressure behavior at elevated and high pressures without introducing any special provisions for grain crushing
- Ivšić and Gojmerac Ivšić [9] demonstrated that constants A and C for critical state line are correlated to the chemical composition of mineral sands.

Figure 2 depicts the experimental results [11] for isotropic compression and at critical state in a common semi-log diagram. In addition, Eq. (1) is fitted to the both sets of data, thus demonstrating that it fits the experimental data over the wide range of pressure. Furthermore, according to Eq. (1) the values of specific volume and void ratio asymptotically approach two ($v = 2$) and one ($e = 1$) respectively, as pressure tends to zero. In addition, the specific volume appears to asymptotically approach value of one as pressure tends to infinity. Finally, for limiting value of $A/C = 4$ isotropic compression line (ICL) and CSL are proportional and they merge at zero and infinite pressures. Thus, the model satisfies the criteria stated in [5]. The trends of experimental data observed at the pressures smaller than approximately 1000 kPa are further discussed in Sect. 3.

2.2 Stability Criteria

The domain of applicability of the van der Waals equation in reduced pressure-volume coordinates and “corresponding states” was discussed in detail in [8, 9]. The values of

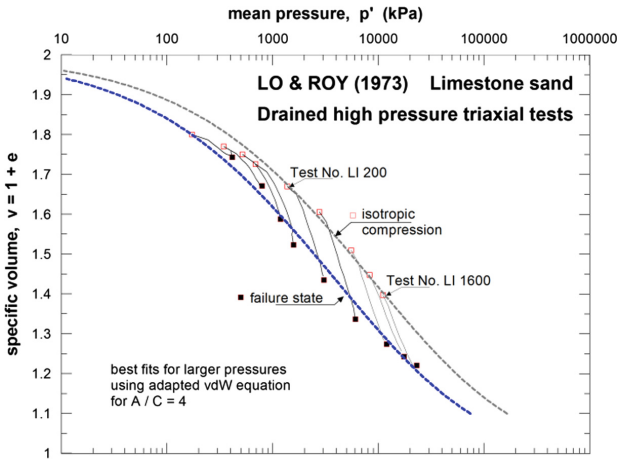


Fig. 2. The interpretation of limestone sand test results by using Eq. (1)

specific volume less than one (1) are excluded by definition (as in Fig. 1). The area where the basic condition for the thermodynamic state equation is not fulfilled (i.e. $dp/dv < 0$) is also excluded, and in the remaining part there are possible stable states for liquids and gases. These criteria for adapted isothermal equation (Eq. 1) give the range of specific volumes between one (1) and two (2), in which the stable states of material in the sense of classical thermodynamics, can be achieved. At the limit value of $v = 2$, the pressure $p = 0$, and the limiting ratio of constants is $A/C = 4$. Also, at this point in accordance with theory, $dp/dv = 0$, thus implying that the corresponding “bulk modulus” is zero, which can be interpreted as a lack of resistance of a body to any force. This range of specific volumes is common for sands. Values of specific volume that are larger than two can be found in presence of additional internal forces such as capillary forces in moist sand that give rise to apparent cohesion. In this case a loose grain structure forms in sand and sand can exist at porosity larger than 50%, thus having more voids than solid particles. The grain structure becomes unstable and it collapses upon removal of attractive forces, i.e. disappearance of capillary forces.

From the point of view of physics this implies that granular materials become unstable as they approach zero pressure and collapse into a state, in which the contacts between particles are lost. Physical manifestations of this event in monophasic granular materials are seen in the instability induced collapse on approach to zero effective stress, such as for example a removal of the lateral support.

3 Interpretation of Sand Pre-compaction

Figure 3 depicts results of series of triaxial tests that were conducted on Cambria sand at high pressures [12, 13]. The best fits for CSL and L1CL, which were obtained by using Eq. (1) and $A/C = 4$, are also shown. The presented tests have been performed on highly compacted sands having initial relative densities of about 90%, which corresponds to the initial void ratio of about 0.52–0.53. The void ratios that correspond to various confining

isotropic pressures define the isotropic compression line over a wide range of pressures. The effects of large initial density are pronounced in lower pressure range while they seem to disappear in the high pressure range. This effect of pre-compaction in sands is similar to the effect of preconsolidation in clays.

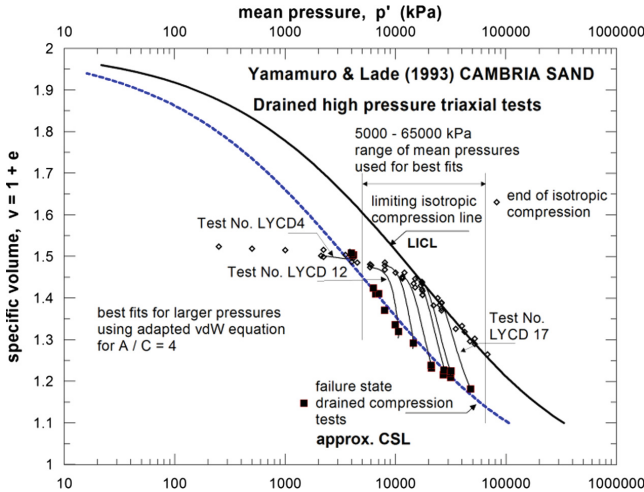


Fig. 3. The interpretation of Cambria sand test results by using Eq. (1)

The results are also interpreted in accordance with the proposed compressible fluid model by using the presentation in auxiliary coordinates [8], $f_p = pv^2$ and $f_v = v^2 / (v - 1)$ as shown in Fig. 4. The auxiliary coordinates emerge after Eq. (1) is rearranged to the following form

$$f_p = C f_v - A \tag{2}$$

The linear function from Eq. (2) is suitable for easy determination of constants A and C (Fig. 4). The interpretation in Fig. 4 shows a clear distinction between the results at lower pressures, where material has memory of previous compaction, and the results for higher pressures where the effects of initial density are erased, similarly to the virgin compression line for clays. The experimental data obtained at lower pressures are fitted to the line denoted by ISO 1 whereby the corresponding linear regression results in the initial void ratio, $e = 0.532$, that corresponds to zero pressure (Fig. 4). As discussed before, the limiting isotropic compression line is expected to have $A/C = 4$. In this case linear regression gives line denoted by ISO2, and corresponding C value is depicted in Fig. 4. The intersection of the two lines (ISO 1 and ISO 2) is determined from the two corresponding equations and its coordinates are provided in Fig. 4.

Next, the results are reverted back to a semi-logarithmic diagram (Fig. 5). It is seen that the influence of initial density spreads much further than would be expected from a common interpretation of preconsolidation and yielding that correspond to the point of maximum curvature in the semi-log plot [4] or similar geometric constructions.

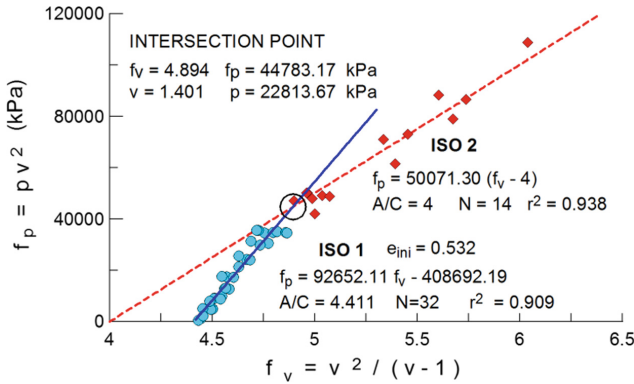


Fig. 4. Isotropic compression of Cambria sand in auxiliary coordinates

Furthermore, the results presented in linear scale often follow a smooth curve whereby deviation and smooth transitions are not directly visible. Nevertheless, by employing semi-log or log-log presentation the transitions become clearly visible. Consequently, the proposed adapted Van der Waals equation is also a smooth curve over a wide range of pressures, thus enabling a description of the appropriate data set with similar accuracy as lines in semi-log plot. When this cubic equation is presented in semi-log diagram (Figs. 2 and 3) the curvature or inflection is found. Nevertheless, it is artificial, originating only from a semi-log presentation rather than from an inherent change of sand properties in certain range of pressures. This also applies to grain crushing attributes or explanations connected to certain appearance in a semi-log presentation. The grain crushing occurs in both, isotropic compression and shear phase of a test and over wide range of pressures. Although the regularities in grain crushing have been found, the reliable indicators or sharp deviations of behavior in common tests, which can be undoubtedly attributed to grain crushing, still remain one of the research topics.

It is also noted that what appears to be the deviation of experimental data (Figs. 2 and 3) from the adapted Van der Waals equation for pressures lower than approximately 1000 kPa can be attributed to: (1) pre-compaction effects in isotropic compression, (2) dilatancy and likely singularity events such as strain localization for data extracted at the critical state. As explained above, Van der Waals equation is still appropriate for the lower pressure range in isotropic compression whereby constants A and C differ from their values at higher pressures. Finally, based on these trends it can be said that the modified Van der Waals equation can capture recoverable and irrecoverable deformations over the large range of pressures.

4 Observations from Shear Phase of Triaxial Test

4.1 Standard Presentation

The concept of instability that occurs at zero pressure, i.e. zero effective stress is further illustrated by analyzing magnitude of radial strains during the shear phase that was observed in conventional triaxial tests conducted over the wide range of pressures on

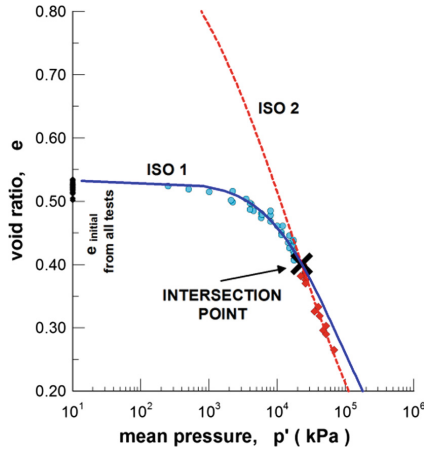


Fig. 5. Interpretation of isotropic compression lines from Fig. 4 in semi-log plot

Cambria sand. The experimental results are presented in Figs. 6a and b. Although a slight deviation between the depicted strains and locally measured strains might exist the presented strains are understood as average uniform strains of the entire sample. Thus, the conventional interpretation implies that the radial strain (e_r) can be obtained from axial (e_a) and volumetric (e_v) strains as

$$e_r = \frac{e_v - e_a}{2} \quad (3)$$

whereby positive normal strains and stresses are compressive. Figure 6b and c show that in the beginning of the shear phase of the tests the volumetric and axial strains are about equal for the tests at higher confining pressures, thus implying that radial strain at this stage is equal to zero. With a decrease in confining pressure the initial response starts to exhibit non-zero initial radial strain. Special conditions occur in test LYCD 4, in which volumetric strain remains approximately equal to zero throughout the entire shear phase of the test. The volume after isotropic compression for this test is close to the CSL volume for this initial cell pressure (and also for failure conditions), so, practically without volume change, the shear phase of the test presents “pure shear” in drained triaxial conditions.

The relation between radial and axial strains is presented in Fig. 6c. For comparison the case of zero volume change ($e_r = -e_a/2$) is also shown. In addition, as expected, in most of the tests volumetric strain rate approaches zero towards the end of the test, as shown in Fig. 6c, thus indicating that the samples have reached the critical state.

Similar results obtained on limestone sand in tests with significantly lower confining pressures are presented in Fig. 7. The results depicted in Figs. 6 and 7 clearly demonstrate that the conditions of zero or very small radial strain, akin to 1D compression, prevail until relatively large axial strains of about 5% are reached. The corresponding value of q/p' ratio is equal to almost 50% of its value at failure. These 1D compression features dominate the test results at higher pressures while they disappear earlier during the course of shearing corresponding to larger q/p' ratios in tests conducted at lower pressures due

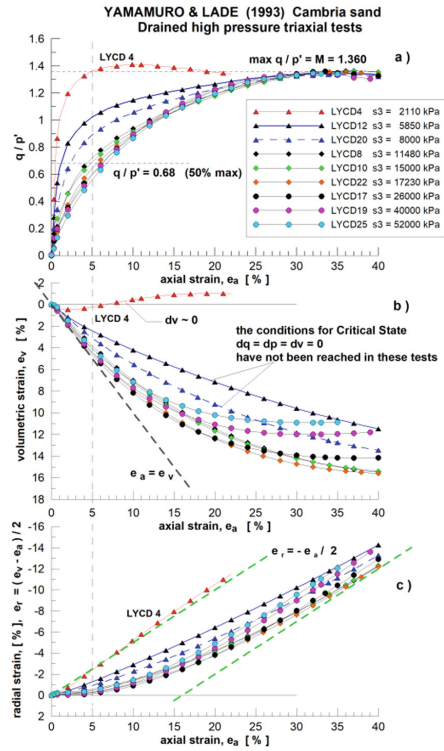


Fig. 6. Results of conventional triaxial tests on Cambria sand at high pressures

to initial density effects. Furthermore, it is hypothesized herein that the magnitude of radial strain during the initial portion of the shear phase is likely to further increase as the confining pressure decreases and eventually approaches zero pressure. This would indicate not only increasing dilatancy but also onset of instability induced collapse on approach to zero effective stress.

It is noted that the conditions of nearly zero lateral strain during the initial part of shearing phase of triaxial test have been noticed by other authors, e.g. Hettler and Vardoulakis [15], although for smaller range of axial strains. These authors reported triaxial tests on dry sands whereby radial strains were measured, unlike herein, and nearly zero values were reported for loose sand samples. On the other side, Kolymbas and Wu [16] also made measurements of radial strain at three levels of a sand sample and did not quite confirm the previous results, at least for dense sand. In addition, the common simple interpretation of e_r on the basis of e_a and e_v , as an average for the whole sample can be easily seen in many other presentations of triaxial test sets on loose sands or sands at elevated or high pressures.

4.2 Alternative Presentation

An alternative presentation of the test results with radial strain as abscissa (Figs. 8 and 9) enhances the observations from previous figures. The q/p' ratio is related to the mobilized

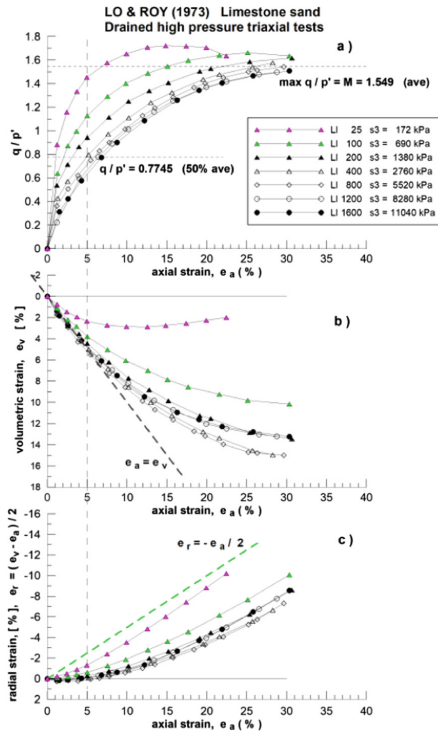


Fig. 7. Results of limestone sand conventional triaxial tests at high pressures

friction, and its maximum value M is a measure of the material strength. Although the failure conditions and strength are obtained for relatively large radial strains, Figs. 8a and 9a again demonstrate that more than a half of the maximum q/p' value is obtained in almost 1D compression conditions in the depicted tests.

The diagrams in Figs. 8b and 9b are inspired by the hypothesis in [8, 9] that the critical state line is a fundamental property of mineral sands, similar to the isothermal state equation for compressible fluid where pressure at CSL is analogous to thermodynamic pressure in fluids. The ordinate ratio, σ_3 (cell pressure)/ p'_{CSL} , positions the shearing phase of triaxial test in relation to the corresponding pressure at critical state, obtained for actual volume during test. To avoid scatter, the values of p'_{CSL} are calculated for each test using the individual constant C at the end of test from Eq. 1 for $A/C = 4$. The diagrams show that during the above mentioned 1D like phase of conventional triaxial compression relatively sudden equalizing of considered pressures takes place. When the cell pressure approaches critical state pressure ($\sigma_3/p'_{CSL} \approx 1$) the change of behavior occurs leading to activation of radial strain. These effects are more pronounced at higher pressures, thus possibly reflecting true material behavior. And again, since there is no significant volume change in the test LYCD4, there is also no significant change in corresponding p'_{CSL} , and the ratio of pressures is almost equal throughout the whole shear phase of the test. This observation also encourages the research based

on compressible fluid concept as an alternative or in addition to the concept of solids commonly used in constitutive soil models [10].

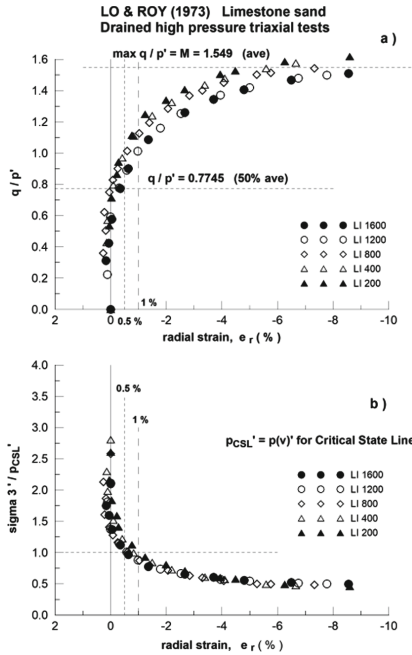


Fig. 8. Conventional triaxial tests on limestone sand at high pressures with e_r on x-axis

5 Conclusions

The pressure-volume behavior of granular materials during isotropic and 1D compressions has been described by various models using several classes of mathematic functions in order to cover wide range of pressures. The novel model proposed herein is based on the analogy with compressible fluids and it captures the response of sands over the wide range of pressures, including low to very high pressures, with a single smooth curve without any additional provisions for grain rearrangement and grain crushing. The proposed relationship presents the adapted isothermal van der Waals state equation, and follows the fundamental principle that the product of pressure and volume is constant. This relation also defines the permissible stable states for sands for specific volumes between $v = 1$ and $v = 2$, which is true for most dry sands. The model can also consistently separate the influences of previous sand compaction, possibly including pre-compaction, from the true material behavior at high pressures where initial density effects are erased. Furthermore, triaxial tests still remain fundamental tests for measuring the soil behavior that is suitable for macroscopic scale constitutive models based on the concept of continuum.

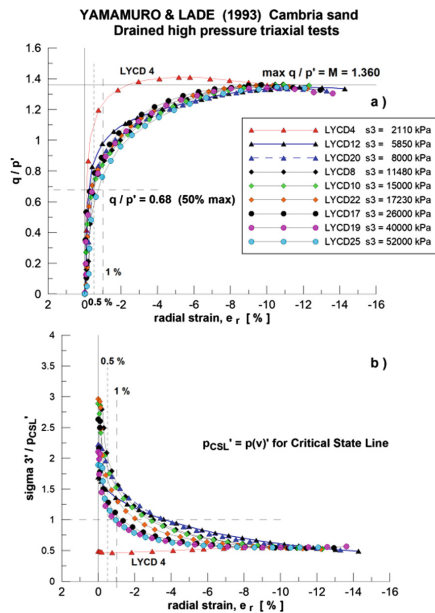


Fig. 9. Conventional triaxial tests on Cambria sand at high pressures with e_r on x -axis

References

1. Terzaghi, K., Peck, R.B.: Soil mechanics in engineering practice. Wiley, New York (1948)
2. Schofield, A.N., Wroth, C.P.: Critical state soil mechanics. McGraw-Hill, Maidenhead, England (1968)
3. Pestana, J.M., Whittle, A.J.: Compression model for cohesionless soils. *Géotechnique* **45**(4), 611–631 (1995)
4. Vallejos, J.: Hydrostatic compression model for sandy soils. *Can. Geotech. J.* **45**(8), 1169–1179 (2008)
5. Chong, S.-H., Santamarina, J.C.: Soil Compressibility Models for a Wide Stress Range. *J. Geotech. Geoenvironmental Eng* **142**(6), 06016003 (2016)
6. Russell, A.R., Khalili, N.: A bounding surface plasticity model for sands exhibiting particle crushing. *Can. Geotech. J.* **41**(6), 1179–1192 (2004)
7. Bauer, E.: Modelling grain fragmentation in hypo plasticity. In: Wu, W. (ed.) *Desiderata Geotechnica*. (Springer Series in Geomechanics and Geoengineering), pp. 1–20. Springer, Cham (2019)
8. Ivšić, T., Galović, A., Kirin, D.: Sand as a compressible fluid. *Phys. A* **277**, 47–61 (2000)
9. Ivšić, T., Gojmerac Ivšić, A.: State equation of mineral sands. *Granular Matter* **14**, 37–50 (2012)
10. Ivšić, T., Ivšić, A.G.: Compressible fluid—an alternative concept within CSSM. In: Yang, Q., Zhang, J.-M., Zheng, H., Yao, Y. (eds.) *Constitutive Modeling of Geomaterials: Advances and New Applications* (Springer Series in Geomechanics and Geoengineering), pp. 179–184. Springer, Beijing, China (2013)
11. Lo, K.Y., Roy, M.: Response of particulate materials at high pressures. *Soils Found.* **13**(1), 1–14 (1973)

12. Yamamuro, J.A., Lade, P.V.: Instability and behavior of granular materials at high pressures, Rep. No. UCLA-ENG-93-26, Civil Engineering Department, School of Engineering and Applied Science, University of California, Los Angeles, CA1 (1993)
13. Yamamuro, J.A., Lade, P.V.: Drained sand behaviour in axisymmetric tests at high pressures. *J. Geotech. Eng. ASCE* **122**(2), 109–119 (1996)
14. Mesri, G., Vardhanabhuti, B.: Compression of granular materials. *Can. Geotech. J.* **46**(4), 369–392 (2009)
15. Hettler, A., Vardoulakis, I.: Behaviour of dry sand tested in a large triaxial apparatus. *Géotechnique* **34**(2), 183–197 (1984)
16. Kolymbas, D., Wu, W.: Recent results of triaxial tests with granular materials. *Powder Technol.* **60**(2), 99–119 (1990)



Predicting the Yield Stress of Geomaterials from Their Microstructure

Martin Lesueur¹ (✉), Xinrui Zhang¹, Thomas Poulet², and Manolis Veveakis³

¹ Delft University of Technology, Delft, Netherlands
m.lesueur@tudelft.nl

² CSIRO Mineral Resources, Perth, Australia

³ Duke University, Durham, USA

Abstract. The seminal work of Gurson (J Eng Mater Technol 99:2–5, 1977) on a simplified pore structure, a single spherical pore, first provided a theoretical relationship between the yield stress and the porosity. This contribution extends the approach to determine the macroscopic yield of a porous material by taking explicitly into account its internal structure. As the yielding of a porous material is controlled by the geometry of its internal structure, we postulate that it is nearly independent of the constitutive plastic behaviour of the material. Here, we show that the influence of that internal structure on the yield could be retrieved from a finite element computation with just an elastoplastic ideal (J2) material equivalent of the skeleton's. With some basic knowledge about the skeleton's mechanical properties, this process allows the determination of the yield stress without requiring the experimental compression of the material. We showcase the predictive power of the method against experimental testing, initially for a unit cell following Gurson, i.e., unique cylindrical void in a 3D printed cylinder sample. Eventually, the applicability of the method is demonstrated on a complex 3D printed rock microstructure, reconstructed from a sandpack's CT-scan.

Keywords: Yield stress · 3D printing · Microstructure

1 Introduction

Many studies are aiming at accounting for the micro-structural influence on rock mechanical properties, whether on elastic properties [9, 15], rock strength [3, 6, 7, 10], or plastic flow law [6, 7], to cite only a few. This contribution focuses on the yield value, as necessary step to model a rock's behaviour past its limit of elasticity. Some models already account for the impact of microstructure on yield through the simplest parameter describing that microstructure: porosity [5–8]. In this contribution, we look at the microstructure from a more general perspective.

The only unambiguous determination of mechanical yield point is possibly restricted to the simplest case of ideal non-porous linear elastic and ideally plastic materials, such as metals for instance. Indeed, experimental compression tests of such materials lead to

characteristic stress-strain curves displaying a sharp transition between the linear elasticity and ideal plasticity. For more complex materials, however, including real geomaterials like porous rocks, a homogenisation procedure is necessary.

A convenient starting point to study the links between microstructure and yield is to consider the theoretical scenario of the simplest configuration, which consists of a single spherical pore, following the seminal work from [7]. To avoid any non-essential complexity and restrict the study to the influence of microstructure, he selected a rigid and ideally plastic material. The outer geometry of the unit cell was taken as spherical, like the void shape, in order to retain the geometrical isotropy and benefit from the symmetry in the analysis. Using the upper-bound limit analysis method, Gurson obtained an approximate upper solution to the yield surface of the hollow sphere geometry, which proved to be precise enough to fit experimental data [18, 20]. Numerous studies followed, extending his work and improving on the model. These include derivations accounting for other shapes of voids (e.g. elliptical [5]), the interaction between voids [4, 19], or the consideration of more complex matrix materials (e.g. viscoplasticity [1]).

By taking an ideally plastic material, the constitutive relationships extracted can indeed be solely attributed to the microstructure, i.e. without any interfering influence of other material properties. Gurson's analysis was an important first step towards our understanding of the influence of the microstructure. We aim now at verifying how the information gathered above holds for physical materials, by complementing our theoretical analysis with an equivalent experimental study on a real material. We verify that the yield of a porous material is equal to that of a virtual porous material with an equivalent ideal elasto-plastic skeleton, instead of considering its more realistic plastic behaviour (including rheology). Additionally, we propose to extend Gurson's type of analysis from limit load to macroscopic yield, measured on stress-strain curves with an energetic method, following Lesueur et al. [14].

The material selected in this contribution is 3D printed polylactic acid (PLA), whose mechanical response from laboratory experiments is plotted and modelled in Fig. 1. 3D printing presents great advantages for the experimental validation of our approach. The 3D printing technique allows a perfect control of the samples' internal structure, whose influence we are characterising. In addition, the printed material has a very reproducible behaviour, as observed by the superposition of curves in Fig. 1. 3D printed PLA is particularly well-suited to test our hypothesis because its plastic response is far from ideal plastic (see Fig. 1). This material displays a strong viscoplasticity and we selected a sample size such that deformation pattern is shearbanding, which results in a weakening before reaching the limit load (see Fig. 1). Moreover, the printing process influences the plastic properties of the resulting material [16]. It is therefore of great interest to select this material to test our approach, which eliminates the need for characterisation of the viscoplasticity and weakening law of the printed PLA. The method is first validated for a cylinder sample with the simplest microstructure, consisting of a single pore as Gurson studied. Then, we present an application of the method for a rock's microstructure, reconstructed from segmented μ CT scan images.

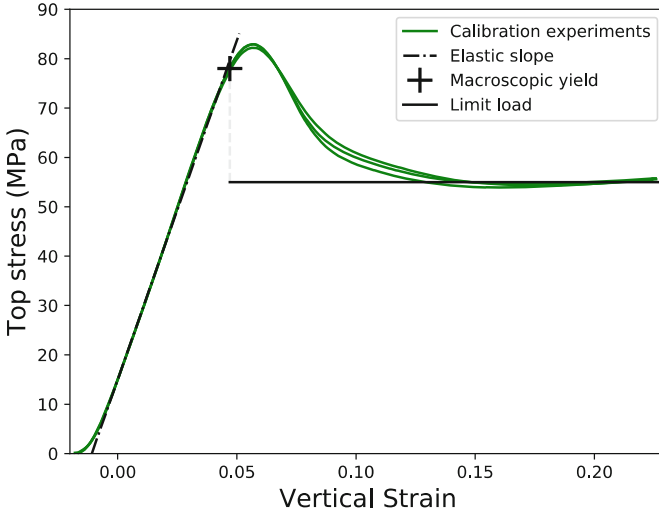


Fig. 1. Three stress strain curves of uniaxial compression of 3D printed full cylinders of PLA to observe the plastic response of the material and assess the reproducibility of mechanical tests on 3D printed samples. The proposed elasto-plastic model in this study is superposed to the curves and determined by three parameters: the slope of the linear elastic part, the macroscopic yield value, and the limit load (displayed on a wide range of strain for visualisation purposes).

2 Validation Against Analytical Yield Criterion

In this section, we verify that our hypothesis stating that the yield stress is mostly influenced by internal structure and not rheology stands for the simplest microstructure, a unique spherical pore. For this ideal structure, a yield criterion has already been derived semi-analytically by Gurson, as detailed in the introduction. Therefore, further simulations are only required in the following section for more complex structures.

The rheology considered is the one of the 3D printed PLA material displayed in Fig. 1. The polymer is known to be pressure insensitive which allows the uniaxial compression tests to characterise the limit load q_y^{ref} of the material, found around 54 MPa. In order to 3D print the structure corresponding to Gurson's model, we simplify the geometry to 2D and the hollow sphere becomes a hollow cylinder with cylindrical hole which is easy to 3D print and the yield surface follows Gurson's criterion, expressed as

$$\frac{q_y}{q_y^{ref}}^2 = 1 + \phi^2 - 2\phi \cos h\left(\frac{3}{2} \frac{p_y}{q_y^{ref}}\right), \quad (1)$$

with p_y , q_y respectively the mean stress and Von Mises stress at yield and ϕ the porosity, equal to 0.25 in this study. The yield surface predicted by Gurson of the hollow cylinder of 3D printed PLA of height 48 mm and diameter 32 mm with a cylindrical hole of diameter 16 mm is plotted in Fig. 2.

FDM-based 3D printers are selected for this work, as they are one of the most popular consumer-level printers [2]. We used the Ultimaker 2+ printers available at the Shaping

Matter Lab of Delft University of Technology, which prints polymers composites based on the extrusion additive manufacturing (AM) system. Slicing parameters are selected such as to produce 3D printed samples of high quality and homogeneity which allows for the reproducibility of results as illustrated by the superposition of the stress-strain curves of Fig. 1. It is worth specifying that the infill density is set at 100% to keep the solid parts non-porous as the present study only considers porosity at a sample-scale level. The mechanical loading is done in uniaxial compression which gives one point of verification on the yield surface. A loading rate of 0.0016 mm/s is applied on the 3D printed hollow cylinder. In this section, we focus on the limit load since it corresponds to the state predicted by Gurson's yield criterion and the supplementary study on the macroscopic yield stress can be found in the study of Lesueur et al. [13]. The limit load is determined on the stress-strain curve similarly to Fig. 1. It is found at 39.1 Mpa, corresponding for a uniaxial compression stress path to a mean stress of 13.3 Mpa. This yield point falls exactly on the analytical yield surface as shown in Fig. 2, which proves that the yield stress for a simple structure can be approximated by an ideal elasto-plastic model.

3 Prediction of the Microstructure Influence on the Yield

The method is now tested against the complex microstructure of a real rock. The selected specimen is a cubic subsample of size 0.5 mm of the Berea sandstone [11].

Using the stack of segmented 2D μ CT scan images, the geometry is meshed in 3D following the methodology described by Lesueur et al. [12]. In order to be processed by the Ultimaker machine for printing, the mesh is converted to an STL file format. The sample is printed as a cube of size 22 mm. The quality of the printed sample is quite remarkable as it captures very well the overall complexity of the original rock. Still, some details of the print remain imperfect, as can be seen in Fig. 3, due to the limit of the Fused Deposition Modelling printing technique for overhanging parts at an angle greater than 45°.

Five identically printed samples are then tested in uniaxial compression following the experimental procedure described in the previous section, with a loading speed of 0.08 mm/min. The resulting stress strain curves, plotted in Fig. 4a, resemble each other, that is, they share the same elastic properties and similar hardening tendencies but have noticeably different values of macroscopic yields. We can only infer that the lack of reproducibility is due to the insufficient printing resolution and quality because the curves of Fig. 1, whose samples' printing quality was high, superposed completely. Compared to Fig. 1, the curve of the sample shows no softening nor limit load, but instead hardens continuously. The complex pore network in the μ CT scan results in a very disperse pore collapse over the whole sample (see plastic deformations in Fig. 2b) that could prevent therefore a homogeneous shearband from forming, which would explain the absence of softening.

In order to numerically determine the yield of this example, we simulate in Finite Element with REDBACK [17] the same uniaxial compression on a digital version of that same microstructure, reconstructed from μ CT scans and meshed following the method of Lesueur et al. [12], with 796,636 structured elements. The boundary conditions applied

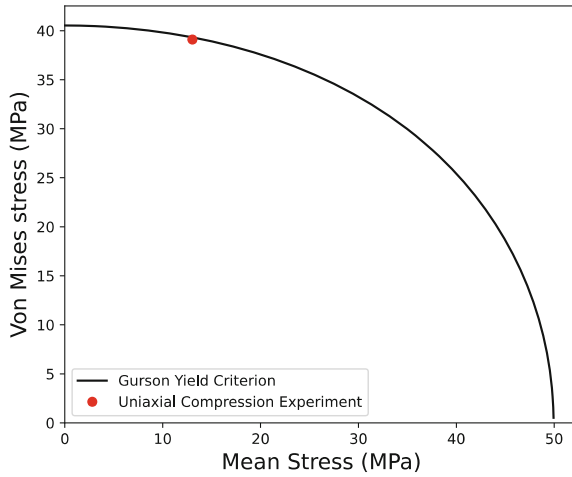


Fig. 2. Theoretical yield surface predicted by Gurson of the 3D printed hollow cylinder with a cylindrical hole. The red dot is the macroscopic yield point obtained from the uniaxial compression experiment on this specimen.

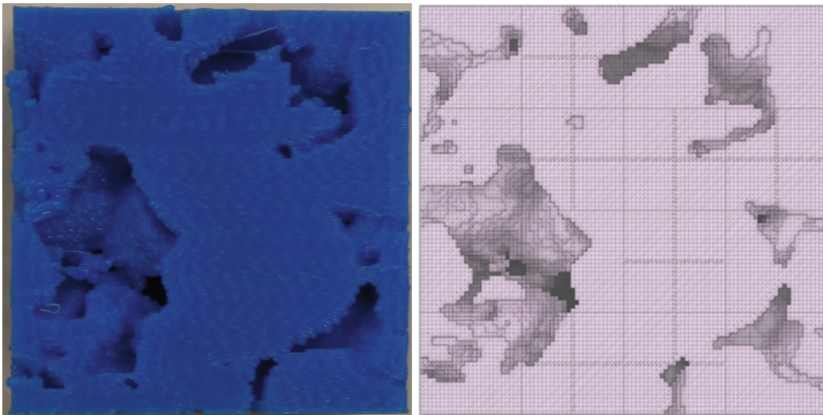


Fig. 3. Side face of the printed microstructure (a) compared to the digital rock (b).

are meant to reproduce a uniaxial compression and loaded with a prescribed strain rate. To retrieve exclusively the influence of the internal structure on the yield, we take an ideal J_2 model for the plasticity of the matrix material and calibrate this model to resemble the behaviour of the printed PLA. The resulting stress strain curve is plotted in Fig. 2a.

We note that for both numerical and experimental approach, we do not reach indeed a limit load as in Fig. 1. This confirms our interest in extending Gurson’s exclusive study of the limit load to the macroscopic yield because the limit load does not exist for every material.

Despite that the match of Fig. 2a is not as impressive as that of Fig. 1 due to the precision loss on the 3D printing, the numerical and experimental curves still match

qualitatively and display a similar shape. In this more complex example, the porous material appears to be stiffer and stronger (higher macroscopic yield) with the experimental approach. This could be explained by the reinforcement of the structure due to the existence of artificial bridges between pores that were created during the imperfect printing process. The suboptimal printing quality adds to the uncertainty of the experimental results, which brings us more confidence in the value of elasticity and macroscopic yield determined with the numerical approach.

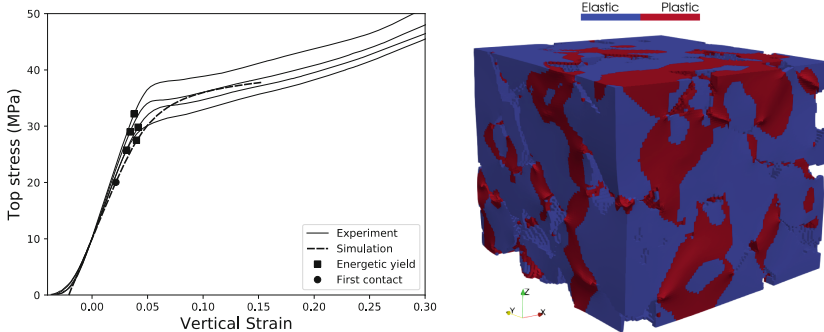


Fig. 4. (a) Experimental and numerical stress-strain curves of the uniaxial compression of 3D printed samples of the Bera sandstone [11]. (b) Visualisation of plastic deformations on the numerical uniaxial compression at 12% strain.

4 Conclusion

In this contribution, we presented an approach to determine the macroscopic yield of a porous material from finite element compression of its microstructure, replacing the traditional destructive testing approach. By focusing the study on the macroscopic yield instead of the complete mechanical behaviour, we have shown that the complex skeleton material can be satisfactorily approximated by an equivalent ideal elasto-plastic material before reaching the macroscopic yield. By reducing the complexity of the material implemented, simulations of mechanical compressions become more achievable.

References

1. Besson, J.: Damage of ductile materials deforming under multiple plastic or viscoplastic mechanisms. *Int. J. Plast.* **25**(11), 2204–2221 (2009)
2. Dizon, J.R.C., Espera Jr, A.H., Chen, Q., Advincula, R.C.: Mechanical characterization of 3D-printed polymers. *Addit. manufact.* **20**, 44–67 (2018)
3. Dunn, D.E., LaFountain, L.J., Jackson, R.E.: Porosity dependence and mechanism of brittle fracture in sandstones. *J. Geophys. Res.* **78**(14), 2403–2417 (1973)
4. Fritzen, F., Forest, S., Bohlke, T., Kondo, D., Kanit, T.: Computational homogenization of elasto-plastic porous metals. *Int. J. Plast.* **29**, 102–119 (2012)

5. Gologanu, M., Leblond, J.-B., Perrin, G., Devaux, J.: Recent extensions of gurson's model for porous ductile metals. In: *Continuum Micromechanics*, pp. 61–130. Springer Vienna, (1997)
6. Green, R.J.: A plasticity theory for porous solids. *Int. J. Mech. Sci.* **14**(4), 215–224 (1972)
7. Gurson, A.L.: Continuum theory of ductile rupture by void nucleation and growth: Part I—yield criteria and flow rules for porous ductile media. *J. Eng. Mater. Technol.* **99**(1), 2–15 (1977)
8. Hamiel, Y., Lyakhovskiy, V., Agnon, A.: Coupled evolution of damage and porosity in poroelastic media: theory and applications to deformation of porous rocks. *Geophys. J. Int.* **156**(3), 701–713 (2004)
9. Hashin, Z., Shtrikman, S.: A variational approach to the theory of the elastic behaviour of multiphase materials. *J. Mech. Phys. Solids* **11**(2), 127–140 (1963)
10. Hoshino, K.: Effect of porosity on the strength of the clastic sedimentary rocks. In: *Advances in rock mechanics: Proceedings of the 3rd Congress of International Society of Rock Mechanics*, volume IIA, pp. 511–516, Denver, Colorado (1974)
11. Imperial College Consortium On Pore-Scale Modelling: Berea sandstone. (2014). <https://doi.org/10.6084/m9.figshare.1153794>
12. Lesueur, M., Casadiego, M.C., Veveakis, M., Poulet, T.: Modelling fluid-microstructure interaction on elasto-visco-plastic digital rocks. *Geomech Energy Environ* **12**, 1–13 (2017)
13. Lesueur, M., Poulet, T., Veveakis, M.: Predicting the yield strength of a 3d printed porous material from its internal geometry. *Addit. Manuf.* **44**, 102061 (2021)
14. Lesueur, M.: Influence of multiphysics couplings across scales: from digital rock physics to induced fault reactivation. PhD thesis, UNSW Sydney, School of Minerals and Energy Resources Engineering (2020)
15. Mackenzie, J.K.: The elastic constants of a solid containing spherical holes. *Proceedings of the Physical Society. Section B* **63**(1), 2–11 (1950)
16. Popescu, D., Zapciu, A., Amza, C., Baci, F., Marinescu, R.: FDM process parameters influence over the mechanical properties of polymer specimens: a review. *Polym. Test.* **69**, 157–166 (2018)
17. Poulet, T., Paesold, M., Veveakis, M.: Multi-physics modelling of fault mechanics using redback: a parallel open-source simulator for tightly coupled problems. *Rock Mech. Rock Eng.* **50**(3), 733–749 (2017)
18. Springmann, M., Kuna, M.: Identification of material parameters of the gurson–tvergaard–needleman model by combined experimental and numerical techniques. *Comput. Mater. Sci.* **33**(4), 501–509 (2005)
19. Tvergaard, V.: Influence of voids on shear band instabilities under plane strain conditions. *Int. J. Fract.* **17**(4), 389–407 (1981)
20. Xie, S.Y., Shao, J.F.: Elastoplastic deformation of a porous rock and water interaction. *Int. J. Plast.* **22**(12), 2195–2225 (2006)



Perturbations in Granular Materials: Subtleties in DEM Modeling

Mojtaba Farahnak¹(✉), Richard Wan¹, Mehdi Pouragha², and François Nicot^{1,3}

¹ University of Calgary, Calgary, AB T2N 1N4, Canada

{mojtaba.farahnaklang, wan}@ucalgary.ca

² Carleton University, Ottawa, ON K1S 5B6, Canada

³ Université Savoie Mont Blanc, EDYTEM, Chambéry, France

Abstract. The current study reveals subtleties in the proper modeling of strain perturbations during the instability analysis of granular materials and their incremental behavior using the Discrete Element Method (DEM). Multi-directional strain probings are conducted at different states along an initial stress-strain curve. The influence of the particles' inertia at the beginning of each strain probe is highlighted and remedies to minimize inertia effects toward reaching a static equilibrium are discussed. An instability analysis of the strain probes as a function of fluctuations in the stress-strain curve demonstrates a difference in material response in the presence of kinetic micro-avalanches. Finally, the nature of the incremental behavior in stress responses is explored with respect to size of the strain probes and energy characteristics.

Keywords: Granular materials · DEM strain probing · Second-order work

1 Introduction

The complex incremental behavior of granular materials is commonly explored via multi-directional loading probes. For instance, experimental and numerical approaches have been carried out incorporating strain or stress probing to investigate the incremental behavior of these materials [1–4]. Given the critical role of the micromechanical features, e.g., contact gain and loss between particles, and structural (fabric) evolution in characterizing the behavior of granular media, a DEM modeling approach is herein used effectively to improve current understanding of their multi-directional incremental behavior.

The current study addresses challenges encountered in the DEM modeling of multi-directional loading/unloading probes in granular materials. In particular, subtleties of DEM probing are discussed by performing a series of strain perturbations at different material stress-strain states. In this regard, the influence of inertia at the beginning of strain probes, instability behaviors within the fluctuations of the stress-strain curve, and nature of the material response with respect to the size of probes in DEM simulations are elaborated. The results demonstrate how these issues can change the material response so that caution must be exercised to ensure a reliable micromechanical instability analysis.

The micromechanical characteristics of granular materials are connected to the evolution of fabric during loading history, where perturbations at different states of a stress-strain loading path are desired for an incremental analysis. At each current state, the particles have inertia in accordance with the ongoing quasi-static loading. The influence of particles' inertia on the material response during the strain probes is demonstrated and two remedies are proposed to reach the static equilibrium: loading with a lower strain rate and resting of the sample, along with limitations that ensue in the latter approach.

The stress-strain curve of a triaxial test on granular materials often exhibits fluctuations with quasi-static kinetic micro-avalanches [5]. A material instability analysis through the second-order work criterion [6] shows a dependency of incremental behavior of material on the stress-strain state with respect to the associated fluctuations.

Finally, a series of DEM simulations are carried out in which the nature of stress responses and non-linearity of the incremental material behavior are investigated with respect to the size of probing. To this end, the elastic energy stored at contacts during the probes are compared to the total energy stored at the beginning of the probes to quantitatively propose a criterion that defines a limit for linearity in material response.

2 DEM Simulations

DEM numerical simulations are herein carried out to perform strain probing at different states during the deviatoric loading in a plane strain test. The open-source YADE code [7] has been used for the simulation of loading paths on a REV consisting of spherical particles.

The mechanical interactions between solid particles are characterized by a classical linear elastic-plastic contact law that is described by a local Coulombian friction coefficient $\mu = \tan \phi = 0.5$ and two ratios $k_n/\bar{D} = 10$ MPa and $k_t/k_n = 1$ representing the local elastic stiffness with respect to the average particle diameter $\bar{D} = 0.02$ mm ($D_{\max}/D_{\min} = 2$).

DEM simulations begin with isotropic compression of a non-contacting cloud of 65,536 spherical particles within a parallelepiped (with a height/width = 2) until reaching the desired confining pressure of $p_0 = 10$ kPa. A very low interparticle friction is adopted to obtain a relatively dense packing state with porosity equal to 0.366. Subsequent to the isotropic compression, the deviatoric loading is applied in vertical (Y) direction ($\dot{\epsilon}_{yy} = \text{const}$) while the stress is fixed in lateral X direction ($\dot{\sigma}_{xx} = 0$), and the plane strain condition is satisfied in lateral Z direction ($\dot{\epsilon}_{zz} = 0$). During all loading steps in the simulations, the quasi-static condition is constantly checked against a very low level of inertial number or unbalanced force ratio ($< 10^{-4}$).

The stress-strain response of the sample is illustrated in Fig. 1, where the stress ratio q/p is plotted versus deviatoric strain ϵ_d , indicating the softening phase after the peak and a clear tendency of dilatancy as a typical volumetric response of dense granular materials. Three states, named A, B, and C, chosen during deviatoric loading are selected to perform the strain probing at $q/p = 0, 0.5, 1.09$, respectively. Multi-directional strain probes with a magnitude of $\|\mathbf{d}\boldsymbol{\epsilon}\| = 0.00002$ are subsequently performed within a three-dimensional spherical space with range spanned by 15° in both altitude (θ) and azimuth (ϕ) angles into 266 probes. Ideally, the strain probe magnitude is selected to preserve the linear stress response, the influence of which will be further discussed later on.

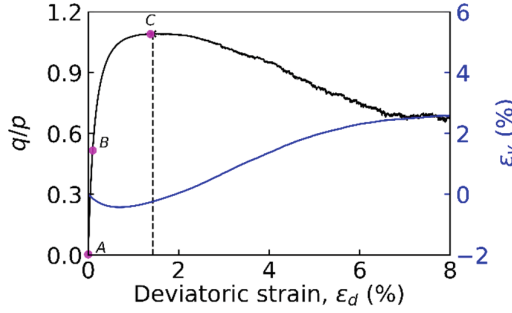


Fig. 1. Stress-strain and volumetric responses of the sample during DEM simulation of the plane strain test

2.1 Inertia Effect

Particles in each state on the master, so-called backbone, stress-strain curve of the plane strain test possess inertia due to the existence of unbalanced forces during the quasi-static DEM simulation. As such, the material response to the probing is very sensitive to the particles’ inertia at the beginning of probing. The strain rate $\dot{\epsilon}_{yy} = 0.1$ was selected for the backbone plane strain test to ensure that the average unbalanced forces always remain several orders smaller than the average contact force ($< 10^{-4}$). It is worth noting that the simulation costs several weeks in run time incorporating such a small strain rate.

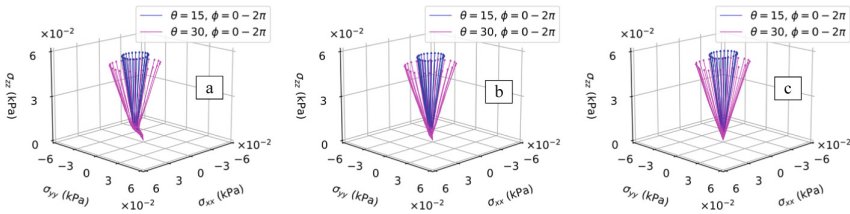


Fig. 2. The influence of particles’ inertia on stress responses to the strain probes with $\theta = 15^\circ$ and 30° , and $\phi = 0 - 2\pi$ using strain rates ($\dot{\epsilon}_{yy}$) of (a) 0.1 , (b) 0.05 , and (c) 0.01.

However, as illustrated in Fig. 2a, the influence of particles’ inertia prevails at the beginning of strain probes at state C, where the stress responses are non-linear with a kink effect; it takes time for the assembly to adjust with the strain perturbations. Figure shows the stress responses for only two probing altitude angles of 15° and 30° for the sake of a better visualization.

As a remedy to minimize the influence of inertia at the beginning of the strain probes, the saved states on the backbone test are loaded with lower strain rates $\dot{\epsilon}_{yy}$ equal to 0.05 and 0.01. This approach is suggested to bypass the tedious run times for repeating the whole simulation of backbone test with lower strain rates. Figure 3 shows the good agreement for the strain-stress loading curves with different strain rates. Two states on the loading curves with strain rates of 0.05 and 0.01 are selected as C_1 and C_2 in a same

manner to demonstrate the effect of inertia on the stress response as a result of decreasing the strain rate.

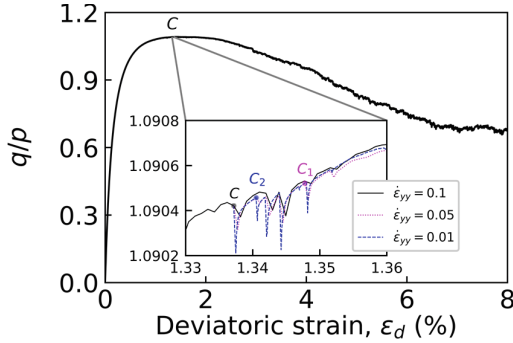


Fig. 3. Reloading the state C with lower strain rates of 0.05 and 0.01.

As illustrated in Fig. 2b and Fig. 2c, the influence of inertia is minimized by decreasing the strain rate in the backbone test. Incorporating $\dot{\epsilon}_{yy} = 0.01$, the strain probes performed at states A, B, and C, and the corresponding stress response envelopes are visualized in Fig. 4. As anticipated, the DEM simulation results show a directional dependence of the plastic response on the strain increment direction. Such a directional dependency is exacerbated when getting closer to the peak, i.e., state C.

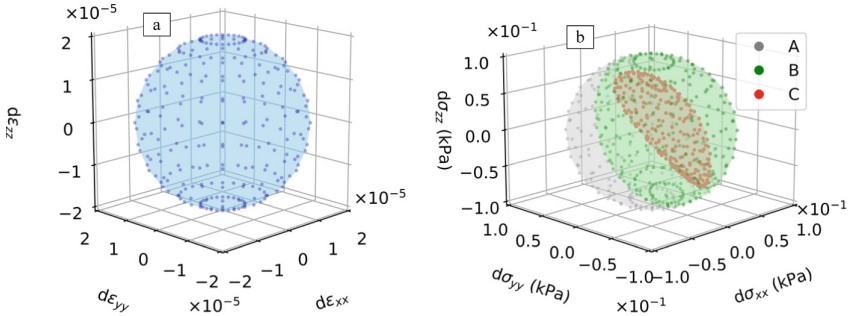


Fig. 4. (a) Applied strain probes visualized as a sphere in vectorial strain space, and (b) the stress responses for states A, B, and C.

As an instability analysis, the second-order work criterion [6] is herein employed to capture the instability of material states during the directional probes when $W_2 = d\sigma : d\epsilon < 0$. The polar diagrams of normalized second-order work defined as $W_2^n = \frac{d\sigma : d\epsilon}{\|d\sigma\| \|d\epsilon\|}$ are given in Fig. 5 for states A, B, and C. In these diagrams, an arbitrary constant value c is added to the polar value of W_2^n to obtain $W_2^n + c > 0$. The points inside the dashed circle correspond to a negative second-order work. Figure 5c shows negative W_2^n at a high deviatoric stress level, i.e., state C, with the strain probing directions of $(\theta, \phi) = (90^\circ, 150^\circ)$ and $(105^\circ, 150^\circ)$. The results are in agreement with those reported in classical

triaxial tests [2], noting that a transformation of the direction from strain space to stress space is necessary (boundaries of instability cones with negative second order work are normal in the two spaces, i.e., $d\sigma : d\epsilon = 0$).

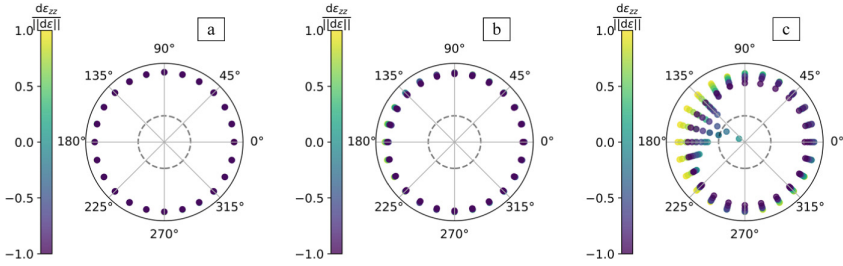


Fig. 5. Polar diagrams of normalized second-order work for A, B, and C states. The points inside the dashed circle show negative W_2^n .

2.2 Resting

As an alternative to the proposed loading of the sample at saved states with a lower strain rate, a resting of the sample might also be considered [8]. In such a numerical technique, after the expected value of stress (q/p) is attained during the backbone test, the specimen is left rested under constant boundary stresses to reach static equilibrium where the particles experience a quiescent state. Subsequently, the strain probing is applied on the rested sample and the corresponding stress responses are given in Fig. 6a. As illustrated, the effect of inertia at the beginning of probes is also limited using this approach.

However, it must be noted that the resting of the sample transforms the material into a different state which is no longer necessarily on the stress-strain path of the backbone test. In order to demonstrate such a transformation, the instability analysis on the rested sample of state C is carried out where the normalized second-order work for multi-directional strain probing as illustrated in Fig. 6b. Results show the transformation of material state at which the instability, i.e., the negative second-order work does not occur for the directions of instability cone that existed at the state C, as shown in Fig. 5c.

2.3 Fluctuations

Intrinsic to the nature of granular materials, the stress-strain curve of a loading test often exhibits fluctuations with quasi-static kinetic micro-avalanches [5] that can be captured via DEM modeling. The fluctuation in boundary stress, driven by the strain loading, is triggered by a release in elastic energy due to the rearrangement of particles, and the resulting change in the force chain. Such a micro-avalanche is accompanied by an increase in kinetic energy that will be dissipated over time with frictional sliding. For dense assemblies, the fluctuations are concentrated closer to the peak of deviatoric stress. In this regard, the state at which strain probing is performed might be selected

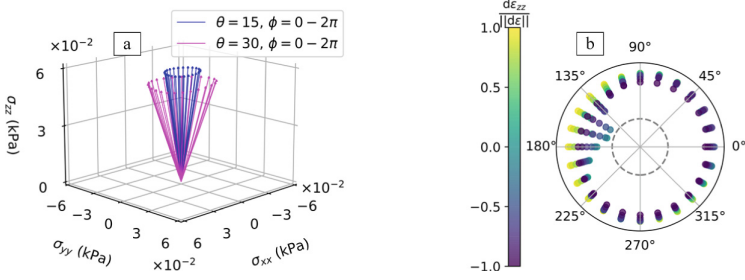


Fig. 6. Effect of resting on state C: (a) stress response to the strain probing, and (b) the polar diagram of the normalized second-order work W_2^n .

before, on or after an avalanche. Herein, three states are selected on the loading curve with $\dot{\epsilon}_{yy} = 0.01$. In accordance with the previous sections, the state C_2 is located on an avalanche, while two other states, i.e., C_3 and C_4 are selected in between two micro-avalanches and after an avalanche, respectively, as shown in Fig. 7.

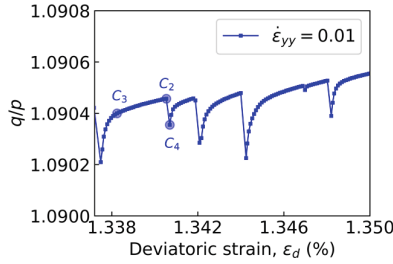


Fig. 7. Fluctuations close to the peak of shear stress and the kinetic micro-avalanches.

The instability analysis presented in Fig. 8 shows the dependency of the incremental behavior of material on the stress-strain state with respect to the fluctuations. In fact, this observation suggests unstable directions for which $W_2^n < 0$, so-called cone of instability, is maximized for the state on a micro-avalanche.

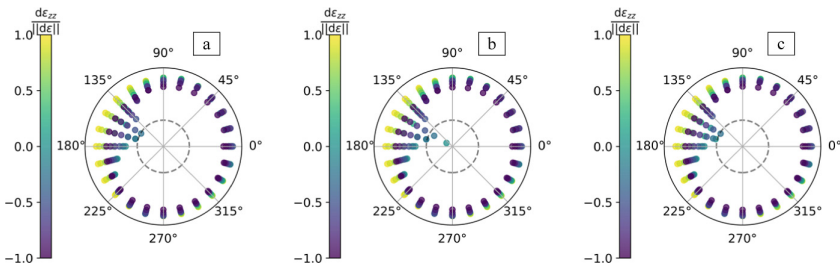


Fig. 8. Normalized second-order work for probing at: (a) C_3 , (b) C_2 , and (c) C_4 .

2.4 Probing Size

The size of stress probing increment is commonly compared with the confining pressure of the assembly (p_0), while also reported to depend on contact stiffness between particles [8]. Previous studies have incorporated values ranging $\|d\sigma\|/p_0 = 0.1 - 0.001$ [3]. The probe increment must be sufficiently small to ensure the strain/stress response to remain linear, while also being sufficiently large to perturb the sample for a meaningful analysis of the material’s incremental behavior, and for obtaining reasonable micromechanical measures. In order to investigate the proper size of the perturbation, three more strain probing with increment sizes of $\|d\epsilon\| = 0.0002, 0.0005$ and 0.001 are performed to demonstrate the nature of the responses with respect to the size of probing. Figure 9 shows the stress responses for the altitude angle of $\theta = 105^\circ$ where the instability occurs as shown earlier. The non-linearity of stress responses is observed when increasing the magnitude of probing after $\|d\epsilon\| = 0.0002$, as illustrated in Fig. 9b and Fig. 9c.

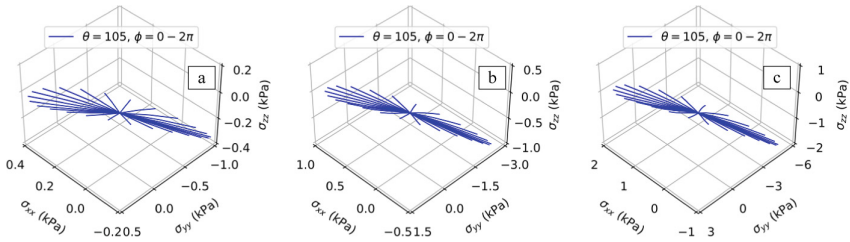


Fig. 9. Stress responses to strain probing with magnitudes of: (a) $\|d\epsilon\| = 0.0002$, (b) 0.0005 , and (c) 0.001 . Curved stress response vectors signal non-linearity.

The magnitude of perturbation can be investigated by comparing the elastic energy stored (dE^{el}) at all contacts c between particles during probing, $E^{el} = \sum_c \left(\frac{f_n^2}{2k_n} + \frac{f_t^2}{2k_t} \right)$, to the total elastic energy stored at the beginning of probing (E_i^{el}). The summarized results in Table 1 along with the observations in Fig. 9 indicate that the non-linearity of material response occurs for perturbations when the ratio dE^{el} / E_i^{el} goes beyond a few percent.

Table 1. Characteristics of strain probing with different magnitudes.

$\ d\epsilon\ $	$\ d\sigma\ /p_0$		dE^{el} / E_i^{el}	
	min	max	min	max
0.00002	0.0006	0.01	0.000002	0.004
0.0002	0.003	0.1	0.00004	0.04
0.0005	0.007	0.25	0.0004	0.1
0.001	0.01	0.5	0.001	0.2

3 Conclusions

The subtleties in the DEM modeling of perturbations in granular materials have been addressed in this study. The effect of inertia at the beginning of the strain probes is demonstrated and two remedies including either a loading with lower strain rate or a resting are described to reach the static equilibrium. The latter technique is shown to change the instability characteristics of the assembly during the probes. The instability analysis considering the strain-stress curve fluctuations shows expansion of the cone of instability at the kinetic micro-avalanches. Finally, the magnitude of strain probing is linked to the change in energy characteristics of the assembly during the perturbation. The numerical results show a non-linear behavior in response to perturbations whenever the ratio of elastic energy stored at the contacts during probing to the total elastic energy is higher than a few percent. This provides an energy-based criterion that eliminates guesswork when choosing the appropriate probing size for an objective material instability analysis.

References

1. Calvetti, F., Viggiani, G., Tamagnini, C.: A numerical investigation of the incremental behavior of granular soils. *Riv. Ital. di Geotec.* **3**, 11–29 (2003)
2. Sibille, L., Nicot, F., Donzé, F.V., Darve, F.: Material instability in granular assemblies from fundamentally different models. *Int. J. Numer. Anal. Methods Geomech.* **31**(3), 457–481 (2007)
3. Kuhn, M.R., Daouadji, A.: Multi-directional behavior of granular materials and its relation to incremental elasto-plasticity. *Int. J. Solids Struct.* **152**, 305–323 (2018)
4. Pouragha, M., Kruyt, N.P., Wan, R.: Fabric response to strain probing in granular materials: Two-dimensional, isotropic systems. *Int. J. Solids Struct.* **156**, 251–262 (2019)
5. Baró, J., Pouragha, M., Wan, R., Davidsen, J.: Quasistatic kinetic avalanches and self-organized criticality in deviatorically loaded granular media. *Phys. Rev. E.* **104**(2), 021901 (2021)
6. Wan, R., Nicot, F., Darve, F.: *Failure in geomaterials: a contemporary treatise*. Elsevier, New York (2017)
7. Šmilauer, V. et al.: *Yade documentation (2nd edn)*, The Yade Project (2015)
8. Froiio, F., Roux, J.N.: Incremental response of a model granular material by stress probing with DEM simulations. *AIP Conf. Proc.* **1227**, 183–197 (2010)



Modelling of Capillary Pressure-driven Water Flow in Unsaturated Concrete Using Coupled DEM/CFD Approach

Marek Krzaczek^(✉), Michal Nitka, and Jacek Tejchman

Gdańsk University of Technology, Gdańsk, Poland

marek.krzaczek@pg.edu.pl

Abstract. A novel coupled approach to modelling capillary-driven two-phase water flow in unsaturated concrete was formulated. By merging the discrete element method (DEM) with computational fluid dynamics (CFD) under isothermal settings, the process was numerically studied at the me-so-scale in two-dimensional conditions. Small concrete specimens of a simplified particle meso-structure were subjected to fully coupled hydro-mechanical simulation tests in isothermal conditions. A simple uniaxial compression test was used to calibrate the pure DEM represented by bonded spheres, while permeability and sorptivity tests for an assembly of bonded spheres were used to calibrate the pure CFD. For simplified specimens of the pure mortar, mortar with aggregate, and mortar with aggregate and interfacial transition zone (ITZ) of a given thickness, DEM/CFD simulations were performed sequentially. The numerical results of permeability and sorptivity were compared to the data found in the literature. The primary purpose of the re-search was to demonstrate the impact of ITZ on fluid flow in unsaturated concrete caused by capillary pressure.

Keywords: DEM-CFD · Capillary flow · Concrete

1 Introduction

At the meso-scale, aggregates, cement matrix, interfacial transition zones (ITZs) between aggregates and mortar, and macro-pores make up concrete, which is a highly heterogeneous, discontinuous, and porous composite material. ITZs are seen near aggregates and suggest significant compositional changes when compared to the mortar matrix [1]. They have more and larger pores, smaller particles, and less anhydrous cement and C-S-H (calcium silicate hydrate) gel than the cement matrix, resulting in higher transport characteristics (permeability, diffusivity, and conductivity) [2]. They make it easier for external aggressive substances to penetrate concretes, causing both the concrete and the reinforcing to deteriorate. They also help to transmit humidity through concrete. Concrete pores range in size from a few tenths of nanometers to several tens of micrometers. Water may be absorbed into concrete by capillary forces emerging from

the contact of very small pores with a liquid phase if the moisture content inside the concrete is less than its saturation threshold. This is a common water flow mechanism in concrete that is observed in field applications that are subjected to wetting and drying cycles.

The current work shows how to model viscous and capillary-driven two-phase fluid flow in unsaturated uncracked concrete at the meso-scale under isothermal conditions using a novel mathematical mesoscopic approach. Aggregates and ITZs were explicitly considered in the model. Numerical models are especially effective for isolating and quantifying the effect of various parameters on transport qualities that are difficult to get from experimentation. They are also significantly more efficient and cost-effective. At the meso-scale of concrete, numerical simulations were carried out using a fully coupled 2D DEM/CFD technique that included solid mechanics and fluid mechanics (DEM—discrete element method, CFD—computational fluid dynamics). Because a thorough understanding of pore-scale behaviour is required for accurate interpretation and prediction of macroscopic behaviour, DEM was used to capture concrete's mechanical behaviour, and CFD was used to describe the laminar viscous two-phase liquid/gas flow in pores between the discrete elements by employing a channel network, because an understanding of pore-scale behaviour is essential for successful interpretation and prediction of macroscopic behaviour. The pure DEM was represented in simplification by spheres of various diameters and calibrated using a standard uniaxial compression test, whereas the pure CFD was calibrated using a standard permeability (a measure of a material's ability to transmit fluid) and sorptivity (a measure of a material's capacity to absorb/desorb liquid by capillarity) test.

The main purpose of our simulations was to demonstrate the effect of ITZs on fluid flow in unsaturated concretes, which is influenced by both hydraulic and capillary pressure and is difficult to assess empirically. Unsaturated specimens of a simplified meso-structure emulating the pure mortar, mortar including aggregate, and mortar including aggregate with ITZ of a given thickness were subjected to fully coupled hydro-mechanical modeling tests. The interfacial tension, contact angle, and throat radius were used to compute the capillary pressure. The impact of external load direction, water saturation volume, and gas-phase content on fluid flow patterns was also investigated. The numerical results of permeability and sorptivity were compared to published data. Previously, the authors' fully coupled DEM/CFD model was effectively applied to simulate a hydraulic fracturing process in rocks with one- or two-phase fracturing laminar viscous fluid flow made up of a liquid/gas mixture [3, 4].

2 DEM for Cohesive-Frictional Materials

For DEM calculations, the 3D spherical explicit discrete element open code YADE [5] was utilized. The method allows for a small overlap between two touched bodies (the so-called soft-particle model). As a result, an arbitrary micro-porosity can be created using DEM. The model assumes a cohesive bond at the grain contact that fails brittle under the critical normal tensile load [6]. Under normal compression, shear cohesion failure causes contact slip and sliding, which follows the Coulomb friction law. If a cohesive joint between spheres vanishes after reaching a critical threshold, damage occurs. If

any contact between spheres emerges after a failure, the cohesion does not reappear. In quasi-static analyses, a simple local non-viscous dampening is utilized to accelerate convergence. The DEM model does not take into account material softening. Bond damage in tension is the most important micro-scale process for damage in the pre-failure regime (although bonds can also break by shear). For DEM simulations, five key local material parameters are required: E_c (elastic modulus of the grain contact), ν_c (Poisson's ratio of the grain contact), μ (the Coulomb inter-particle friction angle), C_c (cohesive contact force) and T_c (tensile contact force). Furthermore, particle radii R , particle mass density ρ , and damping parameter α_d must be known. The particle breakage was ignored. The material constants are generally identified in DEM using simple laboratory experiments on the material (uniaxial compression, uniaxial tension, shear, biaxial compression). The detailed calibration procedure for frictional-cohesive materials was described in [6–8], and it was based on real simple standard laboratory tests (uniaxial compression and uniaxial tension) of concrete specimens by running several DEM simulations of experiments on discrete element specimens. DEM was shown to be useful for local and global simulations of macro- and micro-cracks in concrete under bending (2D and 3D studies), uniaxial compression (2D and 3D simulations), and splitting tension (2D analyses) [6–8].

3 CFD Model

The authors' paper [4] provided detailed descriptions of the 2D laminar two-phase fluid flow model and a coupling scheme. Two domains coexisted in the original system: a 3D discrete domain (spheres) and a 2D fluid domain (continuum represented by a grid of channels). A grid was used to separate the fluid and solid domains. As a result, each pore was divided into a number of triangles (VP). The gravity centers of the mesh triangles (VP) in the continuous domain between the discrete elements were connected by channels composed of two parallel plates that created a virtual network of pores (VPN) to properly reproduce their changing geometry (shape, surface and position). Two types of channels are introduced [3, 4]: (1) channels between spheres in contact (referred to as virtual channels to mimic real flow in 3D,) and (2) channels connecting grid triangles in pores (referred to as actual channels). The hydraulic aperture (height) of virtual channels was assumed a function of the hydraulic aperture for the infinite normal stress, the hydraulic aperture for the zero normal stress, the effective normal stress at the particle contact and the aperture coefficient [3]. The hydraulic aperture of actual channels was related to the geometry of the neighbouring triangles, and included also a reduction factor to keep the maximum Reynolds number along the primary flow channel below the critical value for laminar flow at all times [3]. Triangles, by definition, had no fluid flow. VPs stored fluid phase fractions and densities as well as accumulating pressure. The density change in a fluid phase caused pressure variations, which was related to the mass change in VPs. In triangles, the momentum conservation equation was thus ignored, but the mass was still conserved throughout the full volume of triangles. The density of fluid phases contained in VPs was calculated using state and continuity equations. The fluid phase fractions in VPs were computed using the continuity equation for each phase, with the assumption that all fluid phases had the same pressure. The fluid flow in channels

was calculated by solving continuity and momentum equations for incompressible fluid laminar flow. Initially, the liquid and gas may exist in virtual pores. The key fluid flow mechanisms in capillary-driven water flow calculations were piston displacement, snap-off physics, and viscous flow. The cooperative pore filling effect was indirectly taken into account due to the discretization of a single pore. The liquid phase was thought to be a wetting (invading) fluid, while the gas phase was thought to be non-wetting (defending). There were three flow regimes: (a) single-phase gas flow, (b) single-phase liquid flow, and (c) two-phase (liquid and gas) flow. When VP was totally pre-filled with a liquid (wetting) phase and was close to VP, capillary pressure was only evaluated in the flow regime (b). The Washburn equation [9] was used with the Poiseuille equation to link viscous and capillary forces. As a result, for the flow regime (single-phase flow) through channels (capillaries), the mass flow rate of the capillary-driven flow along channels was calculated.

$$M_x = \rho \frac{h^3}{12\mu} \frac{P_i - P_j - P_c}{L} \quad (1)$$

where M_x —the mass fluid flow rate (per unit length) across the film thickness in the x -direction [kg/(m s)], h —the hydraulic channel aperture (its perpendicular width) [m], ρ —the fluid density [kg/m³], t —the time [s], μ —the dynamic fluid (liquid or gas) viscosity [Pa s] and P —the fluid pressure [Pa], P_i and P_j are the pressure in adjacent VPs [Pa], P_c is the capillary pressure [Pa] and L is the length of the channel connecting VPs [m]. Young-Laplace law gives the capillary pressure P_c due to the interface between the two phases (a meniscus).

$$P_c = \frac{2\sigma \cos \Theta}{r_t} \quad (2)$$

where σ is the interfacial tension [N/m], Θ is the contact angle [deg] and r_t is the throat radius equal to half the channel aperture [m]. The coupled DEM-CFD model was implemented into the open-source code YADE [5]. The model has 6 constants for the liquid, 5 for the gas and 6 for the liquid flow network.

4 Model Calibration

A simple uniaxial compression test was used to calibrate the pure DEM represented by spheres, while permeability and sorptivity tests for an assembly of bonded spheres were used to calibrate the pure CFD. In contrast to our prior thorough 3D simulations [6], a simplistic 2D DEM mesoscopic structure was chosen to replicate the mortar/concrete in the first calculation step. Only spheres were chosen as discrete elements. 400 spheres were integrated in a tiny bonded granular specimen of 10×10 mm². Along with the specimen depth, one layer of spheres was applied. The sphere diameter was in the range of 0.25–0.75 mm (with $d_{50} = 0.5$ mm as the mean value). For the sake of simplicity, the macro-pores were ignored. In all simulations, the same simplified concrete meso-structure was assumed. Three different bonded granular specimens were used in the DEM/CFD calculations (Fig. 1): (1) a pure mortar specimen (also known as one-phase concrete), (2) a mortar specimen with one aggregate (also known as two-phase concrete),

and (3) a mortar specimen with one aggregate with ITZ surrounding it (also known as three-phase concrete). The free region between the spheres was represented by micropores. A rigid non-breakable cluster made up of 12 spheres was used to mimic a non-spherical aggregate. ITZ was considered to have three layers of $d = 0.25$ mm spheres around the aggregate with a porosity of $p = 20\%$ (the mortar had a porosity of $p = 5\%$). Experiments [11] were used to calculate the starting porosities of the cement matrix (5%) and ITZ (20%). The width of ITZ was in simulations around 0.75 mm, which was 10 times higher than in real concrete.

In all DEM specimens, the following material constants were used: $E_c = 16.8$ GPa, $\nu_c = 0.20$, $C_c = 180$ MPa and $T_c = 28$ MPa ($C_c/T_c = 5.5$), $\mu = 18^\circ$ and $\rho = 2600$ kg/m³. Previous computations [6–8] calibrated on uniaxial compression, tension, and bending tests were used to choose those values. The results were unaffected by the estimated damping parameter $\alpha_d = 0.20$. The specimen's bottom and top were both smooth. Based on early calculations, a time step of 5×10^{-8} s was assumed. All numerical curves behaved too linearly in a pre-peak region and were too brittle after the peak stress due to large simplifications considered in 2D calculations. The pure mortar with one aggregate had the highest strength, whereas the mortar with one aggregate concrete including ITZ had the lowest. The computed maximum compressive normal stress varied between 52 MPa and 62 MPa. The failure mode was defined by one nearly vertical macro-crack and a few minor vertical and skew cracks.

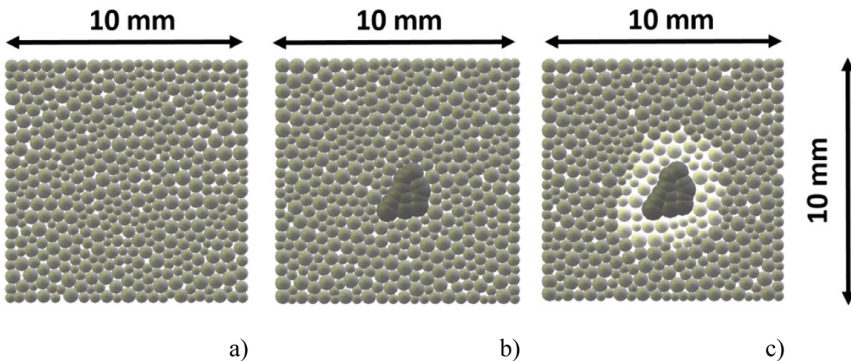


Fig. 1. Numerical specimens in DEM/CFD calculations: (a) pure mortar (grey colour) with initial porosity $p = 5\%$, (b) mortar including aggregate (dark grey colour) with initial porosity $p = 5\%$ and (c) mortar including aggregate with initial porosity $p = 5\%$ and ITZ layer around it (light grey colour) with initial porosity $p = 20\%$

The calibration process of the fluid flow model was split into two parts: (1) permeability tests (Darcy test) and (2) sorptivity tests. A simple permeability Darcy test with two mortar specimens of Fig. 1a was performed for calibration purposes of the CFD model. Single-phase flow was assumed. Two 2D DEM specimens with different initial porosity were prepared. Their size was again 10×10 mm². The first specimen

'1' simulated the mortar and had the initial porosity of $p = 5\%$ and the second specimen '2' simulated ITZ around aggregates and had the initial porosity of $p = 20\%$. The bottom edge was subjected to a constant water pressure of 4.0 MPa, while the top edge was subjected to a constant water pressure of 1.0 MPa. The zero-flux conditions were applied at the left and right edges. For the reference pressure $P_0 = 0.1$ MPa, the dynamic viscosity of water was $\mu = 10.02 \cdot 10^{-4}$ Pa s, its compressibility 10^{-10} Pa⁻¹, and its density $\rho_0 = 998.321 \frac{\text{kg}}{\text{m}^3}$. The virtual channel apertures were $h_{inf} = 4.5 \cdot 10^{-8}$ m and $h_0 = 3.25 \cdot 10^{-6}$ m, respectively. In actual channels, the reduction factor was equal to $\gamma = 0.012$, and the aperture coefficient was equal to $\square\square 1.0$. Both factors γ and \square were multiplied by the same channel aperture factor hc to mimic the differing permeability. The macroscopic permeability coefficient κ was determined using Darcy's law, assuming that the volumetric flow rate at horizontal walls was the same at equilibrium. The findings of the permeability tests differed depending on the channel aperture factor ch ($ch = 1-6$ and 20). The more porous specimen '2' has a higher estimated permeability coefficient of concrete. It ranged from $2e-17$ m² to $3.8e-14$ m² for the specimen '1' ($p = 5\%$) and from $2e-16$ m² to $2e-13$ m² for the specimen '2' ($p = 20\%$). For the subsequent numerical tests, a permeability coefficient of $\kappa = 4e-16$ m² was assumed for the mortar and of $\kappa = 4e-15$ m² for ITZ (10-times lower). Both predicted values were similar to the permeability of cement pastes without and with ITZ (water/cement ratio of 0.5, hydration duration of 28 days, water saturation degree of 0.95), which was determined using a DEM-based technique [2] that was calibrated using experiments (e.g. [12, 13]). In the sorptivity test, the dry porosity 5% specimen was employed. The initial pressure of the fluid (gas phase) was 0.1 MPa. At the bottom specimen edge, constant pressure of 0.14 MPa was used as a boundary condition to fill up the pores in contact with water. The boundary pressure maintains a small pressure gradient on the boundary simulating a slight fluid flow, replenishing the water in the specimen. A constant pressure of 0.10 MPa was defined at the specimen's upper edge. Along the specimen's vertical edges, no mass flow rate was defined. The simulations were run at a temperature of 293.16 K in isothermal circumstances. The calculated sorptivity of the mortar specimen was 0.405 mm/min^{1/2}, being in agreement with laboratory test results [14].

5 Results of Capillary-Driven Fluid Flow in Mortar

Three of the bonded granular specimens from Fig. 1 were chosen for capillary-driven fluid flow testing once more. For all specimens, the initial and boundary conditions were the same. The fluid's initial pressure (gas and liquid phase) was set to 0.1 MPa (close to the atmospheric pressure). The liquid fraction was 97% and the gas fraction 3%. A constant pressure of 0.14 MPa was chosen to replicate the pore filling with water. The boundary pressure maintained a small pressure gradient on the boundary simulating a minor fluid flow, replenishing the water in the specimen (it was defined in pores in contact with the specimen bottom). Before the capillary pressure became effective, this pressure was slightly greater than the initial pressure in the fluid domain (0.1 MPa) to fill in the pores with water. A mass flux rate of zero was defined along the remaining specimen boundaries. As a result, the capillary pressure was the primary driver of fluid flow. The transient process occurred in an isothermal environment. In the solid-fluid realm,

a constant and uniform temperature of 293.16 K was established. The distribution of the capillary pressure, water phase fraction, water saturation state and high hydraulic pressure zone in 3 specimens of Fig. 1 are presented in Figs. 2, 3 and 4.

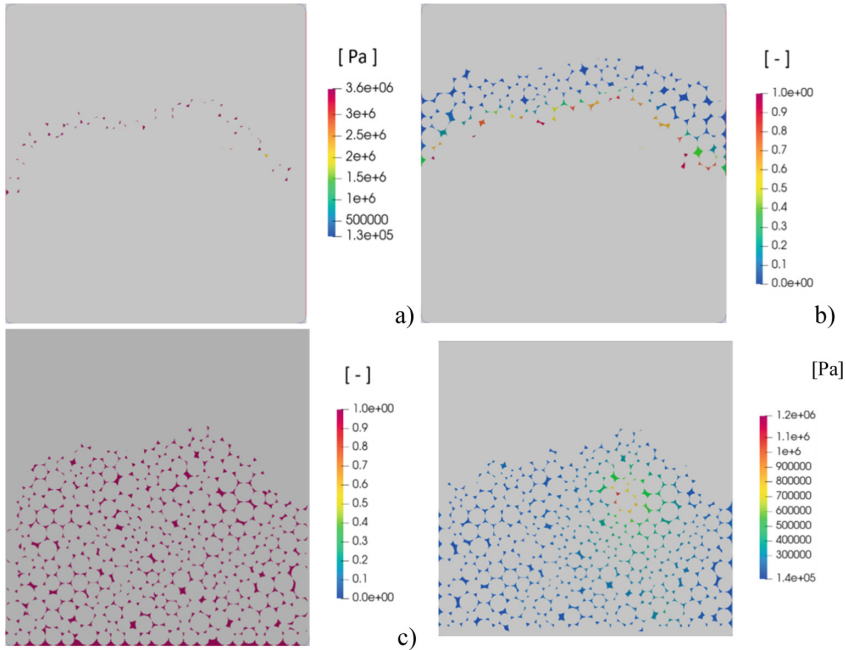


Fig. 2. Computation results of capillary-driven fluid flow in mortar specimen: (a) capillary pressure, (b) water phase fraction, (c) water saturation state and (d) high hydraulic pressure zone

The coupled DEM-CFD calculation results show that the maximum capillary pressure was $P_{cmax} = 3.6$ MPa. The sorptivity by Hall [14] was 0.405 mm/min^{1/2} (mortar), 0.401 mm/min^{1/2} (mortar + aggregate) and 0.276 mm/min^{1/2} (concrete). It was reduced by the presence of both the barrier in the form of the aggregate and porous ITZ. The height of the full saturation area was reduced by ITZ due to its high porosity. The high liquid phase fraction and the high hydraulic pressure dominated in ITZ.

It can be concluded that ITZs in concrete decelerate the capillary fluid flow and consequently reduce sorptivity. In unsaturated concretes, however, the hydraulic pressure, not the capillary pressure, becomes the major component driving fluid flow when the hydrostatic pressure of water on the outer surface of a structural element constructed of concrete is sufficiently high. Because ITZs have a higher permeability than the cement matrix, they speed up the fluid movement and the process of filling the pores with water.

6 Summary and Conclusions

A new hydro-mechanical DEM/CFD model of multi-phase fluid flow in unsaturated concretes under isothermal conditions is proposed in this paper. The model allows for

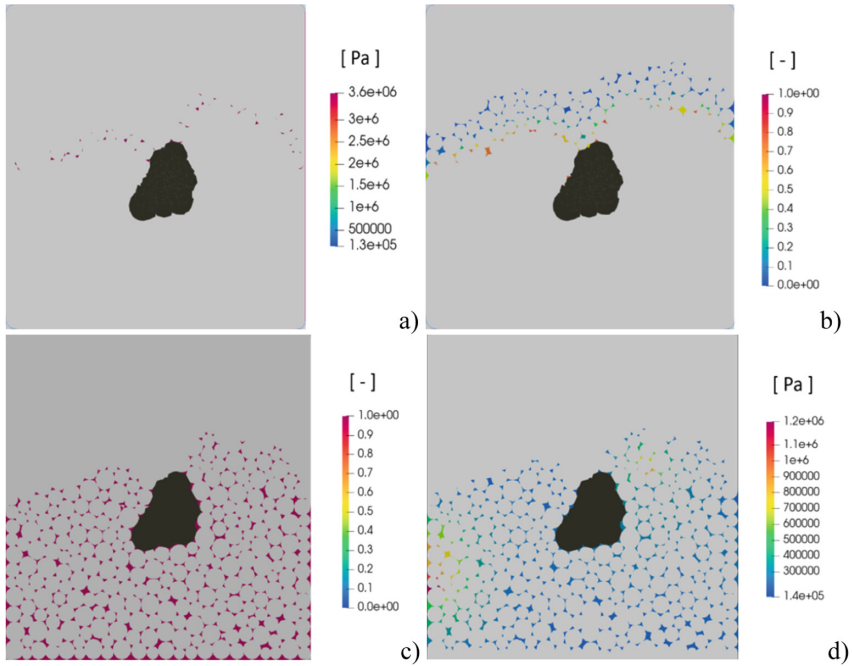


Fig. 3. Computation results of capillary-driven fluid flow in mortar specimen with aggregate: (a) capillary pressure, (b) water phase fraction, (c) water saturation state and (d) high hydraulic pressure zone

the precise tracking of liquid/gas fractions in pores and cracks, including their geometry, topology, size, and location. The results of the model help to clarify the impacts of ITZ on water transport through cementitious materials. Our numerical investigations on permeability and sorptivity of cement matrices and concretes have led us to the following main conclusions:

Porous ITZs in concretes reduce sorptivity by slowing the capillary fluid flow. In unsaturated concretes, sufficiently high hydraulic water pressures become the major factor driving fluid movement. Porous ITZs speed the full saturation of pores in this situation. Capillary pressure becomes the major force driving fluid flow in unsaturated concretes at low hydraulic pressures. Porous ITZs slow the full saturation of pores in this scenario. Under capillary pressure, aggregates without ITZs increase the fluid flow time compared to the pure mortar but have no effect on fluid flow under hydraulic pressure.

The fluid flow is fastest when the external pressure is horizontal, and it is slowest when the external pressure is vertical. As the gas volume content increases, the full saturation process takes longer.

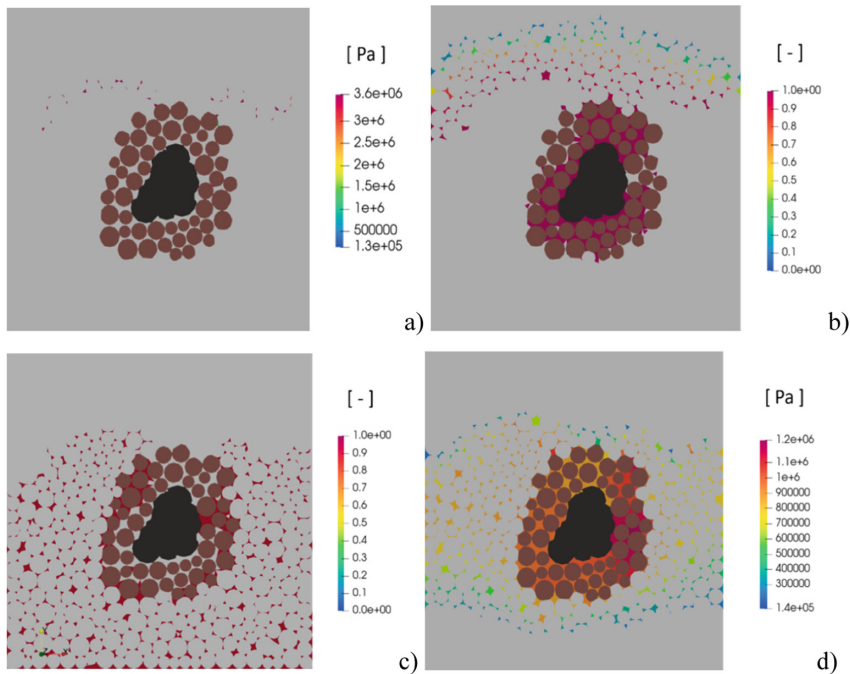


Fig. 4. Computation results of capillary-driven fluid flow in mortar specimen with aggregate and ITZ: (a) capillary pressure, (b) water phase fraction, (c) water saturation state and (d) high hydraulic pressure zone

Acknowledgements. The present study was supported by the research project “Fracture propagation in rocks during hydro-fracking—experiments and discrete element method coupled with fluid flow and heat transport” (years 2019–2022) financed by the National Science Centre (NCN) (UMO-2018/29/B/ST8/00255).

References

1. Bentz, D.P., Stutzman, P.E., Garboczi, E.J.: Experimental and simulation studies of the interfacial zone in concrete. *Cem. Conc. Res.* **22**(5), 891–902 (1992)
2. Li, K., Stroeven, P., Stroeven, M., Sluys, L.J.: A numerical investigation into the influence of the interfacial transition zone on the permeability of partially saturated cement paste between aggregate surfaces. *Cem. Concr. Res.* **102**, 99–108 (2017)
3. Krzaczek, M., Nitka, M., Kozicki, J., Tejchman, J.: Simulations of hydro-fracking in rock mass at meso-scale using fully coupled DEM/CFD approach. *Acta Geotech.* **15**(2), 297–324 (2019). <https://doi.org/10.1007/s11440-019-00799-6>
4. Krzaczek, M., Nitka, M., Tejchman, J.: Effect of gas content in macro-pores on hydraulic fracturing in rocks using a fully coupled DEM/CFD approach. *Int. J. Numer. Anal. Meth. Geomech.* **45**(2), 234–264 (2021)
5. Kozicki, J., Donzé, F.V.: A new open-source software developer for numerical simulations using discrete modeling methods. *Comput. Methods Appl. Mech. Eng.* **197**, 4429–4443 (2008)

6. Nitka, M., Tejchman, J.: A three-dimensional meso scale approach to concrete fracture based on combined DEM with X-ray μ CT images. *Cem. Concr. Res.* **107**, 11–29 (2018)
7. Suchorzewski, J., Tejchman, J., Nitka, M.: Discrete element method simulations of fracture in concrete under uniaxial compression based on its real internal structure. *Int. J. Damage Mech* **27**(4), 578–607 (2018)
8. Suchorzewski, J., Tejchman, J., Nitka, M.: Experimental and numerical investigations of concrete behaviour at meso-level during quasi-static splitting tension. *Theoret. Appl. Fract. Mech.* **96**, 720–739 (2018)
9. Washburn, E.W.: The dynamics of capillary flow. *Phys. Rev.* **17**, 273 (1921)
10. Abdi, R., Krzaczek, M., Tejchman, J.: Comparative study of high-pressure fluid flow in densely packed granules using a 3D CFD model in a continuous medium and a simplified 2D DEM-CFD approach. *Granular Matter* **24**(1), 1–25 (2021). <https://doi.org/10.1007/s10035-021-01179-2>
11. Nitka, M., Tejchman, J.: Meso-mechanical modelling of damage in concrete using discrete element method with porous ITZs of defined width around aggregates. *Eng. Fract. Mech.* **231**, 107029 (2020)
12. Zamani, S., Kowalczyk, R.M., McDonald, P.J.: The relative humidity dependence of the permeability of cement paste measured using GARField NMR profiling. *Cem. Concr. Res.* **57**, 88–94 (2014)
13. Kameche, Z.A., Ghomari, F., Choinska, M., Khelidj, A.: Assessment of liquid water and gas permeabilities of partially saturated ordinary concrete. *Constr. Build. Mater.* **65**, 551–565 (2014)
14. Hall, C.: Water sorptivity of mortars and concretes: a review. *Mag. Concr. Res.* **41**(147), 1–61 (1989)



DEM Analyses of Interface Behaviour Between Cohesionless Sand and Rigid Wall of Different Roughness

Aleksander Grabowski^(✉), Michał Nitka, and Jacek Tejchman

Gdańsk University of Technology, Narutowicza 11/12, Gdańsk, Poland
{aleksander.grabowski, micnitka}@pg.edu.pl

Abstract. The paper deals with three-dimensional numerical simulations of quasi-static shear between cohesionless sand and rigid walls in a direct wall shear apparatus. The roughness of the bottom rigid walls varied from smooth to very rough. The constant normal pressure acted on the top wall. Numerical simulations were carried out with the discrete element method (DEM). Sand grains were described as spheres with contact moments or as non-symmetric irregular clumps. The influence of the surface roughness on the macroscopic force-displacement curves as well as on microscopic results at the grain level was studied. The height of the shear localized zone, grain rotations, and the ratio between grain slips and rotations were calculated for the different wall roughness. Two different boundary conditions along the interface were proposed for micro-polar continua, considering grain rotations and slips, and normalized interface roughness. The DEM results offer a better understanding of the interface behaviour between granular bodies and rigid structures. The results can be used as constitutive law of the slip contact in non-geometry models. In future work, the different roughness of the silo walls will be investigated and its influence on pressures and safety.

Keywords: DEM · Interface · Sand

1 Introduction

The granular material interaction with interfaces is a complex issue in many engineering problems e.g. in silos, foundations, tunnels, and retaining walls. The interface behaviour is characterized by the formation of a shear zone with a certain thickness in the soil adjacent to structures, i.e. thin zones of intense shearing with both pronounced grain rotations and volume changes [1, 2]. In order to describe the interface behaviour, the Coulomb's friction law is usually taken into account with a constant ratio between shear and normal stresses on the wall. However, the wall friction is not a state variable, as it depends on several factors, such as boundary conditions, pressure level, initial stress state, and specimen size [1, 2].

Besides the experimental studies, several numerical DEM and FEM analyses were carried out to investigate the interface behaviour in granular materials. Modelling the interface thickness within continuum mechanics using FEM can be only performed with

constitutive models possessing a characteristic length of microstructure [3–6]. To better understand microscopic phenomena during wall friction, DEM calculations were also carried out. There exist many numerical studies of wall friction using DEM under 2D conditions [7–9] and only a few under 3D conditions [10–13]. However, no effort is known to us that was performed in experiments and numerical DEM simulations on wall friction to determine the ratios between grain rotations and slips, shear stresses and couple stress and forces and moments at the wall of different roughness. These ratios are of importance for defining wall boundary conditions within models of micro-polar continua.

This paper focuses on comprehensive numerical analyses of the quasi-static interface behaviour using the real mean grain diameter of sand by taking into account the effect of different wall roughness (height, distance, and inclination of grooves). The wall was rigid. All calculations were performed in 3D conditions with DEM. Finally, wall boundary conditions were proposed for micro-polar continua.

The findings presented in this paper help to better understand both: (1) the wall friction mechanism when using particles of a different shape in DEM analyses and (2) wall boundary conditions of different roughness for micropolar continua to simulate large soil-structure systems.

2 DEM for Cohesionless Sand

The discrete element method (DEM) was used for the numerical simulations. This method is more and more popular for granular materials calculation, due to the capability of reproducing the discrete nature of sand grains. The results can be studied both at the micro- and macro-level. In this paper, the open-source 3D DEM platform YADE was used [14, 15]. The method uses a description of element interactions in terms of contact forces and moments. First, interaction forces between discrete particles are calculated, based on constitutive laws. Next, Newton's 2nd law is applied to find the resulting acceleration for each particle, which is then time-integrated to find the velocity and finally a new position of particles. This algorithm is repeated every time step. To mimic the real shape of sand particles two methods were used. First, spherical elements with contact moments were assumed in simulations. Second, non-symmetric irregularly-shaped grain clusters composed of 4 spheres of different diameters. The aspect index (the ratio between the maximum and minimum clump diameter) was 1.50, the convexity index '1' (the ratio between the smallest sphere volume encompassing the cluster and the cluster volume) was 2.07 and the convexity index '2' (the ratio between the smallest convex volume encompassing the cluster and the cluster volume) was 1.16. The DEM approach with clumps is more time-consuming but more accurate. In this paper, both grain models were used for comparison purposes.

During a calibration process, 5 main parameters for spheres and 3 for clumps have to be determined: E_c (modulus of elasticity of the grain contact), ν_c (Poisson's ratio of the grain contact), μ (inter-particle friction angle) and β (rolling stiffness coefficient) and η (limit rolling coefficient). In addition, a particle radius R , particle mass density ρ , and numerical damping parameter α_d are required. The numerical calibration of the sand material was based on homogeneous axisymmetric triaxial laboratory test results

on Karlsruhe sand with different initial void ratios and lateral pressures as compared to the experiments [16, 17]. The procedure for determining the material parameters in DEM was described in detail by Kozicki et al. [18, 19]. Note that the representative elastic contact parameters E_c and ν_c differ from the elastic moduli of grains. The full description of the used model can be found in [20]. The grain diameter of sand linearly varied between 0.25 mm and 0.75 mm with the mean grain diameter of $d_{50} = 0.5$ mm (as in the experiment [1, 2]). The used numerical parameters (based on the triaxial calibration tests) are presented in Table 1.

Table 1. Material parameters assumed in DEM simulations

Material parameters	Value Spheres or clusters
Modulus of elasticity of grain contact E_c (MPa)	300
Poisson's ratio of grain contact ν_c [–]	0.3
Inter-particle friction angle μ [°]	18 or 26
Rolling stiffness coefficient β [–]	0.7 or no
Moment limit coefficient η [–]	0.4 or no
Damping coefficient α_d [–]	0.08

3 3D DEM Simulations of Direct Wall Shearing Test

The granular specimens for monotonic wall shearing included 80,000 spheres with contact moments or grain clumps (Fig. 1). The specimen length was equal to 100 mm and its height to 20 mm as in experiments [1, 2]. The width of the specimen was equal to 100 mm (as in the experiment) for spheres and 5 mm ($10 \times d_{50}$) for clusters to reduce the calculation time. The reduction of the specimen width had an insignificant influence on the results [20]. The small gap between the top and bottom part of the box was introduced to prevent grain locking (Fig. 1A). All walls confining the sand specimen were assumed as rigid boundaries. The top and side walls were movable whereas the bottom wall was fixed. To induce wall shearing along the bottom (Fig. 1C), the sand was horizontally sheared under a constant velocity (from the left to the right) until the horizontal displacement reached the limit of 7 mm.

The bottom wall had a variable roughness (Fig. 1C). It had a regular saw-tooth surface with different heights but the same distance, thus different inclinations of groves were obtained. The interface roughness was characterized by the normalized interface roughness parameter $R_n = h_g/d_{50}$, where h_g is the groove height and d_{50} is the mean grain diameter [2, 21–23]. The parameter R_n was chosen as 2.0, 1.0, 0.75, 0.50, 0.25, 0.10 and 0.01 (Fig. 1C). The distance s_g was always the same ($s_g = 2 \times d_{50}$). The groove inclination to the bottom α_g diminished with decreasing R_n (e.g. $\alpha_g = 45^\circ$ for $R_n = 1.0$). The constant pressure equal to 100 kPa was applied to the top wall. The calculations

were limited to initially dense sand with an initial void ratio $e_o = 0.55$. The numerical friction between walls and sand was assumed as $\varphi_w = \mu = 18^\circ$.

Effect of interface roughness on mobilized friction angle

The evolution shape of the curves $\varphi_w = f(u_x)$ and $\varepsilon_v = f(u_x)$ are presented in Fig. 2. The peak $\varphi_{w,max}$ and the residual interface friction angle $\varphi_{w,res}$ continuously grew with increasing roughness parameter. The peak values of $\varphi_{w,max}$ were very similar for both clumps and pure spheres (Fig. 2), however, the residual angles $\varphi_{w,res}$, and residual volumetric strains were slightly lower for clumps with the normalized interface roughness parameter $R_n \geq 0.25$ (e.g. they were lower by 3° for $R_n \geq 0.5$ and by 6° for $R_n = 0.25$).

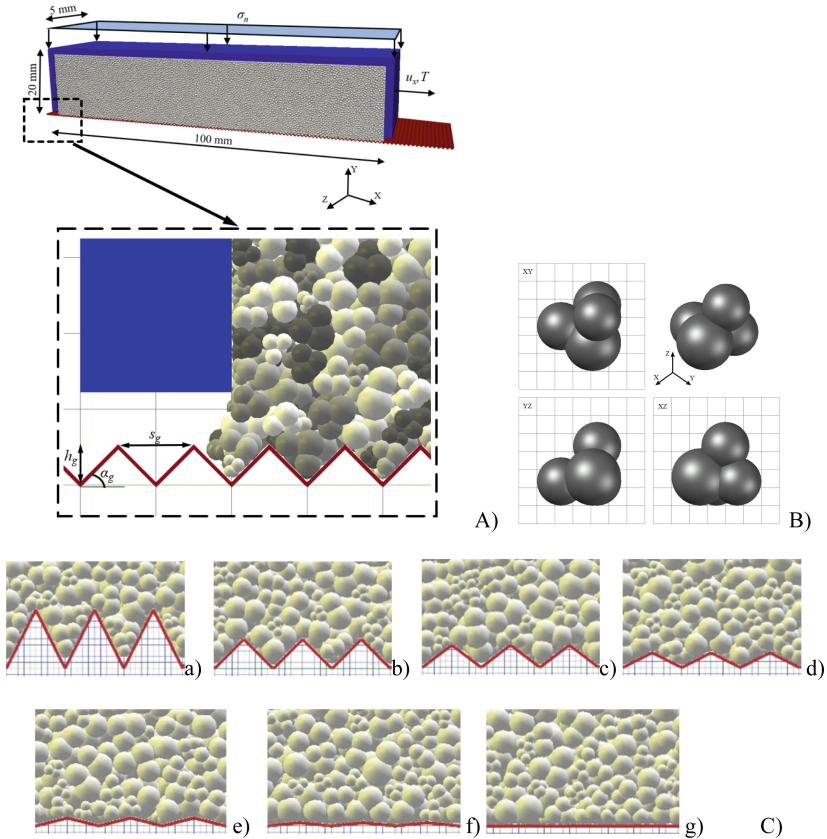


Fig. 1. Direct wall-shear test in DEM: A) geometry of three-dimensional DEM model, and B) non-symmetric irregularly-shaped convex clumps composed of 4 spheres and C) rigid bottom wall sections with different normalized interface roughness parameter $R_n = h_g/d_{50}$: a) $R_n = 2.0$, b) $R_n = 1.0$, c) $R_n = 0.75$, d) $R_n = 0.50$, e) $R_n = 0.25$, f) $R_n = 0.10$ and g) $R_n = 0.01$ (h_g —groove height, s_g —groove distance, α_g —groove inclination and d_{50} —mean grain diameter, u_x —horizontal displacement, T —horizontal force)

The relationship between the values of $\varphi_{w,max}$ and R_n was more parabolic for clumps in opposite to a bi-linear one for pure spheres although the changes of the peak interface friction angle were small for clumps above the value of $R_n \geq 0.75$. The relationship between the values of $\varphi_{w,res}$ and R_n was, however, bilinear for both clumps and pure spheres.

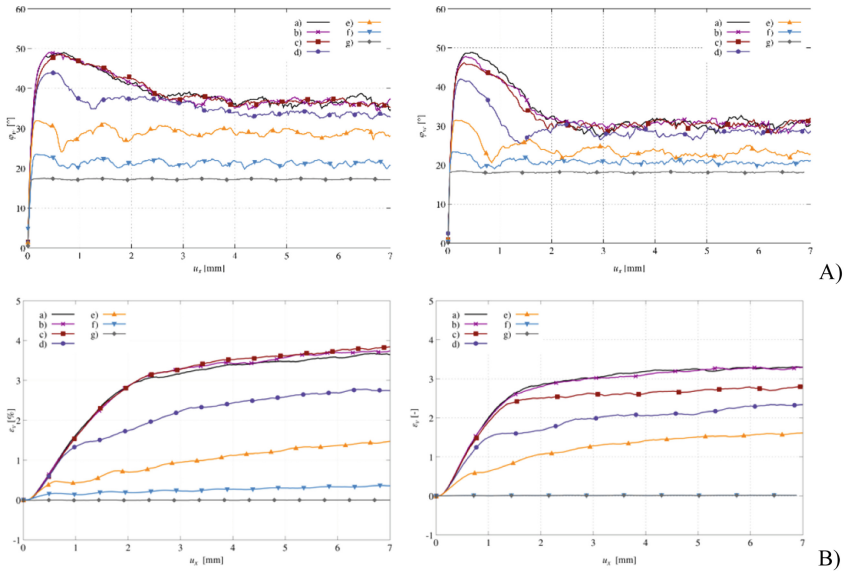


Fig. 2. Mobilized wall friction angle φ_w along interface (A) and volumetric strain ε_v versus horizontal displacement u_x (B) for spheres with contact moments (left) and clumps (right) for different normalized interface roughness parameter R_n : a) $R_n = 2.0$, b) $R_n = 1.0$, c) $R_n = 0.75$, d) $R_n = 0.50$, e) $R_n = 0.25$, f) $R_n = 0.10$ and g) $R_n = 0.01$

Distribution of particle rotation, particle displacements and void ratio

The distribution of spheres rotation in the residual state is shown in Fig. 3. The values of rotations were calculated from the cubic REV with a side length equal to $5d_{50}$. In this paper, the effect of 3 different wall roughnesses was presented for spheres with contact moments and clusters.

Figure 4 presents the zoom on single sphere rotations in the residual state for three different wall roughnesses. The particle rotations are the best indicators of shear localization [1, 2, 20, 24–26]. Based on particle rotations (Figs. 3 and 4), it can be seen that during interface shearing with the different normalized interface roughness parameter R_n , an almost horizontal dilatant shear zone was created at the interface ($R_n \geq 0.01$). The grain rotations had nearly always the same positive sign (clock-wise rotation) (Fig. 4). More grains rotated in the opposite direction for clusters as compared to pure spheres with contact moments.

The thickness of the wall shear zone was estimated, based on an inflection point in the distribution of sphere rotations ω . The thickness was lower than for spheres by

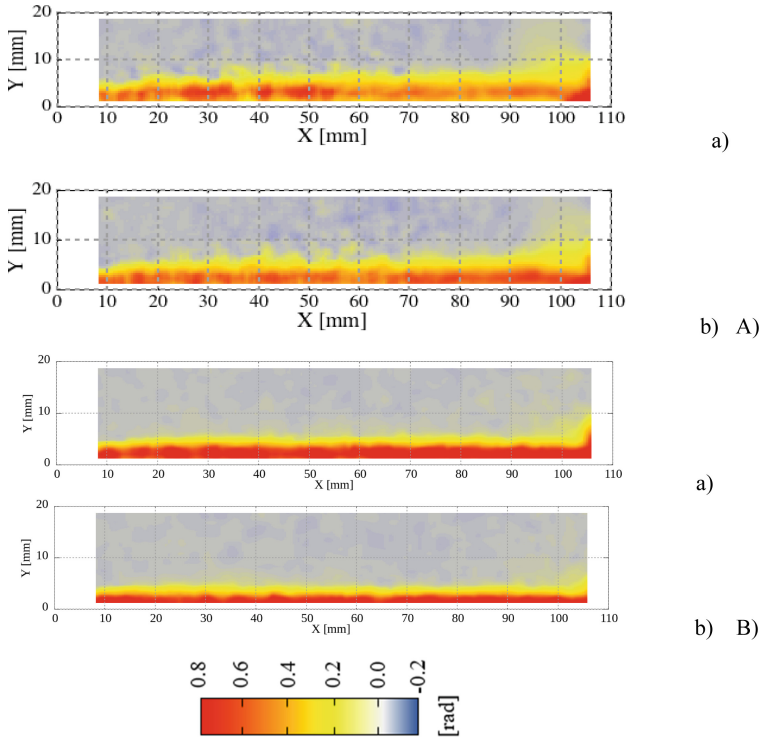


Fig. 3. Distribution of sphere rotations ω with attached scale in [rad] at residual state for $u_x = 7$ mm with: A) spheres with moments and B) clusters for different normalized wall roughness parameter R_n : a) $R_n = 2.0$, b) $R_n = 0.75$ (positive sign—clockwise rotation, negative sign—anti-clockwise rotation)

15–40% for $R_n \geq 0.50$ due to higher grain rotations at the wall. The largest grain rotation was located slightly above the interface ($h/d_{50} = 3-5$) for $R_n > 0.5$, and for $R_n \leq 0.5$ it was directly located at the interface, where it diminished with the reduction of R_n . For $R_n > 0.5$, the sphere rotations approached zero at the bottom wall (equal to the situation with particles trapped in asperities). Above the shear zone, all spheres were almost motionless. The maximum residual grain rotation for $R_n \geq 0.75$ was equal to about 60° for clusters and 45° for pure spheres with contact moments.

Micropolar boundary conditions

The horizontal grain displacement u and the ratio $A = \omega d_{50}/u$ (ratio between the interface grain rotation multiplied by the mean grain particle and interface grain slip) along the wall obviously decreased with increasing R_n (Figs. 5 and 6). This ratio $\omega d_{50}/u$ was approximately equal to $0.5R_n$ [$A = (\omega d_{50})/u \cong 0.5R_n$] for clusters in contrast to pure spheres with contact moments, where [$A = (\omega d_{50})/u \cong R_n$] for $R_n \leq 0.75$. It was caused by greater grain rotations of clumps than of pure spheres with contact moments. Thus, the ratio A also depends on the grain shape.

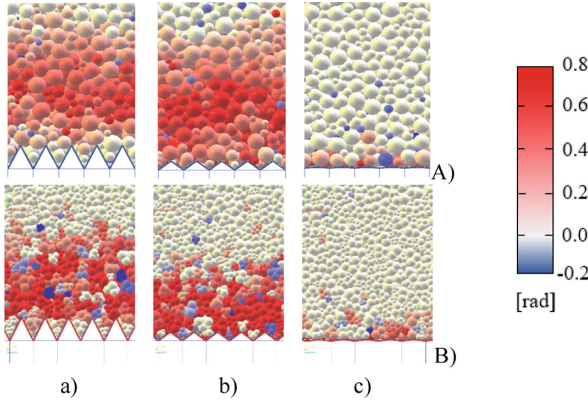


Fig. 4. Zoom on distribution of single grain rotations with attached scale in [rad] at residual state for $u_x = 7$ mm with: A) spheres with moments and B) clusters for different normalized wall roughness parameter R_n : a) $R_n = 2.0$, b) $R_n = 0.75$ and c) $R_n = 0.10$ (positive sign—clockwise rotation, negative sign—anti-clockwise rotation)

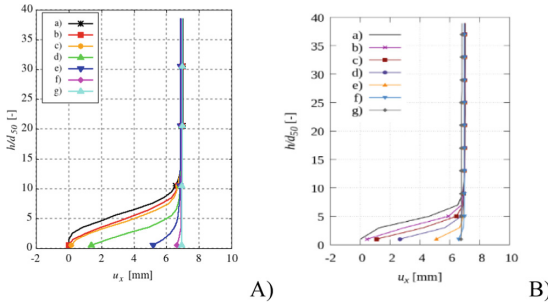


Fig. 5. Distribution of horizontal sphere displacement u at wall across normalized specimen height h/d_{50} at specimen mid-point in residual state for $u_x = 7.0$ mm from DEM with different normalized wall roughness parameter R_n : a) $R_n = 2.0$, b) $R_n = 1.0$, c) $R_n = 0.75$, d) $R_n = 0.50$, e) $R_n = 0.25$, f) $R_n = 0.10$ and g) $R_n = 0.01$ for A) spheres with moments and B) clumps

Based on DEM results, the following three boundary conditions at the interface, based on the ratios $A = (\omega d_{50})/u$, $B = u/u_x$ and $C = (t \times d_{50})/m$ and may be used [20] (t - tangential wall force, and m —tangential moment along the wall). Those ratios slightly depend on the particle shape. For the case of $R_n \geq 0.75$, where all grain rotations ω tend to zero at the interface, the boundary condition can be simplified as $\omega = 0$, $u = 0$, and $v = 0$ (no rotations and displacements) as in the experiment [1, 2].

The calculated ratios A , B and C may be approximated in the range $0 \leq R_n < 0.75$ [9] as: $A = (\omega d_{50})/u \cong 0.5R_n$, $B = u/u_x = 1 - R_n$, $C = (t' \times d_{50})/m' = 1/R_n$.

All ratios depend in a simple way on R_n only. The proposed boundary conditions may be prescribed in nodes of FE meshes along the interface in micropolar simulations (the particle rotation ω may be replaced by the micropolar (Cosserat) rotation ω^c) [2, 27]. To fully validate the suggested boundary conditions, the DEM interface simulation

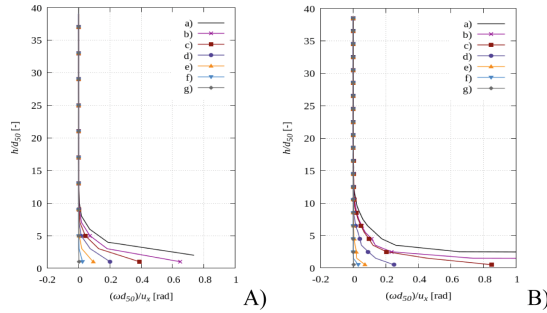


Fig. 6. Distribution of ratio $A = \omega d_{50}/u$ across normalized specimen height h/d_{50} at specimen mid-point in residual state for $u_x = 7.0$ mm from DEM with different normalized wall roughness parameter R_n : a) $R_n = 2.0$, b) $R_n = 1.0$, c) $R_n = 0.75$, d) $R_n = 0.50$, e) $R_n = 0.25$, f) $R_n = 0.10$ and g) $R_n = 0.01$ for A) spheres with moments and B) clumps

results should be extended by the effect of different grain shapes, grain size distributions, and mean grain sizes.

4 Conclusion

The normalized interface roughness had a huge influence on the mobilized wall friction angle and thickness of the wall shear zone. The wall friction resistance increased with increasing wall roughness. The peak and the residual wall friction angle grew with the raising roughness parameter. The relationship between the peak/residual wall friction angle and normalized wall roughness was parabolic/bilinear. The residual wall friction angle was by 3° – 7° lower than for pure spheres with contact moments ($R_n \geq 0.25$).

The wall friction resistance was strictly combined with the thickness of the wall shear zone wherein pronounced grain rotations occurred. The thickness of the wall shear zone increased with the growing normalized wall roughness parameter in a bilinear way as the residual wall friction angle. The thickness of the wall shear zone expanded in a parabolic way from $1 \times d_{50}$ up to $12 \times d_{50}$ for $R_n = 0.01$ – 2.0 . It was smaller by 15–40% than for pure spheres with contact moments ($R_n \geq 0.25$).

For very rough walls ($R_n \geq 0.75$), the largest sphere rotation was located slightly above the bottom wall ($h/d_{50} = 3$ – 5) and for $R_n \leq 0.5$ it was directly located at the bottom wall where it diminished with the reduction of R_n . For $R_n \geq 0.75$, the sphere rotations were approaching zero at the wall (the spheres were trapped in asperities). The largest wall rotation was higher by 30% than for pure spheres with contact moments ($R_n \geq 0.25$).

The ratio between the wall grain rotation multiplied by the mean grain diameter and wall grain slip was almost the same during shearing along the wall. It systematically reduced with decreasing normalized wall roughness parameter. It was twice smaller as for pure spheres with contact moments.

Three different relationships were proposed to describe the wall boundary conditions in micropolar continua. They included the ratio between the micro-polar rotation multiplied by the mean grain diameter and slip along the wall, the ratio of the slip at

the wall and total imposed horizontal displacement and the ratio between the horizontal tangential force multiplied by the mean grain diameter and horizontal tangential moment along the wall. All ratios were related to the normalized wall roughness only.

Acknowledgements. The research work has been carried out within the project “*Autogenous coupled dynamic-acoustic effects in granular materials—experiments and combined DEM/CFD approach*” financed by the National Science Centre, Poland (NCN) (UMO-2017/27/B/ST8/02306).

References

1. Tejchman, J.: Scherzonenbildung und Spannungseffekte in Granulaten unter Berücksichtigung von Korndrehungen. Publ. Ser. Inst. Soil and Rock Mech., University Karlsruhe 117, 1–236 (1989)
2. Tejchman, J., Wu, W.: Experimental and numerical study of sand-steel interfaces. Int. J. Numer. Anal. Methods Geomech. **19**(8), 513–537 (1995)
3. Ebrahimiyan, B., Bauer, E.: Numerical simulation of the effect of interface friction of a bounding structure on shear deformation in a granular soil. Int. J. Numer. Anal. Meth. Geomech. **36**(12), 1486–1506 (2012)
4. Huang, W., Bauer, E., Sloan, S.W.: Behaviour of interfacial layer along granular soil-structure interfaces. Struct. Eng. Mech. **15**(3), 315–329 (2003)
5. Unterreiner, P., Vardoulakis, I., Boulon, M., Sulem, J.: Essential features of a Cosserat continuum in interfacial localisation. In: Chambon, R., Desrues, J., Vardoulakis, I. (eds.) Localisation and Bifurcation Theory for Soils and Rocks, pp. 141–155. Balkema, Amsterdam (1994)
6. Vardoulakis, I., Shah, K.R., Papanastasiou, P.: Modelling of tool-rock shear interfaces using gradient-dependent flow theory of plasticity. Int. J. Rock Mech. Min Sci. Geomech. **29**(6), 573–582 (1992)
7. Frost, J.D., Dejong, J.T., Recalde, M.: Shear failure behavior of granular-continuum interfaces. Eng. Fract. Mech. **69**(17), 2029–2048 (2002)
8. Gu, X., Chen, Y., Huang, M.: Critical state shear behavior of the soil-structure interface determined by discrete element modeling. Particuology **35**, 68–77 (2017)
9. Jensen, R.P., Bosscher, P.J., Plesha, M.E., Edil, T.B.: DEM simulation of granular media-structure interface: effects of surface roughness and particle shape. Int. J. Numer. Anal. Meth. Geomech. (1999)
10. Chen, W.-B., Zhou, W.-H., Jing, X.-Y.: Modeling geogrid pullout behavior in sand using discrete element method and effect of tensile stiffness. Int. J. Geomech. **19**(5), 04019039 (2019)
11. Feng, S.J., Liu, X., Chen, H.X., Zhao, T.: Micro-mechanical analysis of geomembrane-sand interactions using DEM. Comput. Geotech. **94**, 58–71 (2018)
12. Jing, X.Y., Zhou, W.H., Zhu, H.X., Yin, Z.Y., Li, Y.: Analysis of soil-structural interface behavior using three-dimensional DEM simulations. Int. J. Numer. Anal. Meth. Geomech. **42**(2), 339–357 (2018)
13. Zhang, N., Evans, T.M.: Three dimensional discrete element method simulations of interface shear. Soils Found **58**(4), 941–956 (2018)
14. Kozicki, J., Donze, F.V.: Yade-open dem: an open-source software using a discrete element method to simulate granular material. Eng. Comput. **26**, 786–805 (2009)
15. Šmilauer, V., Chareyre, B.: Yade DEM Formulation. Manual (2011)
16. Kolymbas, D., Wu, W.: Recent results of triaxial tests with granular materials. Powder Technol. **60**(2), 99–119 (1990)

17. Wu, W.: Hypoplastizität als mathematisches Modell zum mechanischen Verhalten granularer Stoffe. Heft 129, Institute for Soil- and Rock-Mechanics, University of Karlsruhe (1992)
18. Kozicki, J., Tejchman, J., Mühlhaus, H.-B.: Discrete simulations of a triaxial compression test for sand by DEM. *Int. J. Num. Anal. Methods Geom.* **38**, 1923–1952 (2014)
19. Kozicki, J., Tejchman, J., Mróz, Z.: Effect of grain roughness on strength, volume changes, elastic and dissipated energies during quasi-static homogeneous triaxial compression using DEM. *Granular Matter* **14**(4), 457–468 (2012)
20. Grabowski, A., Nitka, M., Tejchman, J.: 3D DEM simulations of monotonic interface behaviour between cohesionless sand and rigid wall of different roughness. *Acta Geotech.* **16**(4), 1001–1026 (2020). <https://doi.org/10.1007/s11440-020-01085-6>
21. Zhang, N., Evans, T.M.: Three dimensional discrete element method simulations of interface shear. *Soils Found.* **58**(4), 941–956 (2018)
22. Uesugi, M., Kishida, H.: Frictional resistance at yield between dry sand and mild steel. *Soils Found.* **26**(4), 139–149 (1986)
23. Uesugi, M., Kishida, H.: Influential factors of friction between steel and dry sands. *Soils Found.* **26**(2), 33–46 (1986)
24. Tejchman, J., Herle, I.: A “class A” prediction of the bearing capacity of plane strain footings on granular material. *Soils Found.* **39**(5), 47–60 (1999)
25. Tejchman, J., Górski, J.: FE study of patterns of shear zones in granular bodies during plane strain compression. *Acta Geotech.* **5**(2), 95–112 (2010)
26. Tejchman, J., Wu, W.: FE-investigations of non-coaxiality and stress-dilatancy rule in dilatant granular bodies within micro-polar hypoplasticity. *Int. J. Numer. Anal. Methods Geomech.* **33**(1), 117–142 (2009)
27. Tejchman, J., Wu, W.: FE-investigations of micro-polar boundary conditions along interface between soil and structure. *Granular Matter* **12**, 399–410 (2010)



Modelling Recurrent Stress Drops in Porous Media

David Riley, Itai Einav, and François Guillard^(✉)

The University of Sydney, Sydney, NSW 2006, Australia
francois.guillard@sydney.edu.au

Abstract. Riley, David; Einav, Itai; Guillard, François. Brittle porous media subjected to confined compression experience rate-dependent compaction behaviour ranging from smooth stress-strain to one with recurrent abrupt drops in stress. Micromechanical investigations suggest that stress drops correlate with the collapse of the meso-scale structure. As such, we develop a novel model that qualitatively generates such behaviour. A vital feature of the model is the meso-related temperature, which characterises the fluctuating velocities at the meso-scale and, importantly, in general to all heterogeneous porous media. We assume that such temperature induces a loss of strength at the macro-scale and leads to a stress drop. Additionally, the meso-related temperature decays into micro-related (thermal) temperature, thus allowing stress to recover following a stress drop. Our model exhibits the different stress drop regimes and provides insight into the physical mechanisms required to generate these compaction patterns in brittle porous media.

Keywords: Porous media · Stress drops · Rate-dependent · Meso-scale

1 Introduction

Understanding compaction phenomena in brittle porous media are of significance for petroleum engineering, geotechnical engineering, and material science. These materials can exhibit intriguing behaviours such as rate dependence and the occurrence of recurrent stress drops. These stress drops have been observed in a variety of porous materials (e.g., sand [1], snow [2,3], cereals [4,5], and foam [6]) and typically correspond to localised compaction. However, little research has been performed to model stress drops directly, despite using continuum models to study localisation phenomena [7].

We present a continuum model that generates these recurrent stress drops while only using state variables relevant to general porous media. The key to the model's success is the meso-related temperature, which is related to the velocity fluctuations at the meso-scale and is used as a softening mechanism for the material. The meso-related temperature is first generated by macroscale dissipative processes and then feeds into thermal energy through a two-stage irreversible

process [8]. This temperature is assumed to be the physical mechanism responsible that could potentially lead to a drop in stress. The stress can recover after the softening since the meso-related temperature is dissipated into thermal temperature. Furthermore, we show that this model generates rate-dependent behaviour similar to that observed in puffed rice cereal [5] and dust [9], where increasing strain rates result in the evolution from stress drops to stress undulation with no sharp event of stress instability.

2 Model

The model developed herein depends on state variables general to all porous media. Since porous media are composed of a solid matrix, the elastic strain tensor ε_{ij}^e is a necessary state variable. We can define a bulk density ρ and solid density ρ_s since the solid material is interspersed with pores. The evolution of the bulk density ρ is determined by the mass balance equation, while a constitutive assumption gives the evolution of the solid density ρ_s . In our model, we assume that ρ_s does not change and therefore use the unstressed solid density ρ_s^* , which is constant for a given material. The introduction of these two densities naturally allows us to define a third state variable, the solid fraction $\phi = \frac{\rho}{\rho_s} \approx \frac{\rho}{\rho_s^*}$, which is critical for capturing plastic pore collapse.

The above state variables are typically applied for modelling porous media. In addition, we also include the meso-related entropy s_m to represent the mesoscopic degrees of freedom of the meso-structure [8]. The conjugate of the meso-related entropy is the meso-related temperature, which characterises the velocity fluctuations of the material at the meso-scale and is related to the thermodynamic pressure p^T in a manner that will be shown in Sect. 2.2. Our model assumes that the meso-related temperature is the phenomenological cause of macroscale softening. For example, in sand, the meso-related temperature could be generated from mechanical dissipation such as plastic pore collapse or grain breakage; alternatively, in a cellular solid, the meso-related temperature is generated from the local collapse of the solid skeleton structure. These dissipative events create new degrees of freedom that allow the local material to develop fluctuating velocities. The fluctuating velocities then decay into thermal temperature. We assume that the culmination of a potentially large number of these meso-scale regions with fluctuating velocities could induce meso-scale weakening and collapse, thus leading to macroscale softening.

Consequently, we consider the internal energy density u to be given by

$$u(\rho, \varepsilon_{ij}^e, s_m) = u^e(\rho, \varepsilon_{ij}^e) + u^m(s_m), \quad (1)$$

where u^e and u^m are the elastic energy and meso-related energy densities, respectively.

2.1 Elastic Internal Energy

We assume that the porous media can be modelled as a linear elastic material, but also include a linear dependence on density ρ . Thus, we consider the following

form for the elastic internal energy density:

$$u^e(\rho, \varepsilon_{ij}^e) = \left(\frac{\rho}{\rho_s^*} \right) \left(\frac{K}{2} \varepsilon_v^e + \frac{3}{2} G \varepsilon_s^e \right). \tag{2}$$

Here $\varepsilon_v^e = \varepsilon_{ii}^e$ is the volumetric elastic strain and $\varepsilon_s^e = \sqrt{\frac{2}{3} \varepsilon_{ij}^e \varepsilon_{ij}^e}$ is the triaxial elastic strain, where ε_{ij}^e is the deviatoric component of the elastic stress tensor. Finally, K and G are the bulk stiffness and the shear stiffness, respectively.

The elastic pressure and triaxial shear stress can then be given by

$$p^e = \frac{\partial u^e}{\partial \varepsilon_v^e} = \frac{\rho}{\rho_s^*} K \varepsilon_v^e, \tag{3}$$

$$q^e = \frac{\partial u^e}{\partial \varepsilon_s^e} = 3 \frac{\rho}{\rho_s^*} G \varepsilon_s^e. \tag{4}$$

where the triaxial stress invariants can also be determined from the elastic stress tensor σ_{ij}^e by $p^e = \frac{1}{3} \sigma_{ii}^e$ and $q^e = \sqrt{\frac{3}{2} \sigma_{ij}^e \sigma_{ij}^e}$.

2.2 Meso-related Internal Energy, Temperature, and Thermodynamic Pressure

The meso-related internal energy was first introduced to capture the meso-related degrees of freedom for a porous media [8] and later modified [10] to the present form:

$$u^m(s_m) = \frac{s_m^2}{4}. \tag{5}$$

Through differentiation of the meso-related temperature is found to be

$$T_m = \frac{\partial u^m}{\partial s_m} = \frac{s_m}{2}. \tag{6}$$

The evolution of the meso-related temperature was derived from the corresponding entropy balance [10]. Meso-related temperature is first generated by macroscale dissipative processes and then feeds into thermal energy through a two-stage irreversible process [8], which is captured through a source term from macro-scale dissipation and sink term that depends on the current state of meso-related temperature. Furthermore, the entropy balance accounts for the advection of the meso-related temperature, which results in a Laplacian term in the evolution equation. The concepts of two-stage irreversibility and non-local interactions guide us to the form of the evolution law of the meso-related temperature, given by:

$$\partial_t T_m^2 = k_m \nabla^2 T_m + \mathcal{D} - \eta T_m^2. \tag{7}$$

Here k_m is a meso-related diffusivity constant, η is a coefficient controlling the rate of energy sink from the meso-scale to the micro-scale, and

$$\mathcal{D} = p^e \varepsilon_v^p + q^e \varepsilon_s^p, \tag{8}$$

is the mechanical dissipation, where $\dot{\varepsilon}_v^p$ and $\dot{\varepsilon}_s^p$ are the plastic volumetric and triaxial shear strain rate invariants, respectively. For simplicity, we assume η is a constant. Note that the current paper seeks to explore only local phenomena, and thus the second gradient term in Eq. (7) will be neglected from here on.

The two-stage irreversibility concept results in a cascading of energy from meso-related temperature to the micro-related (thermal) temperature T , which results in the following form of the micro-related temperature evolution:

$$\partial_t T = k_T \nabla^2 T + \frac{\eta}{c_T \rho} T_m^2, \quad (9)$$

where k_T is the micro-related diffusivity coefficient and c_T is the specific thermal heat capacity of the porous media.

The thermodynamic pressure can be given through the following expression

$$p^T = - \left. \frac{\partial(u/\rho)}{\partial(1/\rho)} \right|_{\frac{z_m}{\rho}, \varepsilon_{ij}^e} = T_m^2. \quad (10)$$

We then recognise that the total pressure p consists of two terms in this model, $p = p^e + p^T$.

2.3 Plastic Strain Rates and Solid Fraction Evolution

Generally, many porous materials exhibit irreversible deformations with no apparent purely elastic regime, e.g., puffed rice cereals and sand. As such, we use a combination of bounding surface plasticity [11] and h^2 plasticity [12] in a similar manner to [10], such that the material undergoes plastic deformations at any load. Moreover, mechanical dissipation grows instantaneously upon loading, which results in a continuous rise in the thermodynamic pressure.

From hydrodynamic derivations, it was determined that the elastic stresses are equivalent to the effective stresses [13]. Thus, we apply similar assumptions of effective stress theory that the bounding surface y and loading surface y_a depend on the elastic (effective) stresses. The bounding surface in this model is

$$y = \left(\frac{2p^e}{p_y} - 1 \right)^2 + \left(\frac{2q^e}{Mp_y} \right)^2 - 1 = 0, \quad (11)$$

where M is the slope of the critical state line (CSL) and p_y is the isotropic yield pressure, which depends on the solid fraction and thermodynamic pressure, as will be discussed later.

Importantly, an elliptical surface bounds both p^e and q^e , and as such it guides the plastic strains under both shear and pressure loading conditions. Furthermore, elliptical surfaces such as the one chosen for y have been used in modelling of sands [14], snow [15, 16], and carbonate rock [17]. While specific shapes of a yield surface may better capture the phenomenology of particular materials, changing the shape will not negate the generation of a stress drop as long as the stress is capped in both p^e and q^e .

Now a loading surface that passes through the current stress state can be determined. We choose the loading surface to take the following form

$$y_a = \left(\frac{2p^e}{\xi p_y} - 1 \right)^2 + \left(\frac{2q^e}{\xi M p_y} \right)^2 - 1 = 0, \quad (12)$$

where ξ is determined from the above equation using the current state variables. The mapping variable ξ is bounded between 0 and 1, and when $\xi = 1$ the loading surface coincides with the bounding surface. This ensures that at any non-zero stress state that $y_a = 0$ and guarantees the generation of plastic processes.

The rates of the plastic strain invariant are

$$\dot{\varepsilon}_v^p = \xi |\lambda_a| \frac{\partial y_a}{\partial p^e}, \quad (13)$$

$$\dot{\varepsilon}_s^p = \xi |\lambda_a| \frac{\partial y_a}{\partial q^e}, \quad (14)$$

where λ_a is the auxiliary non-negative plasticity multiplier. The auxiliary non-negative plasticity multiplier is solved for by the consistency condition and temporarily assuming $\xi = 1$. However, the rates of plastic strains are reduced by taking the actual value of ξ from Eq. (12). Thus, the stress state progresses away from the current loading surface for $\xi < 1$. However, if $\xi = 1$, then λ_a would keep the stress state on the loading surface which coincides with the bounding surface in this instance. Additionally, the mechanical dissipation is always non-negative since an associative flow rule was chosen and the loading surface is elliptical.

By using the conservation of mass, the evolution of solid fraction can be expressed as

$$\partial_t \phi = \phi (\dot{\varepsilon}_v^p + (1 - \tau) \dot{\varepsilon}_v^e), \quad (15)$$

where τ can either be related to the solid material's Poisson ratio [18] or equivalently a relative solid fraction [10]. In this paper, we assume that only plastic volumetric processes produce changes in the solid fraction ($\tau = 1$). Thus, Eq. 15 reduces to $\dot{\phi} = \phi \dot{\varepsilon}_v^p$.

Following typical conventions of modelling porous media, we take the size of the bounding surface to enlarge with increasing density but also assume that it contracts with a rise in thermodynamic pressure (kinetic softening). To account for density hardening, p_y is taken to depend nonlinearly on ϕ like that used for snow [19]. The introduction of kinetic softening is motivated by the concepts introduced in Sect. 2.2 and experimental findings in aqueous foams [20] and granular solids [21], where it was observed that stress fluctuations could induce yielding. To this end, we assume p_y declines as a function of the kinetic number $I_k = \frac{p^T}{p^e + p^T}$, which is bounded between 0 and 1 [10]. The specific form of the isotropic yield pressure is

$$p_y = \beta^* K \left((1 - \phi)^{-3} - 1 \right) e^{-c I_k}, \quad (16)$$

where β^* is a dimensionless positive constant, and c is a positive constant, which characterises the material sensitivity to kinetic softening. The choice of an exponential function ensures that when $p^T = 0$, the material undergoes no softening. Moreover, as $\phi \rightarrow 0$, the yield stress approaches zero, which could be further accentuated if $p^T \gg p^e$ ($I_k \rightarrow 1$). Notably, the dependence of the isotropic yield pressure on the thermodynamic pressure results in a rate-dependent plasticity model, which will be shown in Sect. 3.1.

3 Results

All simulations are oedometric tests with a constant boundary velocity V , similar to typical experimental conditions. The material parameters were assumed and chosen to be reasonable for brittle highly porous media and are used unless otherwise specified. As such, we assume that the initial solid fraction $\phi_0 = 0.25$ to represent materials such as puffed rice cereal [22], dust particles [9], and calcareous sand [23]. The shear stiffness is determined based on a chosen bulk stiffness K and Poisson's ratio ν by $G = \frac{3K(1-2\nu)}{2(1+\nu)}$. For Poisson's ratio, we assume $\nu = 0.25$, which is within the range of typical values for sand [24] and rock [25]. We assume that $M = 1.5$ is relevant for puffed rice cereals as the grains are angular and internally porous, similar to calcareous sand [26]. However, we explore the effect of different values in Sect. 3.2. Finally, we choose $c = 10$ as the value was found to generate repetitive stress drops. Table 1 summarises the chosen constants for the simulations.

Table 1. Model constants used for the simulations, unless otherwise indicated in the text.

K (kPa)	ν	β^*	M	ρ_s^* ($\frac{kg}{m^3}$)	ϕ_0	c	$\dot{\epsilon}_v$ (s^{-1})	η (s^{-1})
10^3	0.25	$\frac{1}{10}$	1.5	600	0.25	10	0.01	10^3

3.1 Rate Dependence and Density Dependence

To relate to the dependencies observed in experiments, we explore the rate sensitivity of the model, showing that it can conceptually capture diverse rate-dependent phenomena. The simulations use a constant boundary velocity V , which is varied by several orders of magnitudes in the same manner that was done experimentally for puffed rice cereals [27]. Note that this results in an increasing instantaneous volumetric strain rate $\dot{\epsilon}_v$ throughout the simulation.

For all scenarios in Fig. 1, the normalised axial stress initially increases with a simultaneous rise in p^T and ϕ . This steady rise continues until there is a sharp runaway of p^T (or meso-related temperature), which can be interpreted as the destruction of the meso-structure (kinetic softening). Simultaneously, there is a

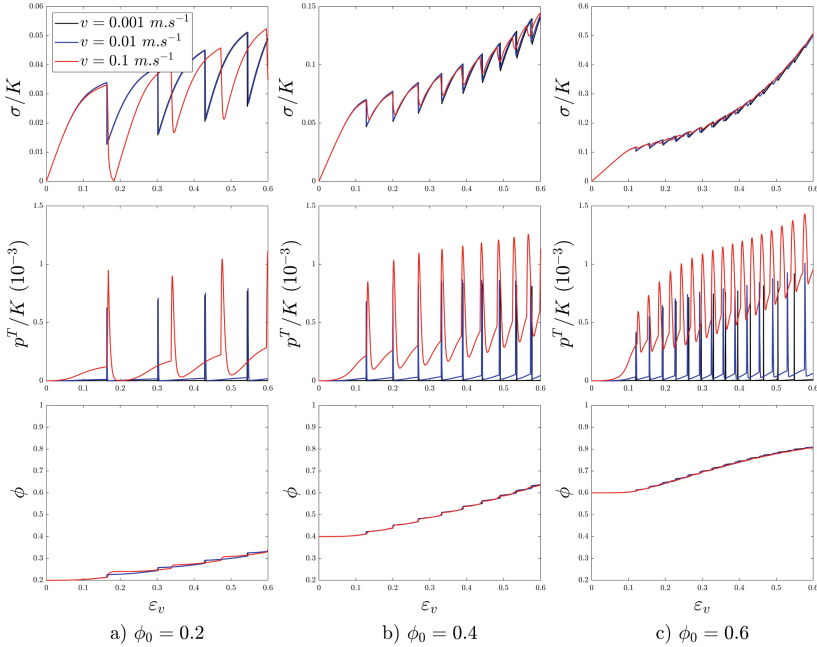


Fig. 1. The effect of strain rate and initial density on the constitutive behaviour. Panels (a–c) shows the response for three different velocities V . Here, the effects are shown for the evolution of normalised axial stress σ/K (top), normalised thermodynamic pressure p^T/K (middle), and solid fraction ϕ (bottom), for three different values of initial solid fractions, ϕ_0 , all against ε_v .

sharp increase in ϕ and a rapid decline in the normalised axial stress. However, for the chosen constants, the sink term in Eq. (7) mitigates the runaway events when it becomes larger than the mechanical dissipation, which causes a decline in p^T (middle row). The decline in p^T allows for the normalised axial stress to recover. We imagine this phenomenological cycle representing competition between the destruction of the meso-structure and density hardening, which supports the development of recurrent drops in stress (top plots).

From Fig. 1, it is evident that the model exhibits rate-dependent behaviour, particularly at low initial density ($\phi_0 = 0.2$). For higher V , the thermodynamic pressure attains higher magnitudes and takes more time to dissipate into thermal temperature, as shown by the middle row of subplots. This results in a build-up of the meso-related temperature over time for the highest velocity. However, it should be noted that the model shows little change in behaviour at velocities below $V = 0.01 \text{ m s}^{-1}$. Furthermore, the thermodynamic pressure’s time-dependent relaxation results in a smoother increase in ϕ during a stress drop and generates a smoother transition from the decline in axial stress to stress recovery. Importantly, as ϕ_0 increases, the model predicts a transition from abrupt stress drops to smoother undulating drops in stress as observed exper-

imentally in dust particles and modelled for snow. Furthermore, Fig. 1 shows that under increased strain rates, the σ - ε_v curve becomes smoother, which is in line with experimental observations [5]. While the model qualitatively predicts the transition from abrupt drops in stress to a smooth σ - ε_v curve, it does not quantitatively agree with these behaviours at the appropriate initial densities or velocities. The agreement with a specific material could be improved to better capture phenomenology by using a density-dependent η or c value or a term for viscous hardening.

3.2 Critical State Slope

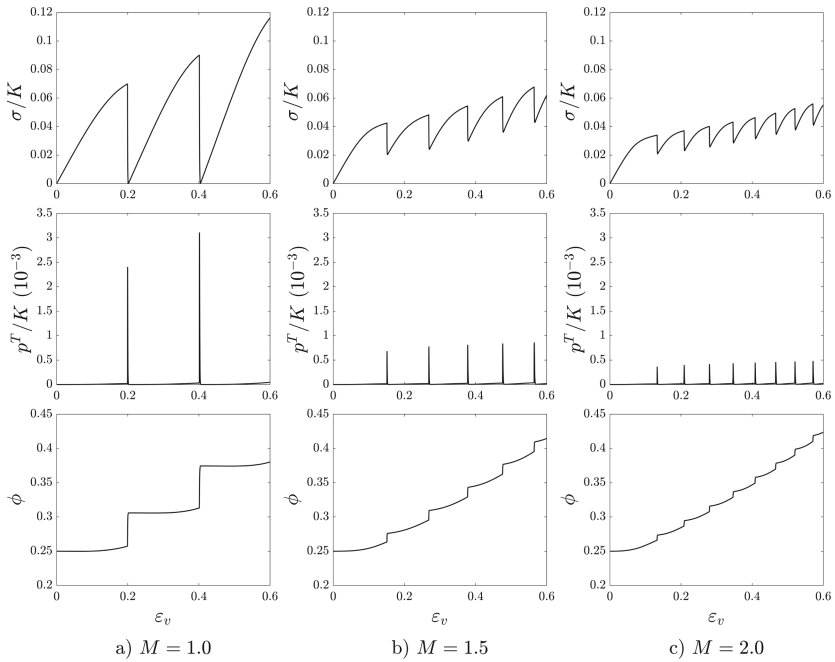


Fig. 2. The effect of the slope of the CSL on the constitutive behaviour. Panels (a-c) shows the response for three different M (in Eq. 11). Here, the effects are shown for the evolution of the normalised axial stress σ/K (top), normalised thermodynamic pressure p^T/K (middle), and solid fraction ϕ (bottom), all against ε_v .

Initially, $M = 1.5$ was assumed to be potentially reasonable for puffed rice cereals and calcareous sand, but now we explore the effect on the constitutive response. It is important to explore this as some porous materials could be relatively spherical and smooth, which leads to a lower M , such as glass beads, and still generate stress drops [7]. In granular materials, M is correlated with the internal friction angle, and thus one might expect that it could impact the material's

susceptibility to the destruction of the meso-scale. Thus, M was varied from 1 to 2 to identify its impact on the model response. In this section we prescribe $V = 0.01 \text{ m s}^{-1}$.

From Fig. 2, the decrease of axial stress during an axial stress drop is significantly larger and occurs less frequently for a low M , which matches experimental observations in glass beads [9]. These substantial drops in stress correspond to a significant increase in solid fraction ϕ and thermodynamic pressure. We interpret this as a result of low internal friction, resulting in more pronounced destruction of the meso-scale structure from velocity fluctuations at the meso-scale (meso-related temperature). As M increases, the stress drop magnitudes decrease, where in granular media, this phenomenology could be a result of higher internal friction that prohibits the destruction of the meso-scale. Moreover, these drops increase in frequency and result in a higher amount of plastic pore collapse (bottom plots).

4 Conclusions

Brittle porous media have been shown to exhibit fascinating rate-dependent compaction patterns. We develop a constitutive model, which generates recurrent abrupt stress drops and reproduces the rate-dependent transitions in compaction as observed experimentally. The critical component to the generation of these features is the introduction of the meso-related temperature, which captures in a phenomenological manner the entropy production associated with meso-scale velocity fluctuations. This temperature is assumed to destroy the meso-scale structure in heterogeneous porous media. Thus, we use the meso-related temperature to induce macroscale kinetic softening.

The occurrence and frequency of the abrupt recurrent stress drops are dependent on the competition between the destruction of the meso-structure (kinetic softening) and density hardening. Moreover, internal friction within the material is accounted for, which can moderate the magnitude of stress drops. Thus, the model can reproduce the behaviours of materials ranging from glass beads to cereals. Additionally, the time-dependent nature of sinking meso-related temperature to micro-related temperature results in rate dependence similar to that observed in puffed rice cereal [27] and dust particles [9], where the stress drops transition from abrupt to undulating with a reduced magnitude. However, these results occurred at different initial densities than those expected from experimental results. A better quantitative agreement could be achieved by using state-dependent functions for c or η or including a viscous hardening term, but these are left for future research.

While this model was developed to be general for all porous media that undergo pore collapse and density hardening, it could be enhanced to capture specific material's behaviour. The extension of the model to specific materials should be possible as the model's behaviour emerges from state variables that are useful in describing all porous media. For example, in the case of sand, the combination of breakage and pore collapse contributes to plastic dissipative processes

and could be accounted for by combining this model with breakage mechanics [18]. Alternatively, the model could be tuned to reproduce the behaviours of metallic foam by applying a yield surface shape known to produce behaviours associated with such materials.

References

1. Michlmayr, G., Cohen, D., Or, D.: Shear-induced force fluctuations and acoustic emissions in granular material. *J. Geophys. Res.: Solid Earth* **118**(12), 6086–6098 (2013)
2. Yosida, Z., Oura, H., Kuroiwa, D., Huzioka, T., Kojima, K., Kinosita, S.: Physical studies on deposited snow. IV.; mechanical properties (3). *Contrib. Inst. Low Temperature Sci.* **13**, 55–100 (1958)
3. Löwe, H., Zaiser, M., Möisinger, S., Schlee, S.: Snow mechanics near the ductile-brittle transition: compressive stick-slip and snow microquakes. *Geophys. Res. Lett.* **47**(4), e2019GL085491 (2020)
4. Valdes, J.R., Fernandes, F.L., Einav, I.: Periodic propagation of localized compaction in a brittle granular material. *Granular Matter* **14**(1), 71–76 (2012)
5. Valdes, J.R., Guillard, F., Einav, I.: Evidence that strain-rate softening is not necessary for material instability patterns. *Phys. Rev. Lett.* **119**(11), 118004 (2017)
6. Papka, S.D., Kyriakides, S.: In-plane crushing of a polycarbonate honeycomb. *Int. J. Solids Struct.* **35**(3–4), 239–267 (1998)
7. Kuhn, M.R., Daouadji, A.: Stress fluctuations during monotonic loading of dense three-dimensional granular materials. *Granular Matter* **21**(1), 1–14 (2019). <https://doi.org/10.1007/s10035-018-0861-7>
8. Jiang, Y., Liu, M.: Granular solid hydrodynamics. *Granular Matter* **11**(3), 139–156 (2009)
9. Pacheco-Vázquez, F., Omura, T., Katsuragi, H.: Undulating compression and multistage relaxation in a granular column consisting of dust particles or glass beads. *Phys. Rev. Res.* **3**(1), 013190 (2021)
10. Alaei, E., Marks, B., Einav, I.: A hydrodynamic-plastic formulation for modelling sand using a minimal set of parameters. *J. Mech. Phys. Solids* **151**, 104388 (2021)
11. Dafalias, Y.F.: Bounding surface plasticity. I: Mathematical foundation and hypoplasticity. *J. Eng. Mech.* **112**(9), 966–987 (1986)
12. Einav, I.: The unification of hypo-plastic and elasto-plastic theories. *Int. J. Solids Struct.* **49**(11–12), 1305–1315 (2012)
13. Einav, I., Liu, M.: Hydrodynamic derivation of the work input to fully and partially saturated soils. *J. Mech. Phys. Solids* **110**, 205–217 (2018)
14. Roscoe, K., Burland, J.: On the generalized stress-strain behaviour of wet clay. In: *Engineering Plasticity*, pp. 535–609 (1968)
15. Meschke, G., Liu, C., Mang, H.A.: Large strain finite-element analysis of snow. *J. Eng. Mech.* **122**(7), 591–602 (1996)
16. Gaume, J., Gast, T., Teran, J., Van Herwijnen, A., Jiang, C.: Dynamic anticrack propagation in snow. *Nat. Commun.* **9**(1), 1–10 (2018)
17. Abdallah, Y., Sulem, J., Stefanou, I.: Compaction banding in high-porosity carbonate rocks: 2. A gradient-dependent plasticity model. *J. Geophys. Res.: Solid Earth* **125**(12), e2020JB020610 (2020)
18. Tengattini, A., Das, A., Einav, I.: A constitutive modelling framework predicting critical state in sand undergoing crushing and dilation. *Géotechnique* **66**(9), 695–710 (2016)

19. Barraclough, T.W., Blackford, J.R., Liebenstein, S., Sandfeld, S., Stratford, T.J., Weinländer, G., Zaiser, M.: Propagating compaction bands in confined compression of snow. *Nat. Phys.* **13**(3), 272–275 (2017)
20. Debregeas, G., Tabuteau, H., Di Meglio, J.M.: Deformation and flow of a two-dimensional foam under continuous shear. *Phys. Rev. Lett.* **87**(17), 178305 (2001)
21. Pouliquen, O., Forterre, Y., Le Dizes, S.: Slow dense granular flows as a self-induced process. *Adv. Complex Syst.* **4**(04), 441–450 (2001)
22. Einav, I., Guillard, F.: Tracking time with ricequakes in partially soaked brittle porous media. *Sci. Adv.* **4**(10), eaat6961 (2018)
23. Lv, Y., Wang, Y., Zuo, D.: Effects of particle size on dynamic constitutive relation and energy absorption of calcareous sand. *Powder Technol.* **356**, 21–30 (2019)
24. Coduto, D.P., Kitch, W.A., Yeung, M.C.R.: *Foundation Design: Principles and Practices*, vol. 2. Prentice Hall, USA (2001)
25. Gercek, H.: Poisson’s ratio values for rocks. *Int. J. Rock Mech. Mining Sci.* **44**(1), 1–13 (2007)
26. Zhang, J., Luo, M.: Dilatancy and critical state of calcareous sand incorporating particle breakage. *Int. J. Geomech.* **20**(4), 04020030 (2020)
27. Guillard, F., Golshan, P., Shen, L., Valdes, J.R., Einav, I.: Dynamic patterns of compaction in brittle porous media. *Nat. Phys.* **11**(10), 835–838 (2015)



Multiscale Modeling of Elasto-Plasticity in Heterogeneous Geomaterials Based on Continuum Micromechanics

Mahdad Eghbalian¹ , Mehdi Pouragha² , and Richard Wan¹ 

¹ Department of Civil Engineering, University of Calgary, Calgary, AB, Canada
{meghbali, wan}@ucalgary.ca

² Department of Civil and Environmental Engineering, Carleton University, Ottawa, ON, Canada

mehdi.pouragha@carleton.ca

Abstract. In this paper, we investigate some micromechanical aspects of elasto-plasticity in heterogeneous geomaterials. The aim is to upscale the elasto-plastic behavior for a representative volume of the material which is a very challenging task due to the irreversible deformations involved. Considering the plastic strains as eigen-strains allows us to employ the powerful tools offered by Continuum Micromechanics which are mainly developed for upscaling of eigen-stressed elastic media. The validity of such eigen-strain based formulation of multiscale elasto-plasticity is examined in the current work by comparing its predictions against Finite Element (FE) simulations. The great agreement between the multiscale analytical model predictions and numerical values confirms that plastic strains can be considered as eigen-strains.

Keywords: Multiscale · Plasticity · Eigen-strain · Finite elements

1 Introduction

Elastic properties, plastic deformations and failure strength of geomaterials are strongly influenced by their underlying heterogeneous microstructure, including shape and topology of individual material phases. Advances made in multiscale modeling techniques have allowed the development of macroscopic models for geomaterials that are predicated on the inherent microstructural features. Most notably, as an extension to classical linear homogenization techniques, Pichler and Hellmich [1] generalized the primitive Transformation Field Analysis (TFA) of Dvorak and Benveniste [2] developed for eigen-stressed elastic composite media, to arbitrary ellipsoidal shape and directional orientation of the material phases. For an elasto-plastic composite, on the other hand, complexities pertaining to the dissipative behavior of the material naturally arise; in particular, regarding the upscaling of plastic strains. The idea of considering the plastic strains as eigen-strains in homogenization was first proposed in the early 1990s (see Dvorak [3]). Such an assumption appears to be reasonable given that the plastic strains are kinematically incompatible, thus qualify as free strains [4]. As such, the homogenization of

elasto-plasticity would be greatly simplified in that, the elasto-plastic material can be replaced with an equivalent eigen-stressed elastic media. Such an approach was adopted by Morin et al. [4] within the generalized TFA framework of Pichler and Hellmich [1]; and later on by the authors [5] who extended the framework to model the poro-elasto-plastic behavior of clays. The current work examines the validity of the eigen-strain formulation of plastic strains by comparing the multiscale model predictions against FE results.

2 Eigen-Strain Based Multiscale Elasto-Plasticity Framework

Let us consider a heterogeneous Representative Elementary Volume (REV) of the material comprising elasto-plastic phases (denoted by the set \mathcal{N}). The phases generally have differing properties, shapes and directional orientations. The objective is to formulate the overall elasto-plastic constitutive relation of the REV by upscaling the local heterogeneous strain and stress fields within the REV.

Notations: Mathematical double-struck capital letters denote fourth-order tensors, while second-order tensors and scalars are shown in normal type. Moreover, variables referring to the macroscopic scale are accented with an overline.

2.1 Homogenization of Microscopic Elasto-Plasticity

We assume all phases to show an elastic-perfectly plastic behavior and undergo small strains. A fundamental assumption is considering the plastic strains as eigen-strains. Under these conditions, the stress state inside the REV can be written as:

$$\boldsymbol{\sigma}_\alpha = \mathbb{C}_\alpha \boldsymbol{\varepsilon}_\alpha + \boldsymbol{\zeta}_\alpha \quad \forall \alpha \in \mathcal{N} \quad (1)$$

where $\boldsymbol{\sigma}$ and $\boldsymbol{\varepsilon}$ are stress and strain tensors, \mathbb{C} is the elasticity tensor, and $\boldsymbol{\zeta} = -\mathbb{C} : \boldsymbol{\varepsilon}^P$ is the eigen-stress tensor. The evolution of plastic strains ($\boldsymbol{\varepsilon}^P$) is assumed to follow the flow rule:

$$\dot{\boldsymbol{\varepsilon}}^P = \dot{\lambda} \frac{\partial G}{\partial \boldsymbol{\sigma}} \quad (2)$$

where the plastic potential G is generally different from the yield function. The yield function F and the plastic multiplier λ satisfy the Melan-Kuhn-Tucker conditions.

In the constitutive relation (Eq. 1), the microscopic stress $\boldsymbol{\sigma}$ satisfies the momentum balance condition, while the strain $\boldsymbol{\varepsilon}$ is kinematically compatible. Moreover, the REV is subjected to uniform macroscopic strain $\bar{\boldsymbol{\varepsilon}}$ at its boundary (Hashin boundary condition). Such boundary condition guarantees that the volume average of strains inside the REV is equal to the prescribed macroscopic strain. Upon using the Levin's theorem for pre-stressed heterogeneous composite media, the macroscopic stress is obtained as:

$$\bar{\boldsymbol{\sigma}} = \bar{\mathbb{C}} : \bar{\boldsymbol{\varepsilon}} + \bar{\boldsymbol{\zeta}} \quad (3)$$

where the macroscopic elasticity $\bar{\mathbb{C}}$ and eigen-stress $\bar{\boldsymbol{\zeta}}$ are defined in terms of average properties of phases and a strain concentration tensor \mathbb{A} (see Sect. 2.2) as:

$$\bar{\mathbb{C}} = \sum_{\alpha \in \mathcal{N}} f_\alpha \mathbb{C}_\alpha : \mathbb{A}_\alpha \quad (4)$$

$$\bar{\boldsymbol{\varepsilon}} = \sum_{\alpha \in \mathcal{N}} f_{\alpha} \mathbb{A}_{\alpha}^{\top} : \boldsymbol{\varepsilon}_{\alpha} = - \sum_{\alpha \in \mathcal{N}} f_{\alpha} \mathbb{A}_{\alpha}^{\top} : \mathbb{C}_{\alpha} : \boldsymbol{\varepsilon}_{\alpha}^{\text{p}} \quad (5)$$

In the above relations, f denotes the volume fraction. Equation 3 can be re-stated in form of the classical constitutive relation for an elastic-perfectly plastic material:

$$\bar{\boldsymbol{\sigma}} = \bar{\mathbb{C}} : (\bar{\boldsymbol{\varepsilon}} - \bar{\boldsymbol{\varepsilon}}^{\text{p}}) \quad (6)$$

with the following definition for the macroscopic ‘‘plastic’’ strain $\bar{\boldsymbol{\varepsilon}}^{\text{p}}$:

$$\bar{\boldsymbol{\varepsilon}}^{\text{p}} = \bar{\mathbb{C}}^{-1} : \left(\sum_{\alpha \in \mathcal{N}} f_{\alpha} \mathbb{A}_{\alpha}^{\top} : \mathbb{C}_{\alpha} : \boldsymbol{\varepsilon}_{\alpha}^{\text{p}} \right) \quad (7)$$

2.2 Multiscale Return-Mapping Algorithm

In this section, we present the procedure for numerical integration of the multiscale elasto-plasticity equations over discrete time steps. Under applied loading, the state variables of the REV evolve, including the induced plastic strains at the microscopic scale. Tracking the evolution of microscopic plastic strains requires access to a localization relation for the strain inside the REV. Based on the generalized TFA formulation [1], the phase averaged strains of the pre-stressed media can be related to the boundary strain and all the eigen-stresses occurring in all the other phases through employing the so-called concentration and influence tensors \mathbb{A} and \mathbb{B} as:

$$\boldsymbol{\varepsilon}_{\alpha} = \mathbb{A}_{\alpha} : \bar{\boldsymbol{\varepsilon}} - \sum_{\beta \in \mathcal{N}} \mathbb{B}_{\alpha\beta} : \mathbb{C}_{\beta}^{-1} : \boldsymbol{\varepsilon}_{\beta} = \mathbb{A}_{\alpha} : \bar{\boldsymbol{\varepsilon}} + \sum_{\beta \in \mathcal{N}} \mathbb{B}_{\alpha\beta} : \boldsymbol{\varepsilon}_{\beta}^{\text{p}} \quad \forall \alpha \in \mathcal{N} \quad (8)$$

Closed-form expressions for the concentration and influence tensors are presented in the works of Pichler and Hellmich [1], Morin et al. [4] and Eghbalian [5] for different homogenization schemes. A fully strain-controlled loading scheme is considered here, while the extension to hybrid stress-strain loading can be found in Eghbalian [5]. Knowing the REV state at time step n ($\boldsymbol{\varepsilon}^n$, $\boldsymbol{\varepsilon}^{\text{p},n}$, $\boldsymbol{\sigma}^n$, $\bar{\boldsymbol{\varepsilon}}^{\text{p},n}$ and $\bar{\boldsymbol{\sigma}}^n$) and given the increment in the macroscopic strain ($\bar{\boldsymbol{\varepsilon}}^{n+1}$), the aim is to obtain the state variables at step $n+1$, i.e. $\boldsymbol{\varepsilon}^{n+1}$, $\boldsymbol{\varepsilon}^{\text{p},n+1}$, $\boldsymbol{\sigma}^{n+1}$, $\bar{\boldsymbol{\varepsilon}}^{n+1}$, $\bar{\boldsymbol{\varepsilon}}^{\text{p},n+1}$ and $\bar{\boldsymbol{\sigma}}^{n+1}$. For the macroscopic strain, we can write:

$$\bar{\boldsymbol{\varepsilon}}^{n+1} = \bar{\boldsymbol{\varepsilon}}^n + \bar{\boldsymbol{\varepsilon}}^{n+1} \quad (9)$$

Next, in a trial attempt, we assume no additional microscopic plastic strains are induced in the REV during the current step. The trial microscopic strains and stresses at step $n+1$ are thus calculated for each phase α using the localization relation (Eq. 8) and constitutive relation (Eq. 1) as:

$$\boldsymbol{\varepsilon}_{\alpha}^{n+1,\text{tr}} = \mathbb{A}_{\alpha} : \bar{\boldsymbol{\varepsilon}}^{n+1} + \sum_{\beta \in \mathcal{N}} \mathbb{B}_{\alpha\beta} : \boldsymbol{\varepsilon}_{\beta}^{\text{p},n} \quad \forall \alpha \in \mathcal{N} \quad (10)$$

$$\boldsymbol{\sigma}_{\alpha}^{n+1,\text{tr}} = \mathbb{C}_{\alpha} : \left(\boldsymbol{\varepsilon}_{\alpha}^{n+1,\text{tr}} - \boldsymbol{\varepsilon}_{\alpha}^{\text{p},n} \right) \quad \forall \alpha \in \mathcal{N} \quad (11)$$

Next, the assumption of purely elastic behavior (trial attempt) is checked for all phases via inserting the trial stresses into the yield criterion F :

$$\mathcal{F}_\alpha^{\text{tr}} = F\left(\boldsymbol{\sigma}_\alpha^{n+1,\text{tr}}\right) \quad \forall \alpha \in \mathcal{N} \quad (12)$$

If $\mathcal{F}_\alpha^{\text{tr}} < 0 \alpha \in \mathcal{N}$, the REV is elastic and the calculated trial strains and stresses are accepted. If for at least one phase $\mathcal{F}_\alpha^{\text{tr}} > 0$, the REV is plastic and return mapping should be performed. Referring to Eqs. 1, 8, 10 and 11, the phase strains and stresses at step $n + 1$ can generally be stated based on their trial values as:

$$\boldsymbol{\varepsilon}_\alpha^{n+1} = \boldsymbol{\varepsilon}_\alpha^{n+1,\text{tr}} + \sum_{\beta \in \mathcal{N}} \dot{\lambda}_\beta^{n+1} \mathbb{B}_{\alpha\beta} : \frac{\partial G}{\partial \boldsymbol{\sigma}_\beta} \quad \forall \alpha \in \mathcal{N} \quad (13)$$

$$\boldsymbol{\sigma}_\alpha^{n+1} = \boldsymbol{\sigma}_\alpha^{n+1,\text{tr}} + \mathbb{C}_\alpha : \left(\sum_{\beta \in \mathcal{N}} \dot{\lambda}_\beta^{n+1} \mathbb{B}_{\alpha\beta} : \frac{\partial G}{\partial \boldsymbol{\sigma}_\beta} - \dot{\lambda}_\alpha^{n+1} \frac{\partial G}{\partial \boldsymbol{\sigma}_\alpha} \right) \quad \forall \alpha \in \mathcal{N} \quad (14)$$

We denote the set of elastic and plastic phases by \mathcal{N}_e and \mathcal{N}_p , respectively. For the elastic phases we have $\dot{\lambda}_\alpha^{n+1} = 0 \quad \forall \alpha \in \mathcal{N}_e$, while for the plastic phases $\dot{\lambda}^{n+1}$ is determined by satisfying the yield criterion:

$$F\left(\boldsymbol{\sigma}_\alpha^{n+1}\right) = 0 \quad \forall \alpha \in \mathcal{N}_p \quad (15)$$

resulting in a system of nonlinear equations that can be solved using the Newton iterative scheme. The calculated plastic multipliers are then used in Eqs. 13 and 14 to update the microscopic stresses and strains, from which the macroscopic stresses and strains can be updated using Eqs. 6 and 7. It should be pointed out that upon updating the microscopic stresses, it is possible that some of the phases that were initially deemed elastic also become plastic. It is also possible that the converged plastic multipliers become negative for some phases, which means those phases are no longer plastic. In both cases, the set of plasticized phases should be updated in an iterative process until convergence.

3 Validation Against FE Results

In this section, we validate the predictions of the multiscale formulation (Sect. 2) against FE simulations where multiple phases are explicitly modeled. A 3D spherical REV of unit radius is considered which includes 26 oblate spheroidal inclusions with aspect ratio of 0.35 and total volume fraction of 0.143 distributed isotropically inside a matrix. The matrix is elastic, while the inclusions obey an associated Drucker-Prager elastoplasticity:

$$F = G = \boldsymbol{\sigma}_{\text{eq}} + \boldsymbol{\sigma}_m \tan \phi - \boldsymbol{\sigma}_0 \quad (16)$$

where $\boldsymbol{\sigma}_m$ is the mean stress, $\boldsymbol{\sigma}_{\text{eq}}$ is the equivalent deviatoric stress, ϕ is the friction angle and $\boldsymbol{\sigma}_0$ is the failure stress under pure shear. The material properties of the REV are listed in Table 1. The REV is subjected to uniaxial compression loading by prescribing a total

vertical strain of -0.001 and zero lateral stresses, followed by unloading to half the total vertical strain. For the eigen-stress based multiscale analysis, the Mori-Tanaka scheme is used for calculation of concentration and influence tensors. FE simulations are performed using the Abaqus software [6]. Due to symmetry of the problem, only 1/8 of the REV is modeled. Different views of the REV are shown in Fig. 1 together with the boundary conditions. The flat sides of the REV are constrained in the normal direction while the loading is applied on the outer surface of the sphere. The REV is discretized using approximately 120,000 quadratic tetrahedron elements.

In order to apply the loading on the curved surface of the REV, we define a ghost point (see Fig. 2) and constrain its degrees of freedom to those of the nodes on the outer surface of the REV using the built-in Multi Point Constraint option in ABAQUS. The loading on the REV is then simply controlled by prescribing the displacement or force of the ghost point.

Figure 3 shows the evolution of macroscopic axial stress ($|\bar{\sigma}_{33}|$) versus the macroscopic axial ($\bar{\epsilon}_{33}$) and lateral ($\bar{\epsilon}_{11}$) strains. For comparison purposes, the problem is also solved for the case where the inclusions are elastic. It is seen that the multiscale model predicts well the REV response in both the loading and unloading regimes. Next, the components of local average strains for three inclusions (labeled in Fig. 1) are plotted in Fig. 4 against the prescribed macroscopic axial strain in the loading regime. Slight differences are observed between the model predictions and FE results for inclusions #1 and #3 which are due to the severe interactions between inclusions in the FE model leading to heterogeneous strain/stress fields within inclusions. This is in contrast with the assumption in the multiscale model where the strain (and stress) fields inside inclusions are assumed homogeneous. Nevertheless, it appears that when these discrepancies are volume averaged over the whole REV, they cancel out each other, leading to a good match between the overall responses in the multiscale model and FE (Fig. 3).

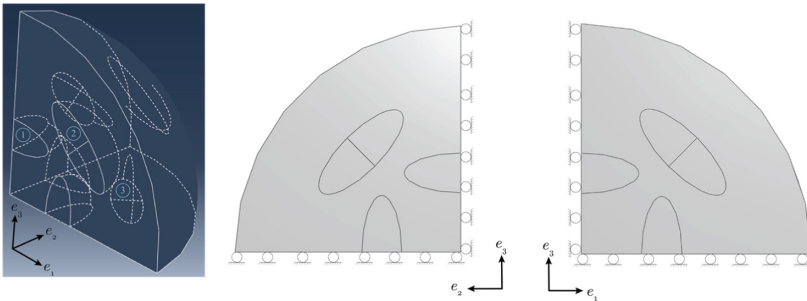


Fig. 1. Different views of the REV considered for the numerical homogenization in this work. 1/8 of the sample REV used for FE simulations.

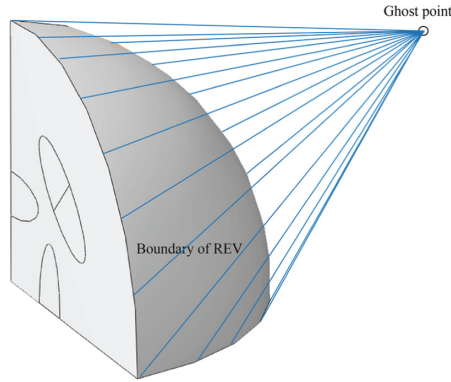


Fig. 2. The ghost point used for applying the homogeneous boundary conditions on the REV.

Table 1 Material properties of the sample REV.

	Parameter	Value
Matrix	Young’s modulus (MPa)	100
	Poisson’s ratio	0.25
Inclusions	Young’s modulus (MPa)	1000
	Poisson’s ratio	0.25
	Friction angle ϕ (radian)	0.0
	Failure stress σ_0 (MPa)	0.12

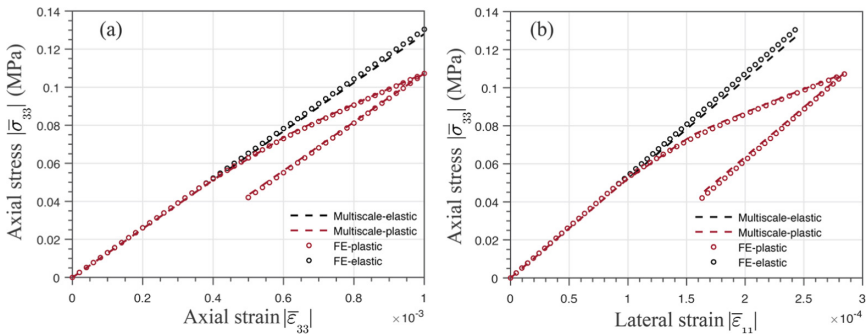


Fig. 3. Variation of macroscopic axial stress versus macroscopic (a) axial and (b) lateral strains. Comparison between the multiscale model predictions and FE results.

Finally, returning to Eq. 7, $\bar{\epsilon}^P$ is the macroscopic residual strain that is not recovered upon the removal of the external load on the REV and is classically referred to as “plastic” strain. It consists of a plastic part which is the volume of average of microscopic plastic strains, and a “frozen” elastic strain which does not recover in the unloading regime.

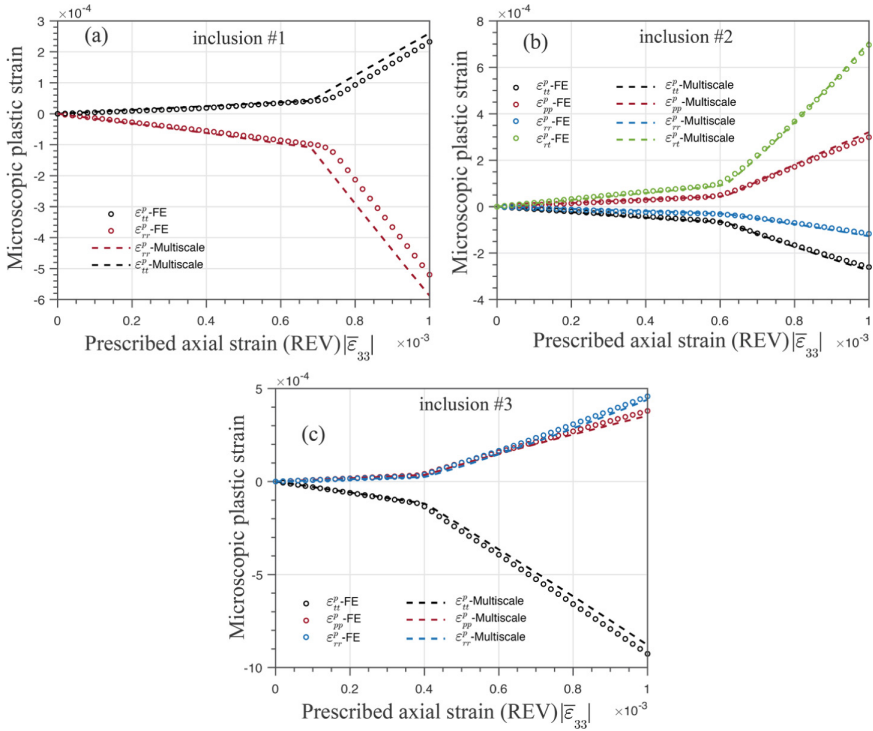


Fig. 4. Variation of average plastic strain versus prescribed macroscopic axial stress for the three inclusions shown in Fig. 1. The local direction r coincides with the axis of symmetry of the inclusion, while t and p refer to in-plane directions.

The macroscopic “plastic” strain together with its plastic part are plotted in Fig. 5 for both the multiscale and FE models. The model correctly predicts the macroscopic plastic strain demonstrating its capability in modeling the macroscopic unloading regime (as also seen in Fig. 3).

4 Concluding Remarks

The study investigates the robustness of an eigen-strain based multiscale model formulated within the extended TFA framework for upscaling the elasto-plastic behavior of a heterogeneous REV. Comparing the model predictions with FE simulations of a sample REV shows that such formulation is indeed capable of capturing the macroscopic response of the elasto-plastic REV as well as evolution of microscopic stress and strain fields inside the REV, in both the loading and unloading regimes, with acceptable accuracy. The current formulation thus emerges as a simple, yet powerful, tool for strength predictions of heterogeneous geomaterials.

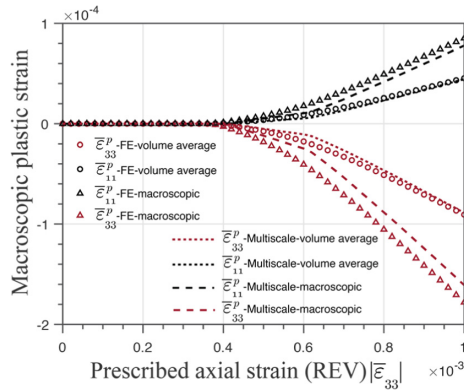


Fig. 5. Volume average of microscopic plastic strain versus the macroscopic “plastic” strain.

Acknowledgement. This work was funded by the Natural Sciences and Engineering Research Council of Canada (Grant No. RGPIN-2016-04086 held by R.W. and Grants No. RGPIN-2020-06480 and DGEGR-2020-00411 held by M.P.).

References

1. Pichler, B., Hellmich, C.: Estimation of influence tensors for eigenstressed multiphase elastic media with nonaligned inclusion phases of arbitrary ellipsoidal shape. *J. Eng. Mech.* **136**(8), 1043–1053 (2010)
2. Dvorak, G.J., Benveniste, Y.: On transformation strains and uniform fields in multiphase elastic media. *Proc. R. Soc. Lond. A* **437**(1900), 291–310 (1992)
3. Dvorak, G.J.: Transformation field analysis of inelastic composite materials. *Proc. R. Soc. Lond. A* **437**(1900), 311–327 (1992)
4. Morin, C., Vass, V., Hellmich, C.: Micromechanics of elastoplastic porous polycrystals: theory, algorithm, and application to osteonal bone. *Int. J. Plast* **91**, 238–267 (2017)
5. Eghbalian, M.: Hydro-mechanical coupling and failure behavior of argillaceous sedimentary rocks: a multi-scale approach. Ph.D. thesis, University of Calgary (2019)
6. Abaqus.: Dassault Systemes Simulia Corporation. Johnston, Rhode Island (2019)

Author Index

A

Alshibli, Khalid A., [87](#)

B

Baud, Patrick, [31](#)
Benahmed, N., [74](#)
Bennett, Terry, [41](#)
Borja, Ronaldo I., [155](#)
Bui, Ha H., [41](#)

C

Calo, Victor M., [24](#)
Chen, Ruoyu, [144](#)
Cier, Roberto J., [24](#)
Crespo-Parraga, Leonardo, [51](#)

D

Darve, Félix, [3](#)
del Castillo, Enrique M., [155](#)
di Prisco, Claudio, [162](#)
Dight, P., [173](#)
Dyskin, A. V., [173](#)
Dyskin, Arcady V., [127](#), [136](#), [182](#)

E

Eghbalian, Mahdad, [251](#)
Einav, Itai, [51](#), [240](#)

F

Farahnak, Mojtaba, [212](#)
Fávero Neto, Alomir H., [155](#)
Flessati, Luca, [162](#)

G

Grabowski, Aleksander, [230](#)

Guillard, François, [51](#), [240](#)
Gutierrez, Marte, [13](#)

H

He, Junxian, [127](#)
Hickman, Randall, [13](#)
Hu, Manman, [59](#), [67](#)
Huang, Lingcao, [31](#)
Hueckel, Tomasz, [144](#)

I

Imseeh, Wadi H., [87](#)
Ivšić, Tomislav, [193](#)

J

Jeffcoat-Sacco, B., [173](#)

K

Kenesei, Peter, [87](#)
Krzaczek, M., [114](#)
Krzaczek, Marek, [220](#)

L

Lesueur, Martin, [205](#)
Lindqwister, Winston, [144](#)
Liu, Chong, [59](#)

M

Meng, Fanbao, [31](#)
Mouydeaux, Anthony, [3](#)

N

Nguyen, Giang D., [41](#)
Nicot, François, [3](#), [212](#)

Nitka, M., [114](#)
Nitka, Michal, [220](#)
Nitka, Michal, [230](#)

P

Pasternak, E., [173](#)
Pasternak, Elena, [127](#), [136](#), [182](#)
Perić, Dunja, [193](#)
Phan, Dat G., [41](#)
Poulet, Thomas, [24](#), [205](#)
Pouragha, Mehdi, [212](#), [251](#)

R

Regenauer-Lieb, Klaus, [59](#), [67](#)
Riley, David, [240](#)
Rojas, Sergio, [24](#)

S

Sharma, Hemant, [87](#)
Stathas, Alexandros, [99](#)
Stefanou, Ioannis, [99](#)

Sun, Qingpei, [67](#)

T

Tejchman, J., [114](#)
Tejchman, Jacek, [220](#), [230](#)

V

Veveakis, Manolis, [24](#), [144](#), [205](#)

W

Wan, Richard, [3](#), [212](#), [251](#)
Wang, H., [173](#)
Wautier, A., [74](#)
Wautier, Antoine, [3](#)
Wong, Rui X., [182](#)
Wong, Teng-fong, [31](#)

Z

Zhang, Xinrui, [205](#)
Zuo, J., [74](#)